AD

AMMRC TR 81-14

BRITTLE MATERIALS DESIGN, HIGH TEMPERATURE GAS TURBINE

Technical Report By:

Arthur F. McLean, Ford Motor Company, Dearborn, Michigan 48121
Eugene A. Fisher, Ford Motor Company, Dearborn, Michigan 48121

March, 1981

DTIC
ELECTE
NOV 4 1981
A
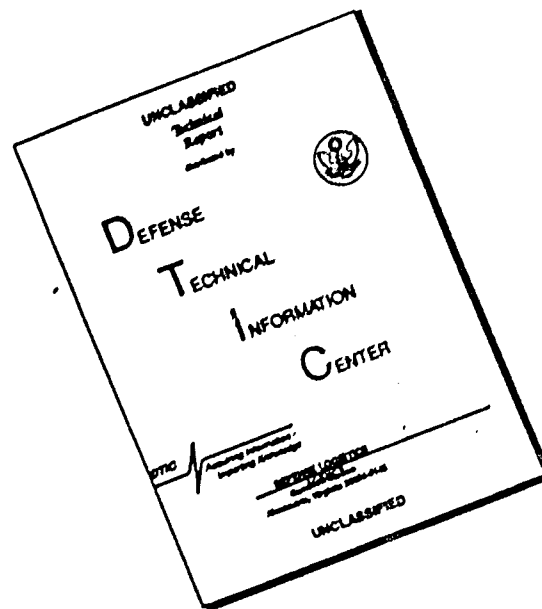
Prepared for

ARMY MATERIALS AND MECHANICS RESEARCH CENTER
Watertown, Massachusetts 02172

81 11 03 015

DISCLAIMER NOTICE

THIS DOCUMENT IS BEST QUALITY AVAILABLE. THE COPY FURNISHED TO DTIC CONTAINED A SIGNIFICANT NUMBER OF PAGES WHICH DO NOT REPRODUCE LEGIBLY.

The view and conclusions contained in this document are those of the authors and should not be interpreted as necessarily representing the official policies, either expressed or implied, of the Defense Advanced Research Projects Agency of the U.S. Government.

Mention of any trade names or manufacturers in this report shall not be construed as advertising nor as an official indorsement or approval of such products or companies by the United States Government.

DISPOSITION INSTRUCTIONS

Destroy this report when it is no longer needed.
Do not return it to the originator.

REPORT DOCUMENTATION PAGE		READ INSTRUCTIONS BEFORE COMPLETING FORM
1. REPORT NUMBER AMMRC TR81-14	2. GOVT ACCESSION NO. AD-A106670	3. RECIPIENT'S CATALOG NUMBER
4. TITLE (and Subtitle) Brittle Materials Design, High Temperature Gas Turbine		5. TYPE OF REPORT & PERIOD COVERED Final Report 7-1-71 to 8-31-79
		6. PERFORMING ORG. REPORT NUMBER
7. AUTHOR(s) E. F. McLean, Ford Motor Company A. A. Fisher, Ford Motor Company		8. CONTRACT OR GRANT NUMBER(s) DAAG 46-71-C-0162, ARPA Order-1849
9. PERFORMING ORGANIZATION NAME AND ADDRESS Ford Motor Company, Dearborn, MI 48121		10. PROGRAM ELEMENT, PROJECT, TASK AREA & WORK UNIT NUMBERS D/A Project: ARPA Order 1849 AMCMS Code: Agency Accession: DA OD 4733
11. CONTROLLING OFFICE NAME AND ADDRESS Army Materials and Mechanics Research Center Watertown, Massachusetts 02172		12. REPORT DATE March 1981
		13. NUMBER OF PAGES
14. MONITORING AGENCY NAME & ADDRESS(if different from Controlling Office)		15. SECURITY CLASS. (of this report) Unclassified
		15a. DECLASSIFICATION/DOWNGRADING SCHEDULE

16. DISTRIBUTION STATEMENT (of this Report)

Approved for public release: distribution unlimited.

17. DISTRIBUTION STATEMENT (of the abstract entered in Block 20, if different from Report)

18. SUPPLEMENTARY NOTES

19. KEY WORDS (Continue on reverse side if necessary and identify by block number)

Gas Turbine Engine	Silicon Nitride
Brittle Design	Silicon Carbide
Ceramics	Non-Destructive Test
High Temperature Materials	Mechanical Properties

20. ABSTRACT (Continue on reverse side if necessary and identify by block number)

(See Reverse Side)

DD FORM 1473 EDITION OF 1 NOV 65 IS OBSOLETE
1 JAN 73

ABSTRACT

Starting in July 1971, the Defense Advanced Research Projects Agency (DARPA) sponsored a joint program with the Ford Motor Company to demonstrate and encourage the use of brittle materials in engineering design. The program, which was to be a total systems iterative approach to high temperature structural design with ceramics in highly stressed applications, focused on the development of ceramic components for gas turbine application. A goal of 200 hours of engine or engine rig demonstration for representative duty cycle temperatures in a regenerated vehicular gas turbine was chosen, with uncooled ceramic components to operate at least 25 hours at 2500°F, considerably beyond the temperatures possible with uncooled metal components. The total systems approach included major efforts in ceramic design, materials development, fabrication process development, and test and evaluation methodology. Considerable progress was made in each of these areas during the course of the program. For example, the strength of reaction bonded silicon nitride (RBSN) used in the stator and rotor blades was more than tripled between July 1971 and July 1977.

By the end of the program, 200 hours of duty cycle durability on turbine test rigs (between 1930°F — 2500°F) was attained on RBSN stationary components including stators, nose cones and turbine rotor tip shrouds. Similarly, 200 hours of duty cycling on test rigs was attained with reaction sintered SiC combustors and stators. A 200 hour test of a duo-density silicon nitride rotor with 1800°F rim temperatures, with maximum blade temperatures of approximately 2200°F, was run at speeds to 50,000 rpm. Engine tests of up to 100 hours duration were run with an entire uncooled ceramic stationary flow path (only the rotors being metallic) at up to 87% of engine design speed at 1930°F. A 37 hour engine rig test was run with an uncooled ceramic rotor at temperatures up to 2500°F and speeds up to 50,000 RPM (100% Design E speed).

The program demonstrated that design with brittle materials in highly stressed applications is possible and, in particular, that ceramics as major structural components in gas turbine engines are feasible.

FOREWORD

This report is the final technical report of the "Brittle Materials Design, High Temperature Gas Turbine" program initiated by the Defense Advanced Research Projects Agency, DARPA Order Number 1849, and Contract Number DAAG-46-71-C-0162. Late in the program, additional support was provided by DOE and NASA. This was an incrementally-funded program.

Since this was an iterative design and materials development program, design concepts and materials selection and/or properties presented in this report will probably not be those finally utilized. Thus all design and property data must be considered tentative, and the report should be considered to be illustrative of the design, materials, processing, and NDE techniques being developed for brittle materials at the close of the experimental portion of this program on August 31, 1979.

A central role in the initiation and continued support of this program was played by two individuals: Dr. Maurice J. Sinnot who was Director of Material Science at DARPA, whose foresight succeeded in establishing what, at the time, was a very unconventional program, and Dr. Alvin E. Gorum who was Director of AMMRC and whose concept of participative monitoring played an important role in the success of the program.

The principal investigator of this program was Mr. A. F. McLean, Ford Motor Company, and the technical monitors of this work were E. S. Wright, E. M. Lenoe, and R. N. Katz, AMMRC. The authors would like to acknowledge the valuable contributions to the performance of this work by the following people:

Ford Motor Company

D. Alexander, R. L. Allor, B. J. Amman, G. W. Andrews, N. Arnon, J. R. Baer, R. R. Baker, P. Beardmore, P. Berry, H. Blair, J. Bomback, J. Borchanian, G. T. Bretz, J. H. Buechel, D. J. Cassidy, K. Casstevens, J. C. Caverly. G. J. Chaundy, H. A. Cikanek, W. D. Compton, W. B. Copple, A. B. Czarnecki, D. A. Davis, G. C. DeBell, E. F. Dore, R. C. Elder, J. Errante, A. Ezis, W. A. Fate, J. Gault, M. Goodyear, R. K. Govila, J. W. Grant, D. L. Hartsock, J. J. Harwood, P. H. Havstad, J. A. Herman, E. R. Herrmann, B. T. Howes, D. W. Huser, R. C. Innes, R. A. Jeryan, C. F. Johnson, R. Kazmarek, K. H. Kinsman, C. A. Knapp. J. T. Kovach, J. G. Lafond, D. MacKenzie, J. A. Mangels, T. W. McLaughlin, W. E. Meyer, R. C. McGovern, M. Millberg, J. J. Mittman, R. E. Mogridge, T. G. Mohr, B. J. Moore, J. T. Neil, P. F. Nicholls, J. M. Nicholson, M. D. Noldy, A. Paluszny, J. M. Pieprzak, R. L. Predmesky, L. V. Reatherford, D. E. Ries, J. J. Schuldies, M. Seaman, J. R. Secord, N. L. Smith, E. D. Stiles, K. H. Styhr, M. J. Susko, L. R. Swank, G. Tennenhouse, D. M. Tracy, W. Trela, J. Uy, C. Vassallo, N. F. Waugh, T. J. Whalen, R. M. Williams, W. Wu, S. Zyck.

Army Materials and Mechanics Research Center

J. J. Burke, G. E. Gazza, D. R. Messier, H. Priest.

Defense Advanced Research Projects Agency

A. L. Bement, E. C. Van Reuth

TABLE OF CONTENTS

TABLE OF CONTENTS

TABLE OF CONTENTS

EXECUTIVE SUMMARY

Introduction

The major purpose of this Defense Advanced Research Project Agency (DARPA) program was the demonstration of brittle materials for demanding high temperature structural applications in order to encourage wider use of these materials in engineering systems. The program goal was to show by a practical demonstration that efforts in (1) ceramic design, (2) materials and processes, (3) fabrication, and (4) testing and evaluation could be drawn together and developed to establish a brittle materials technology base for application to engineering use. The vehicle selected for this demonstration was the gas turbine engine.

Both the Ford Motor Company and the Westinghouse Electric Corporation had been investigating the possibility of ceramics for application to high temperature gas turbine engines — in Ford's case, small (~200 hp) vehicular gas turbine engines and in Westinghouse's case, large (~30 MW) stationary gas turbines for electricity generation. Ford believed that high temperature engineering ceramics, made from vastly abundant raw materials, offered promise of a relatively low-cost, efficient, uncooled 2500°F (1372°C) turbine engine. Westinghouse saw ceramics as a means of developing a large combined cycle (combustion/steam) power plant with a thermal efficiency of 50 percent. Both engines offered the potential for multi-fuel capability and low exhaust emissions.

By 1971, the Defense Advanced Research Projects Agency perceived the possibility of a brittle ceramic materials technology for structural, high temperature applications. It needed to be interdisciplinary and all-encompassing, including ceramic design, materials, processing, component fabrication, non-destructive evaluation, component rig testing, and engine testing and evaluation. This type of program naturally fitted with DARPA's charter to explore risky, innovative areas with promise of large-scale payoff. DARPA also felt that such an R&D program would help in their commitment to invigorate the materials community. In mid-1971, the Ford Motor Company, with Westinghouse Electric Corporation as subcontractor, were selected for the DARPA program to develop a ceramics technology base. AMMRC, because of its in-house ceramics and structural mechanics expertise, was chosen by DARPA to be technical monitors of the program.

Ford's portion of the program, entitled "Vehicular Turbine Project," was aimed at the development of ceramic materials, processes, designs and test and evaluation techniques for uncooled ceramic components for a 200 hp size, high temperature vehicular turbine engine. The engine, designated Model 820, was specifically designed for experimental flexibility to provide for ceramic component development. Figure 1 illustrates this by showing, in turn, ready removal in the test cell of a ceramic regenerator core, combustor system, turbine inlet nose cone and turbine stator.

The program objective dealt with the question, "Can ceramics work?" and, as such, the intent of the program was the development and demonstration of high temperature durability. In parallel, Ford conducted company-funded research to develop engine and drivetrain performance though this work was postponed in 1974 due to both the economic effects of a recession and the application of increased effort to the critical ceramic technology work. However, one noteworthy achievement was the successful installation and test drive of the engine in a Ford Torino automobile using a mixture of ceramic and metallic components (metal rotors) in the hot flowpath.

In 1976, DOE and NASA joined with DARPA and AMMRC in funding portions of the program which were appropriate for their emerging role in supporting automotive gas turbine technology. Reports [13,70] on this DOE supported work have been issued.

Under the DARPA/Ford Program, attainment of ceramic designs, materials, processes and testing technologies was to be demonstrated by 200 hours of testing over a representative duty cycle, with 25 hours at turbine inlet temperatures of 2500°F. The final report of the program presents a comprehensive review of the approach and activities to meet this challenging 200 hour/2500°F objective. This Executive Summary briefly reviews the highlights of the program.
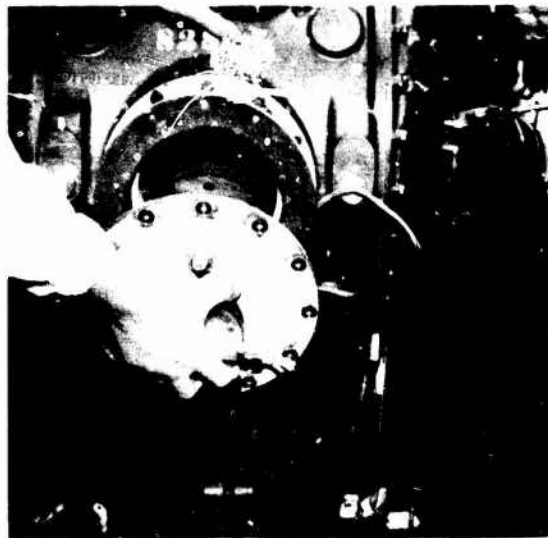
Figure 1a — Regenerator Core Removal

Figure 1b — Combustor Assembly Removal

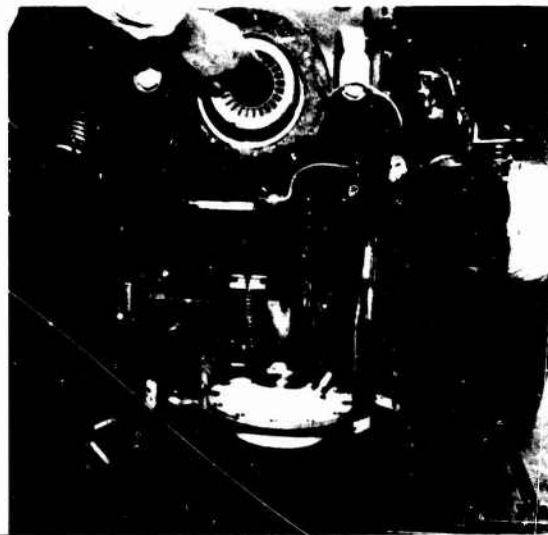
Figure 1c — Inlet Nose Cone Removal

Figure 1d — Stator Removal

Figure 1 — Ceramic Component Removal in Test Cell

Summary of Progress

The most important conclusion of the DARPA/Ford program is the success achieved in the broad objective of encouraging wider use of ceramic materials in engineering systems. By the end of the program, every gas turbine company worldwide as well as automotive companies, ceramics companies and other engine manufacturers had experimental or, at the very least, study programs to use ceramics in engineering applications. Ceramics companies had actually created new organizations for high strength ceramics. The materials community as a whole was stimulated; universities and scientific institutes had expanded or initiated programs in high strength ceramics such as silicon nitride and silicon carbide, and interdisciplinary programs were initiated to more closely relate materials and design disciplines. Government agencies, here and abroad, had begun sponsoring development programs on research and on the application of brittle ceramic materials. DARPA's objective was achieved — the whole area of ceramic materials for engineering applications was vitalized.

The durability objective of the program was demonstrated on the various ceramic flowpath components shown schematically on Page 3 of this report. Specifically, the objective of 200 hours durability (175 hrs. at 1930°F and 25 hours at 2500°F) was successfully met on a multiplicity of ceramic components, both as individual components and as a complete stationary ceramic flowpath. In addition, a complete ceramic flowpath including a duo-density Si_3N_4 rotor was successfully tested in a Ford 820 engine for 37 hours including 2 hours at 50,000 rpm and 2500°F turbine inlet temperature. The

viii

stationary components comprised a reaction bonded silicon nitride (RBSN) nose cone, two stators (both RBSN and reaction bonded silicon carbide (RBSC) were successfully demonstrated), a RBSC combustor and two RBSN tip shrouds. An all-ceramic rotor, consisting of RBSN blades bonded to an HPSN hub, was tested for 200 hours at a rim temperature of 1800°F, with maximum blade temperatures of approximately 2200°F, at speeds up to 50,000 rpm.

The above objectives were achieved using an interdisciplinary systems approach to the program involving three main technological categories: Design, Materials and Processes, and Testing and Evaluation. Conclusions reached in these three categories are discussed in the remainder of this summary.

Two aspects of "Ceramic Design" emerged from the program. One is the practical aspect which calls out "rules of thumb" of ceramic design comprising such items as: generous radii, no sharp corners, crown fitting diameters, etc. The other aspect deals with analytical design codes comprising finite element 2D and 3D stress and heat transfer codes and statistical design codes that can be used to cope with the inductile behavior of ceramic material. For example, a 2D finite element axisymmetric stress model was combined with a two-parameter Weibull model to successfully predict the fast fracture reliability of hot pressed silicon nitride disks which were cold spin tested to failure. An analytical code was generated to handle time-dependent reliability occurring at high temperature where ceramics often exhibit time-dependent strength properties. While this is useful in assessing trends, more work is required in areas such as tensile stress rupture testing to provide a sound base for a time-dependent reliability design code.

The technological category, "Materials and Processing," along with the fabrication development of actual ceramic components received the lion's share of the program effort. The development of RBSN received greatest emphasis since most of the components were made from this material. Through development of starting composition, particle distribution, molding conditions and nitriding techniques, RBSN formed by injection molding was improved in density from 2.2g/cc at the beginning to 2.7g/cc at the end of the program; this resulted in a 300% room temperature strength improvement to 45,000 psi which is substantially retained to 1400°C. From all the flexural stress rupture tests conducted on 2.7g/cc RBSN, there were no time-dependent failures at flexural stresses of 33,000 psi up to 1400°C and 200 hours. Though density had been improved considerably, the 2.7g/cc RBSN was still porous and, therefore, prone to oxidation though to a much lower degree than uncoated super-alloys. Of the many coatings and/or treatments investigated, a pre-oxidation treatment up to 1500°C gave the best results and reduced oxidation weight gain of RBSN by a factor of four. Techniques to produce slip cast RBSN were also developed. At the beginning of the program, though slip casting of clay systems has a long history in the ceramics industry, slip casting of silicon powders was in its infancy. Through development of particle size and distribution, deflocculants, pH and viscosity, green compacts were formed with minimum shrinkage and with densities high enough that, if nitrideable, would yield theoretically dense Si_3N_4. Though experiments to nitride such dense material were unsuccessful, techniques were developed to produce slip cast RBSN with densities as high as 2.8g/cc.

While injection molding and slip casting are processes suitable for making complex shapes, they did not, during the program, lead to a fully dense silicon nitride. Accordingly, development of hot pressing of silicon nitride was undertaken to produce a fully dense, high strength material needed to endure the high operating stresses of the rotor hub. A range of silicon nitride starting powders, pressing additives, milling conditions and hot pressing conditions were investigated to form and simultaneously bond the hub to the blade ring of the duo-density Si_3N_4 turbine rotor. A maximum hot pressing pressure of 1,000 psi was generally adopted to avoid breaking the rotor blade ring during bonding. AME CP-85B powder with 2 to 5 wt. % MgO additions gave 4-point MOR's of ~103,000 psi at room temperature and ~65,000 psi at 2200°F. Continued development of HPSN to improve high temperature strength showed that an 8% Y_2O_3/AME CP-85B powder pressed at 5,000 psi had a 2200°F strength of 105,000 psi; however, this material could not be densified at 1,000 psi so was not used for rotor hubs. While reaction bonded silicon nitride was the primary material investigated for the stator, an alternate development was undertaken on reaction bonded silicon carbide. In this, a SiC-filled thermosetting plastic was molded, carbonized and silicided to form a fully dense SiC-Si material with about 10% free silicon finely dispersed. Strengths were shown to vary depending on specimen shape and finish but were generally in the range 50,000-60,000 psi.

Figure 2 exemplifies ceramic processes developed during this program.
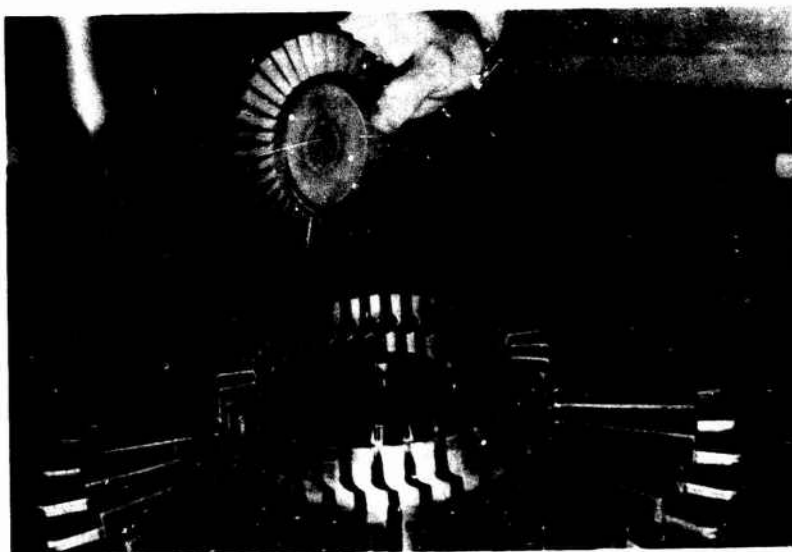
Figure 2a — Injection Molding

GRAPHITE
PISTON

BOND SURFACE

H.P. Si₃N₄ DISC

H.P. Si₃N₄ DISC
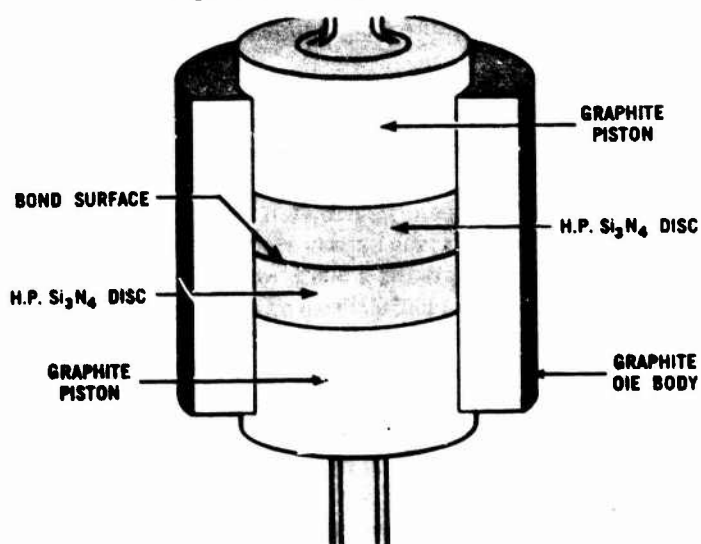
GRAPHITE
PISTON

GRAPHITE
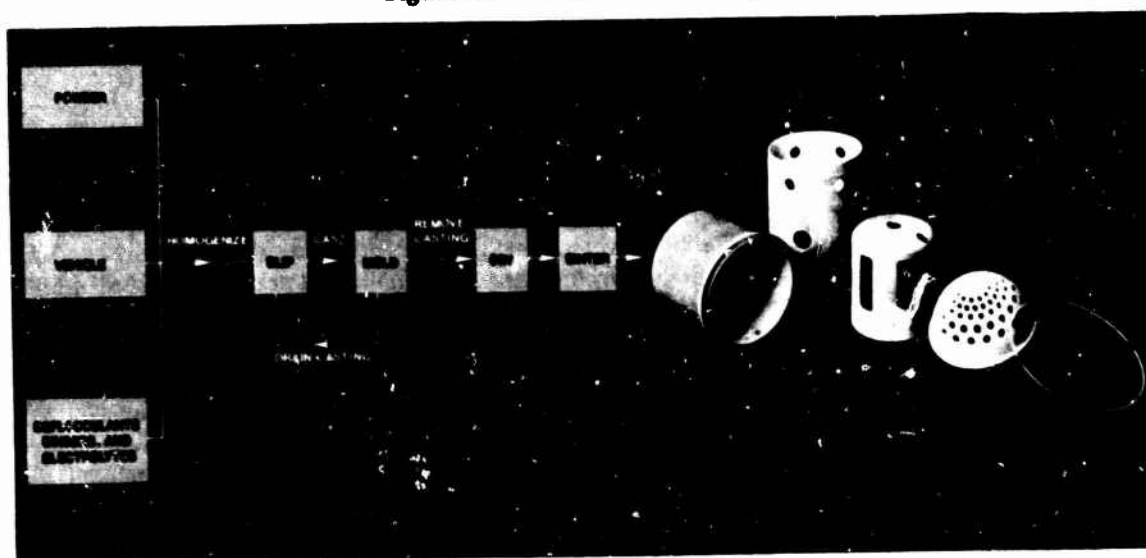OIE BODY

Figure 2b — Hot Press Bonding

Figure 2c — Slip Casting

Figure 2 — Ceramic Processing

The third technological category involved in the interdisciplinary systems approach to achieve the program objectives was "Testing & Evaluation." This activity was an essential element of the program and provided the crucial feedback for meaningful development of design, materials and processes. Testing technology covered many activities from NDE techniques to evaluation of materials and components, to MOR testing to characterize materials, to a range of over twelve types of component test rigs. The scope of the program did not permit in-depth development of all of the various NDE techniques. However, known techniques were at least assessed with respect to their applicability for detecting typical flaws experienced in the various ceramics under investigation. These comprised visual inspection using magnification and dye penetrants, x-ray radiography including Microfocus x-ray, conventional ultrasonics, acoustic emission, infrared thermography, electromagnetic eddy current, holosonics, electrostatic methods, and mechanical loading techniques (proof testing). The latter, while not a direct method of detecting flaws, can be considered a form of NDE. Visual inspection with dye penetrants and x-ray radiography including Microfocus x-ray were found to be the most practical NDE methods for detecting gross fabrication flaws (>200 microns) for example typically experienced with the injection molding process. One of the real problems which emerged was the lengthy and cumbersome nature of the task to non-destructively evaluate a complex-shaped ceramic component; even visual inspection of a 36-bladed rotor is a rather lengthy procedure.

With respect to material characterization, selection of an MOR specimen, test fixture and procedure is in itself an involved subject. In this program an Army Materials & Mechanics Research Center Proposed Standard was adopted. It involved 4-point testing of a 1/8" x 1/4" x 1" ('A'-size) specimen. Young's Modulus and Poisson's Ratio were determined by sonic techniques; thermal expansion values were measured on a differential dilatometer and thermal conductivity was determined using the flash diffusitivity method.

Turning to component testing, engine and component test rigs were used to screen out, qualify and demonstrate component behavior. These included rigs for stator vane bend test, rotor blade bend test, stator shroud pressure test, rotor cold spin test, thermal shock test, rotor disc thermal test, combustor test, light-off qualification test, ceramic structures test, 2500°F flowpath test, hot spin test, turbine rotor test and engine test. A good example of a ceramic component test rig is the hot spin test rig. This rig was designed to test ceramic turbine rotors to failure and incorporated a number of unique and desirable features. For example, a single rotor could be tested, no stationary ceramic components were needed, rotor hub and blade temperatures could be measured, automatic failure detection was provided, containment of all failed rotors was achieved, and a fast turnaround time (<1 week) could be achieved between tests.

Component development was carried out on each of the ceramic components making up the all-ceramic hot flowpath of Ford's experimental Model 820 vehicular turbine engine. This involved the ceramic turbine rotor and the ceramic stationary components comprising stators, nose cones, combustors and rotor tip shrouds. The interdisciplinary systems approach using testing and evaluation to provide feedback proved effective in making many design, materials and process iterations needed to show that "ceramics can work." Some important accomplishments from such iterations on the turbine rotor follow. A multi-stage turbine, with non-twisted, radially and centroidally stacked airfoils can give best reliability for a given efficiency for an axial turbine design. Of course, multi-staging generally implies higher cost so this should also be considered. Many material and process approaches were investigated to make a ceramic turbine rotor including hot pressed and "welded" blades and hub, pseudo-iso-pressed, hot pressed using conformable tooling, CVD silicon carbide and machined rotors. The outcome of this formidable task was to show that a duo-density Si_3N_4 rotor can be made and can work. The following rotor tests are records that stand to this day. Besides the 200-hour durability run, four duo-density rotors successfully completed a 25-hour durability test at 50,000 rpm and 1800°F rim (or platform) temperature. Another duo-density Si_3N_4 rotor successfully completed a 25-hour durability test at 50,000 rpm and 2000°F rim temperature with maximum blade temperatures of 2400°F. Yet another duo-density Si_3N_4 rotor was engine tested for 37 hours including 2 hours at 50,000 rpm with a turbine inlet temperature of 2500°F. One problem revealed during rotor testing was that of cracking of the curvic coupling attachment. While a thin gold-plate lubricant was shown to resolve this problem for short-time operation, a better method is required as a long-term solution.

Figure 3 is a photograph of a duo-density Si_3N_4 turbine rotor being removed from the hot spin test rig after one of the successful durability tests.
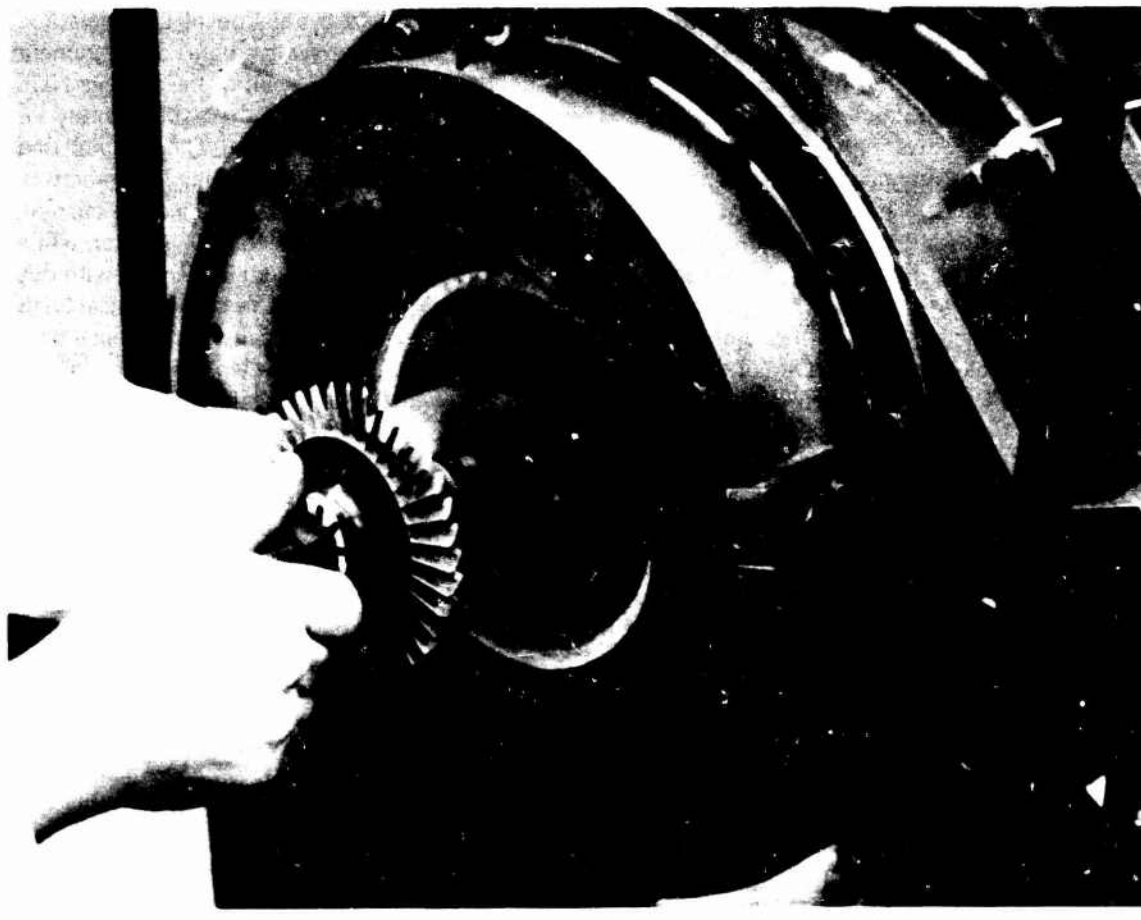

Figure 3 — Duo-Density Rotor Following Successful Durability Test

Similar design, material and process iterations took place on the ceramic stationary components. Injection molded RBSN stators, transfer molded RBSC stators, slip cast RBSN tip shrouds, injection molded RBSN nose cones and iso-pressed RBSC ("Refel") combustors met the 200 hour durability duty cycle objective both individually and as a set. Many hundreds of additional hours were accumulated on such ceramic stationary components during the various screening and qualifying tests that were undertaken — it must be remembered that ceramic flowpath components had to be used as workhorse components for all of the high temperature testing (~2500°F) which was beyond the capability of uncooled superalloys. The most critical and complex-shaped stationary component was the ceramic stator. In the past there has been criticism of a one-piece ceramic stator, but this program was able to demonstrate its viability at least for short-time durability (200 hrs.). This was achieved by adopting the stronger 2.7g/cc RBSN and by modifying the design to eliminate an integral rotor shroud, to "harmonize" the blade/blade base thermal inertia and to slot the inside shroud to permit movement of individual stator vanes. In terms of the combustor, "Refel" RBSC proved to be the most successful material. It is felt that this is because the higher conductivity of silicon carbide better dissipates local hotspots which are very difficult to predict by analysis for all operating conditions. Since the nose cone is not an extremely critical aerodynamic component, its design was allowed to evolve from practical experience by incorporating stress relieving features such as flange scalloping and angular slotting.

Figure 4 is a photograph of an exhibit showing actual ceramic components for the hot flowpath of the 820 engine.
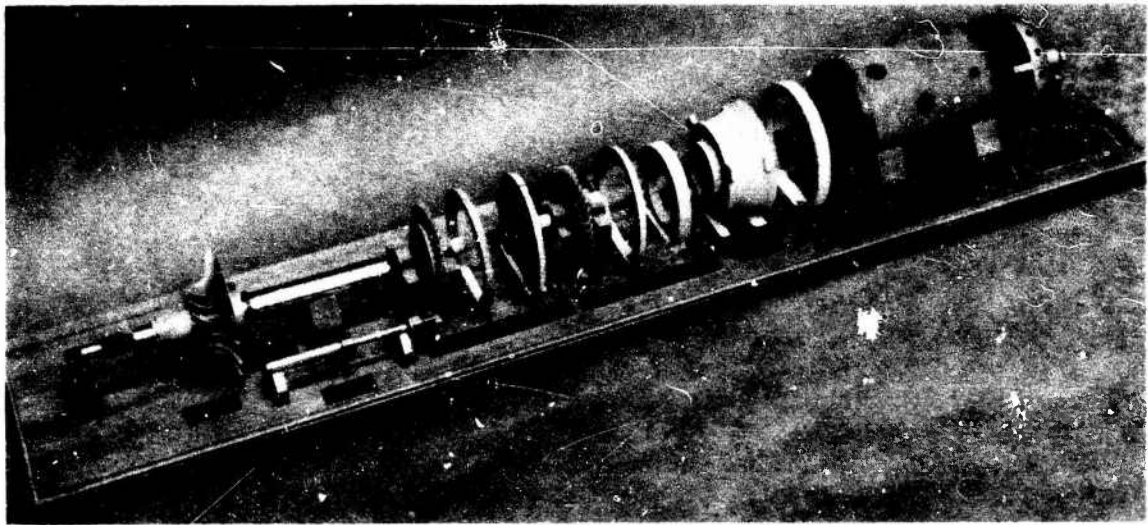
Figure 4 — Exhibit of 820 Ceramic Components

Conclusion

With respect to the question: "Can ceramics work?" the DARPA/Ford program has shown that: "Yes, it can be done." The real question on which we must now focus is: "Can it be done consistently and reliably so that "*it won't fail.*" The potential is there but, until this issue is dealt with, ceramics cannot really be relied upon and, therefore, cannot realize their full potential. With metals, the R&D program shows that *it can be done* and the costly production development program then serves to show *it won't fail.* In ceramics, because of their extremely probabilistic behavior, the "it won't fail" phase really has to be accomplished through research effort. The dilemma is, however, that production development-type funding is not normally applied to address a research issue. As a result, a step-by-step approach should probably be taken. For example, a strategically planned research program, which exploits background experience could probe and explore reliability limits as a basis to establish "realizable potential" in a critical and meaningful component. Such a program would scrutinize materials and processes with respect to reliability and go through the various phases of manufacturing and NDE to actual testing and statistical evaluation to demonstrate achievable, yet practical, reliability levels.

Perhaps as important as individual developments in ceramic materials, processing, design, and test and evaluation is the interrelationship that needs to and has developed between these disciplines. At Ford, we have emphasized the importance of this interrelationship and recognize a "serendipity effect" through continual interaction between disciplines trying to develop ceramic materials for engineering applications. Using this approach over the duration of this DARPA/Ford Program, the establishment and growth of a new ceramic turbine technology has evolved.

1. INTRODUCTION

As stipulated by the Defense Advancement Research Projects Agency (DARPA) of the Department of Defense, the major purpose of this program was the demonstration of brittle materials in demanding high temperature structural applications, in order to encourage wider use of these materials in engineering systems. DARPA's program goal was to show by a practical demonstration that efforts in ceramic design, materials and processes, fabrication, and testing and evaluation could be drawn together and developed to establish brittle materials for engineering use. For reasons discussed below, the vehicle for this demonstration was to be a gas turbine engine.

As is well known by engine designers, the efficiency of an ideal thermodynamic cycle for converting heat into work is directly related to the cycle maximum temperature. Achievement of a high maximum temperature in a practical heat engine is, of course, related to materials and design (e.g. cooling methods). In the case of the gas turbine, from its inception there has been continual pressure to improve engine efficiency and power-to-weight ratio through high temperature materials development. Today's nickel-chrome, cobalt-based and directionally solidified superalloys are all a result of this persistent push.

Both the Ford Motor Company and the Westinghouse Electric Corporation had been investigating the possibility of ceramics as applied to high temperature turbine engines — in Ford's case, small ($\approx$200 hp) vehicular turbine engines and in Westinghouse's case, large ($\approx$30 MW) stationary turbines for electricity generation. Ford believed that refractory ceramics, made from vastly abundant raw materials, offered promise of a relatively low cost, uncooled 2500°F turbine engine. Such an engine would have double the horsepower for the same size with a 20% fuel economy improvement when compared to today's State of the Art metal engines. Westinghouse saw ceramics as a means of achieving a large combined cycle (combustion/steam) power plant with a thermal efficiency of 50 percent. Both engines offered the potential for low exhaust emissions and multi-fuel capability.

By 1971, the Defense Advanced Research Projects Agency perceived the possibility of a ceramic materials technology for structural, high temperature applications. They recognized, however, that such ceramic technology needed to go beyond the traditional materials research framework of, for example, developing a new ceramic material. It needed, in fact, to be interdisciplinary and all-encompassing; to include ceramic design, materials and processing development, component fabrication, non-destructive evaluation, component rig testing and engine testing and evaluation. Clearly, research and development of such a technology was risky but this naturally fitted with DARPA's charter to explore risky, innovative areas with promise of large-scale payoff. DARPA also felt that such an R&D program would help in their commitment to invigorate the materials community.

In mid-1971, the Ford Motor Company, with Westinghouse Electric Corporation as subcontractor, were selected for the DARPA program to develop a ceramic technology base. The coupled relationship of Ford and Westinghouse would provide synergism in applying the same basic materials science and engineering to opposite ends of the turbine power spectrum. Besides having potential for on-highway and off-highway application, the small-type turbine was already in military use for accessory power engines, tanks, aircraft turbo-props, helicopter engines, jet engines, marine engines and small portable power plants. The large (20-70 MW) stationary turbine, on the other hand, was applicable to DOD installations that require on-site power generation, to installations on barges for supplying remote locations only accessible by waterways, and as a potential prime mover for ship propulsion.

The Ford portion of this program, reported herein, was entitled "Vehicular Turbine Project."* The objective was to develop an entire hot flowpath comprising uncooled ceramic components for a 200 hp size high temperature vehicular turbine engine. Attainment of this objective was to be demonstrated by 200 hours of testing over a representative duty cycle at turbine inlet temperatures of up to 2500°F (1372°C).

---

*The final report on the Westinghouse portion of this program was published in December of 1976 as AMMRC TR-76-32 Vol. I-IV.

In this, the final report on the DARPA/Ford program, a comprehensive review is presented of the program approach, the design, materials/processes and testing technologies developed, and the development of the stationary and rotating ceramic hot flowpath components to meet the challenging 200 hour/2500°F objective. Semi-annual progress reports [1-13] were issued during the course of the program which go into more detail on work in these areas.

The thrust of the DARPA/Ford program was the demonstration of ceramic technology, and not the development of a highly efficient vehicular engine and powertrain system. However, Ford did conduct company-funded research concurrent with the earlier years of the DARPA/Ford program to develop engine and drivetrain performance on the dynamometer and in a vehicle. This work was postponed in 1974, due to both the economic effects of a recession and the application of increased effort to the critical ceramic technology work. However, one noteworthy achievement was the installation of the engine in a Ford Torino vehicle followed by successful test driving. The engine contained a mixture of ceramic and metallic components, including metallic rotors, in the hot flowpath.

2. PROGRAM APPROACH

2.1 SYSTEMS APPROACH

At the program beginning, it was recognized that an interdisciplinary systems approach was required.[1] Developments in ceramic designs, probablistic analytical methods, materials science, ceramic processing, nondestructive evaluation, materials characterization, rig and engine testing, and statistical evaluation techniques were integrated into the following three major categories:

- DESIGN

- MATERIALS & PROCESSES

- TESTING & EVALUATION

In terms of project organization, ceramic scientists and engineers, design engineers, and development engineers were teamed together to maximize daily interface of the above areas and create a mutually interdependent research and development effort.

The engine selected for hardware development in the vehicular turbine project was Ford's Model 820 experimental high temperature turbine engine. This was a regenerative single-shaft engine which was specifically designed by the Ford Research Staff for development of high temperature turbine technology. It was designed to easily convert into various test rigs to facilitate evaluation and development of ceramic components, design concepts, assembly procedures, etc. Prior to this contract, Ford had been investigating ceramic stationary components and air-cooled superalloy turbines and it was concluded that blade-cooling of such small turbine wheels was impractical. Therefore, in the program plans it was decided to investigate ceramic rotors as well as stationary parts i.e. an all-ceramic hot flowpath. Figure 2.1 shows a schematic layout of the 820 engine ceramic hot flowpath.
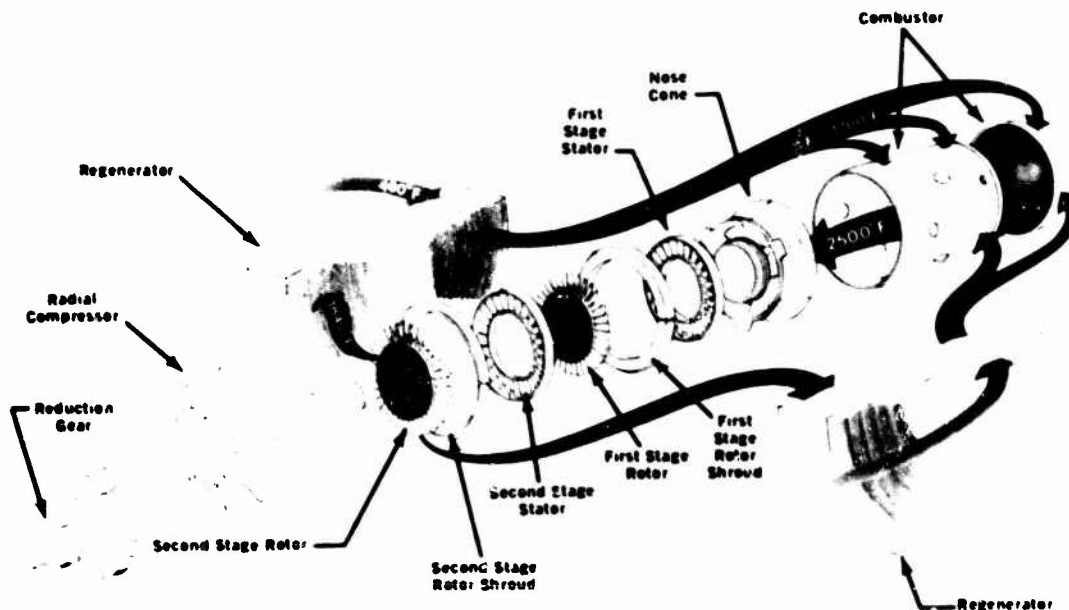

Figure 2.1 — Schematic View of the 820 Engine Ceramic Hot Flowpath (Only Compressor, Shaft, and Gears are Metal)

3

The ceramic hot flowpath is comprised of:

- CERAMIC TURBINE ROTORS

- CERAMIC STATIONARY COMPONENTS
  - Stators
  - Nose Cone
  - Combustor
  - Tip Shrouds

The approach to develop these components was to provide for an iterative development program as shown in the block diagram of Figure 2.2. For any major iteration, the starting point is the initiation or change in design concept. From this, design layouts are prepared and analyzed leading to detailed design and analysis of the ceramic components. Ceramic materials and process development proceeds in parallel with the design phase. Material science and property characterization are used to improve materials and processes. Feedback between design and materials prompts optimization trade-offs. Tooling is then designed and made for fabrication development of ceramic components. Non-destructive and screening tests are developed for early evaluation of ceramic components and appropriate feedback to design, and materials and process development. In parallel, all metal parts for engine rigs are made per detailed design requirements. Ceramic and metal parts are dimensionally inspected and instrumented in preparation for testing. Ceramic assembly techniques are developed and components are evaluated in engine test rigs. Failure analysis provides one of the most important feedback loops for corrective action; any or all of the factors involved in the development could be affected. This, then, was the systems approach adopted for this research program — an approach which provided broad flexibility for minor and/or major iterations.
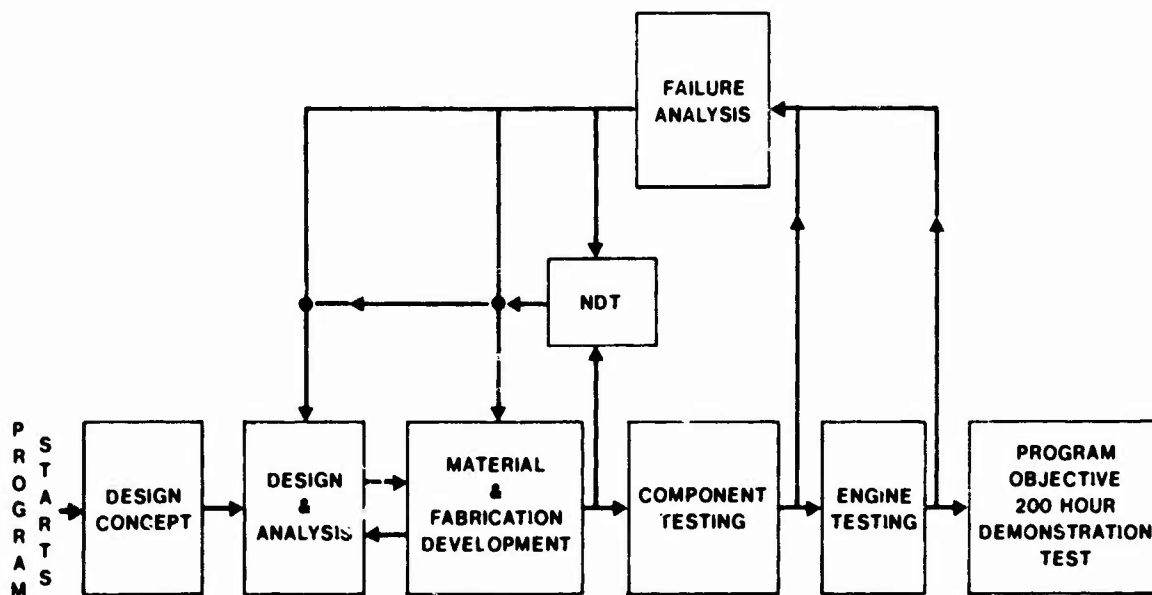

Figure 2.2 — Ceramic Turbine Program Interactive Development Process

The need to develop the specific ceramic components maintained a continual thread between the various interdisciplinary technologies of CERAMIC DESIGN, MATERIALS & PROCESSES AND TESTING & EVALUATION. While some progress had been made in these areas prior to 1971, all aspects were generally in a state of relative infancy at the beginning of this program. The following sub-sections present a brief discussion of the state-of-the-art at that time along with a discussion of the approaches followed in each to meet the goals of the program.

2.2 DESIGN APPROACH

At the beginning of the program, the status of ceramic design technology could be described as follows:

1) No set design guides for ceramics existed

2) Limited analytical design tools were available

3) Experience with the behavior of ceramics in an engine-type environment was limited

4) The computer tools available were too cumbersome and costly for the detailed analyses required of brittle structures

5) A rationale to assess the strength of ceramic component design configurations under engine loading conditions was lacking

6) The conventional, deterministic approach to strength evaluation of ceramic components was considered inadequate due to the inductile behavior of ceramics.

As a result of these shortcomings, a basic design approach was adopted for this program which involved addressing and developing two aspects of brittle materials design technology as follows:

1) The practical aspect, which would be composed of general guidelines and design concepts for ceramic-ceramic and ceramic-metal interfaces, e.g., attachments, assemblies, etc.

2) The theoretical aspect, which would comprise the modification of existing analytical codes and generation of new analytical procedures to theoretically assess the integrity of ceramic components in a service environment.

As the program proceeded, available analytical codes were modified and new analytical codes were generated to assist in the design of all the critical flowpath components. Component responses, such as material temperatures, stresses and deformations, were analyzed using finite element and/or finite difference computer codes.

A statistical approach was selected to determine the reliability of a ceramic component under engine loading conditions. In this connection, a probabilistic analysis based on Weibull's model of brittle strength was developed along the general guidelines suggested by Dukes.[14] (The codes and analyses are described in Section 3.1 of this report.) In addition, experimentation on design ideas or concepts, using test rigs or engines, provided important feedback for ceramic design.

The approach was to develop these new design tools and use them as a basis for the design iterations of ceramic components that took place during the program.

2.3 MATERIAL AND PROCESSING APPROACH

At the beginning of this program, materials and process development had resulted in the following:

1) Silicon nitride (Si_3N_4) and silicon carbide (SiC) had been identified as viable candidate materials for ceramic turbine components. Evaluation of test samples made from several grades of these materials in test rigs confirmed these selections, although failures were encountered.

2) The very complex shapes of the turbine engine components had led to a search for reasonable forming and processing techniques. These manufacturing process studies were designed to develop near net shape fabrication capabilities. Injection molding, isostatic pressing, and slip casting were selected as the most promising forming methods.

3) Reaction bonded silicon nitride (RBSN) was selected as the most attractive material for the stationary hot flowpath components. The low thermal expansion and relatively high strength of this material gave an advantage over other materials in the high thermal stress, low mechanical stress environment imposed upon these components. Early development work on injection molding of RBSN components having airfoils, such as stator vane segments and rotor blades with bulb-shaped root sections, established that injection molding was a very attractive forming technique but further development was needed. The initial RBSN material used for these components was of low density (2.2 g/cc) and low strength (12-14000 psi MOR). Much more development was needed on stronger materials and on improved nitriding procedures.

4) Very little detailed mechanical and thermo-physical characterization of turbine ceramic materials had been done, primarily because improved materials were expected from ongoing development efforts.

5) Process controls to insure component uniformity were just starting to be developed.

6) Critical inspection and evaluation of component quality, other than dimensional inspection, was in a state of relative infancy. Non-destructive evaluation (NDE) was being investigated and several NDE methods had been given preliminary evaluation. Some of these NDE methods had been selected for development and application for ceramic components, and promising emerging NDE techniques were being evaluated.

Many of the design and analytical techniques available today for use on ceramic components had not yet been developed at the start of this program. Consequently, well-formulated design goals were unavailable during much of the material and process development which took place. Therefore, most of the ceramic material and process development for ceramic turbine components proceeded along the lines of 'learn by doing.'

For the case of structural ceramic components, since operating stresses were thought to be relatively low, RBSN was selected as the principal candidate material, with RBSC as the backup. Development work in both injection molding and slip casting was intensified. Isostatic pressing was used early in the program for forming of combustor tubes but there was little opportunity to utilize this process for the other, more complex components and therefore this work was terminated. Material improvements were initiated in RBSN, resulting in several materials of increased density and strength, along with continuing effort to improve nitriding; results of RBSN improvements are discussed in more detail in Sections 3.2.1 and 3.2.2 of this report. Work on fabrication improvements on structural components is noted in Section 4.4.2.

Much of the program effort was directed toward the ceramic turbine rotor, due to the very high operating stresses which were unprecedented in terms of ceramic material requirements. The goal was to attempt to fabricate an all-ceramic rotor using near net shape forming techniques as much as possible, since the ultimate economics of vehicular ceramic turbine engines requires reasonable and low-cost fabrication processes. Many approaches to rotor fabrication were conceived, evaluated, and most were discarded as being unlikely to achieve success, at least within the constraints of this program. These investigations are discussed in Section 4.3.2.2 of this report. The development of the duo-density Si_3N_4 turbine rotor utilizing RBSN for the blades and fully dense HPSN for the hub became the leading edge of ceramic material, process, and NDE development for the program. Section 4.3.2.3 of this report details this effort.

2.4 TESTING AND EVALUATION APPROACH

At the beginning of this program, many ceramic materials had been tested at room and elevated temperatures to evaluate relative strength, thermal shock resistance, erosion characteristics, stability, etc. As mentioned in the previous section, the majority of testing during this program was conducted on silicon nitride and silicon carbide. The approach was to determine physical and mechanical properties of both hot pressed and reaction bonded silicon nitride along with reaction bonded silicon carbide, as required by the design activity. With respect to non-destructive evaluation (NDE), the approach was to develop new and improved NDE techniques initially for application to material samples and modulus of rupture bars to correlate with destructive test results generated when determining mechanical properties. Later in the program, when components were being processed, the NDE approach focused on the evaluation of macroscopic flaws in complex-shaped ceramic components such as blade rings and stator vanes as opposed to minute flaws in simpler-shaped ceramic test bars.

Testing of ceramic components was planned to play a major role in the program as a means of providing feedback to design, analysis, and material and process development. The test and evaluation of the complete ceramic engine was impossible at the onset of the program as all of the ceramic hot flowpath components were not available. In addition, it was felt that the testing of a multiplicity of undeveloped ceramic components at once was not sound engineering judgement and would make assessments of any failures very difficult, if not impossible.

The approach, therefore, was to devise several different test rigs, which utilized portions of the 820 experimental gas turbine engine to facilitate the rapid evaluation of individual ceramic components, design concepts and assembly procedures. It was also expected that testing of a ceramic component over the complete engine duty cycle would make the task of determining the critical part of the duty cycle more difficult; therefore, the planned approach was to test and evaluate components over separate portions of the duty cycle.

The testing approach devised was twofold: 1) utilize metal components along with the ceramic components under test when a full set of flowpath hardware was required. Metal turbine rotors were particularly useful as they allowed evaluation of stationary ceramic components over a major portion of the engine duty cycle prior to the availability of ceramic turbine rotors; and 2) test and evaluate individual ceramic parts in special test rigs through portions of the duty cycle. The screening of stationary ceramic flowpath components would utilize a test rig programmed to repeatably perform a sequence of cold lights and hot shutdowns. Operating without turbine rotors, the test rig would reduce complexity, minimize secondary damage effects, and eliminate dynamic influences without invalidating the transient thermal evaluation of the stationary components. This approach gave clear and early definition to the modes of failure since the compounding effect of rotors was absent and the single mode of operation isolated the failure environment.

Stationary components which successfully completed the screening test were subjected to steady-state thermal environments. Initial steady-state testing identified "infant mortality" failures. The resulting iterative development feedback was of importance to the material and process development activities. Extended steady-state testing identified time-dependent problems. This iterative development feedback was of importance to the material development and reliability analysis activities. Subsequent testing of improved stationary components which successfully completed the steady-state duty cycle objectives involved testing under a combination of steady-state environments. This coupling of environments identified new situations and moved the development of stationary ceramic flowpath components one step closer to successful testing over the complete duty cycle.

Ceramic turbine rotors were also screened by component testing for minimum strength and quality levels. The first step was a complete inspection. If the rotor was dimensionally acceptable, its quality was assessed using visual NDE techniques such as dye penetrant inspection and microscopic viewing. Ceramic rotors judged unacceptable for dynamic testing were used to provide feedback to the material and development activity; ceramic rotors judged acceptable were first evaluated by spin testing in a vacuum spin pit at room temperature.

A specially designed hot spin rig became the major testing vehicle for the evaluation of ceramic turbine rotors. The hot spin rig eliminated the stationary ceramic components and enabled the testing and evaluation of a single all-ceramic turbine rotor subjected to high rotating speeds and controllable temperature gradients. Furthermore, the hot spin rig was used to evaluate other features unique to ceramic turbine design technology, such as ceramic to metal interfacing, unique mounting systems, possible physical changes of the ceramic rotor occurring during operation, bolt cooling air requirements versus those predicted, etc. The use of dedicated test rigs, such as the hot-spin rig, produced much valuable information during the course of the program.

3. TECHNOLOGY DEVELOPMENT

An important objective of the program was to develop general purpose technology in the fields of ceramic design, materials and processing, and testing and evaluation which was not necessarily confined to vehicular gas turbine application. While in practice this technological development was closely allied to the development of actual ceramic components, the attempt is made in this final report to separate out the fundamental technology for convenience to the reader with general purpose interest. This section of the report therefore covers technology development in the area of design, materials and processing, and testing and evaluation. A subsequent section deals with actual ceramic component development.

3.1 DESIGN

3.1.1 INTRODUCTION

The successful application of ceramic materials to structural components requires the development of design tools that will enable the designer to cope with the inductile behavior of these materials. Inductility is manifested as limited strain tolerance, low fracture toughness, and a considerable variability in strength properties. The first two manifestations necessitate very accurate determination of critical service loadings and the resultant stresses. For the solution of the complex structural and thermal loading problems typically encountered in a heat engine, advanced finite difference and finite element computer analyses were acquired and integrated into a quasi-automated system.

The treatment of the variability in strength properties required development of 1) statistical tools for processing and interpretation of test data, and 2) a probabilistic strength analysis which provided the groundwork for a reliability based design methodology. The probabilistic strength analysis was derived from Weibull's "weakest link" model of brittle strength. Later this analysis was expanded to the time-dependent reliability problems associated with the observed (in certain ceramics) static fatigue phenomenon that results from subcritical crack growth.

3.1.2 THERMAL AND STRUCTURAL ANALYSES

3.1.2.1 Two-Dimensional Axisymmetric Code

A number of structural engine components either have or can be approximated to have rotational symmetry with respect to both geometry and loading. The mechanical analysis of such components is considerably simplified because the distributions of temperatures, stresses, and deformations under typical loading conditions can be fairly accurately determined by way of two-dimensional numerical analyses.

Three basic computer codes were acquired and developed to conduct two-dimensional analyses:[1]

1) FDHT — Two-dimensional finite difference heat transfer with coolant streams

2) FEHT — Two-dimensional, axisymmetric, finite element heat transfer with two coolant streams with self generation of convective coefficients for flow over a disc rotating in an adiabatic housing

3) FEST — Two-dimensional, axisymmetric, finite element stress and strain analysis with a capacity for calculating inertial loadings as typically encountered in centrifugally stressed turbine rotors.

The three codes were executed sequentially with the thermal code output serving as input to the stress code for the computation of stresses and deformations. Both the heat transfer and the stress codes allow variability of physical properties with temperature and allow for anisotropy in material properties.

The determination of loadings and boundary conditions for input into the computer codes was considerably more complex. Components operating in an engine environment interact with the struc-

tures surrounding them. This interaction causes additional loads and constraints to be applied to the components. An analytical procedure was devised to solve these complex loading and boundary problems. With it, the interaction of many components could be economically studied to the desired level of detail. A schematic of this process as applied to the design analysis of a turbine rotor-shaft assembly is displayed in Figure 3.1.2-1.

In general, the analysis of a structure begins with a study of the overall assembly using a relatively crude mathematical model, as shown in Figure 3.1.2-2. This crude model, which is composed of all structures surrounding and interacting with the component under investigation, provides realistic boundary conditions for a more detailed model. The model is progressively refined until the component can be studied with the desired degree of detail, as illustrated in Figures 3.1.2-3 through 3.1.2-6.
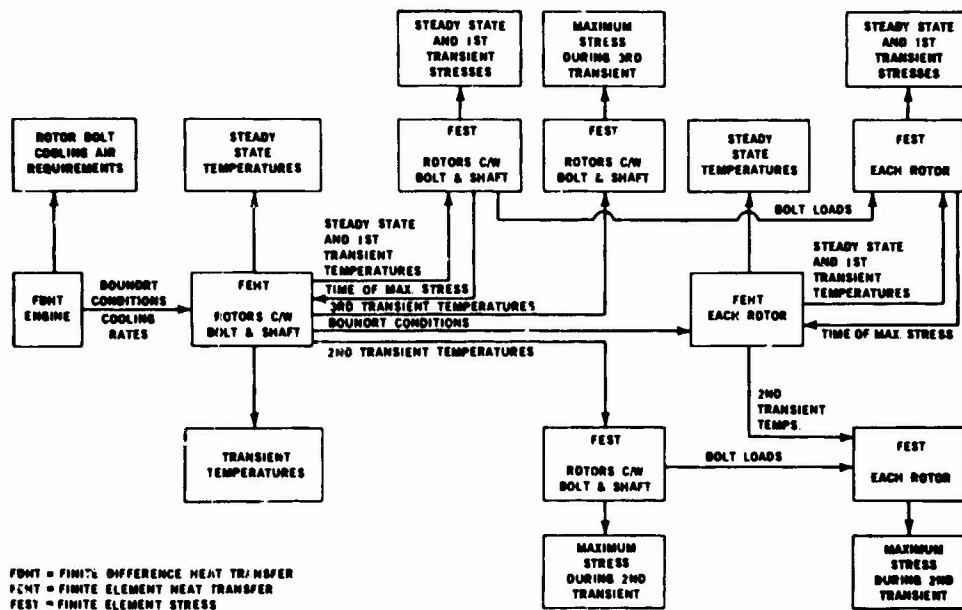

Figure 3.1.2-1 — Schematic Diagram of the Design Process for Ceramic Turbine Rotors and Attachment Techniques
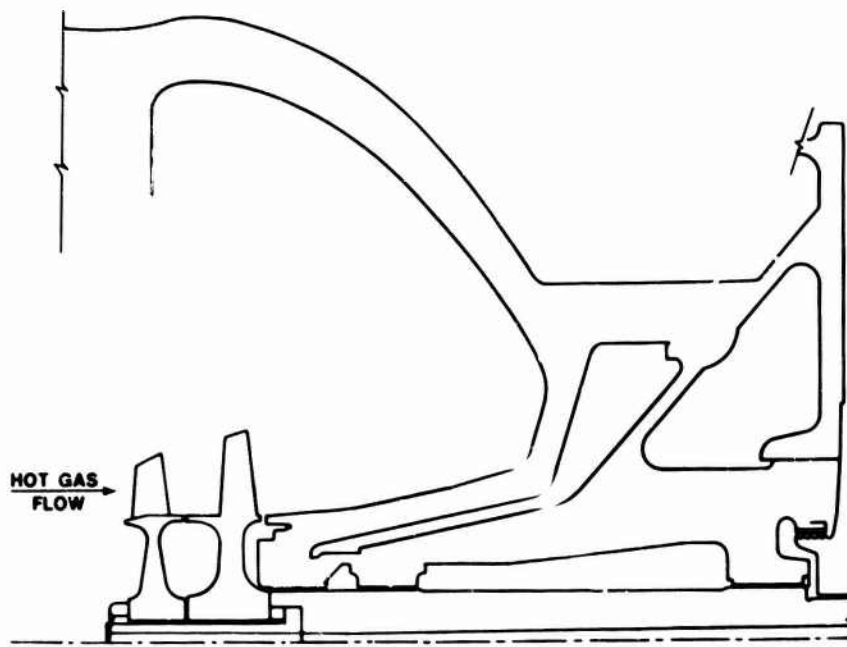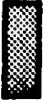

Figure 3.1.2-2 — Model of Hot Flow Section
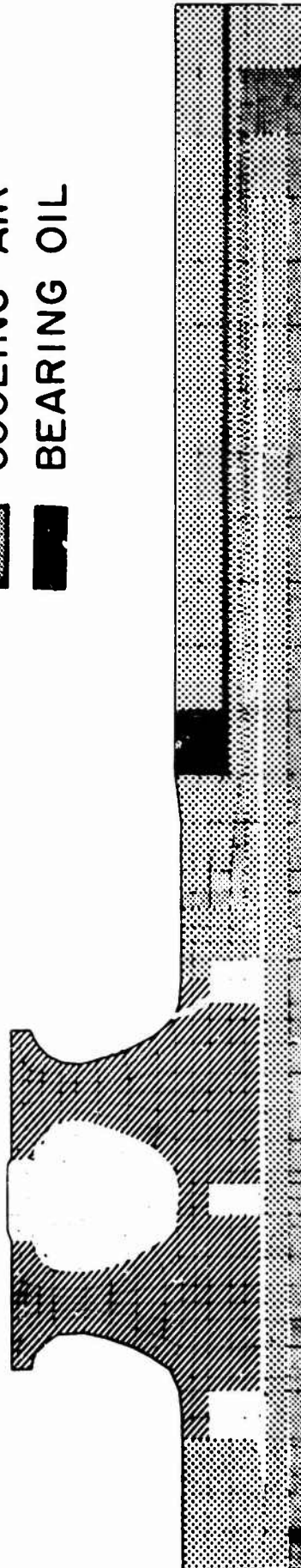
CERAMIC DISK
METAL HARDWARE
COOLING AIR
BEARING OIL

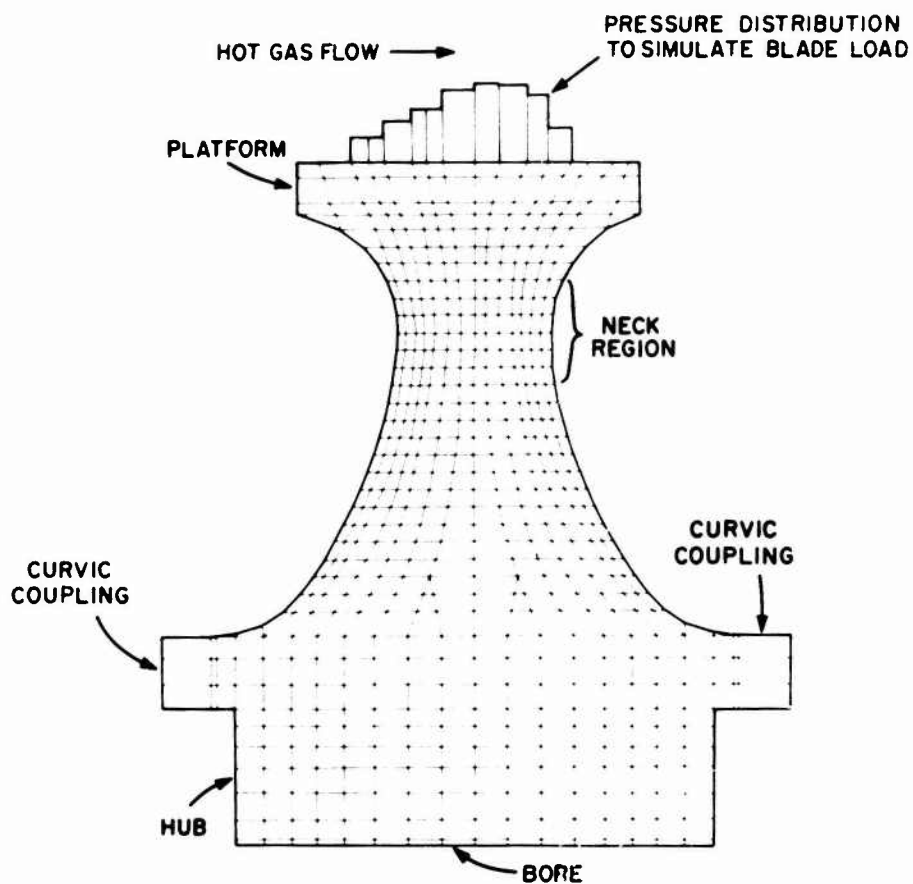Figure 3.1.2-3 — Two Dimensional Model of Turbine Rotor Assembly

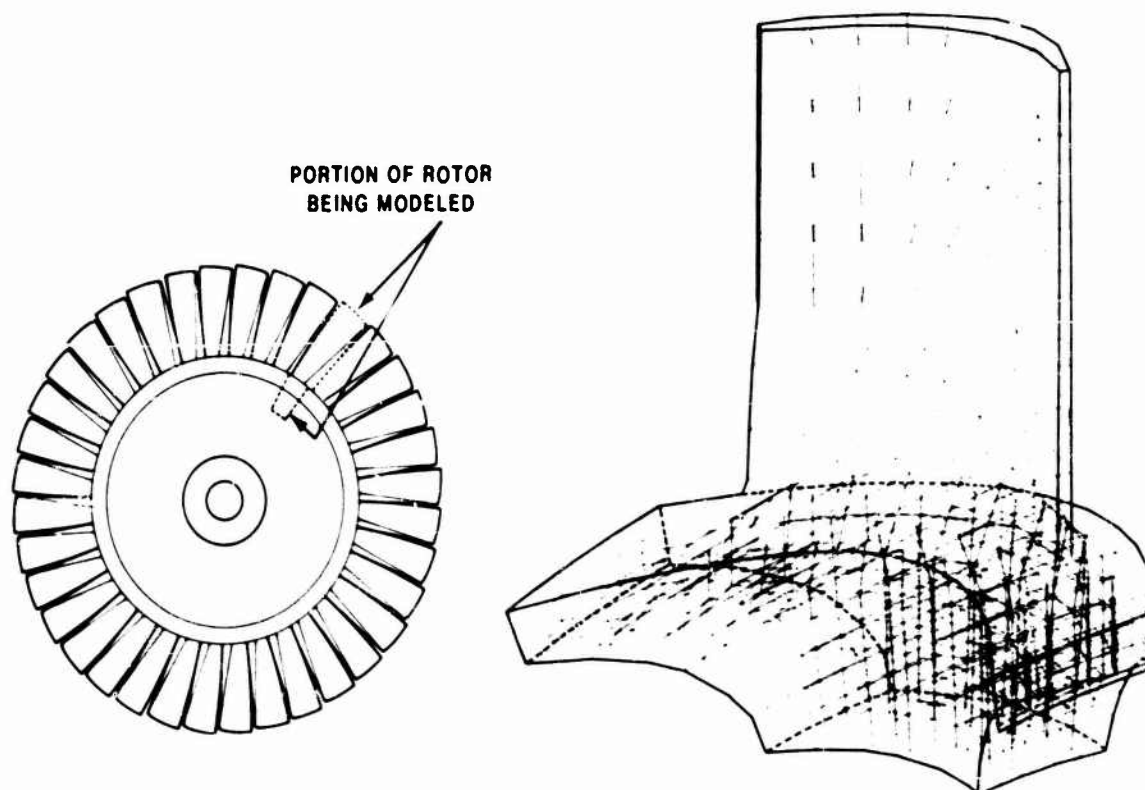Figure 3.1.2-4 — Axisymmetric Finite Element Model of First Stage Turbine Rotor Disk

Figure 3.1.2-5 — Three Dimensional Finite Element Model of First Stage Turbine Rotor Disk and Blade Segment
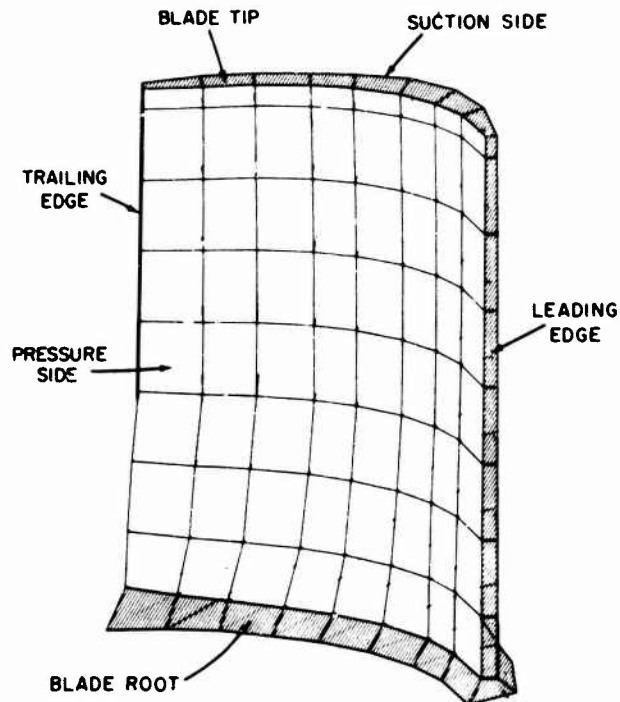
Figure 3.1.2-6 — Three Dimensional Finite Element Model of First Stage Turbine Rotor Blade

The output of the FEHT and FEST axisymmetric codes is available as either printout or two-dimensional contour maps, shown in Figures 3.1.2-7 and 3.1.2-8. Contour maps of structural responses to applied loadings (temperature, stresses and deformations) are powerful design aids. They can quickly identify potential problem areas of peak temperatures, stresses, stress gradients, the volume or area under high stress and potential interferences. These are all important considerations in brittle materials design.
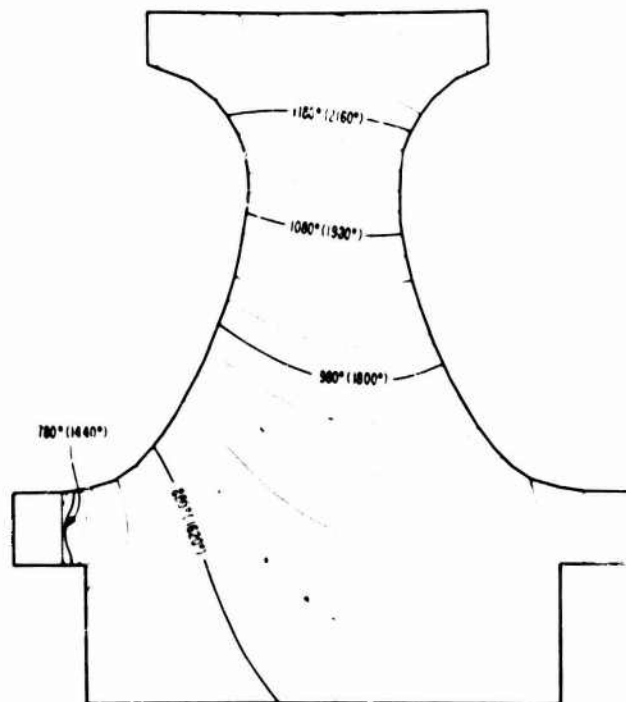

Figure 3.1.2-7 — Two Dimensional Temperature Contour Map of First Stage Turbine Rotor Disk at 1370°C (2500°F) Turbine Inlet Temperature and Full Speed
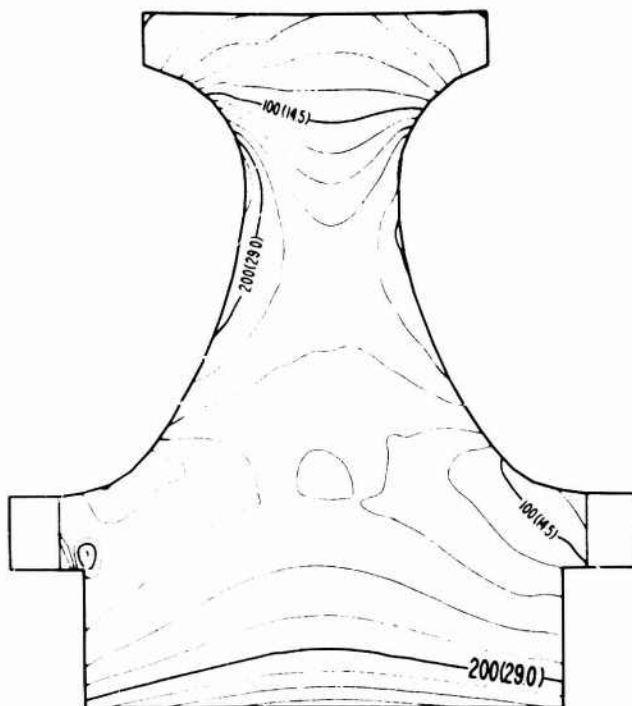
Figure 3.1.2-8 — Two Dimensional Stress Contour Map in MN/m² (KSI) of First Stage
Turbine Rotor Disk at 1370°C (2500°F) Turbine Inlet Temperature and
Full Speed

3.1.2.2 Three-Dimensional Codes

A full three-dimensional analysis was required for detailed studies of thermal and structural re-
sponses of axisymmetric three-dimensional structures or certain features of these structures. In the
latter category were the rotor blades, stator vanes and, most importantly, the junction of these elements
with the axisymmetric body. This junction required very careful evaluation as it was the most likely
site of stress concentration.

To facilitate these analyses, additional computer programs were procured, modified as needed, and
made compatible with each other for ease of processing. Included were two finite element codes for
computing temperatures (TAP), and stresses (SAP), and three special purpose programs for calculating
convective heat transfer coefficients and aerodynamic loadings on airfoil structures (TSONIC BLA-
YER and ADFORCE)[10]. These programs functioned and communicated through the use of various
buffer, geometry generation, storage, data handling and plotting routines.

The heat transfer program — TAP, as purchased from Engineering Analysis Corporation of Re-
dondo Beach, California, would handle both steady state and transient problems, and admit heat input
by convection, conduction and heat generation internal to elements. This program was modified to
allow solution of thermal problems involving temperature-dependent properties. Output from this
program could be stored on tape and used as input to the stress program — SAP.

A more advanced version of the original SAP program, SAP III, was developed by Professor E. L.
Wilson of the University of California at Berkeley, Division of Structural Engineering. It is a general
purpose three-dimensional static finite element stress program. The basic elements are linear eight
noded and parabolic twenty noded isoparametric solids with elastic properties and thermal expansions
fully orthotropic and varying with temperature. SAP III was modified to handle centrifugal loading, a
required feature for turbine blade analysis.

The program, in its original form, would accept boundary conditions consisting of point loads,
pressures and displacements. A different type of boundary problem arises, however, in the analysis of

structural features which are periodic in nature; examples are the structural interactions of blades with a disk or of stator vanes and their attached shroud. These problems were more economically analyzed by the use of the 'principle of repeatability', a method where a typical segment containing the repeating feature is analyzed. This method required that the displacements and rotations of the two surfaces bounding the segment be matched. Modifications to SAP III to handle this type of repetitive boundary problem failed to provide a stable solution when executed on a Honeywell H6080 computer. However, a close simulation was achieved, with the unmodified SAP III program, through coupling corresponding boundary nodal points by way of rigid trusses and executing the solution in double precision.

All five programs (TAP, SAP III, TSONIC, BLAYER and ADFORCE) compose the basic units of an analytical process devised for the three-dimensional analysis of turbine flowpath components. A schematic diagram of the process developed for the stator study is displayed in Figure 3.1.2-9. The three-dimensional finite element models generated and used in the analysis of the first stage rotor and stator are displayed in Figures 3.1.2-5 and 3.1.2-10. The stator model, as shown, was generated by the Lawrence Livermore Laboratories under a separate ARPA contract.
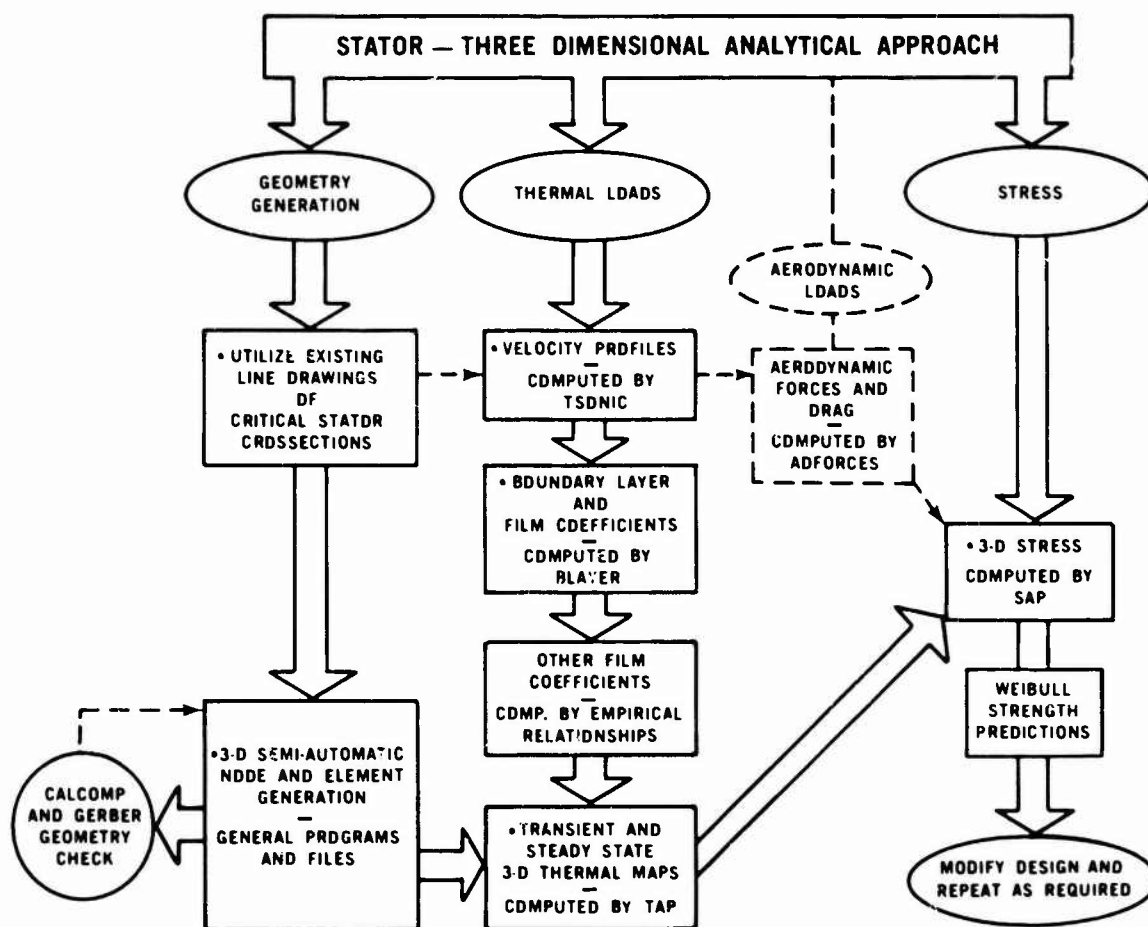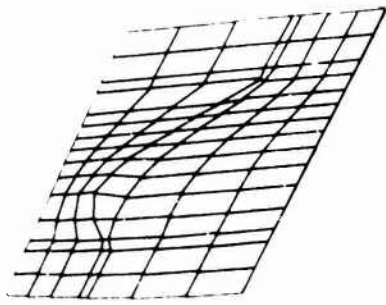

Figure 3.1.2-9 — Schematic Diagram of Three Dimensional Analytical Process as Applied to Ceramic Stator
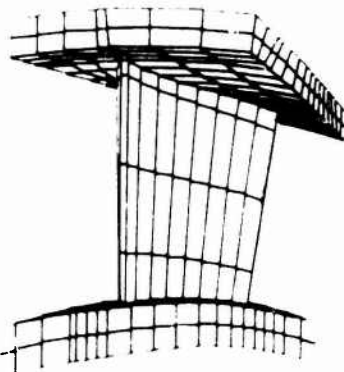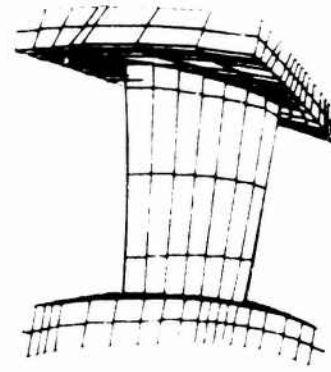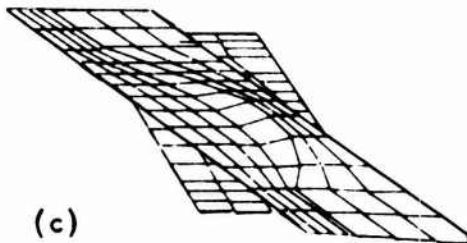
(a)

Outer shroud

Air foil

Inner shroud

(b)

(d)

(c)

Figure 3.1.2-10 — Three Dimensional Finite Element Model of First Stage Stator

3.1.3 RELIABILITY ANALYSIS

Two analytical methods evolved during the program for the design of structural ceramic components: (1) a method to calculate the fast fracture reliability, and (2) a method to calculate the time-dependent reliability.

3.1.3.1 Fast Fracture Reliability Analysis

Like all structural materials, ceramics have flaws; but, being brittle, ceramics lack plastic flow to relieve localized stress concentrations caused by these flaws. Since flaws are distributed randomly, the strength of ceramic components varies not only from component to component but also within the same component. If the flaws within a component could be characterized by size, shape, and location with non-destructive testing, then a deterministic type analysis could accurately predict the failure load of a structure using fracture mechanics relationships. Conversely, for a given application and desired reliability, the required accuracy of flaw detection and characterization varies with the fracture toughness of the material.

The non-destructive flaw detection techniques currently available for ceramics lack the capability to detect and characterize flaws of the size that often cause failure in ceramic turbine components; therefore, a probabilistic approach to the calculation of fast fracture reliability was developed and, in particular, utilized the probability of failure theory devised by Weibull.[15]

The Weibull approach to predicting the probability of failure of a structure is to recognize that each element in the structure has a definite probability of failure and that the structure in its entirety could be considered to be an assembly of individual elements with an associated probability of failure. Vardar and Finnie[16] give an integral formulation of the Weibull approach:

$$P_f = 1 - e^{-B} = 1 - e^{-\int_V \{K \int_A \sigma_n^m dA\} dV} \tag{1}$$

The term in the parenthesis is evaluated on the surface of the unit sphere, illustrated in Fig. 3.1.3.1, over the regions where the normal stress is tensile and neglecting regions where the normal stress is compressive. The reason for neglecting compressive stress is that, for ceramics, compression is not nearly as detrimental in causing fracture as is tension and also it minimizes mathematical complexities.[15,17] The normal stress on the surface of the unit sphere in terms of the maximum principal stresses and the polar and azimuthal angles is given by:

$$\sigma_n = \cos^2\phi \ (\sigma_1 \cos^2\psi + \sigma_2 \sin^2\psi) + \sigma_3 \sin^2\phi. \tag{2}$$
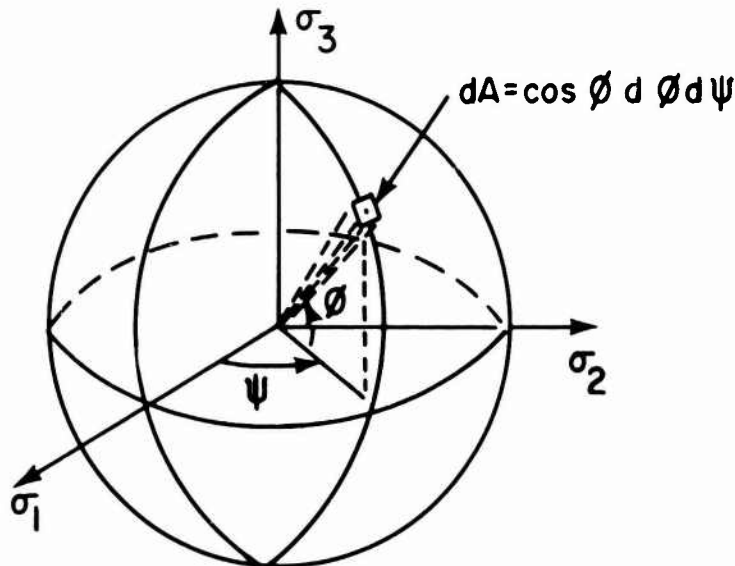

Figure 3.1.3-1 — Geometric Variables Used to Describe Location on a Unit Sphere

The constant, K, is given by:

$$K = \frac{2m + 1}{2\pi \, \sigma_0{}^m} \; . \tag{3}$$

The $(2m + 1)/2\,\pi$ term in Equation 3 is a compatability factor required to make the result of integrating Equation 1, using the normal stress distribution of Equation 2 for uniaxial stress cases, agree with the results obtained from the one dimensional Weibull equation:

$$P_f = 1 - e^{-\int_V \left(\frac{\sigma}{\sigma_0}\right)^m dV} \tag{4}$$

The integration of Equation 1 over an entire structure is accomplished by dividing the structure into finite elements in which the principal stresses can be assumed to be constant. The result of integrating over the unit sphere is constant in each finite element; therefore, the risk of rupture for each element is simply the volume of the element times the integrated result over the unit sphere. This procedure is very convenient when used with finite element stress programs.

In the Weibull formulation σ_0 and m are parameters which show the probability of having a certain strength in any finite element. The values of σ_0 and m are obtained from experimental test results. Weibull showed that the characteristic strength, σ_0, is identical to the ultimate strength of the material in the classical theory as the Weibull modulus, m, increases indefinitely. This provides a physical interpretation of the characteristic strength. The Weibull modulus may be interpreted as a measure of variability or scatter in material; as m increases the variability of the strength diminishes.

The Weibull parameters σ_0 and m are obtained from strength testing. For bend tests, the stress distribution is uniaxial and the risk of rupture is given by:

$$B = \int \left(\frac{\sigma}{\sigma_0}\right)^m dV \tag{5}$$

In a bend test, the stress on the outer fiber at failure is called the modulus of rupture (MOR). In this study four-point bending, with the middle span located symmetrically to the total span, was used and Equation 5 was integrated over the volume of the bar in tension to obtain Equation 6, the expression for the risk of rupture of such a bar:

$$B = \left(\frac{MOR}{\sigma_0}\right)^m \left(\frac{bh}{2}\right) \left[\frac{L_1 + mL_2}{(m + 1)^2}\right] \tag{6}$$

The data obtained from a set of test bars was fitted to Equation 7 with maximum likelihood techniques:[18]

$$P_f = 1 - e^{-\left(\frac{MOR}{MOR_0}\right)^m} \tag{7}$$

The probability of failure of the test bars may also be represented by the Weibull integral formulation which must be equal to Equation 7:

$$P_f = 1 - e^{-\left(\frac{MOR}{MOR_0}\right)^m} = 1 - e^{-\left(\frac{MOR}{\sigma_0}\right)^m \left(\frac{bh}{2}\right)\left[\frac{L_1 + mL_2}{(m + 1)^2}\right]} \tag{8}$$

Substituting the value of the characteristic modulus of rupture MOR_0 for the modulus of rupture MOR into Equation 8 and solving, one obtains Equation 9, the equation for the characteristic strength:

$$\sigma_0 = MOR_0 \left(\frac{bh}{2}\right)^{\frac{1}{m}} \left[\frac{L_1 + mL_2}{(m + 1)^2}\right]^{\frac{1}{m}} \tag{9}$$

The parameters σ_0 and m define the strength of the material and are independent of the volume and geometry of the structure. They are the values used to determine the failure distribution of a complex structure and are generally determined from MOR bar tests. It is important to note that the MOR is not an intrinsic material parameter but depends on the geometry of the MOR bar and test fixture.

The integral formulation of the Weibull equation was programmed for a digital computer. The code used as input the principal stresses calculated with axisymmetric and three dimensional finite element stress codes. The code evaluated the integrals in Equation 1 by numerical integration in each volume element of the finite element mesh assuming that the principal stresses were constant through the element. The code also used as input material strength data in the form of characteristic modulus of rupture and Weibull modulus, both as a function of temperature. The code selected the material strength data according to the temperature of the element.

As developed, the fast fracture reliability code can be used in two ways:

1) The computer code can calculate the survival probability of a certain component under a specified load when input consists of material strength data in the form of Weibull strength parameters (Weibull parameters are the characteristic MOR strength obtained from simple four-point bend tests and the Weibull shape parameter or slope).

2) The computer code can generate sets of Weibull strength parameters required of a material to meet a specified reliability goal, when given the desired reliability level.

Nomenclature

dA	= differential area
B	= risk of rupture
b	= width of specimen
h	= height of specimen
K	= constant defined by Equation 3
L_1	= length between supports
L_2	= length between load points
m	= Weibull modulus
MOR	= modulus of rupture
MOR_0	= characteristic modulus of rupture
P_f	= probability of failure
V	= volume of the structure
$\sigma_1, \sigma_2, \sigma_3$	= principal stresses
σ_n	= normal stress
σ_0	= characteristic strength
ψ	= azimuth angle
ϕ	= polar angle

3.1.3.2 Time-Dependent Reliability Analysis

The previous section covered the development of an analytical method to calculate fast fracture reliability. This calculation of fast fracture reliability is an important first step in the calculation of time-dependent reliability, the subject of this section. Certain ceramics, including hot pressed silicon nitride,[19] exhibit delayed fracture or static fatigue at elevated temperature under loads. This static fatigue is caused by existing flaws in the material growing over a period of time until they are large enough to cause failure. This phenomenon reduces the reliability of the structure with time, so the designer needs to have a method of calculating time-dependent reliability.

The basis for time-dependent reliability analysis is the experimental observation[19] that the velocity of a pre-existing crack can be described with a power law relationship:

$$V = AK_1^n \tag{1}$$

This equation expresses the rate of slow-crack growth caused by grain boundary sliding, typical in such materials as hot pressed silicon nitride. Paluszny[20] combined the power law relationship for crack velocity with the Weibull relationship for fast fracture reliability to arrive at the following equation for reliability versus time:

$$R = \exp -\left[\left[\left(\ln\left(\frac{1}{R_{ff}}\right)\right)^{\frac{n-2}{m}} - \frac{\sigma^n t}{B\sigma_\theta^{n-2}}\right]^{\frac{m}{n-2}}\right] \tag{2}$$

In this equation, the constant B is defined by the following equation:

$$B = \frac{2}{(n-2)\, Y^2\, AK_{1C}^2} \tag{3}$$

These equations apply to a structure under constant load, but Paluszny extended the analysis to time-dependent load by approximating the load history with a simple step function. For a finite element model, Equation 2 is applied to the volume of each element and the reliability of the entire structure is calculated with the following equation:[21]

$$R = \prod_{i=1}^{N} R_i \tag{4}$$

In extending this analysis to multi-axially stressed ceramic turbine structures, some simplifying assumptions were necessary.[19] For the convenience of the reader, these assumptions are summarized here:

1) Omit time-dependent effects such as material instability, high-temperature oxidation, etc.

2) Consider only the normal stress or the opening mode (K_I) of crack propagation; neglect modes K_{II} and K_{III}.

3) When the load varies with time (σ) assume that the orientation of principal stresses throughout the structure remains constant with time.

4) Treat time to failure using Weibull's probabilistic statistical model of fracture with the premise that flaws which control strength are identical for both fast fractures and time-dependent fractures.

The time-dependent reliability equations were programmed for the digital computer. The code utilized the output of the fast fracture reliability code, comprising data on the elemental volume, fast fracture reliability, maximum principal stress, characteristic strength of the elemental structure,[21]

Weibull modulus, and temperature of the element. As programmed, this data was written on tape by the fast fracture reliability code in a format compatible with the time-dependent reliability code.

Two different data bases were available to define the time-dependent characteristics of the material, double torsion and stress rate testing. Double torsion testing[19] was a technique of measuring the velocity of a crack under load in a specially designed double torsion specimen. Analysis of the results gave K_{IC}, n, and "A" the material parameters required for time-dependent reliability calculations. Stress rate testing measured the fracture stress of MOR specimens under varying load rates. The results were sets of fracture stresses at corresponding stress rates.

The data required for time-dependent reliability calculations were calculated with the following formulas:[22]

$$n = 1 - \frac{\ln\left(\dfrac{\sigma_2}{\sigma_1}\right)}{\ln\left(\dfrac{\sigma_{f2}}{\sigma_{f1}}\right)} \tag{5}$$

$$B = \frac{\sigma_f^3}{\sigma(n+1)} \tag{6}$$

The code incorporated the option of inputting double torsion or stress rate material data. The data was inputed in tabular form with the parameters given with their corresponding temperature. The code interpolated the table of material parameters to obtain the value of the material parameter corresponding to the temperature of the element.

As developed, the time-dependent reliability code can be used in the following modes of calculation:

1) Survival probability after the elapse of a specified service life or time at load.

2) Service life available for a specified reliability. This becomes an iterative process as strength degradation in a typical turbine structure is not uniform because stresses and temperatures are seldom uniform.

Nomenclature

A	=	Premultiplier in crack equation
B	=	Constant in reliability versus time equation
K_I	=	Stress intensity
K_{IC}	=	Critical stress intensity, a material parameter
n	=	Crack velocity exponent
N	=	Number of elements in the structure
m	=	Weibull modulus
R	=	Reliability as a function of time
R_i	=	Reliability of ith element
R_{ff}	=	Fast fracture reliability
σ	=	Stress, MPa

σ_θ = Characteristic strength of the structure

σ_f = Fracture stress

σ = Stress rate

t   = Time, hours

V   = Crack velocity

Y   = Stress intensity factor coefficient, non-dimensional

3.2 CERAMIC MATERIALS AND PROCESSING TECHNOLOGY

3.2.1 INJECTION-MOLDED REACTION-BONDED SILICON NITRIDE

3.2.1.1 Introduction

The development of injection-molded reaction-bonded Si_3N_4 (IMRBSN) has involved many areas of material science; polymer technology and processing, powder processing, high-temperature chemistry and physical property testing and analysis. The input from these areas has been blended together to reach the final material development goal, a high density, high strength RBSN. Throughout the development of injection-molded reaction-bonded Si_3N_4, two guidelines were adhered to: 1) the density of the material was to be as high as possible consistent with fabrication limitations — that is, the material must be able to be injection molded and the green compact must be nitrided with no evidence of metallic silicon remaining; and 2) all process modifications were made in an attempt to optimize the room temperature and high-temperature strength properties of the material.

The process of reacting silicon to Si_3N_4 is unique in that, during the course of the process. no dimensional changes occur. The final density of RBSN is solely dependent on one parameter, the green density of the starting silicon compact. This is contrary to most ceramics which shrink and densify as they are processed. Consequently, this phenomenon, which is an advantage when producing components with complex shapes and high dimensional tolerances, is also a problem in producing a high density material since there is no densification taking place through shrinkage.

3.2.1.2 Material Development for Molding

The injection molding composition to produce Si_3N_4 consists of an organic carrier, silicon metal powder, and a nitriding aid (Fe_2O_3). The volume percentage of solids (silicon plus iron oxide) in the total molding batch must be large if a high green density silicon compact is to be produced. Figure 3.2.1-1 shows that to produce a 2.7 g/cc Si_3N_4 compact, a molding mix consisting of 73.5 volume percent solids must be obtained.
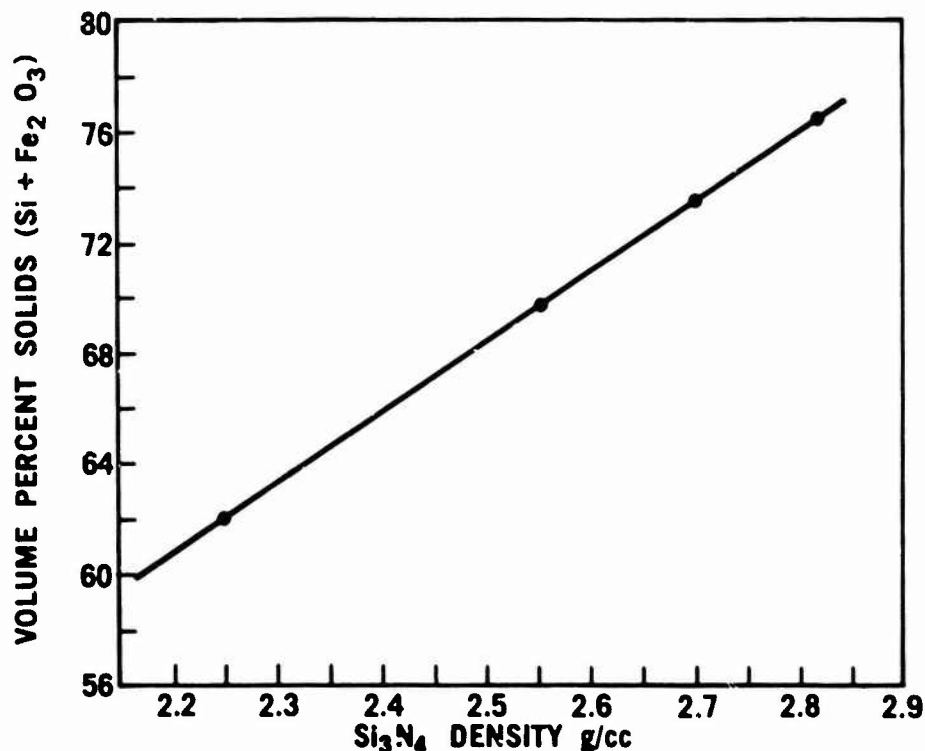

Figure 3.2.1-1 — Final Silicon Nitride Density Vs. Volume Percent Solids in the Starting Composition

A major problem arises in obtaining a batch composition which not only yields the correct density but also has a viscosity which is low enough to be processed by injection molding. Figure 3.2 1-2 illustrates that the relative viscosity of a dispersion of solid spheres in an organic medium is dramatically increased with increased volume percent loading of the solids according to the relation:

$$n_r = \frac{2.5\ V}{1 - kV}$$

where n_r is the relative viscosity, V is the volume fraction of solids and k is a self-crowding and hydrodynamic interaction factor equal to 1.35[23].
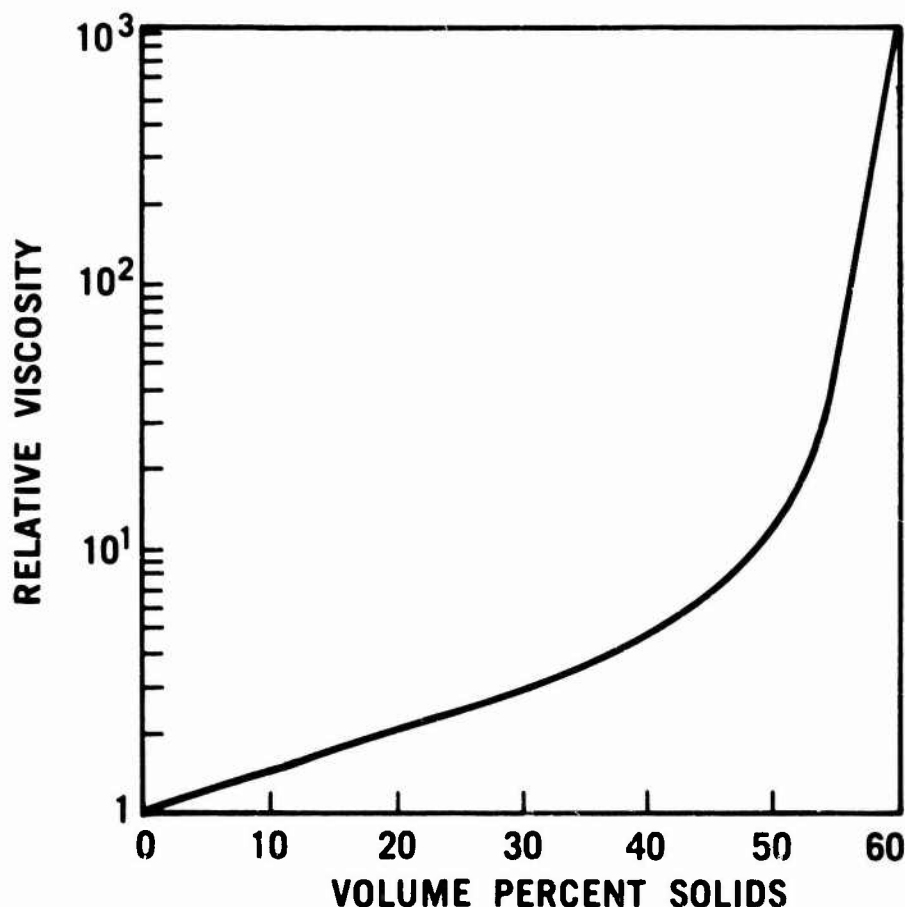

Figure 3.2.1-2 — Relative Viscosity as a Function of Volume Percent Solid Spheres in an Organic Suspension

It was also shown that the viscosity of highly concentrated suspensions could be altered by blending solids of different particle sizes [24]. Figure 3.2.1-3 shows that for a bimodal suspension of spheres (volume of fine spheres = 25%) the volume loading can be increased by approximately 17% with no increase in the viscosity of the system.

The reduction of this theory to practice proved prohibitive because of the difficulties involved in obtaining actual silicon particle distributions required by the theory and in homogeneously blending the distributions which were obtained. In very general terms, however, the theory could be interpreted to say that the required distribution for minimum viscosity should be very broad.

24

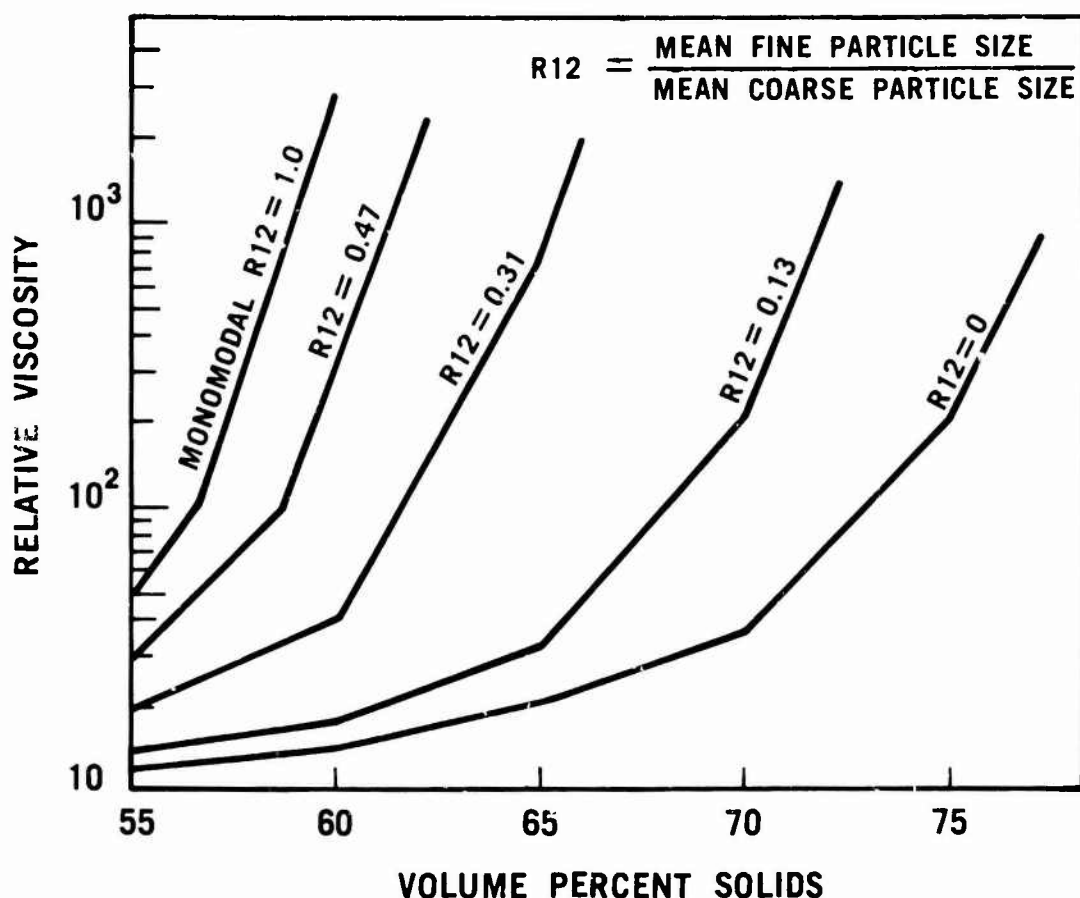$$R12 = \frac{\text{MEAN FINE PARTICLE SIZE}}{\text{MEAN COARSE PARTICLE SIZE}}$$

Figure 3.2.1-3 — Relative Viscosity as a Function of Volume Percent Solid Spheres in a Monomodal and Several Bimodal Suspensions with 25 Percent Volume Fraction of Small Spheres

Injection Molded Material Development

At the start of this program the density level of the IMRBSN was 2.2 g/cc. Components of complex shapes were being produced; however, the quality of the components, or of the RBSN needed improvement. The injection-molding system utilized a mixture of organic material plus silicon metal. A two-component organic system had been used, but was found unsuitable for high silicon loading and also created problems of density variations during molding due to vaporization of one of these components. For these reasons, this system was abandoned for a more conventional wax binder system [25].

Once the wax binder system was defined, a large number of iterations were performed on the silicon powder distributions in an attempt to increase the volume percent loading of the system from 60% to 75%, while keeping the maximum viscosity such that a complex part could still be injection molded.

Initially, the silicon particle size was specified merely as minus 325 mesh, as is shown in Figure 3.2.1-4 as the "0 hr." powder. This distribution contributed to the problem of low density RBSN. It also affected the quality because the large particles present could not be properly nitrided. This is an excellent example of the interaction required between the two stages of RBSN development, fabrication and nitriding.

In order to obtain silicon powder with a very broad particle distribution, dry ball milling was selected. Silicon powder with a starting distribution as shown in Figure 3.2.1-4 (0 hr.) was milled for various times in an alumina ball mill using alumina milling media. A ball-to-charge ratio of 4 to 1 was

maintained. The resultant distributions are also given in Figure 3.2.1-4. The distributions become finer and also broader as the milling times were increased. Since no milling additives were employed, the powder "caked up" in the mills after 24 hours. This resulted in broad distributions being obtained. Spectrographic analysis (Table 3.2.1-1) of the as-received and 140-hour milled powder showed little contamination due to milling. The increase in the oxygen content of the silicon was thought to be due to the oxidation of the freshly cleaved surfaces.
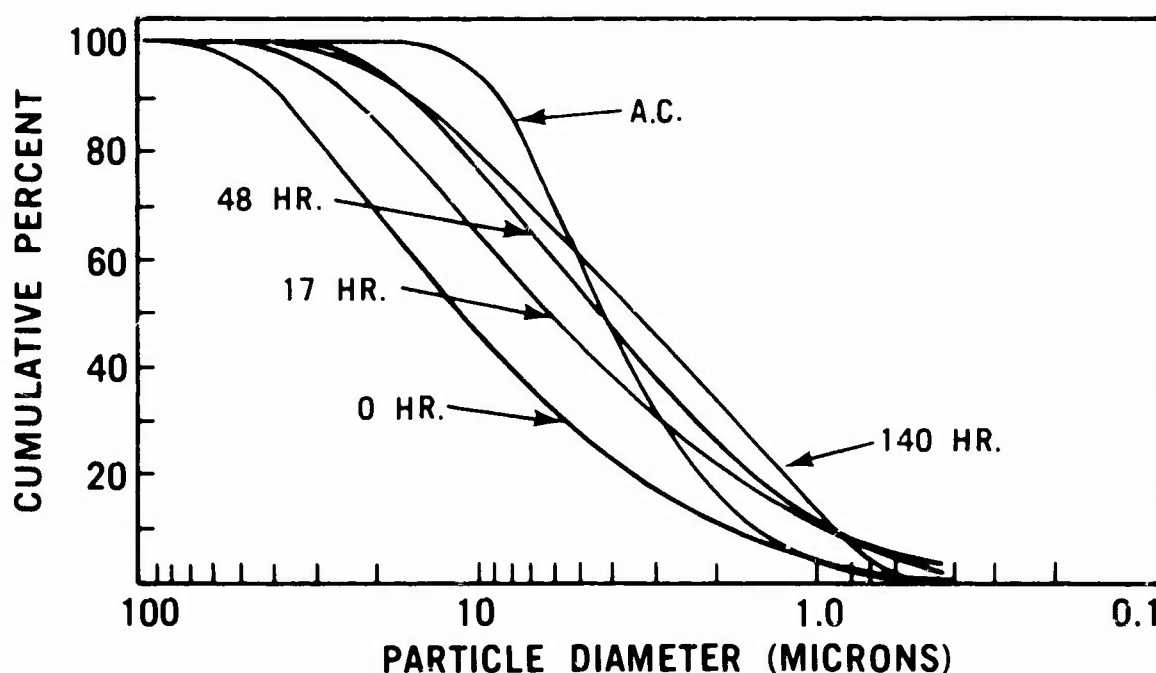

Figure 3.2.1-4 — Silicon Powder Particle Size Distribution Curves, Dry Ball Milled For Various Times

TABLE 3.2.1-1

SPECTROGRAPHIC ANALYSIS OF SILICON POWDER
FOR MAJOR IMPURITY ELEMENTS (WEIGHT PERCENT)

	Fe	Al	Ca	O₂*
As Received	0.60	0.20	0.02	0.77
140-Hour Mill	0.75	0.25	0.02	1.05

The injection molding experiments were conducted using a spiral flow test tool (Figure 3.2.1-5) mounted on a plunger injection machine. The tests were conducted using 2000 psi cylinder pressure and temperatures exceeding the organic melting point by 10°C. The results are expressed in inches of material travel in the spiral flow die, with the higher spiral flow distances indicating lower material viscosities and consequently better moldability. Figure 3.2.1-6 shows the molding results as a function of ball milling time for compositions loaded to 73.5 volume percent solids (2.7 g/cc Si$_3$N$_4$ density). The use of 140-hour grind silicon resulted in the highest flow and best moldability. A finer, sharper distribution curve (Figure 3.2.1-4, A.C.) was obtained by air classifying the starting powder and removing the silicon with a size greater than 15 microns. This powder would not even completely mix with the organic material at the 73.5 volume percent level and was therefore unsuitable for molding. Figure

*Neutron Activation Analysis Performed at AMMRC

26

3.2.1-7 shows by changing the percentage of solids in the molding composition, the rheological properties also change significantly. It was shown that by increasing the percent solids, the spiral flow distance or moldability decreases. It also shows that a molding composition consisting of 76.5 volume percent solids (2.85 g/cc Si$_3$N$_4$ density) has a spiral flow distance of 6 inches, which is suitable for processing into certain turbine components. However, compositions with these density levels may be difficult to nitride.
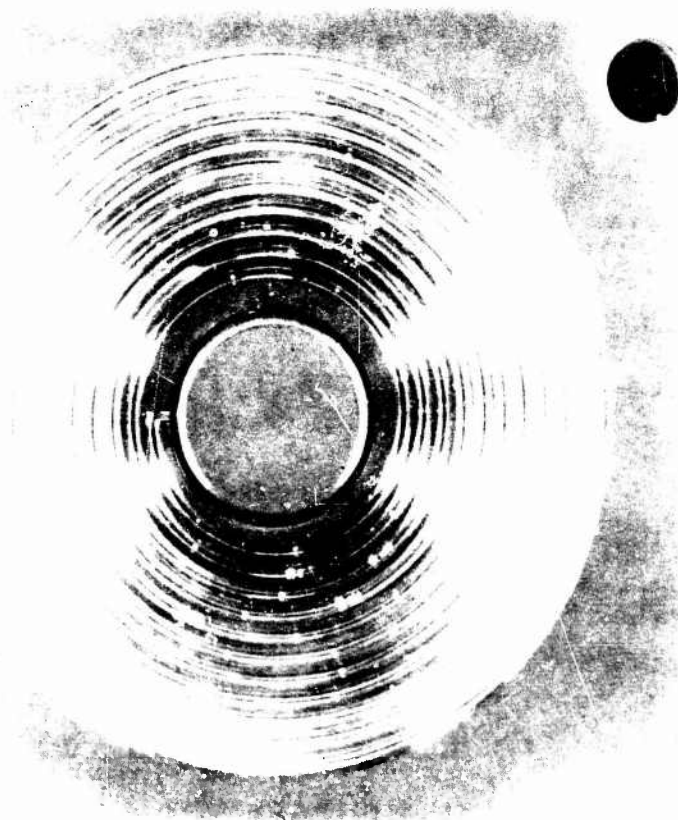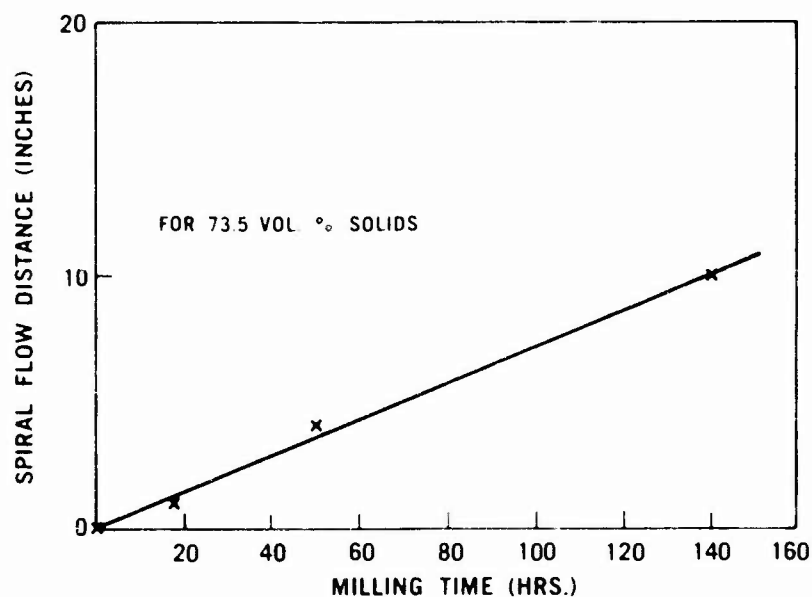

Figure 3.2.1-5 — Spiral Flow Test Tool

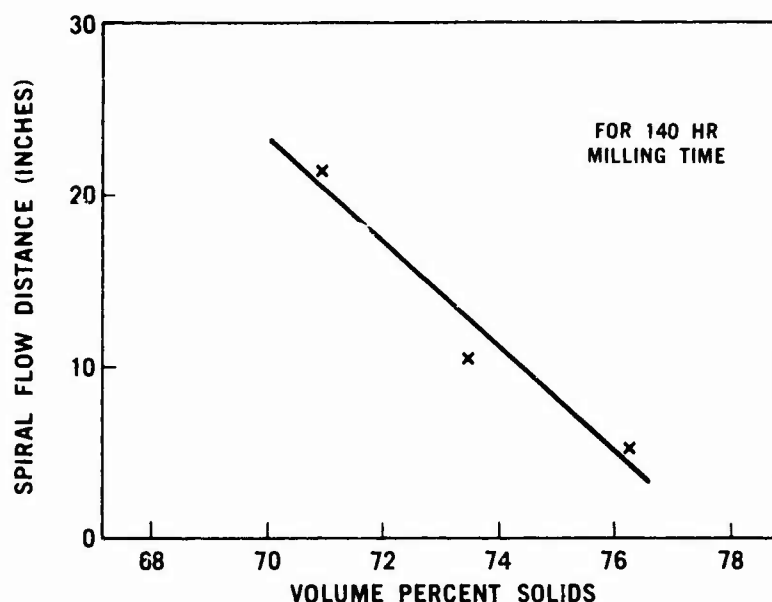Figure 3.2.1-6 — Spiral Flow Distance as a Function of Ball Milling Time at Constant Percent Solids

Figure 3.2.1-7 — Spiral Flow Distance as a Function of Volume Percent Solids Using 140 Hour Ball Milled Silicon Powder

This data shows that the particle size distribution is an important and predictable variable in molding composition development. It shows that by the proper choice of particle distributions, compositions can be made that exceed the current nitriding technology.

Final Composition

At the conclusion of this program, the injection molding composition was as follows:

Binder Composition:	Wax
Volume % Solids:	73.5%
Spiral Flow Distance:	10 inches
Silicon Particle Size:	140-hr. Grind (Figure 3.2.1-4)

These parameters allow all the 820 engine hot flowpath components, nose cones, stators, and rotor blade rings to be injection molded to a 2.7 g/cc density. All the components can be completely nitrided with no unreacted silicon. The four-point bend strength of this IMRBSN is 45.2 Ksi.

3.2.1.3 Molding Process Development

Injection molding was identified as a potentially valuable fabrication process for ceramic turbine components, especially considering the foregoing development of an injection-moldable RBSN material of strength adequate for turbine rotor blade rings and stators. Development of ceramic injection molding technology to successfully mold high quality turbine ceramics is an iterative process involving development work in machinery, tooling and control systems.

Initial injection molding development was done on a Newbury V130T vertical clamp injection machine. The shot capacity of this machine was 1½ oz. of ceramic molding compound making it suitable for injecting test bars and individual stator vanes as shown in Figure 3.2.1-8. Molding development of larger components such as the air inlet nose cone, shown in Figure 3.2.1-9, was conducted on a Reed Prentice 450 TC horizontal clamp, through platen injection machine. Both machines had mechanical toggle clamping and a simple ram injection cylinder. As advanced tooling designs for molding monolithic rotor blade rings and turbine stators were developed, an additional consideration of machine clamp alignment and accuracy became apparent. The brittle nature of green ceramic components makes them sensitive to uncontrolled tooling movement during die unloading. A clamp system having high accuracy is required.

Figure 3.2.1-8 — Injection Molded Silicon Nitride Stator Vane

Figure 3.2.1-9 — As-Molded Air Inlet Nose Cone

Upon analysis of the injection-molder characteristics, determined from previous development work, specifications were developed for an upgraded molder. A molding machine incorporating a vertical hydraulic clamp with optimum platen alignment and through platen injection was designed and built. This machine is pictured in Figure 3.2.1-10.
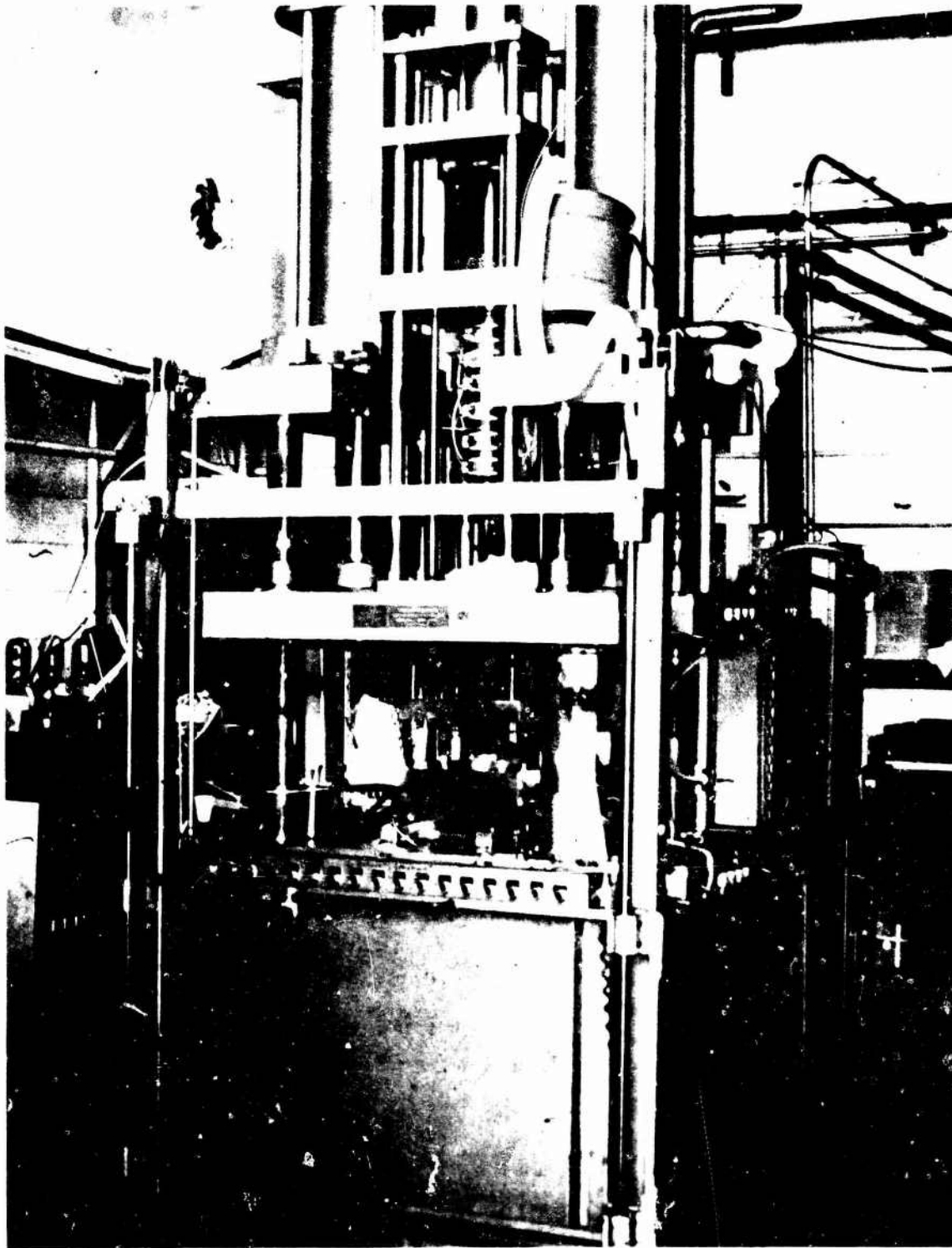
Figure 3.2.1-10 — Vertical Clamp Injection Molding Machine

Tooling development has closely paralleled molding machine development. Tooling required to produce injection-molded RBSN components was initially based on the tooling used to fabricate wax and plastic components. For initial development work a single vane stator tool was designed, followed by a single blade rotor tool. Each tool was of a simple hinged design with several sliding inserts. The tools were constructed with hardened tool steel in the cavity area to prevent abrasion from the ceramic material. The other operational portions of the tool were made of aluminum and mild steel.

From experience gained with these tools, specifications for new tooling were developed. The initial tools lacked stiffness and tended to distort under clamp load. Elimination of aluminum and reduction in the use of non-hardened steel in tool construction solved this problem.

Thermocouples were included in the tool to monitor tool temperature and to control tool heating. Although previous tools were heated by external heaters, new tooling utilized internal heaters close to the tool cavity. Water cooling passages were also included. The temperature control system was made independent allowing a difference in temperature to exist between portions of the tool.

Material entrance was accomplished through a central gate in the stationary tool half. The runner lengths were kept to a minimum and gate area was maximized. In controlling material flow through the tool, it was observed that when two flow fronts of material met, a weld or knit line developed. This could be minimized but not eliminated by gate design. To further minimize weld lines, an overflow reservoir was provided at the point where material from two approaching flow fronts met. The overflow reduced the knit line problem in a large percentage of molded components.

Tooling was designed vacuum tight in order to further control flow and minimize entrapped gas pockets within components. Prior to material injection a vacuum was drawn in the tool. This yielded precisely controlled venting not susceptible to variation from mold release or ceramic residue remaining on tooling surfaces. Normal vents can become plugged with liquid mold release or flash and cease to function. The vacuum system was designed to remain clear, and closed loop vacuum level sensing was employed to prevent tool fill without vacuum

The point at which tool-opening actuation is accomplished can affect the amount of molded-in stress in the component. Component shrinkage in the tool cavity prior to release of the constraining surfaces of the tool impart molding stresses to the component. Determination of the proper time to open the tool is complicated by variations in material temperature, time and pressure. All these factors can cause variable shrinkage of the material. To eliminate the influence of as many of these effects as possible, a thermocouple was provided in the material cavity, the tip of which would intrude into a non-essential surface of each component. The actuation of the die was made dependent upon part temperature level, thus eliminating dependence upon process time.

Tool deflection during the molding process can cause component breakage. To monitor tool deflection, Bently-Nevada proximity probes were mounted on the tools to give quantitative data on tool movement. Such data allowed tool and machine modifications required to reduce tool deflection below 0.0005 inches, a level where no detectable component damage occurred.

Control of temperature, pressure, and time is critical to successful injection molding. The highly loaded ceramic/organic system used in injection molding RBSN increases the sensitivity of the process to these variables. To accurately control the temperature, pressure and time variables, a microprocessor-based control system was developed. This system, in conjunction with commercially available hardware, is utilized to control the molding process. The base microprocessor is an Intel 80-80 system. The control panel is shown in Figure 3.2.1-11. All machine sequencing and timing is controlled by the microprocessor. Tool actuation and machine actuation are controlled based upon time or component temperature. The standard machine sequence for each component is contained within the microprocessor. Additional programming variation can be entered by means of a magnetic tape drive.

Temperature of the molding mix is controlled over four zones utilizing solid state temperature controllers. The controllers have an adaptive rate/reset capability and will control the melt in the cylinder to $\pm 2°F$. Temperature of the molding tool is controlled to $\pm t°F$ using similar controllers. If control of tool actuation is desired based upon component temperature, the microprocessor controls the system based upon inputs from two temperature sensors located within the tool cavity.

Pressure control over the molding system is achieved by use of an adaptive process control. This unit allows electronic control over injection and hold pressures and the resultant molding mix flow rates. Control is also provided for material cushion and feed. The effects of pressure variation on component quality will be discussed later in this section. Sensors for this system include hydraulic pressure ram position and cavity pressure. Based on these inputs the control modulates a flow divider hydro valve regulating injection or hold pressure as a function of ram position versus time.
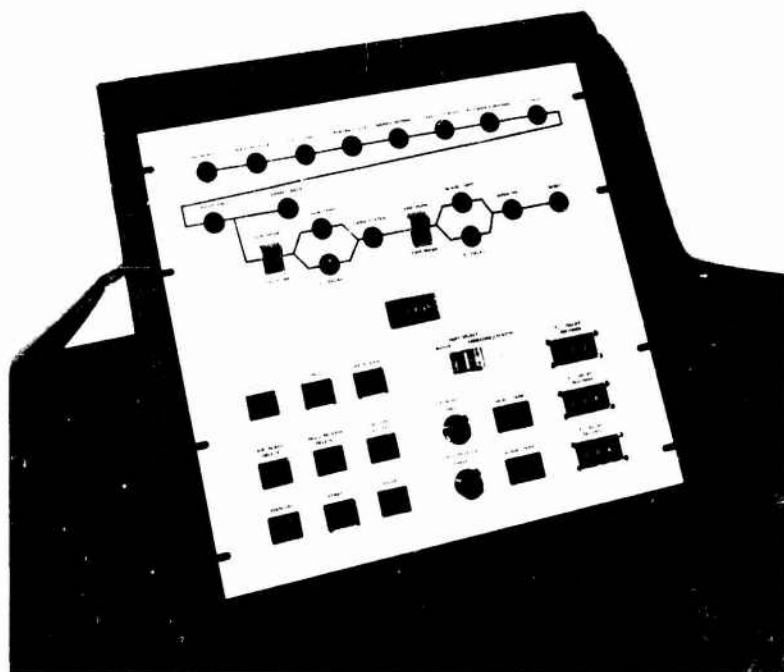
Figure 3.2.1-11 — Automatic Molding Control Unit

Accurate control of molding parameters must be coupled with accurate recording of their values. The availability of adequate data on a timely basis is essential to the successful development of an optimized injection molding process. In a research situation involving constant material refinements, efficient parametric optimization is required. Data acquisition in this injection molding system is accomplished utilizing a Fluke data logger and Tektronix magnetic tape recorder. Data for temperature, time, pressure, ram position and machine sequence data are recorded, stored and subsequently analyzed in digital form. This data acquisition technique reduces analysis time and yields more complete results from molding studies.

In summary, a systems approach has been stressed throughout the molding development work. The molder design, tooling design and control development have all been aimed at an integrated system with the flexibility required to conduct an iterative molding development program aimed at high quality ceramic turbine components.

3.2.1.4 Development of the Nitriding Process

Nitriding research was aimed toward developing a reaction-bonded silicon nitride (RBSN) material with high strength and high density. Throughout this development two guidelines were adhered to:

1) The density of the material is to be as high as possible, consistent with the limitations of fabrication; i.e., the material must be nitrided with no evidence of metallic silicon remaining; and,

2) All process modifications made are to optimize the strength properties of the material at both room and high temperatures.

In this program, nitriding developments were intimately tied to the injection molding process and the development of high 'green' densities, although resulting nitriding cycles were initially applied to slip cast RBSN. Separate company-funded research has been conducted to investigate optimum nitriding methods for slip cast components.

32

The nitriding technology was developed to yield maximum strength of the RBSN at any density level. Various nitriding variables were investigated:

1) Time-temperature cycles
2) Nitriding atmospheres
3) Nitriding aids
4) Furnace controls to monitor and control the reaction
5) Silicon purity
6) Particle size distribution

Quality assessment techniques were also developed; these included:

1) Strength testing
2) Creep testing
3) Stress rupture testing
4) Observation and interpretation of microstructure

Basic Nitriding Process

The nitriding reaction proceeds as follows:

$$3\ Si_{(s)} + 2\ N_{2_{(g)}} \rightarrow Si_3N_{4_{(s)}} \qquad (1)$$
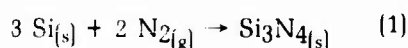
$$\Delta H = -173\ Kcal/mole \qquad (26)$$

One of the reasons it is difficult to form high quality RBSN is because this reaction is very exothermic.

The final density of RBSN is determined by only one parameter, the 'green' density of the starting silicon compact. The reaction of silicon with nitrogen to produce silicon nitride is unique in that no dimensional changes occur. An advantage when producing components of complex shape and high dimensional tolerances, this phenomenon becomes a disadvantage when attempting to produce a high density material, because no densification occurs through shrinkage.

The basic nitriding process employed by Ford in 1971, the state of the art at the time work started on this program, is summarized in Table 3.2.1-2, and is based upon processes proposed in 1960-1961 by Parr [27] and Popper [28] for the production of RBSN.

TABLE 3.2.1-2

NITRIDING STATE OF THE ART
1971

		Reference
Silicon Powder Purity:	0.7 wt. % Fe, 0.48 wt. % Al, 0.40 wt % Ca	(29)
Silicon Particle Size:	-75 microns	(3)
Nitriding Aid:	CaF$_2$ (~1 wt percent)	(29)
Green Density:	1.43 g/cm^3	
Nitrided Density:	2.3 g/cm^3	(1)
Nitriding Cycle:	RT - 1150°C - 15 hrs. 1150°C Hold 24 hrs.	
	1150°C~1460°C - 8 hrs. 1460°C - Hold 24 hrs.	(1)
Nitriding Atmosphere:	Flowing N$_2$	(2)
Phase Composition:	25% α/75% β Si$_3$N$_4$	(2)
Nitrided Strength:	15-17,000 psi	(1)
Microstructure:	See Figure 3.2.1-12	

Since advances in the nitriding process were so closely linked to advances in injection molding, such as changes in silicon particle size, purity and green density, each variable is discussed separately and not necessarily in chronological order, with secondary effects mentioned when necessary.
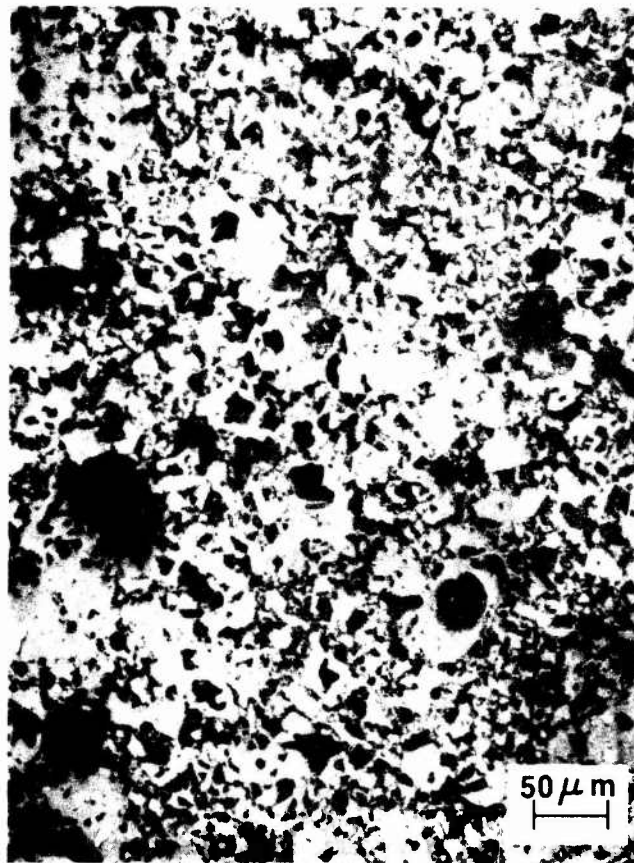
Figure 3.2.1-12 — Typical Microstructure of RBSN at the Program Beginning

The variable most commonly associated with nitriding research is the nitriding cycle. Time-temperature cycles were initially step cycles with at least one temperature hold period both below and above the melting point of silicon as shown in Figure 3.2.1-13. Varying the hold times showed that reducing the high temperature hold from twenty-four to four hours increased strength by 25%.[3] The resulting material contained an overall finer micro-structure with fewer large β grain clusters, as shown in Figure 3.2.1-14. These results had been expected as Evans[30] found that nitridation above the melting point of silicon resulted in large grain size and large porosity due to silicon meltout.

This led to the multistep nitriding cycle proposed by Messier[31] and illustrated in Figure 3.2.1-13. The cycle uses many temperature steps with the maximum nitriding temperature at 1400°C which is below the melting point of silicon. Successful nitridation is achieved because of the nature of nitriding kinetics; rapid nitridation follows each successive temperature increase. When a long hold occurs (over ten hours) the nitridation slows and eventually stops, but is reactivated by the next temperature increase.[31] With this type of cycle, the material strength can increase by approximately 50% over a two-step cycle.[10,32] However, strength reductions can occur due to the presence of large β grain clusters in the microstructure resulting from improper control of the nitriding temperature. Because of the many temperature increases, it is extremely difficult to control the nitriding exotherm and the resulting material temperatures which lead to this microstructure degradation.

34

Figure 3.2.1-13 — Various Nitriding Cycles

Figure 3.2.1-14 — Microstructure of RBSN Showing Effect of Changes in the Two Stage
Nitriding Cycle

    A. Nitrided for 24 Hours at 2300°F Followed by 24 Hours at 2660°F
       (9800x)

    B. Nitrided for 36 Hours at 2300°F Followed by 4 Hours at 2669°F
       (9800x)

The third type of cycle, the constant rate cycle, increases the temperature at about 3°C/hour.[8,9,10,32] It has been shown to change the nitriding kinetics.[11,33] Material showed no immediate improvement when nitrided in a 100% nitrogen (N_2) atmosphere. However, when a hydrogen/nitrogen (H_2/N_2) atmosphere was present, strength increased by 50%, again due to an improved microstructure, as shown in Figure 3.2.1-15.
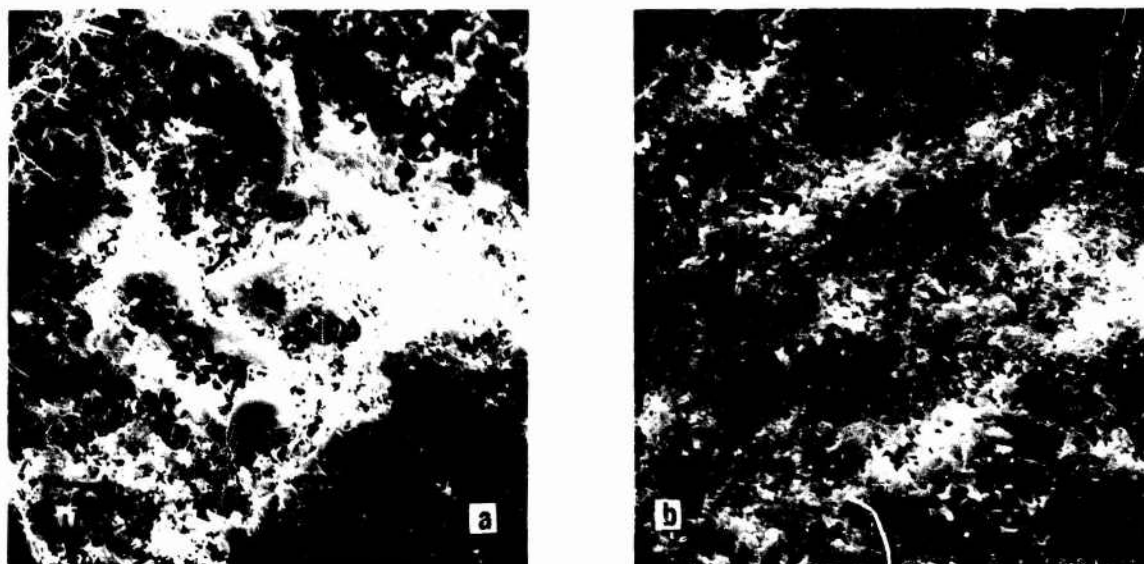
Figure 3.2.1-15 — Microstructure of RBSN, Nitrided Using the Constant Rate Cycle, Showing Effect of an Atmosphere of 100% Nitrogen (Left) and an Atmosphere of 96% Nitrogen, 4% Hydrogen (Right)

The degree of nitriding is independent of the type of nitriding cycle selected over a wide range of material densities, as noted in Table 3.2.1-3. This means that the basic nitriding reaction can be completed in many ways, but that not all of these ways result in high strength RBSN. Other investigators have shown the importance of proper choice of nitriding cycle.[34,35] Time and temperature relations have definite effects on material micro-structure which in turn determines material strength.

TABLE 3.2.1-3

PERCENT OF SILICON CONVERTED TO SILICON NITRIDE
FOR VARIOUS NITRIDING CYCLES AND DENSITY LEVELS

Nitriding Cycle	Atmosphere	2.3 g/cc	2.55 g/cc*	2.7 g/cc*	2.8 g/cc*
3 Step	100% N_2	97.5	97.0	98.5	94.7
	1% - 4% H_2/N_2	97.1	—	96.7	—
Multi-Step	100% N_2	97.0	99.0	98.1	95.9
	1% - 4% H_2/N_2	—	98.3	98.4	95.9
Constant Rate	100% N_2	—	98.3	98.0	—
	1% - 4% H_2/N_2	—	98.3	98.0	94.7

*2.9% Fe_2O_3 added as a nitriding aid. This has been compensated for in the conversion data.

Nitriding Atmosphere

Early nitriding work in this program was performed in a 100% N_2 atmosphere using a flowing gas stream. Altering the atmosphere in the furnace from free flowing to static conditions altered the phase composition of the material. The free flowing system yielded a 25% α/75% β composition and the static system yielded a 65% α/35% β composition [2] Lindley[36] and Jennings[37] made similar observations. Lindley also showed that nitriding in a static atmosphere could increase the material strength by approximately 50% .[36]

In the early stages of RBSN development, investigators used ammonia (NH_3) rather than pure nitrogen (N_2) for their nitriding. Lumby[38] was the first investigator to use atmospheres composed of hydrogen and nitrogen (H_2/N_2) gases to produce silicon nitride (Si_3N_4) powder. It was independently observed that a H_2/N_2 nitriding atmosphere could:

1) Produce a high α Si_3N_4 powder[1]
2) Produce a 42% increase in material strength[4,5,8,9,10,11,30]; and
3) Significantly increase high temperature creep resistance.[5,30]

Strength and creep improvements as a function of the percent of $H_{2(g)}$ in the nitriding atmosphere are displayed in Figure 3.2.1-16. Figure 3.2.1-17 shows that this strength increase occurs for all densities of RBSN.
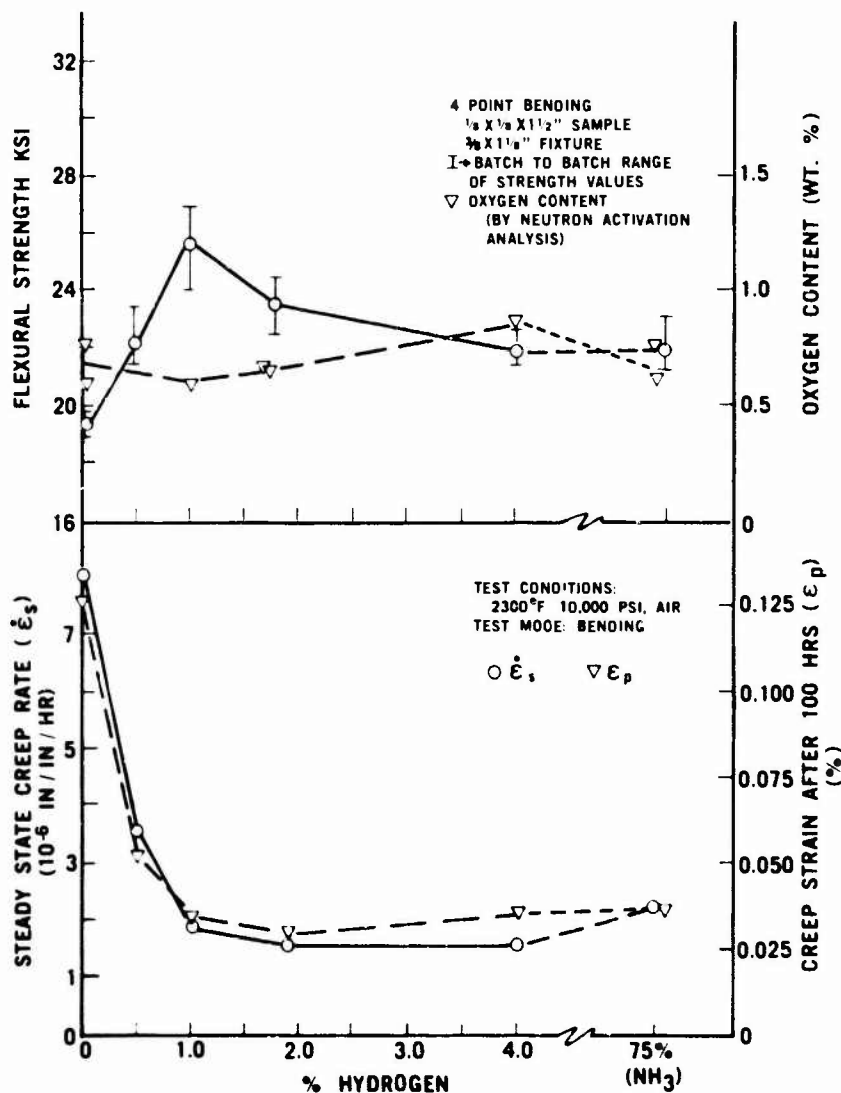

Figure 3.2.1-16 — Effect of Hydrogen in the Nitriding Atmosphere Upon Strength and Creep Resistance of RBSN
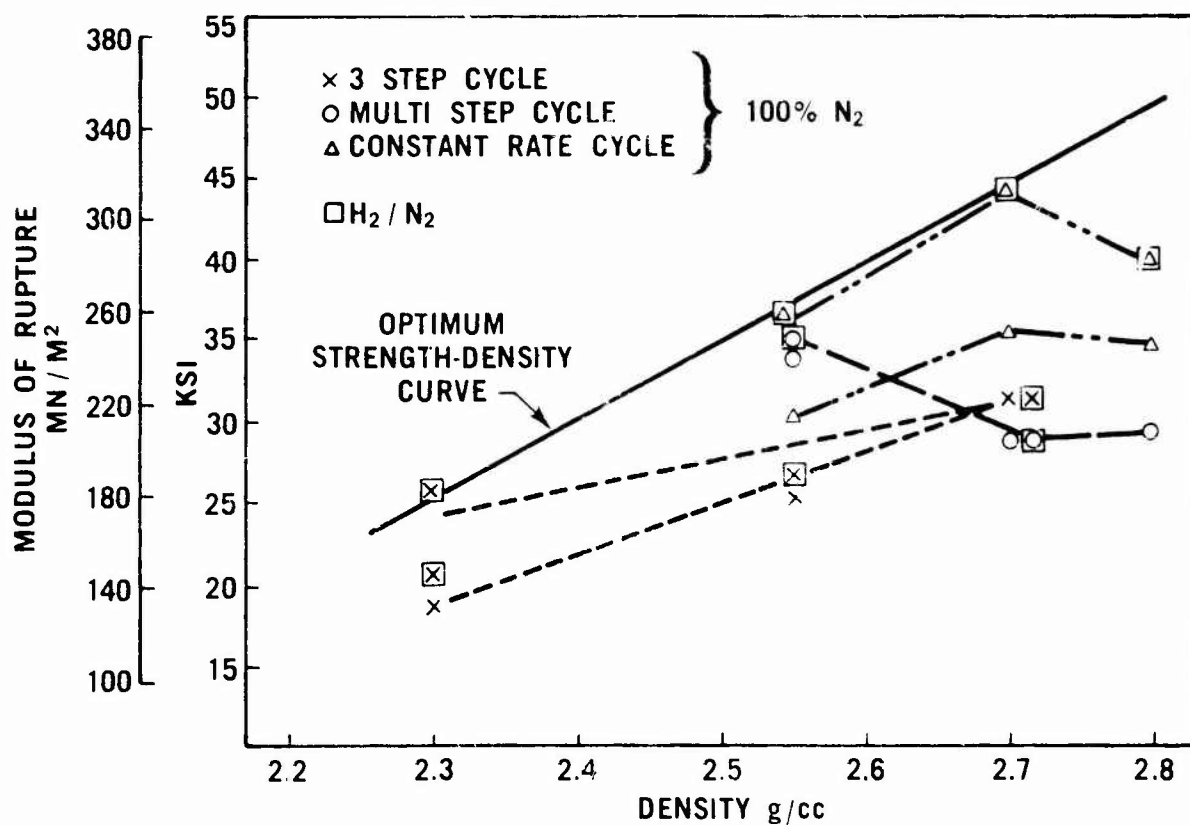
Figure 3.2.1-17 — Effect of Various Nitriding Cycles and Atmospheres Upon Strength of RBSN as a Function of Nitrided Density

Many explanations have been offered for the beneficial effect of $H_{2(g)}$ in the nitriding process. Mangels[29,39] showed that H_2 purified the grain boundary composition and produced an overall finer grain structure. However, no mechanism was offered. Lindley[40] showed that a strength improvement using a flowing H_2/N_2 system was great enough to counteract the detrimental effects of the flowing N_2 atmosphere. Lin[41] showed that large amounts of silicon oxide (SiO) are found in the nitriding furnace when an H_2/N_2 atmosphere was employed. This led to the assumption that H_2 effectively reduces the silicon dioxide (SiO_2) present on the silicon particles thereby improving the nitriding kinetics. SiO was also important in the formation of high α Si_3N_4 composition.[42,43] Therefore, it becomes apparent that a high concentration of α Si_3N_4 is necessary to develop a microstructure conducive to high strength.

The use of H_2/N_2 atmospheres may also help control the exothermic effects of nitriding. Since H_2 has a thermal conductivity ten times greater than that of N_2, these atmospheres may help to dissipate heat generated by the exothermic reaction. This would produce improved microstructures. Experiments using argon (which has a thermal conductivity ten times less than that of N_2) added to nitrogen atmospheres produced nitrided compacts with extensive exusions of silicon.[44] Experiments with helium (He) in He/N_2 and $He/H_2/N_2$ atmospheres produced similar effects as H_2 alone. (He has approximately the same conductivity as H_2.) These results indicate that the thermal conductivity and the chemical effects of the nitriding atmosphere are equally important.

The H_2/N_2 atmosphere, when combined with iron oxide (Fe_2O_3) nitriding aids, could produce an effect similar to that of the Haber process for the production of ammonia (NH_3).[45] In this process the H_2 reduces the Fe_2O_3 to Fe which, in turn, catalyzes the formation of atomic nitrogen (N°). Atomic nitrogen (N°) is much more reactive than diatomic nitrogen (N_2); this may explain the observed beneficial effect on the nitriding kinetics. Experiments in nitriding using high concentrations of atomic nitrogen generated externally to the furnace chamber failed because the N° recombined to form N_2 upon contact with any metal surfaces; the nitrogen atoms never reached the silicon compacts.
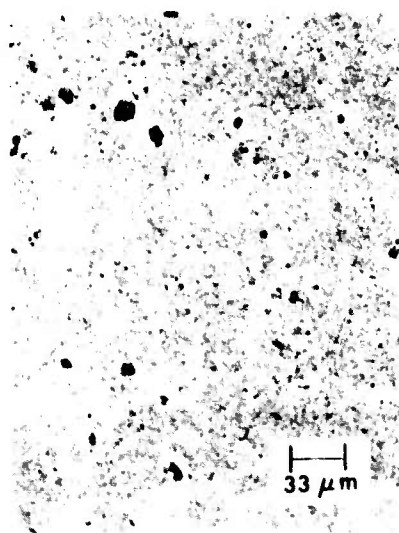
Nitriding Exotherm

As previously described, the nitriding reaction is extremely exothermic (−173 Kcal/mole). Atkinson[26] showed that the internal temperature of a silicon compact can be as much as 40°C higher than furnace temperature. Evans[30] showed the deleterious effect of high temperatures; i.e., exceeding the melting point of silicon, on RBSN microstructure which lowered the material's strength.

Consequently, the exothermic effect makes the production of high quality RBSN very difficult; it also makes actual temperature determinations very difficult if not impossible. The severity of this effect was shown[10] when large furnace loads were nitrided, resulting in temperature overshoots in the furnace chamber (Table 3.2.1-4). These samples were of low strength and had a microstructure which showed evidence of much melted silicon, as illustrated in Figure 3.2.1-18. When an excessive load of 10,000 grams was nitrided, a severe loss of nitrogen pressure was noted and the run was aborted. Even though the furnace temperature was only 1177°C, temperatures exceeding 1420°C were present in the compact. Upon examination, this material showed that severe exusion had occurred.

TABLE 3.2.1-4

LARGE FURNACE LOAD RESULTS

Nitriding Cycle	ATM	Weight of Silicon	Temperature Set Point °C	°F	Temperature Overshoot °C	°F	% Nitrided	Characteristic MOR (ksi)	m	No. of Samples
Constant Rate	4% H$_2$/ 96% N$_2$	1,200 g	1143	2089	None		98.1 %	44.2	7.5	25
Constant Rate	4% H$_2$/ 96% N$_2$	1,600 g	1177	2150	10	18	98.1 %	27.2	8.0	25
Cycle stopped after 2 hours at 1177°C (2150°F)	4% H$_2$/ 96% N$_2$	10,000 g	1177	2150	10	18	Exuded and melted silicon indicating temp. over 1420°C (2588°F)			

NO TEMP OVERSHOOT   **10°C TEMP OVERSHOOT**

Figure 3.2.1-18 — **Effect of Exothermic Reaction During Nitriding Upon Microstructure of RBSN**

The micrographs shown in Figures 3.2.1-19 (A-D), show some degree of silicon melting due to the exotherm. Figure 3.2.1-19D shows the improvement observed by using a H_2/N_2 atmosphere.
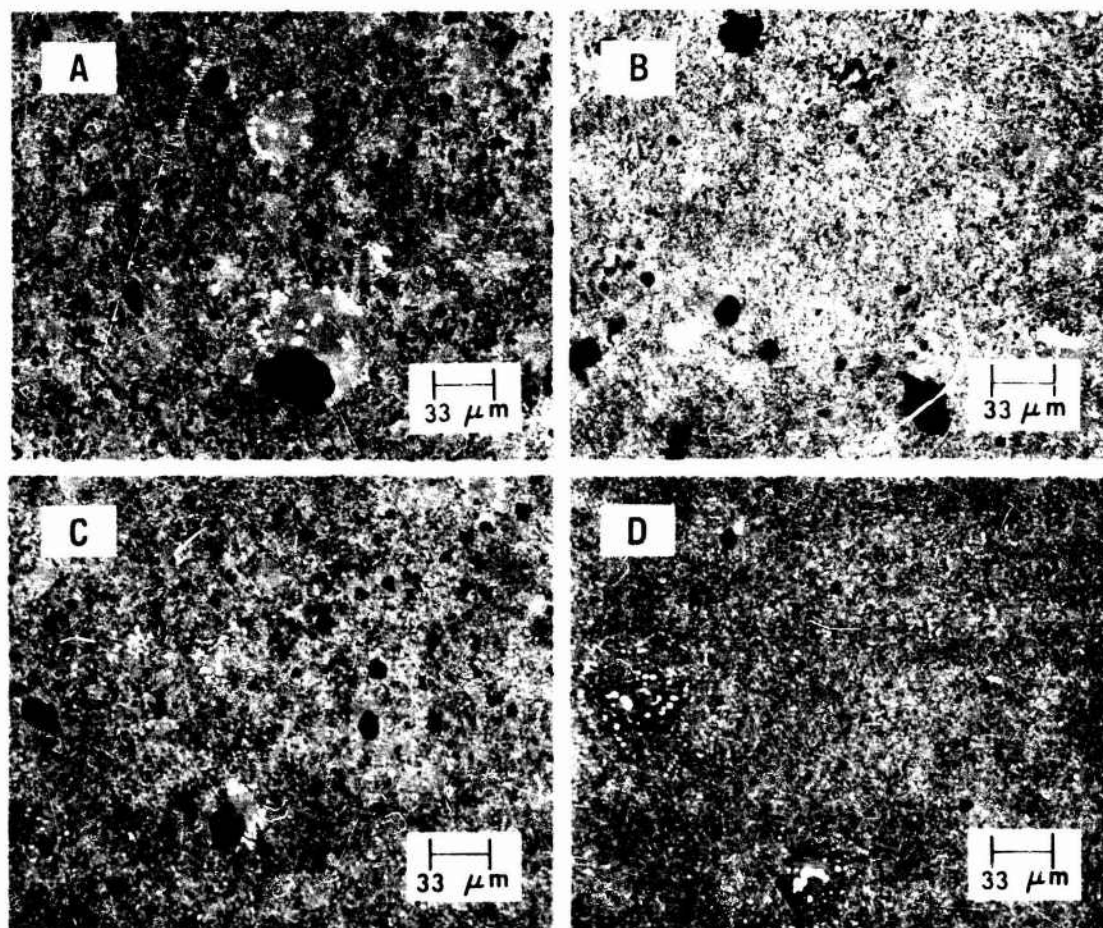

Figure 3.2.1-19 — Optical Micrographs of 2.7 g/cc Density RBSN
    A. Three Step Cycle — 100% N_2
    B. Multi-Step Cycle — 100% N_2
    C. Constant Rate Cycle — 100% N_2
    D. Constant Rate Cycle — 96% N_2/4% H_2

Exothermic effects can vary tremendously depending upon which nitriding cycle is used. These effects were more harmful for step cycles than for constant rate cycles, but neither cycle produced large quantities of high quality RBSN.

Nitrogen Demand Nitriding Cycle

N   ng and microstructure data indicated that the exothermic nitriding reaction could not be cont   i with a programmed temperature cycle. Thus, a control system was devised and developed that   ll..wed the reactants to control the rate of reaction. In contrast to other types of control systems, this system utilized pressure changes within the nitriding furnace as an indicator of the nitriding reaction status. This resulted in a control system which maintains a quasi-static nitrogen condition previously shown to be advantageous. The nitrogen demand system[14] is displayed schematically in Figure 3.2.1-20. A somewhat similar system was also investigated by Wong and Messier [34]

After the furnace has reached 650°C under vacuum, the chamber is backfilled with a gas containing nitrogen mixed with other gases. When the furnace pressure reaches three pounds per square inch of gas (3 psig), this bottle is removed and replaced in the system with another bottle which contains the

nitriding gas. Then, using the programmer, the temperature is increased at a constant rate of 7°C/hour. As the nitriding reaction begins, nitrogen is consumed and the chamber pressure fluctuates. When the pressure fluctuates, the temperature program is instructed to hold and activate a timer which is automatically reset to its starting position. The timer is designed to insure that the reaction has reached equilibrium before the temperature is increased. A hold time of 7-12 minutes is normally used. The timer must complete its cycle before the program is allowed to advance. Then, the cycle begins again and the temperature increases until another pressure fluctuation occurs. This sequence repeats until the maximum programmed temperature (1400°C) is reached; at this point the furnace shuts down. During the nitriding, the weight of the nitriding gas bottle is continuously measured and recorded. This allows accurate gas consumption curves, a measure of the nitriding kinetics, to be produced for each nitriding run.
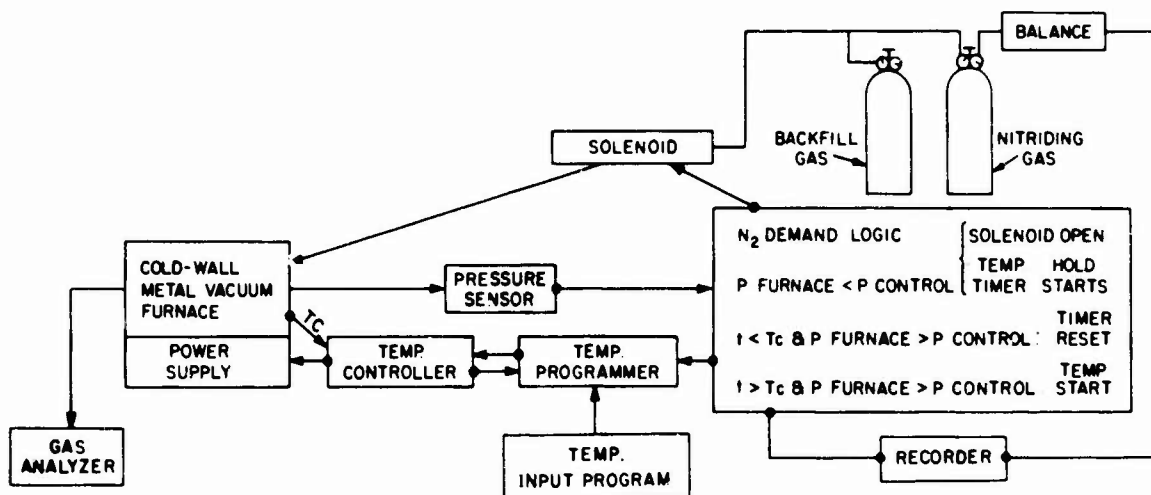
Figure 3.2.1-20 — Schematic Diagram of the Nitrogen Demand Control System

Results of three typical nitriding runs using the nitrogen demand control system are displayed in Figure 3.2.1-21. It is important to note that the actual temperature profiles vary considerably from the programmed temperature input. Also, the length of the nitriding cycles varies with the amount of silicon undergoing nitriding; i.e., more silicon, longer time. Additionally, note that the nitrogen gas consumption curves are linear over the entire nitriding range; this shows that the control system did control the nitriding reaction predictably and in the desired manner.
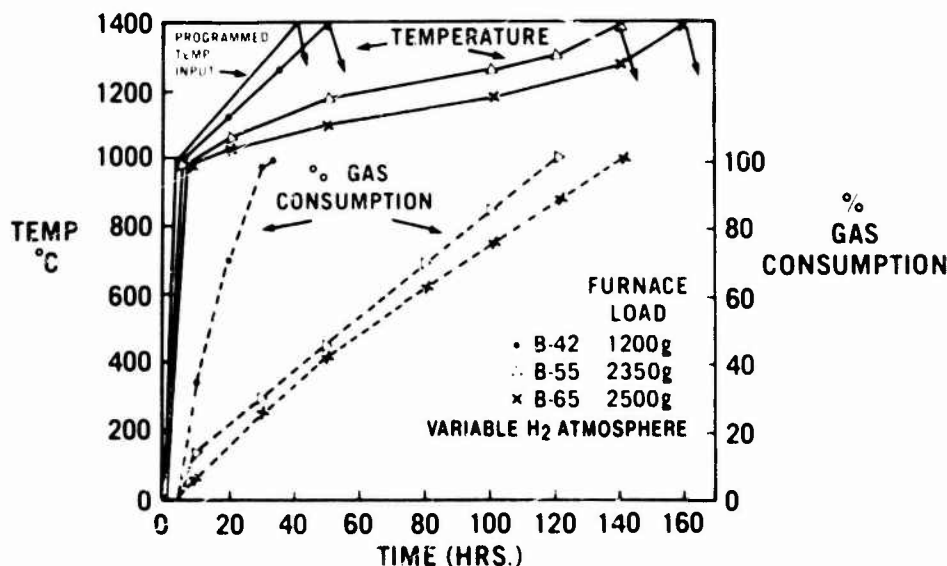

Figure 3.2.1-21 — Time Vs. Temperature and Gas Consumption Vs. Time Profiles of Three Nitrogen Demand Nitridings

Several different combinations of gases were employed for nitriding; the varied results are displayed in Table 3.2.1-5 and Figures 3.2.1-22 and 3.2.1-23. The important results are summarized as follows:

1. Nitriding atmosphere affects the kinetics of the nitriding reaction and the properties of the RBSN. The 100% N_2 atmosphere yielded RBSN with the worst microstructure and lowest strength.

2. Concentration of N_2 in the nitriding gas affects the properties of the RBSN. Atmospheres with N_2 held constant yielded microstructures containing unreacted silicon.

3. Atmospheres where N_2 concentration was decreased as the nitriding progressed (variable H_2 and variable He) yielded RBSN with the best microstructure. However, it was unsafe to use variable H_2 compositions due to the accumulation of potentially explosive gases.

4. Thermal conductivity of the nitriding atmosphere is important for production of high quality RBSN. (Compare the variable He to the variable Ar runs.)

5. The variable He atmosphere (4% H_2/He/N_2) was the best for nitriding. This atmosphere was composed of:

   a) A small amount of H_2 to reduce the surface SiO_2 on the silicon particles to SiO gas and reduce the Fe_2O_3 nitriding aid to Fe which consequently aided in the formation of the more reactive $N°$.

   b) A chemically inert gas to dilute the nitrogen concentration, since nitriding under reduced partial pressures was shown to be beneficial.

   c) Gases with high thermal conductivity to aid in dissipating heat generated by the exothermic nitriding reaction.

TABLE 3.2.1-5

SUMMARY OF NITROGEN DEMAND NITRIDING RUNS

Designation	Backfill Gas	Nitriding Gas	Nitriding Kinetics*	Si_3N_4† Microstructure	2.7g/cm³ RBSN ‡ Strength (ksi)	Final Gas Composition *
100% N_2	100% N_2	100% N_2	linear	Poor (3.2.1-23a)	30	100% N_2
Constant H_2	4% H_2/N_2	100% N_2	linear	Fair (3.2.1-23b)	36-44	4% H_2/N_2
Variable H_2	4% H_2/N_2	4% H_2/N_2	linear	Good (3.2.1-23d)	40	25% H_2/N_2
Constant He	7% He/N_2	100% N_2	linear	Fair (3.2.1-23c)	37	—
Variable He	4% H_2/N_2	7% He/N_2	linear	Good (3.2.1-23e)	45	4% H_2/20% He/N_2
Variable Argon	4% H_2/N_2	10% Argon/N_2	linear	Fair (3.2.1-23f)	39	—

* See Figure 3.2.1-22 for Cycle time versus Load.
† Photomicrographs shown in Figure 3.2.1-23.
‡ Four-point bead strength for several nitriding runs.
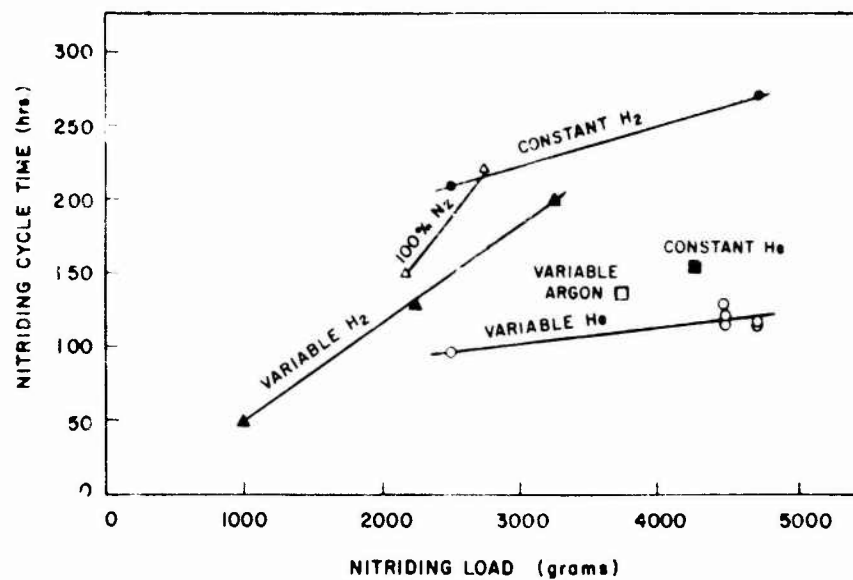✱ Measured using mass spectrometer.

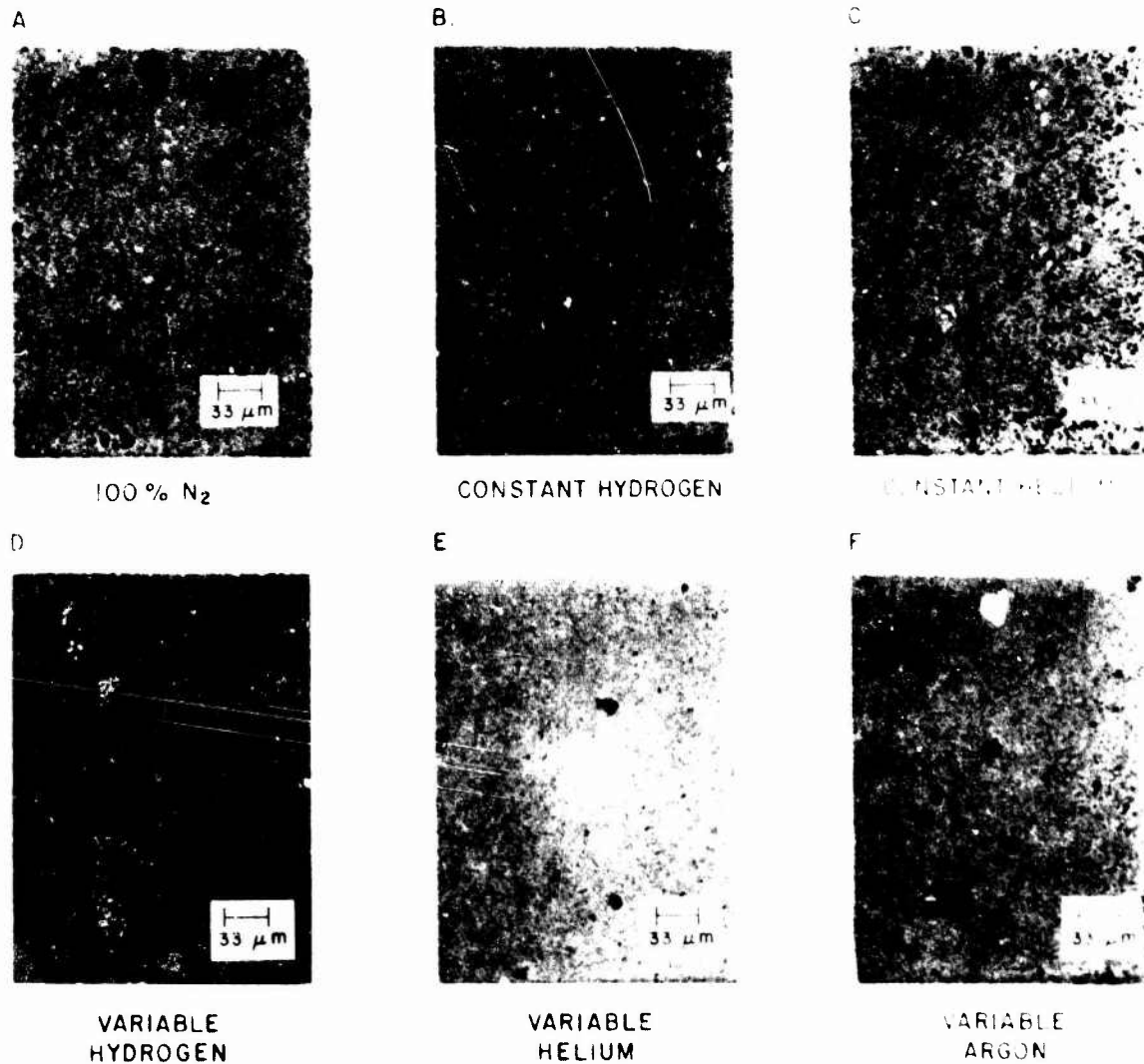Figure 3.2.1-22 — Nitriding Time Vs. Nitriding Load for Various Nitriding Atmospheres

Figure 3.2.1-23 — Typical Microstructures of 2.7 g/cc Density RBSN Nitrided Using the
Nitrogen Demand Cycle and Various Nitriding Atmospheres

Silicon Particle Size

The early literature suggests that the silicon particle size should be below 200 mesh for nitriding to occur in reasonable times. Messier and Wong[34] showed that reducing the maximum particle size below forty microns (40μ) improved the strength of RBSN. Waugh[47] showed that the actual particle distribution affects the character of RBSN. Other researchers [5,7,8,9,33] found that the particle size distribution greatly affects formation of the 'green' compact. Consequently, work on nitriding-particle size interactions was governed by the manner in which various silicon powder distributions could be formed into components having the desired 'green' density levels.

Reducing the overall particle size by increased ball milling time diminished the strength of 2.55 g/cm^3 RBSN[7,8] as displayed in Figure 3.2.1-24. Figure 3.2.1-25 shows changes in RBSN microstructure as a function of ball milling time: as time increased, so did the appearance of large crystals and large pores. This is characteristic of a material processed in an uncontrolled manner where the nitriding exotherm was prominent. Ten — fifteen percent of the particles in material milled for long times were below 1μ in size, as compared to 1-2% of the particles in unmilled material. The extra fine particles may have caused increased reactivity to nitriding and consequent local overtemperature due to the exotherm.
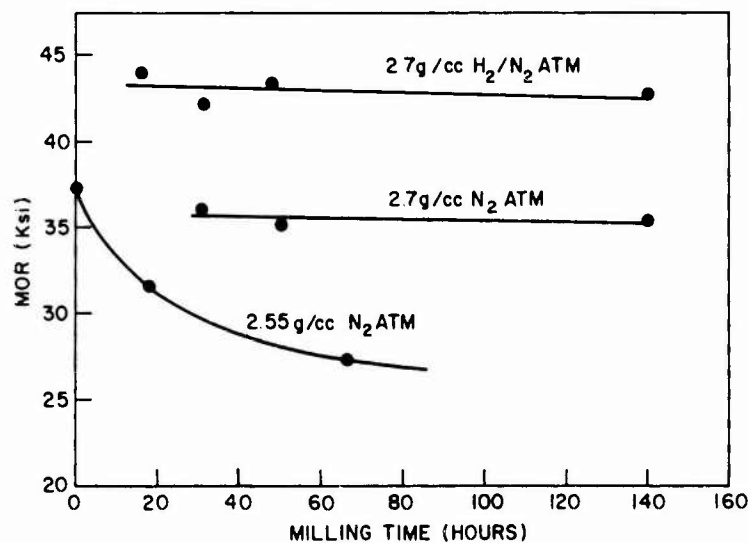

Figure 3.2.1-24 — Strength of RBSN at Two Density Levels as a Function of Silicon Powder Milling Time
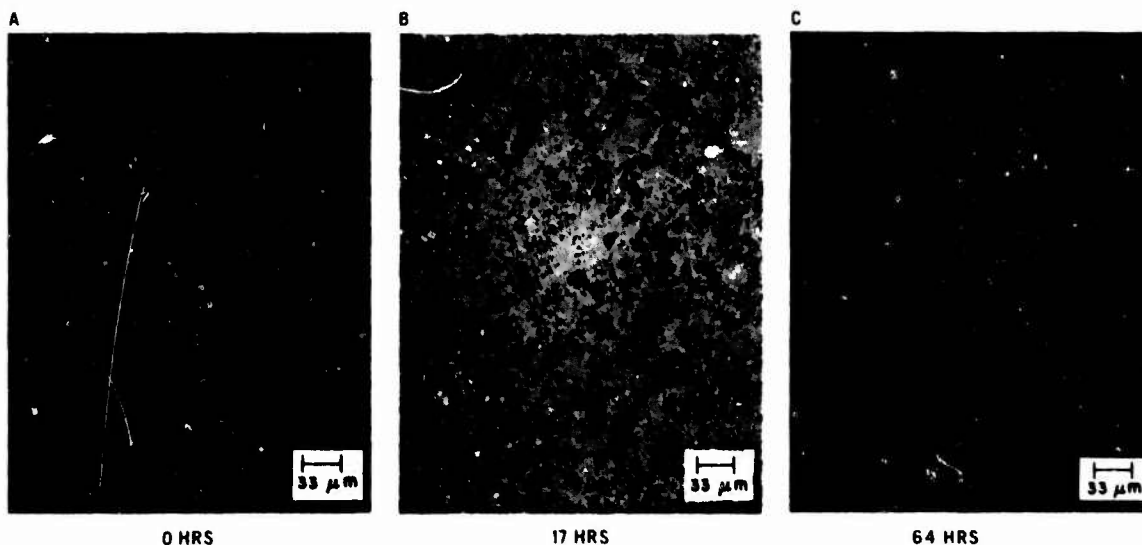

0 HRS   17 HRS   64 HRS

Figure 3.2.1-25 — Microstructure of 2.55 g/cc Density RBSN as a Function of Silicon Powder Milling Time

The strength data for 2.7 g/cm^3 RBSN were different (Figure 3.2.1-24) as strength did not decrease as milling time was increased; however, the unmilled material could not be molded. If large numbers of fine particles could be removed from the 2.7 g/cm^3 material, and if it could still be formed, the strength of the resulting RBSN could possibly be increased.

Nitriding Aids

Very early in the development of RBSN, Popper[28] pointed out that a catalyst was necessary to completely nitride silicon compacts. He proposed calcium fluoride (CaF_2) and ferric oxide (Fe_2O_3) but did not offer mechanisms to explain their advantageous behaviour. Suzuki[48] and Leake & Jayaticaka[49] have investigated a wide variety of additions and had shown that other transition metals, notably chromium, could be useful nitriding aids. Boyer et al[50] has proposed a model for the behaviour of iron (Fe) and Fe_2O_3 as nitriding aids.

During this program, only two nitriding aids were investigated, CaF_2 and Fe_2O_3. CaF_2 produced completely nitrided components with very poor high-temperature properties [4,5,6,29,51]. Calcium concentrated in the grain boundaries and formed a glassy phase of low viscosity. Fe_2O_3 was more effective as it produced completely nitrided components without deleteriously affecting high-temperature properties[5,52].

High-Pressure Nitriding

Using conventional nitriding techniques, silicon compacts with a 'green' density of 1.7 g/cm^3 had easily been nitrided to yield Si_3N_4 with a density of 2.7 g/cm^3. It was also possible to slip-cast silicon compacts with a 'green' density of 2.0 g/cm^3[7]. If these compacts could be nitrided, they would yield theoretically dense Si_3N_4. Conventional nitriding techniques when applied to the high green density compacts yielded a compact with a 0.020-0.030 inch thick case of Si_3N_4 surrounding a core of silicon metal. With the application of high pressure (> 10,000 psi) nitrogen, perhaps enough gas could be forced through the dense surface case and into the silicon interior to complete the reaction.

Several runs were made at nitrogen pressures between 10,000 psi and 20,000 psi with temperatures ranging from 900°C to 1350°C[7,8]. As shown in Figure 3.2.1-26, using Fe_2O_3 aids and higher temperatures yielded the most encouraging results although the microstructure still consisted of a core of silicon surrounded by a case of high density Si_3N_4. (Figure 3.2.1-27). This did demonstrate, however, that 90% dense Si_3N_4 could be completely nitrided. High costs (over $5,000 per run) and the extreme difficulties encountered in performing and controlling the runs resulted in abandoning this approach.
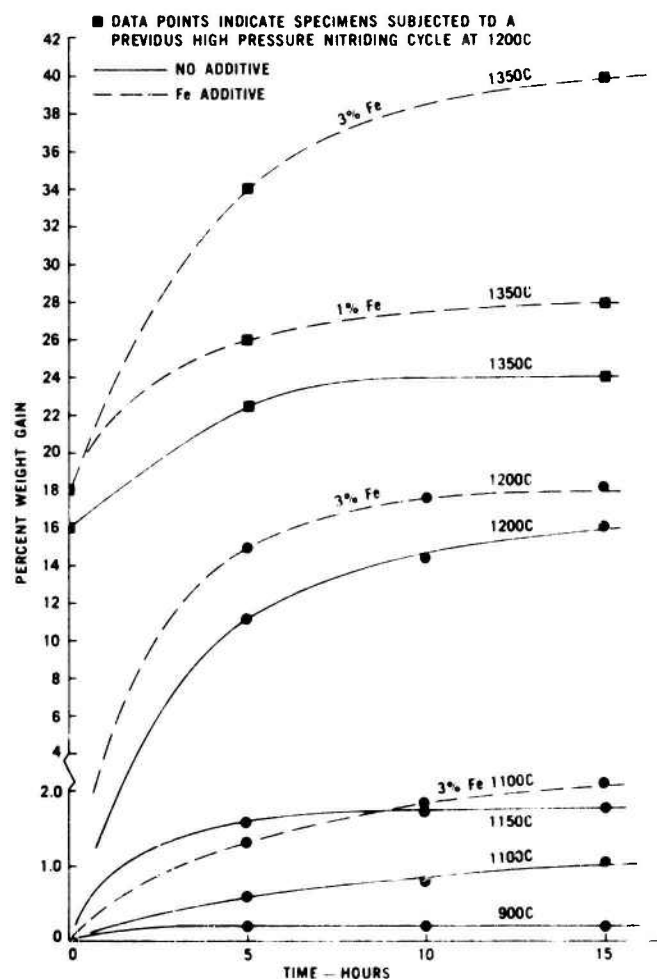
Figure 3.2.1-26 — Nitriding Weight Gain Vs. Nitriding Time for Various High Pressure Nitriding Runs
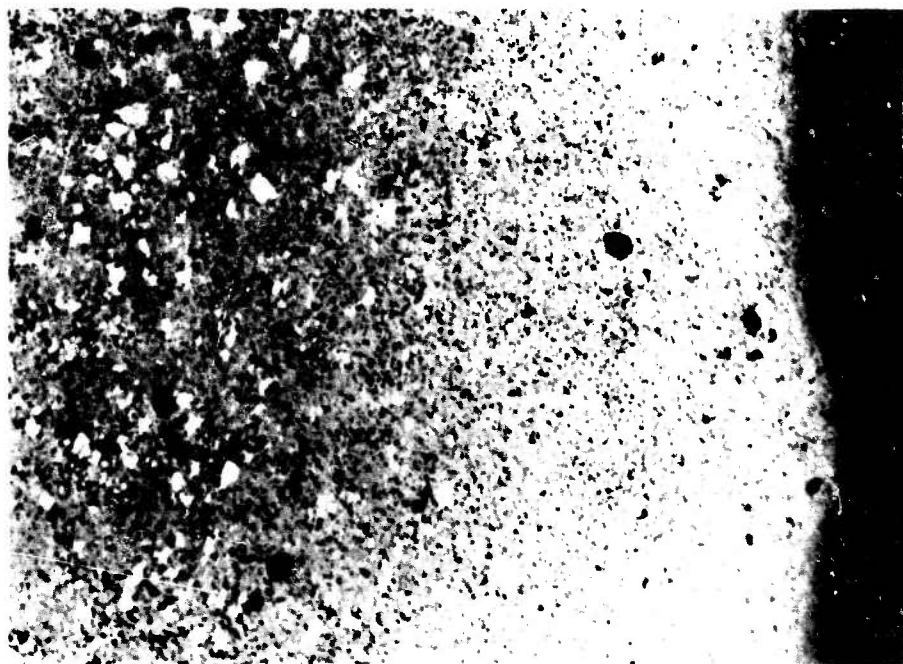

Figure 3.2.1-27 — Microstructure of Silicon Nitride Formed by High Pressure Nitriding

Summary

During this program, the technology to nitride silicon compacts has been significantly improved. Table 3.2.1-6 is a summary of the nitriding state of the art at the conclusion of the program in 1978. By comparing Tables 3.2.1-2 and 3.2.1-6, one can see the following changes in RBSN:

1) Density was increased by 20%

2) Strength was increased by 300% to 45.2 ksi

3) High-temperature properties were greatly improved as a result of the improved ability to nitride higher purity silicon.

TABLE 3.2.1-6

NITRIDING STATE OF THE ART
1978

Silicon Powder Purity:	0.7 wt% Fe, 0.2 wt% Al, 0.02 wt% Ca
Silicon Particle Size:	− 30 microns
Nitriding Aid:	Fe_2O_3 (2 1/2 wt %)
Green Density:	1.68 g/cm^3
Nitrided Density:	2.7 g/cm^3
Nitriding Cycle:	Nitrogen demand cycle
Nitriding Atmosphere:	Variable helium
Phase Composition:	75% α/25% β Si_3N_4
Nitrided Strength:	Characteristic strength: 45.2 ksi
	Weibull modulus: 9.45
Microstructure:	See Figure 3.2.1-28

E.
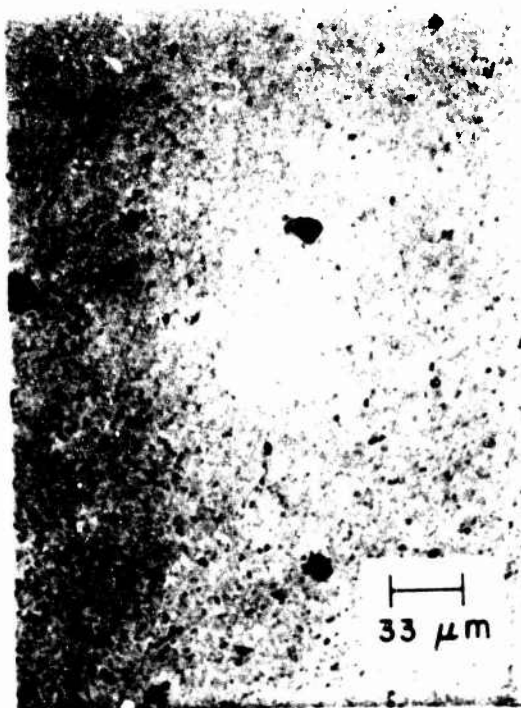
VARIABLE
HELIUM

Figure 3.2.1-28 — Typical Microstructure of RBSN Produced at the End of the Program

Many variables were investigated during the nitriding development process; silicon particle size, silicon purity, 'green density, nitriding cycles, atmospheres and many more. All of these variables were evaluated by examining the microstructure and determining the strength of the resulting RBSN.

From these experiments, an understanding of the interrelationships of these variables developed which led to the development of the final nitriding procedure; i.e., the nitrogen demand nitriding cycle with a variable helium nitriding atmosphere.

3.2.1.5 Physical Property Characterization

Microstructure

Knowledge of microstructure is important in the characterization of any ceramic material. Material strength can usually be understood in these terms. High-temperature behavior of the material can often be explained by the location of minority phases and impurities. In particular, the degree of and size distribution of porosity can affect the oxidation of RBSN.

The microstructure of the Ford 2.7 g/cm^3 density RBSN was studied with many methods: optical microscopy (normal and polarized light), scanning electron microscopy (SEM) with nondispersive X-ray analysis, and transmission electron microscopy (TEM). These tests were augmented by emission spectroscopy for chemical analysis and quantitative X-ray diffraction for phase analysis.

Chemical and Phase Composition

A specification for the starting silicon powder evolved during the program; of greatest significance was the stringent limit placed upon the presence of calcium. Experimental investigation showed that 0.4% by weight of calcium, typically found in early powders, was detrimental to high temperature creep. A reduction to 0.02% by weight Ca improved the creep resistance of the resulting RBSN by three orders of magnitude (10^{-4}/hr to 10^{-7}/hr at 1200°C and 10 Ksi) [5,6]. A nitriding aid (Fe_2O_3), was also added to the silicon. Consequently, the resulting RBSN contained many chemical impurities as shown in Table 3.2.1-7. The Fe content is the total of that already present in the silicon powder plus the amount resulting from the nitriding aid. All other impurities noted were in the as-received silicon powder.

Table 3.2.1-7

IMPURITY ANALYSIS OF IMRBSN (wt %)

Fe	Ca	Al	Mg	Mn	Cr	Na	K	O^2
1.54	0.02	0.20	0.02	0.05	0.06	<0.03	<0.03	1.20

Neutron activation analysis was used to obtain the oxygen analysis. Emission spectrographic analysis showed that the major impurities were iron, oxygen, and aluminum, while alkali and alkaline earth impurities were very low. The phase composition of the IMRBSN is given in Table 3.2.1-8.

Table 3.2.1-8

PHASE ANALYSIS OF IMRBSN (wt %)

αSi_3N_4	βSi_3N_4	Si_2ON_2	Si	FeSi	Fe
75	24	0.4	0.3	Trace	Trace

Optical Microscopy

Optical microscopy was a powerful tool in the study of RBSN. It permitted examination of large areas of pore distribution, general microstructual uniformity, and detection of gross differences in grain size, such as the presence of large β Si3N4 grain clusters. Typical microstructure of the Ford 2.7 g/cm^3 density IMRBSN is shown in Figure 3.2.1-29.
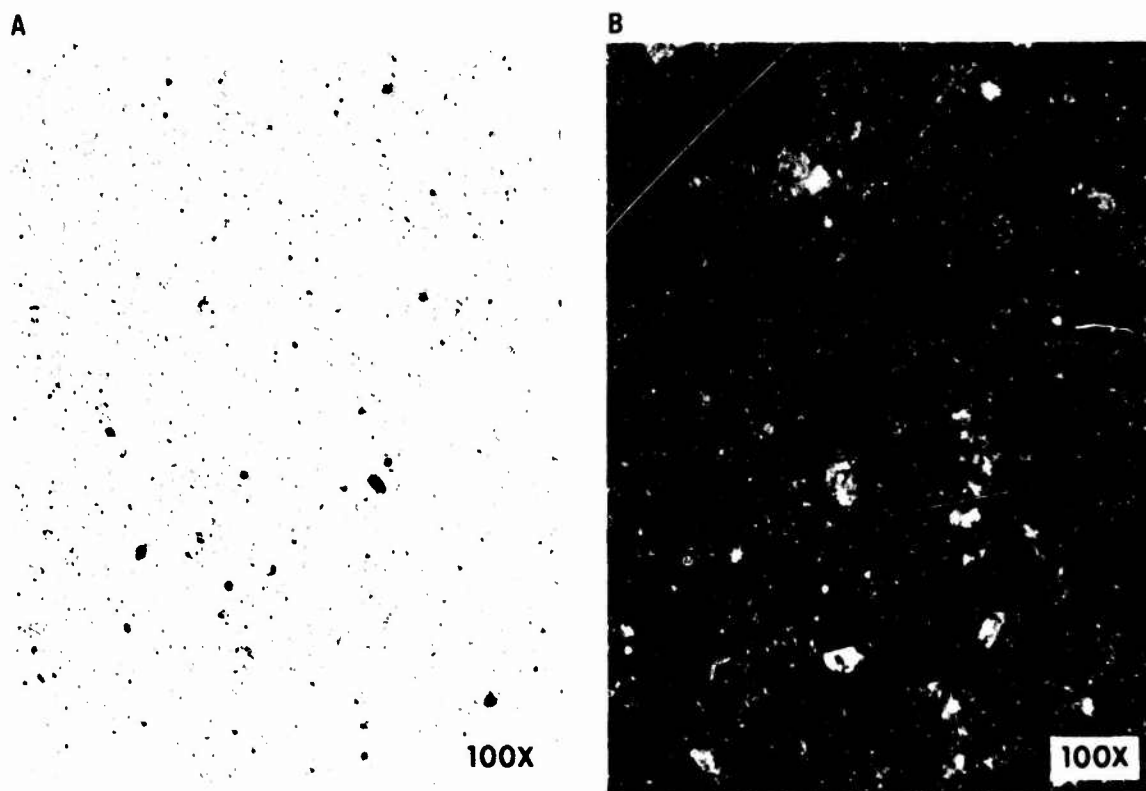

Figure 3.2.1-29 — Optical Micrographs of 2.7 g/cc Density RBSN (100x)
A. Normal Light
B. Polarized Light

Figure 3.2.1-29A shows that the structure was composed of uniformly distributed fine pores (<10 microns) and some isolated pores up to 20 microns in diameter. The white phase is an even distribution of a metal, either FeSi or Si approximately 25 microns in diameter. The gray region is a uniform distribution of Si3N4 with no abnormally large grains. Figure 3.2.1-29B shows the typical even distribution of β Si3N4 (light phase) in a matrix of α Si3N4 (dark phase) under polarized light.

Scanning Electron Microscopy

The Scanning Electron Microscope (SEM) was not too useful for studying the general microstructure of RBSN because fractures produced a featureless surface with little grain structure. Since RBSN contained very little alkali and alkaline earths, grain boundaries were chemically inert. Figure 3.2.1-30A shows a typical fracture surface of IMRBSN etched in HF for four hours. Some porosity can be noted, but little of the grain morphology can be seen.
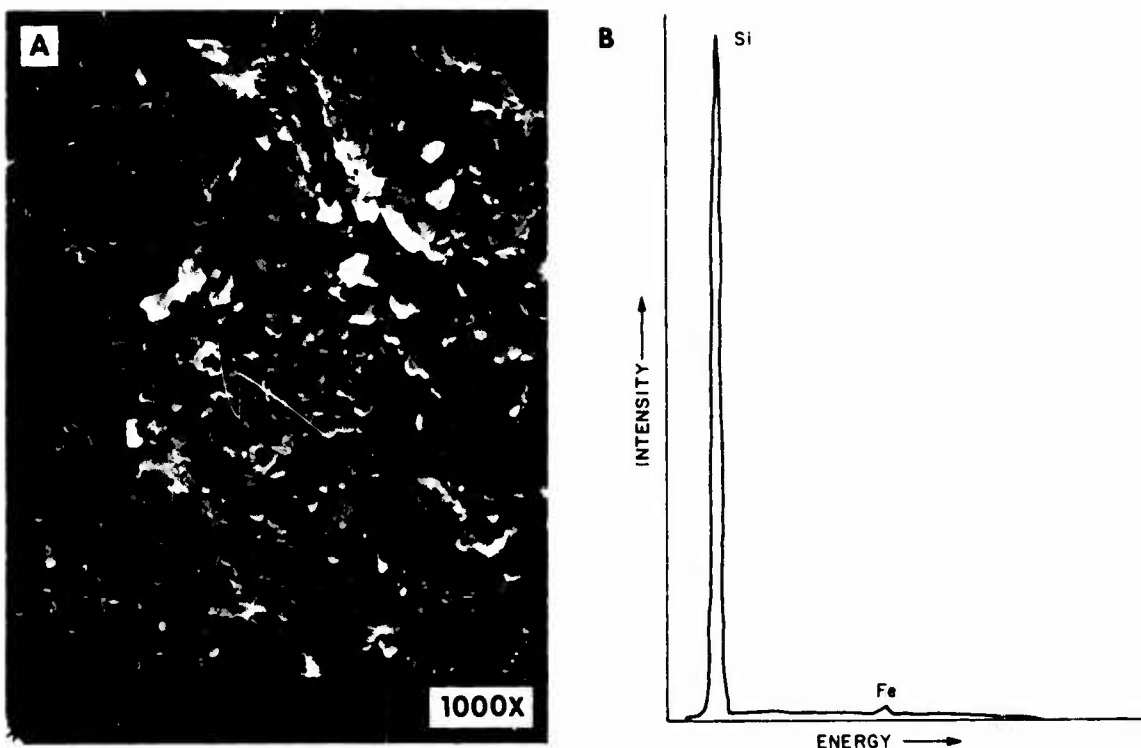
Figure 3.2.1-30 — A. Scanning Electron Micrograph of 2.7 g/cc Density RBSN Fracture
Surface, HF Etch (1000x)
B. Non-Dispersive X-Ray Spectrum of Thin Surface

The SEM, when equipped with a non-dispersive X-ray analyzer, was very useful in studying RBSN. Figure 3.2.1-30B shows the chemical composition of a typical RBSN fracture surface. The only uniformly distributed impurity was iron, which had been added to the silicon as a nitriding aid.

The SEM was also valuable in locating fracture origins and analyzing their chemical composition. Two typical fracture origins are shown in Figure 3.2.1-31. Figure 3.2.1-31A is a pore containing high concentrations of chrome and iron. Figure 3.2.1-31B is an inclusion composed of silicon, chrome and iron; it is probably an iron-chrome silicide. The fracture origins in RBSN most often occur below the surface.

Transmission Electron Microscopy

The transmission electron microscope (TEM) was used to study grain size and grain morphology. Two distinct regions were noted. Figure 3.2.1-32A shows a region of very fine needle shaped and equiaxed grains (0.1 micron). Electron diffraction showed this region to contain α Si_3N_4 with a trace of β Si_3N_4. Scanning transmission electron microscopy (STEM) of this region showed no evidence of phases containing iron.

Figure 3.2.1-32B shows a cluster of large grains (1 to 2 microns) with very sharp boundaries composed of a mixture of α and β Si_3N_4. The STEM showed the presence of an iron containing phase, probably iron silicide. However, no iron was detected in the grain boundary region.

These two distinct morphologies were noted throughout the many samples that were studied. The first region could be the "alpha matt" frequently referred to in the literature, while the second region could have been caused by the growth of the Si_3N_4 phases in the presence of a liquid phase, probably composed of FeSi.

Room temperature strength of 2.7 g/cm³ density RVRBSN was studied using four-point bending. The fixture had a 3/8" top span and a 3/4" beam span. A loading rate of 0.02 in. rate was used. The test specimen size was 1/8" x 1/4" x 1-1/8". The specimens were representative of a large number of batches and nitriding runs. The data therefore represents batch-to-batch variations. The specimens were inspected prior to nitriding, using X-ray radiography to remove any samples with molding defects similar to the method used to evaluate engine components. Table 3.2.1-9 displays the room temperature strength of 2.7 g/cm³ density RMRBSN and Figure 3.2.1-33 shows the room temperature strength as a function of flaw size.
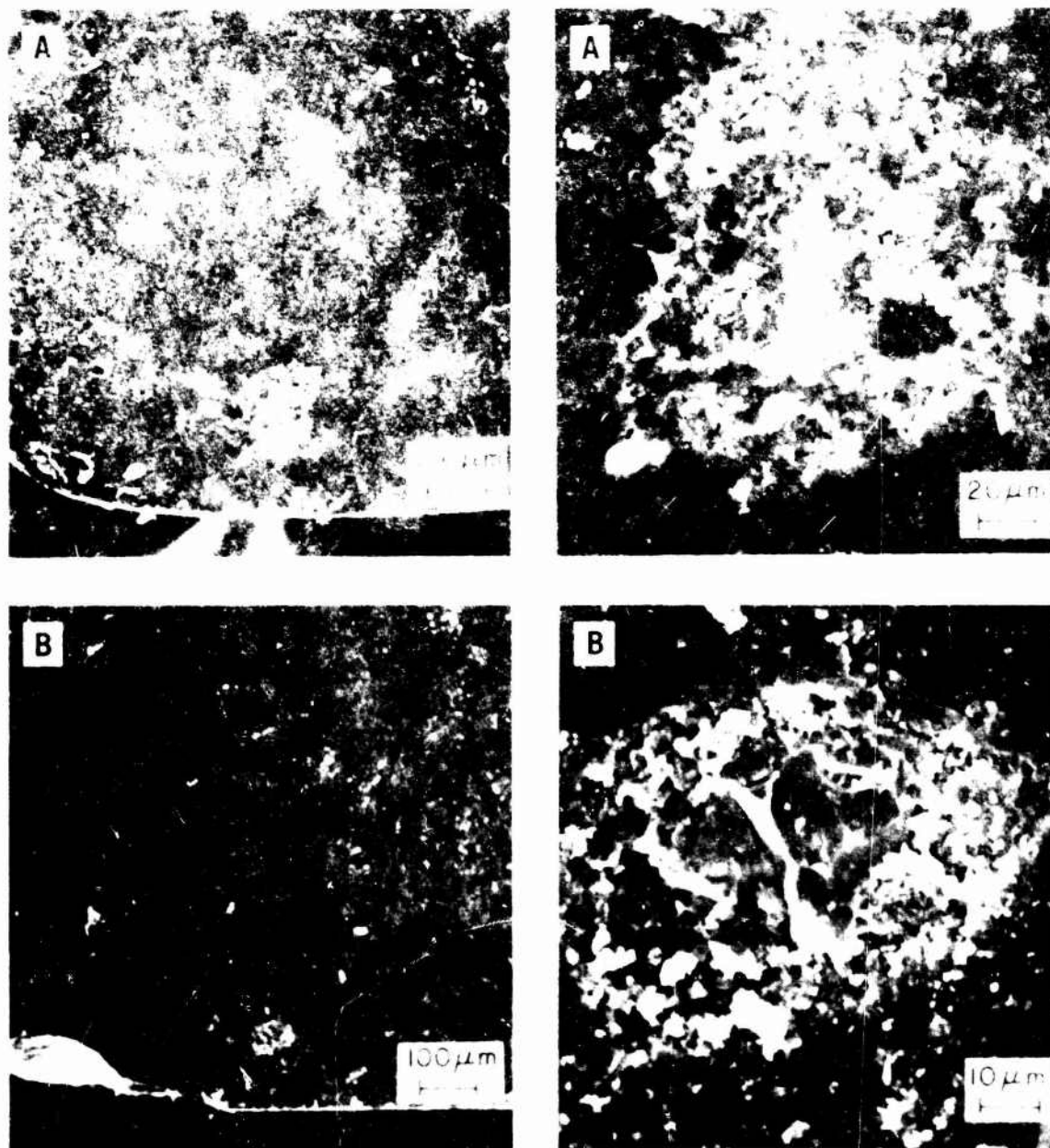
Figure 3.2.1-31 — Scanning Electron Micrographs of Fracture Origins in 2.7 g/cc Density RBSN
A. Pore Containing High Concentration of Cr and Fe
B. Inclusion Containing High Concentration of Si, Cr and Fe
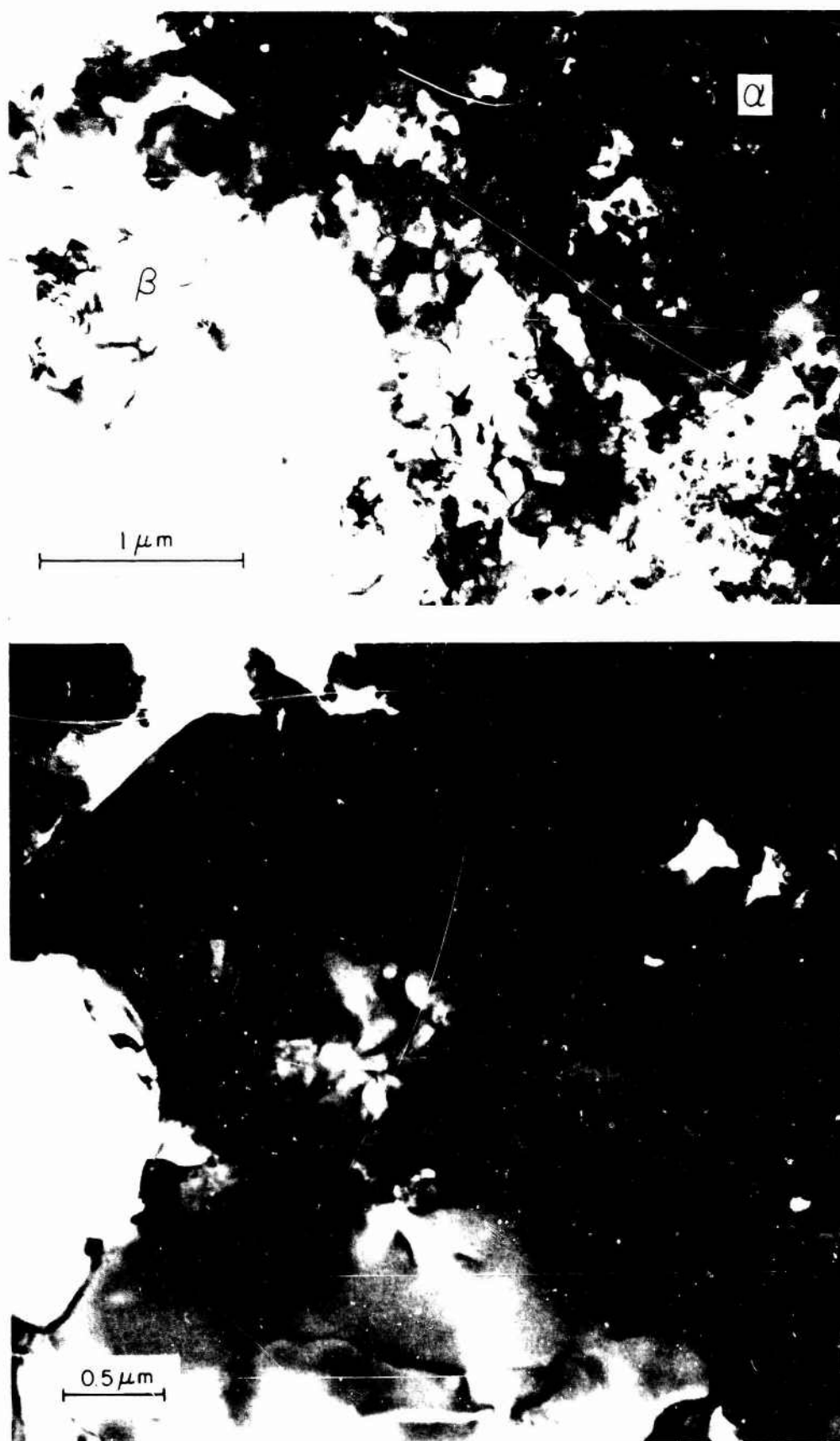
Figure 3.2.1-32 — Transmission Electron Micrographs of 2.7 g/cc Density RBSN
A. Region of Fine α Grains (0.1μ) Plus Some β Grains
B. Region of Large Grains (1-2μ) with Sharp Boundaries

Table 3.2.1-9

ROOM TEMPERATURE STRENGTH OF IMRBSN

Characteristic Strength	Weibull Modulus (m)	Number of Samples (n)
45.2 (44.3 to 46.2)*	9.45 (7.97 to 10.84)*	72

* 90% Confidence Band
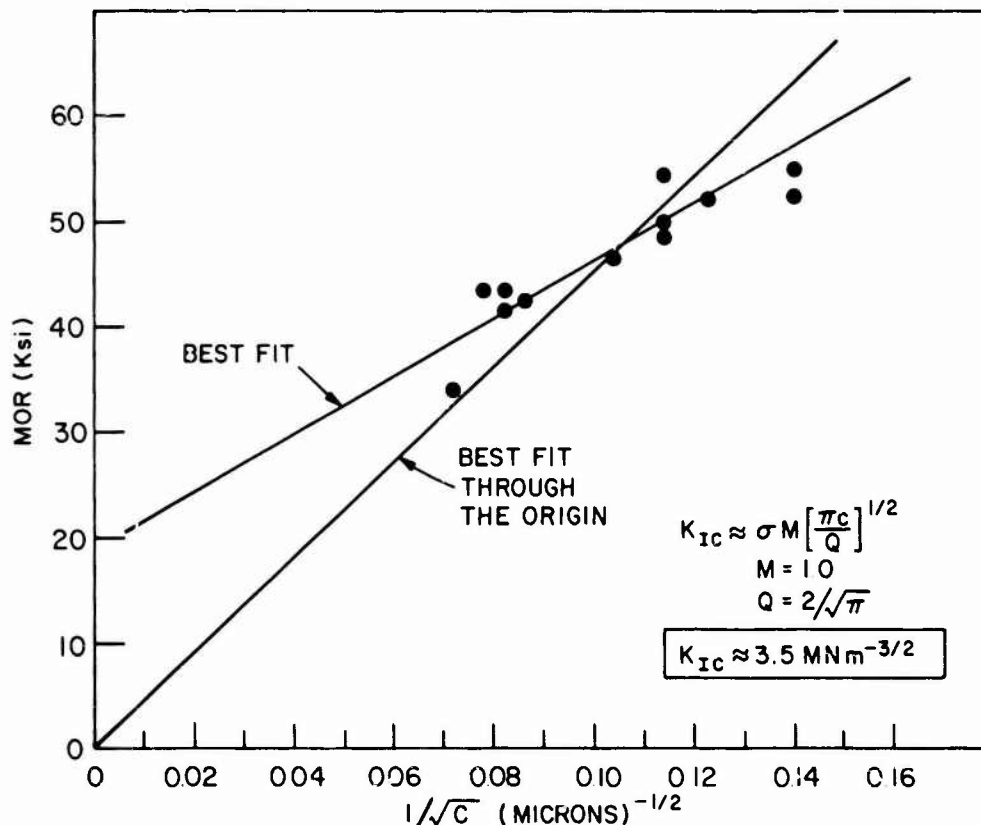
Figure 3.2.1-33 — Room Temperature Strength Vs. Flaw Size for 2.7 g/cc Density RBSN

These flaws were all subsurface pores or inclusions located about 1 to 2 flaw diameters below the tensile surface. The first curve is the "best fit" line through the data. The second curve is the "best fit line" through the origin which was necessary in order to utilize the derivation of K_{IC} [13]. The value K_{IC} = 3.5 MNm−3/2 obtained for IMRBSN using this technique is approximately the same as that obtained for hot pressed Si_3N_4 (3.5 to 4.0 MNm−3/2)[14], slightly higher than that reported for other RBSN materials, such as Norton NC-350 RBSN at high temperature (2.8 MNm−3/2)[53] and considerably higher than that obtained for NC-350 RBSN at room temperature (1.1 to 1.6 MNm−3/2) [53].

High Temperature Strength

The short time high temperature strength of IMRBSN, produced and nitrided in 1976 using a constant rate nitriding cycle and measured using a fast loading rate (0.02 inch/minute), and a strength curve for the latest and best grade of IMRBSN, produced and nitrided in 1978 using a nitrogen demand nitriding cycle are displayed in Figure 3.2.1-34.
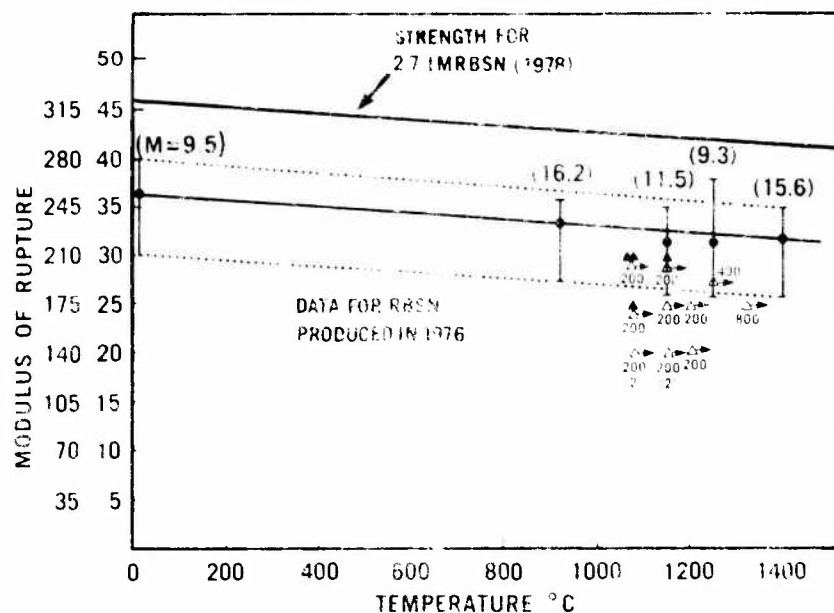
Figure 3.2.1-34 — Short Time High Temperature Strength and Flexural Stress Rupture
Strength of 2.7 g/cc Density RBSN

The temperature dependence of the 1976 material is linear with a modest decrease in strength
(≈5%) at 1400°C. The temperature dependence of the 1978 material is similar to the 1976 material
because its chemistry and phase composition is identical; only the microstructure is different.

Stress-Rupture

The flexural stress-rupture characteristics of IMRBSN were studied early in the development
program. Data for the 1976 grade of material is compiled in Figure 3.2.1-34. For test temperatures
between 1100°C and 1350°C, no time-dependent failures were noted. Some samples failed instantane-
ously upon reaching the desired stress level, but this was expected because many tests were performed
at stress levels within the short-time strength scatter band. Most tests were terminated with no failure
after 200 hours; in longer testing, one sample survived 400 hours at 1260°C and 50 Ksi, and one sample
survived 800 hours at 1350°C and 25 Ksi.

The 1978 grade of material was studied at 1200°C and in a step stress rupture test performed by
AMMRC. Results of the isothermal testing at 1200°C are shown in Figure 3.2.1-35. Some time-depen-
dent failures were noted at the 39 Ksi stress level and at times up to two hours. However, one sample at
34.5 Ksi survived 700 hours of testing with the test still in progress.

A step stress rupture test tested the behavior of the material at various temperatures and stress levels
[54]. It was designed as a screening test to identify areas where concentrated testing should be per-
formed. Results of this testing are shown in Figure 3.2.1-36.

Two samples failed before temperature reached the test conditions. Three samples failed after a
short time at 1000°C and stress levels of 37 Ksi. Two other samples, after surviving 24 hours at 1000°C,
failed after short times at 1100°C. Eight samples survived the entire test. This data indicates that a
potential problem exists at the low-test temperatures of 1000°C and 1100°C; these temperatures corre-
spond to the region of maximum oxidation of RBSN.

A summary of all the stress rupture data shows that the 2.7 g/cm³ IMRBSN does not exhibit time-
dependent failure at stress levels of 33 Ksi at temperatures up to 1400°C and times of at least 200 hours.
These results were expected because this material does not exhibit slow crack growth up to 1400°C, the
maximum temperature investigated. Time-dependent failures at the higher stress levels and lower
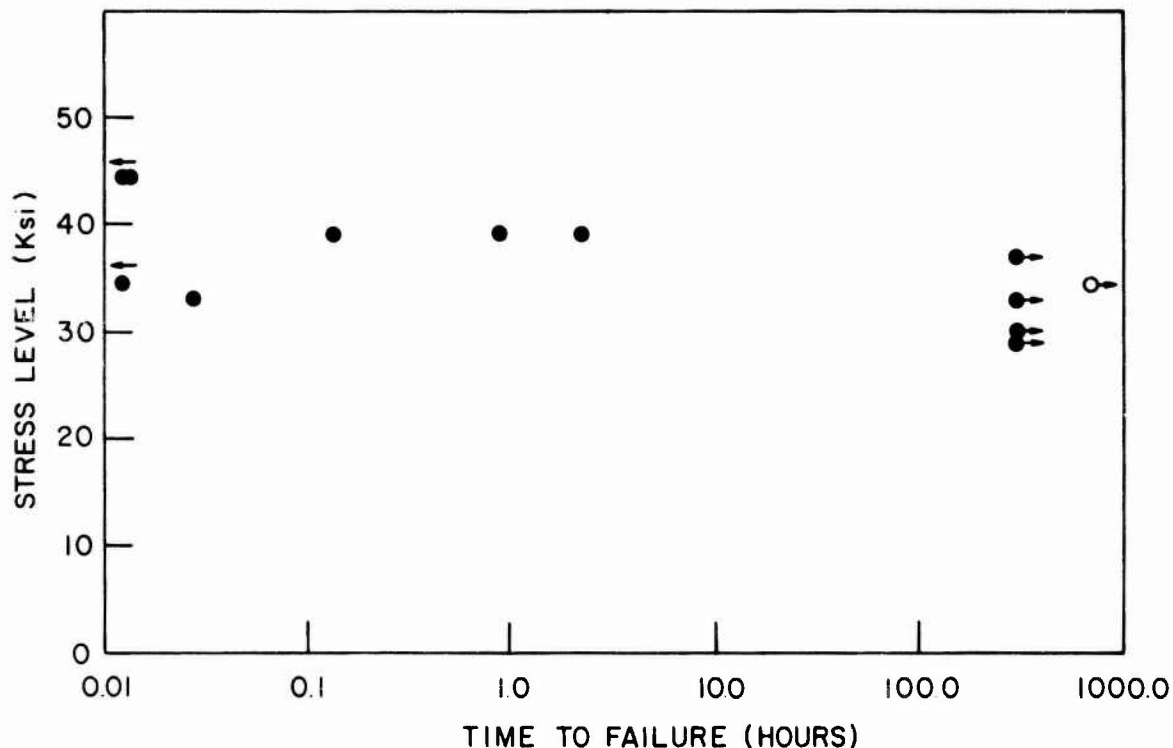temperatures were attributed to oxidation rather than slow crack growth.

54

Figure 3.2.1-35 — Isothermal 1200°C Stress Rupture Test Results, 2.7 g/cc Density RBSN
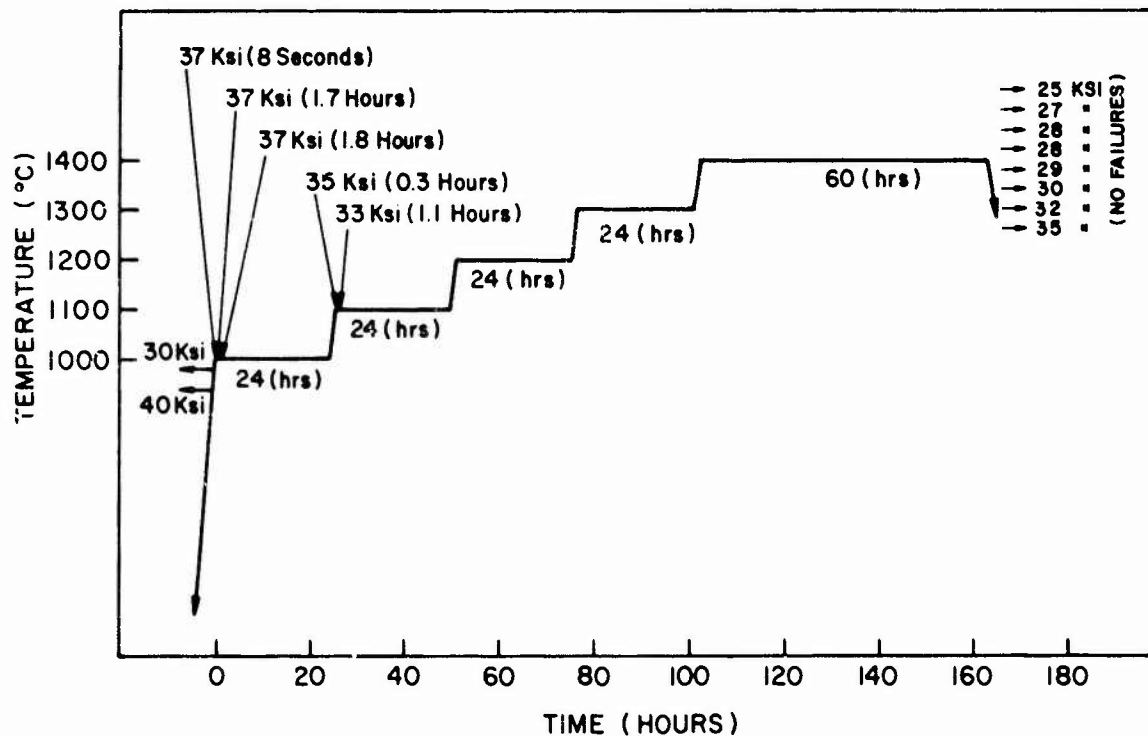Tests Performed by AMMRC

Figure 3.2.1-36 — Step Stress Rupture Test Results at Various Temperatures, 2.7 g/cc
Density RBSN. Tests Performed by AMMRC.

Creep

Creep testing was used extensively to monitor and improve high-temperature behavior of IMRBSN
during its development [4, 5, 6, 20]. The creep resistance of the 1976 2.7 g/cm³ IMRBSN material was

55

measured in bending at 1316°C and stress levels between 17 and 27 Ksi (130 and 200 MN/M^2). These results are compared to lower density IMRBSN and HS-130 HPSN in Figure 3.2.1-37. Creep resistance improved significantly with increases in density. 2.7 g/cm^3 IMRBSN was also superior to HS-130 by over two orders of magnitude.
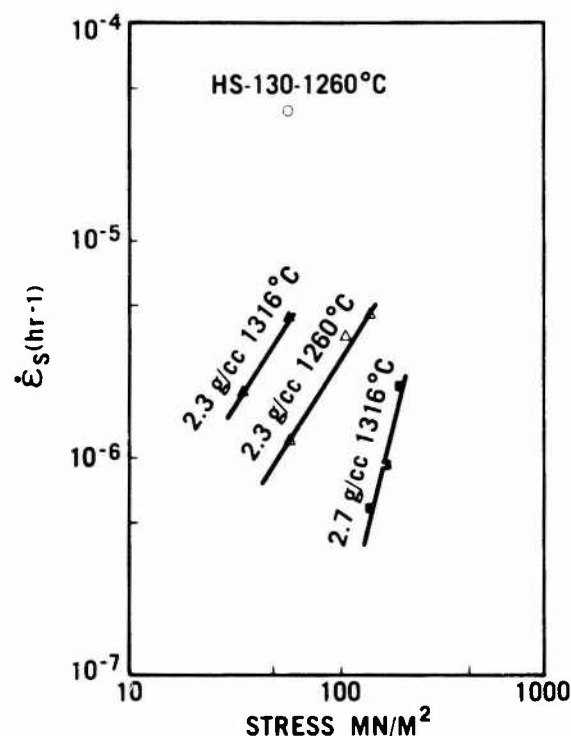
Figure 3.2.1-37 — Creep of Various Grades of Silicon Nitride

Oxidation

The oxidation behavior of RBSN is typified by Figure 3.2.1-38[3, 7]. This shows that oxidation is worse at lower temperatures. This type of behavior could be characterized by an internal oxidation mechanism. Oxidation resistance improved as the material density was increased, as shown in Figure 3.2.1-39.

A second phenomenon identified with the oxidation of RBSN, strength reduction as a function of exposure time and exposure temperature, is displayed in Table 3.2.1-10. No mechanism for this strength reduction has been advanced, but it is possibly associated with the formation of cristobalite as the major oxidation product.

Various methods of improving oxidation resistance have been tried; all attempted to either fill the pores with a material of thermal expansion similar to Si$_3$N$_4$, or to seal the pores by applying a coating.

Chromic acid, magnesium chromate, nickel chromate, iron chromate, and cobalt oxide were impregnated into the RBSN to fill the pores. All of these materials successfully reduced the open porosity of the Si$_3$N$_4$ and reduced the weight gain to less than 0.05% after 200 hours at both 1038°C and 1260°C. However, they also reduced the strength of the material by 25% to 50%. This strength loss was evident after the impregnations were complete and before any oxidation occurred.

Coatings of CVD Si$_3$N$_4$ were applied to RBSN to seal the surface with a high density layer; this approach was also unsuccessful. The CVD Si$_3$N$_4$ was not impervious and the weight gains after oxidation were no different than those of untreated Si$_3$N$_4$. After the coating was applied, large strength losses of 30% to 50% were observed both before and after oxidation.
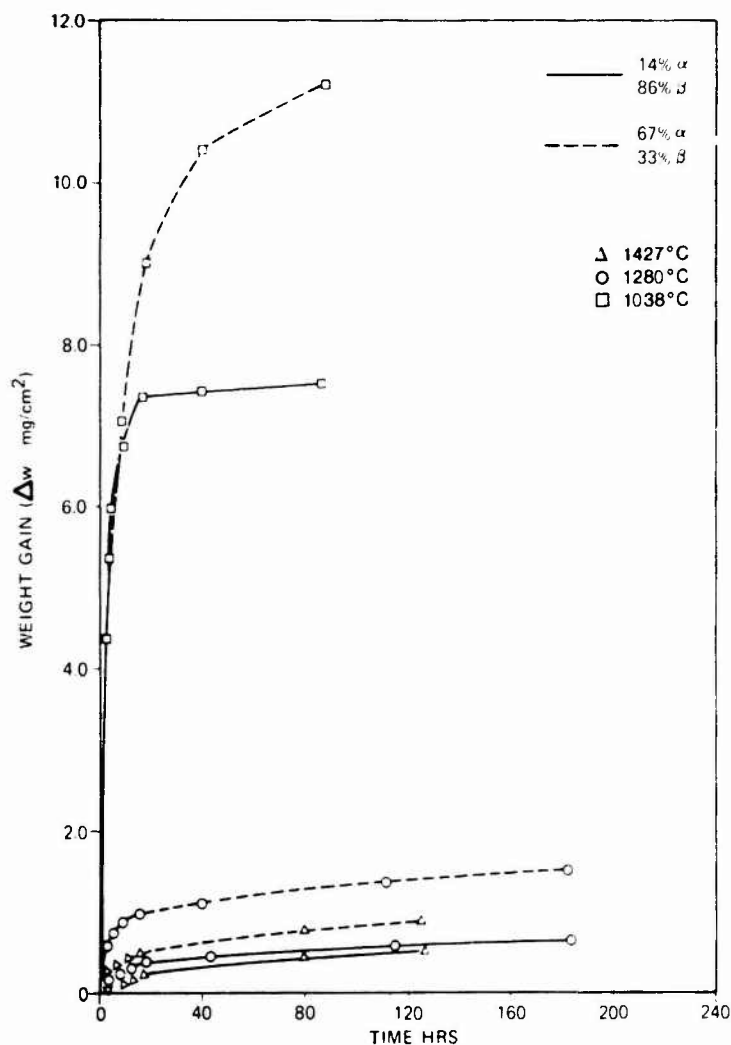
Figure 3.2.1-38 — Weight Gain Due to Oxidation of 2.3 g/cc RBSN of Two Different Phase Compositions as Measured at Various Temperatures.
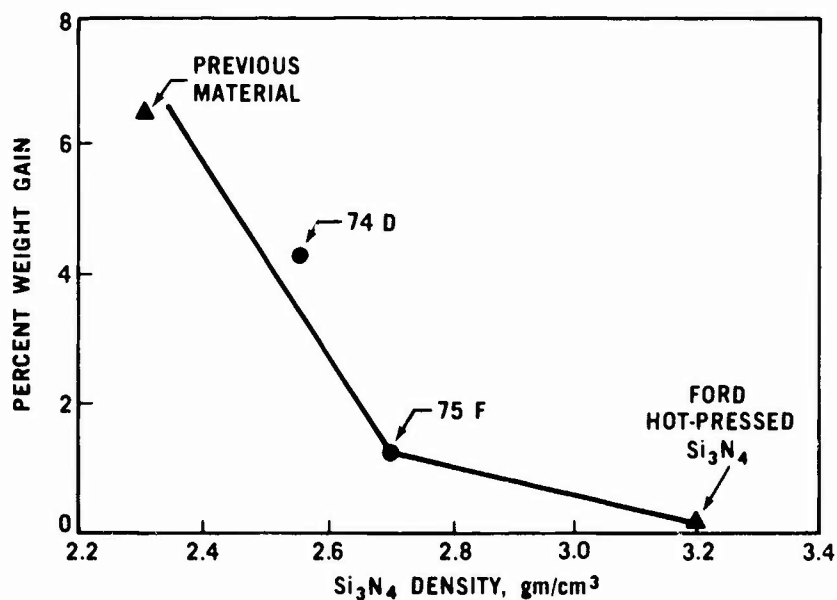

Figure 3.2.1-39 — Oxidation Behavior of Silicon Nitride, Measured Isothermally at 1038°C for 200 Hours, as a Function of Density

Table 3.2.1-10

OXIDATION TESTS ON IMRBSN

RBSN Density (g/cm^3)	Post Nitriding Treatment	Test Temperature (°C)	Exposure Time (hours)	Δ Weight (%)	Δ MOR (%)	Δ Thermal* Expansion (ppm)
2.55	None	1038	200	+3.7	−25	No data
		1260	200	+2.0	−46	No data
2.7	None	1038	200	+0.75	0	+100
		1260	200	+0.55	−22	+150
2.7	Flash Oxidized at 1450°C for 1/2 hour	1038	200	+0.17	0	No change
		1260	200	+0.19	−14	No change

* Maximum difference in thermal expansion up to 900°C.

The best technique found to improve oxidation resistance of RBSN was a Flash Oxidation Treatment [55]. This treatment consisted of rapidly heating the Si_3N_4 from room temperature to between 1370°C and 1500°C in less than one-half hour and maintaining the temperature for between one-half hour and four hours. One particular treatment, shown in Table 3.2.1-10. reduced the weight gains to 0.17% at 1038°C and 0.19% at 1260°C, and reduced the strength losses to 0% and 14% respectively. The thermal expansion of the RBSN did not change.

3.2.2 SLIPCAST REACTION-BONDED SILICON NITRIDE

3.2.2.1 Introduction

Slip casting is a process with a long history of use in the ceramic industry. However, the slip casting of non-clay systems, such as silicon metal powders, has been in a state of infancy. At the beginning of the program very little published information was available on techniques of slip casting silicon. Many of the basic techniques, therefore, were developed from prior work done in refractory metal systems such as molybdenum (Mo) and tungsten (W). Refining these techniques throughout the program resulted in a better understanding of the process and better control over the results.[56,57]

This section of the report outlines techniques developed for the slip casting of silicon and then describes the physical properties of the resulting reaction-bonded silicon nitride material.

3.2.2.2 Material Development for Casting

Basic Slip Casting Process

The basic slip casting process is relatively simple. A stable particulate suspension of the material to be cast (the 'slip') is poured into a rigid absorbent material (the 'mold', usually plaster). The fine pores of the mold draw off much of the liquid fraction of the slip through capillary action; the solids remain and are deposited along the walls of the mold forming a coherent casting. Hollow castings are made by pouring off the slip remaining after the material has been deposited to the desired wall thickness. By replenishing the slip as the liquid is absorbed, one can cast solid pieces. After the casting is removed from the mold it can be dried and fired.

Metal Powder Slip Casting

One of the keys to successful casting is creating a stable suspension of particles in the slip. It is necessary to control the powder parameters (particle size, shape, reactivity and size distribution), the liquid vehicle, and the slip additives (deflocculants, binders and electrolytes.).

Suspensions are formed by two basic mechanisms, one physical and one chemical. For materials with large particles ($>10\mu$) or of high specific gravity, jelling additives physically hold the particles in suspension. Such slips generally have high viscosity and create castings with a low density.

When the particles are small enough to be controlled by ionic surface forces, e.g., London van der Waals, rather than gravity, they are held in a chemical suspension. Chemical suspensions are formed with silicon when most of the particles are within the size range of $1\sim10\mu$.[58]

Characteristics of the particle surfaces are critical factors in establishing a chemical suspension.[59] The usual mechanism suspending particles is the repulsive force of the electrical double layer formed by the oxide skin surrounding most metals. However, under certain conditions, this oxide skin can increase, decrease, totally dissolve or change in type, which results in a sudden shift of rheological properties of the slip.[60]

Particle size distribution is another critical factor because this controls packing efficiency which affects the density of the casting. It also can affect drying shrinkage. A slip with a high proportion of fine particles may shrink excessively while drying and crack, while a slip with a high proportion of coarse particles may not shrink enough to be removed from the mold. The shape of the particles determines both surface area, an important factor when considering ionic surface forces, and packing efficiency.

The liquid vehicle must:

1) Be able to wet the particles, thus providing the lubrication and consequent particle mobility necessary for high packing efficiency;

59

2) Have chemical stability, to avoid adverse reactions with the oxide skin; and

3) Have the proper viscosity.

In addition to these factors, various wetting agents, electrolytes, binders and deflocculants may be added to the slip to alter its rheological properties, which further modify the casting properties of the slip and the physical properties of the cast.

Slip Casting of Silicon

One of the goals of this program was to produce silicon castings of high 'green' density, because the final nitrided density is directly proportional to 'green' density. Moreover, engineering properties such as strength generally increase with increasing density. Chemical suspensions have greater potential to produce higher density castings than physical suspensions. Consequently, the slip system finally developed consisted of:

1) Finely divided silicon metal

2) 0.01-0.06 weight percent of an alkaline deflocculant

3) Nitric acid and ammonium hydroxide as electrolytes

4) Distilled water as the liquid vehicle

Preparation of the Raw Material

The silicon powder as received had a particle size of 325 mesh; this was too coarse to establish a chemical suspension. Thus, it was dry-milled with high density alumina balls in alumina mills to a number of different particle size distributions. Although a number of different distributions were produced and tested, most of the work reviewed here was done with two distributions, 5.5μ and 6.0μ; the distributions were determined by X-ray analysis. (Figures 3.2.2-1 & 3.2.2-2). Typical particle shapes of the powders are shown in Figure 3.2.2-3.
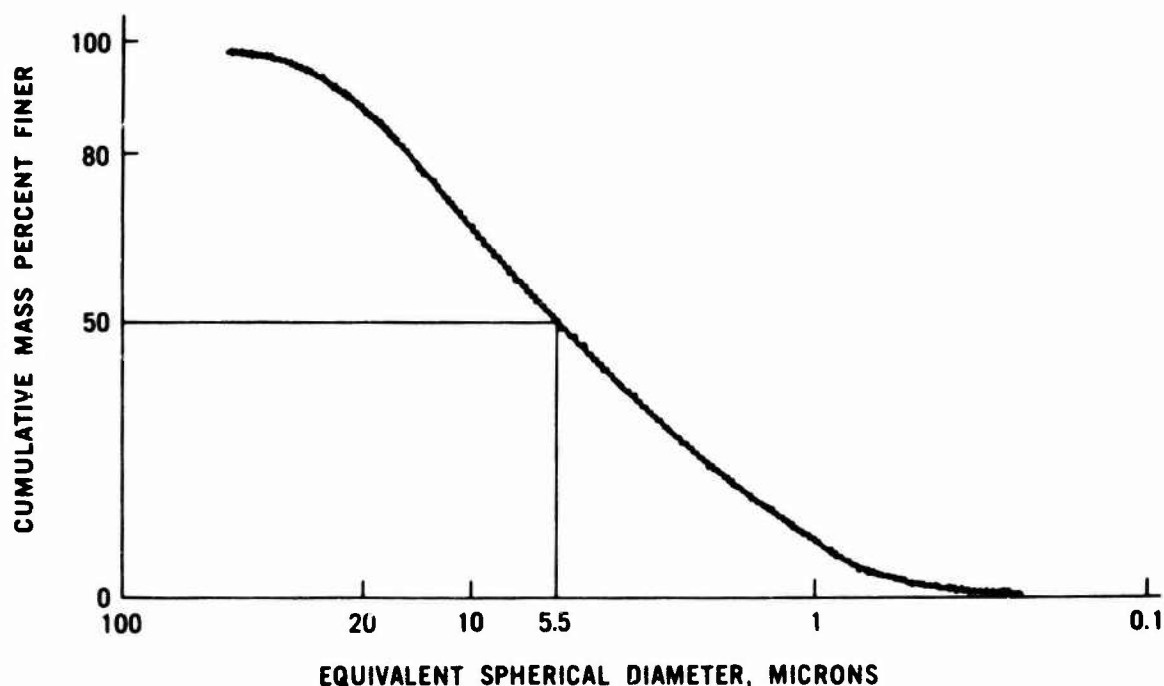
Figure 3.2.2-1 — Particle Size Distribution of Ball Milled Silicon Powder, 5.5μ Median Particle Diameter
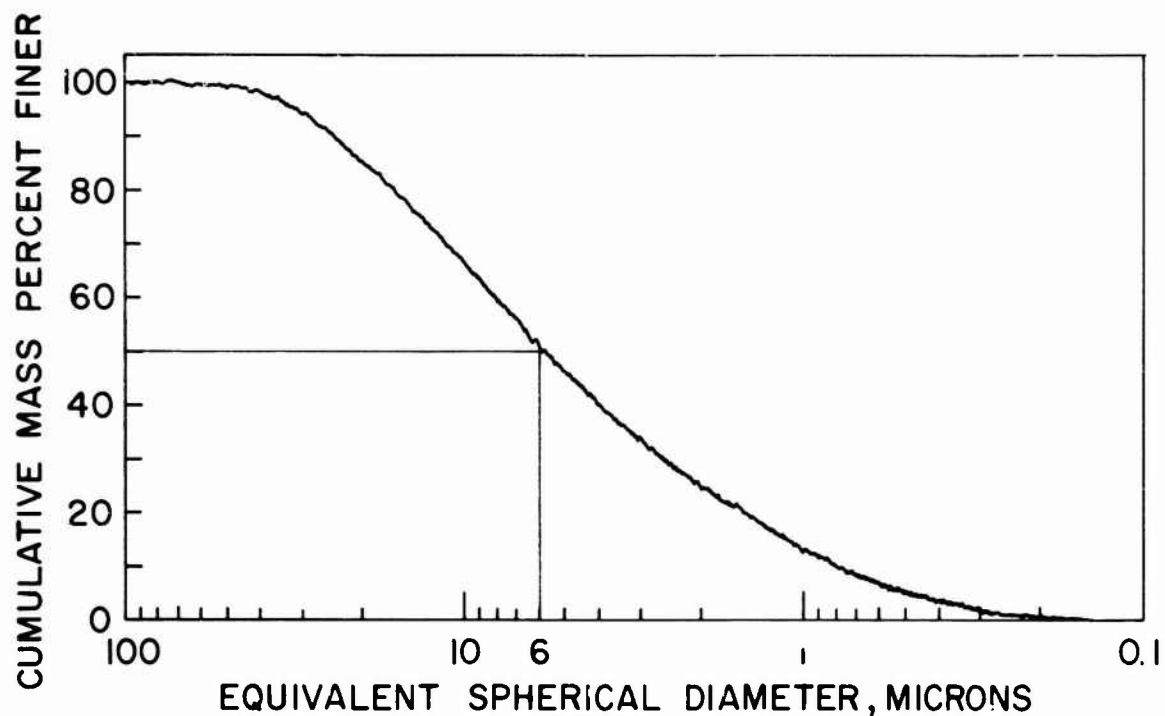
Figure 3.2.2-2 — Particle Size Distribution of Ball Milled Silicon Powder, 6.0μ Medium Particle Diameter

Figure 3.2.2-3 — Microstructure of Cast Silicon Structure (800x)

Slip Stability

In the slip system used, the silicon powder underwent an exothermic reaction accompanied by the release of hydrogen gas. By monitoring the pH, however, it was possible to determine when the slip had achieved a stable equilibrium state. It thus became apparent that the slips needed proper aging before they were suitable for use.

Relationship Between pH and Viscosity

The viscosity of a slip was also found to vary with the pH. Slips were prepared using both the 5.5μ and 6.0μ powders and allowed to stabilize. Slip pH was then altered by small additions of either nitric acid (HNO_3) or ammonium hydroxide (NH_4OH). The resulting viscosity changes are displayed in Figures 3.2.2-4 and 3.2.2-5. The differences between the two responses were due to particle size, particle size distribution and the amount and type of deflocculant used. This experiment demonstrated that by controlling the pH it is possible to control the slip viscosity over a wide range.

Relationship Between pH and Density

Controlling the slip viscosity by controlling the pH also enabled control of the density of the 'green' casting. This relationship is displayed in Figures 3.2.2-6 and 3.2.2-7 for the 5.5μ and 6.0μ slips, respectively. As the slip viscosity decreases, the density of the 'green' casting increases. This implies that the density of the final silicon nitrided article would also increase. (In Figure 3.2.2-6 the silicon nitride densities were calculated, not measured, assuming a 60% weight gain upon conversion of the silicon metal to silicon nitride.)

Relationship Between pH and Green Shrinkage

Although 'green' shrinkage is usually thought to be controlled by the particle size distribution,[61] it is also dependent upon the pH.[62,63]. This relationship for the the 6.0μ slip is displayed in Figure 3.2.2-8. As pH increases the 'green' shrinkage decreases. Minimum 'green' shrinkage indicates a maximum in 'green' density. Moreover, this relationship was found to be true for other slips tested. Since 'green' shrinkage can affect the possibility of having a casting crack while drying and the ease of mold release, control of this characteristic is important.
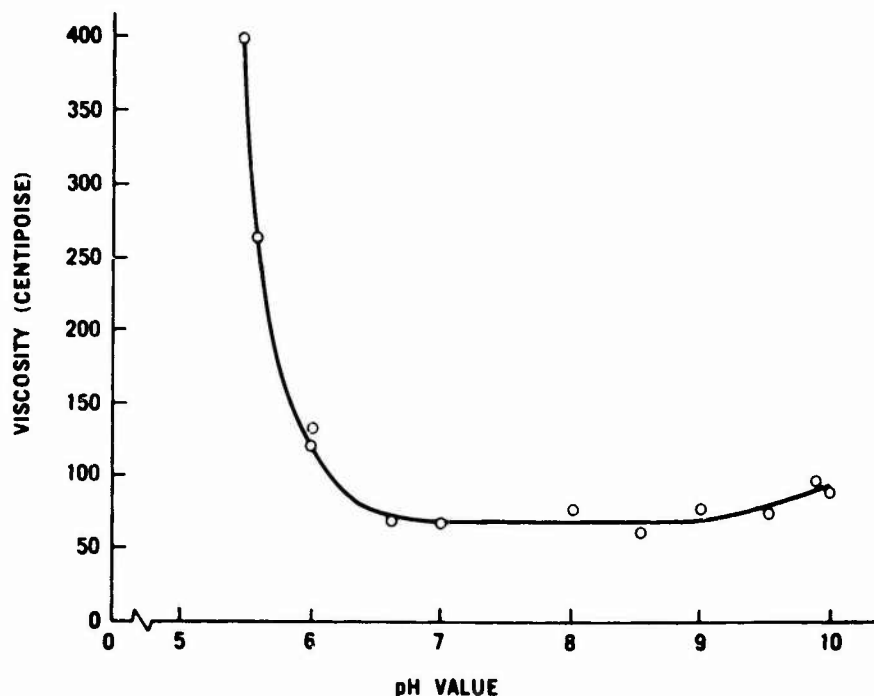

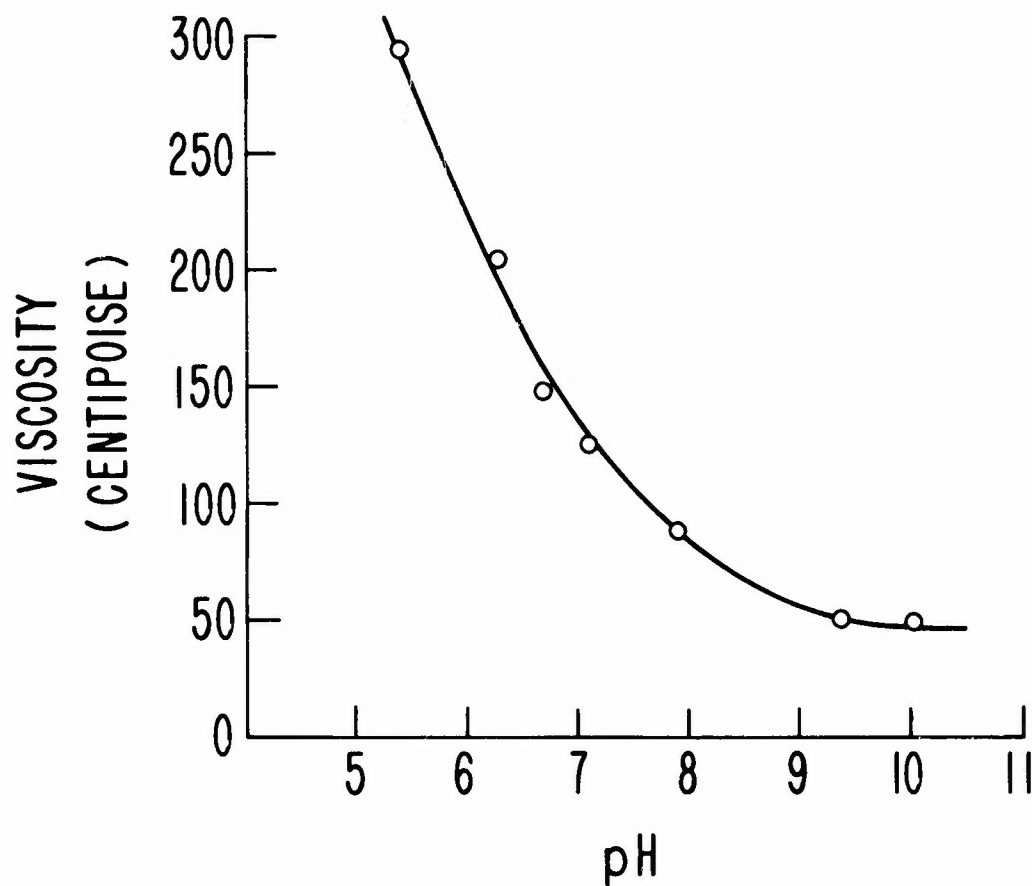Figure 3.2.2-4 — pH Vs. Viscosity Relationship of 5.5μ Silicon Slip

Figure 3.2.2-5 — pH Vs. Viscosity Relationship of 6.0μ Silicon Slip
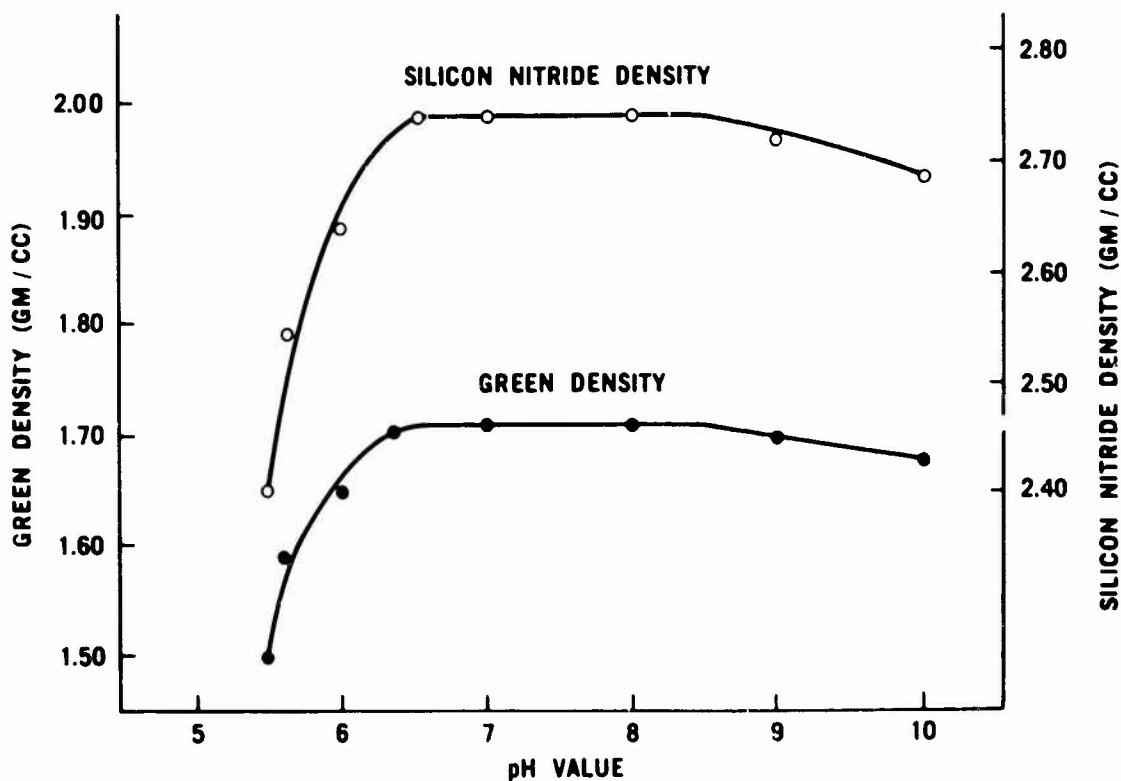

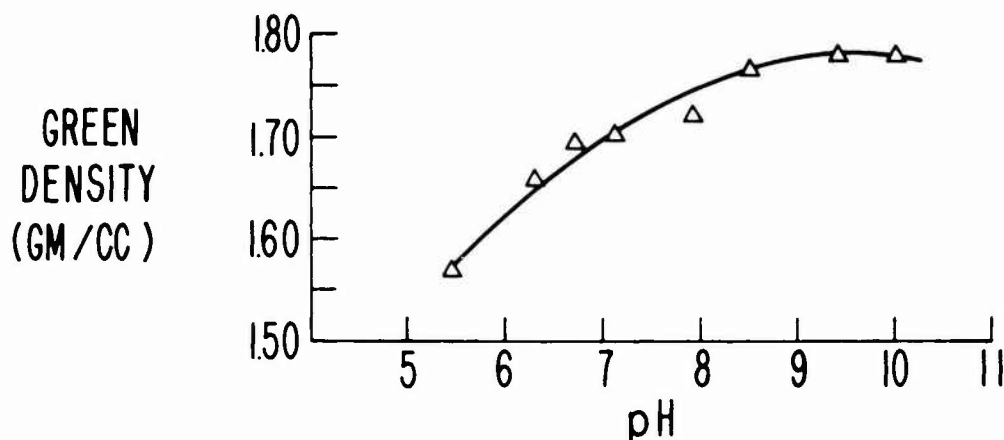Figure 3.2.2-6 — Green Density and Corresponding RBSN Density of 5.5μ Silicon Slip Vs. pH Level of the Slip

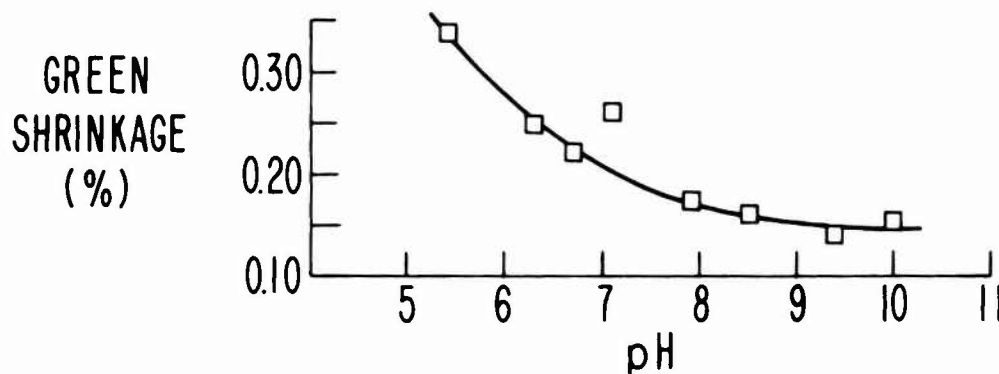Figure 3.2.2-7 — Green Density of 6.0μ Silicon Slip Vs. pH Level of the Slip

Figure 3.2.2-8 — pH Vs. Shrinkage Relationship for 6.0μ Silicon Slip

Effects of Diluting the Slip

The effect of slip dilution upon casting properties was also investigated. Both 5.5μ and 6.0μ slips were diluted with distilled water and their pH adjusted to minimum viscosity. The results are displayed in Figures 3.2.2-9 and 3.2.2-10. Even though a significant reduction in slip viscosity occurred in both cases there was little change in 'green' density. Such low viscosity slips would be useful in casting small and intricate shapes. However, care must be taken since over-diluting may result in slips so thin that the solid particles fall out of suspension.
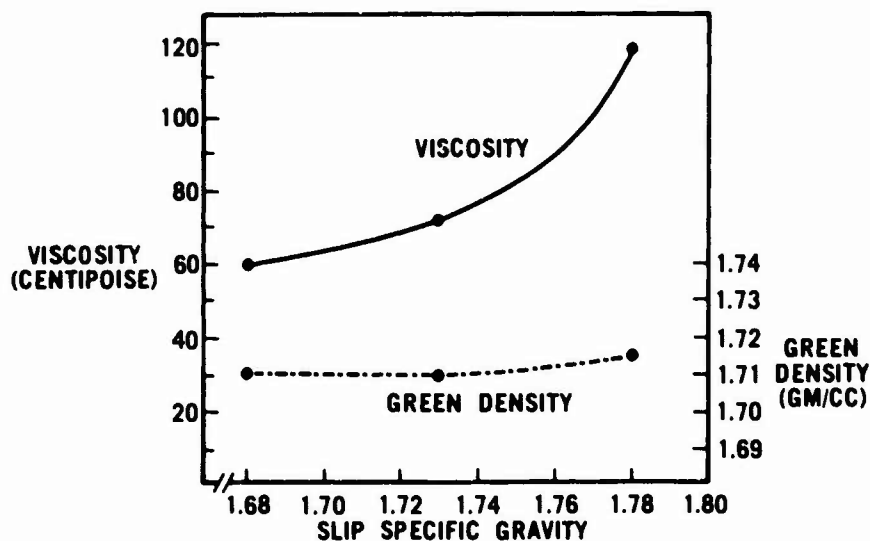
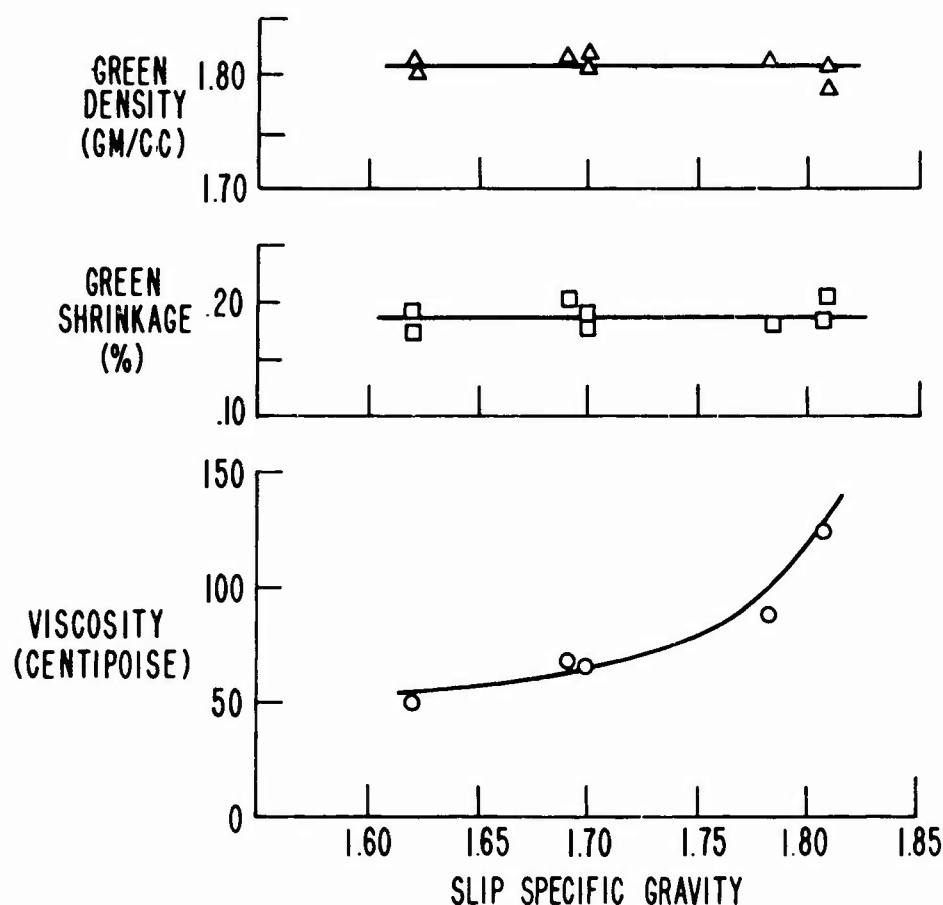Figure 3.2.2-9 — Effect of Dilution of 5.5μ Silicon Slip Viscosity and Green Density of Castings

Figure 3.2.2-10 — Effect of Dilution of 6.0μ Silicon Slip on Viscosity, Casting Shrinkage and Green Density of Castings

Nitriding of Slip Cast RBSN

In this program, slip cast material was nitrided along with injection-molded RBSN. Please refer to the preceeding Section (Section 3.2.1.4) for a description of nitriding development.

3.2.2.3 Physical Property Characterization

Physical properties examined during this program included modulus of rupture (in both three- and four-point bending), creep resistance, thermal conductivity and elastic modulus. All of these were measured over a wide range of temperatures. Throughout the program, work continued on improving these physical properties by modifying the slip rheology, adding various nitriding aids and changing the nitriding schedule and nitriding atmospheres.

Bend Strength

Early work in measuring the strength of slip cast silicon nitride was done primarily in three-point bending using a hydraulically loaded system.[4] The test fixture used carbide knife edges located on 3 inch centers and 0.23 inch x 0.23 inch x 4.00 inch diamond ground test specimens. Cross head speed was approximately 0.1 inch/min. The data displayed in Figure 3.2.2-11, with the exception of two data points, was obtained in this manner. The material had a density of 2.6 gm/cc.

Later work was primarily done in four-point bending using an Instron Universal Tester.[9] The test fixture used silicon carbide edges located on the quarter points of a 0.75 inch span and 0.125 inch x 0.25 inch x 1.00 inch diamond ground test specimens. Cross head speed was 0.02 inch/min. The data are shown in Table 3.2.2-1. The material had a density of 2.82 gm/cm^3 and was nitrided using a 100% N$_2$ atmosphere. Weibull data were calculated using the MLE method.
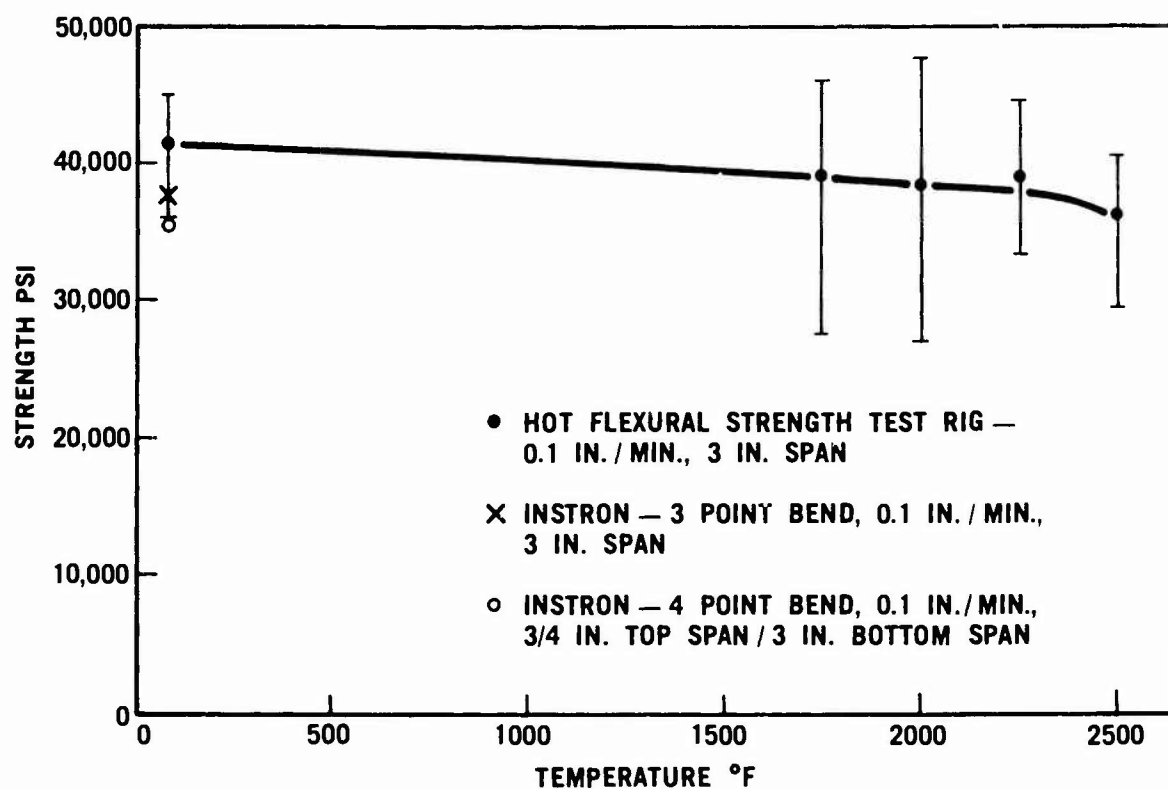
65

Figure 3.2.2-11 — Strength Vs. Temperature for Slip Cast RBSN

TABLE 3.2.2-1

MODULUS OF RUPTURE OF SLIP CAST Si_3N_4
(2.82 gm/cc DENSITY)

Temperature °F	Average MOR* (ksi)	Characteristic Strength (ksi)	m	Number of Samples
Room Temp.	29.7	31.2	8.18	19
1300	32.5	34.5	7.42	20
1700	34.5	36.9	6.54	20
2100	33.7	36.0	6.26	18

*1/8 x 1/4 x 1 inch sample; 3/8 x 3/4 inch bend fixture, 0.02 in/min. load rate.

A study was undertaken to increase the strength of the slip cast material by improved nitridation; the results are shown in Table 3.2.2-2. The results indicated it was possible to obtain a room temperature modulus of rupture of 50.7 ksi for a 2.8 gm/cm^3 material. This was a considerable improvement over the values obtained at the beginning of the program.

TABLE 3.2.2-2

STRENGTH OF SLIP CAST Si_3N_4

Nitriding Atm.	Average** MOR (ksi)	MOR Range (ksi)	Density (gm/cm^3)	Δ Weight (%)	Comments
100 N_2	26 +	25-27	2.67/2.74	60	Chemically adjusted slip to give
4% H_2/96 N_2	26 +	25-27	2.67/2.74	60.3	low density-solid cast
100 N_2	37 +	36-40	2.8	60.1	Solid cast
	50.7 +	46-53	2.8	60.4	Centrifugally cast, sample from rotor hub
4% H_2/96 N_2	43 +	32-50	2.68	59.5	Experimental slip, change in particle size distribution, change in deflocculant
100 N_2	29.7 +	25-37	2.82	59	Solid cast
4% H_2/96% N_2	41 ++	38-46	2.82	59	Centrifugally cast, sample from rotor hub

** Four-point bending 1/8 x 1/4 x 1-1/2 inch samples, load rate 0.02 in./min.
+ 3/8 x 1/-1/8 inch knife edge spacings
++ 3/8 x 3/4 inch knife edge spacings

Creep

Slip cast materials of varying densities and nitriding additions as shown in Table 3.2.2-3, were tested for creep.[5,6] The creep tests were conducted in an air atmosphere in four-point bending over a 0.75" span The sample size was 0.125" x 0.125" x 1.50". The deflection was determined by measuring the movement of the load train with an LVDT transformer mounted outside the furnace. Results of the creep tests are shown in Table 3.2.2-4.

TABLE 3.2.2-3

CREEP SAMPLE PROCESSING HISTORY OF SLIP CAST SILICON NITRIDE

Code No.	Nitriding Additive	Density
NE8	None	2.69 gm/cm^3
NE9	3% CaF_2	2.65 gm/cm^3
NE10	1% Fe_2O_3	2.72 gm/cm^3
NE12	3% Fe_2O_3	2.72 gm/cm^3

TABLE 3.2.2-4

CREEP TEST RESULTS OF SLIP CAST SILICON NITRIDE

Material	Test Temp. (°F)	Stress (ksi)	Duration of Test (hrs.)	$\overset{\circ}{\epsilon}s$ (in./in./hr.)
NE8	2300	10	70	1×10^{-5}
NE9	2300	10	65	3.5×10^{-5}
NE10	2300	10	65	No Detectable Creep
NE10	2400	12	70	No Detectable Creep
NE10	2400	15	70	No Detectable Creep
NE12	2300	10	65	No Detectable Creep
NE12	2300	17	45	No Detectable Creep- then rupture
NE12	2300	20	5	No Detectable Creep- then rupture

Thermal Conductivity

Thermal conductivity of a 2.68 gm/cm^3 slip cast material was measured by Battelle Memorial Institute using a flash diffusion method.[4] The results are shown in Figure 3.2.2-12. For comparison, the thermal conductivity of a 2.23 gm/cm^3 injection-molded material is also shown. The thermal diffusivity data used to calculate the thermal conductivity is shown in Figure 3.2.2-13. Since both materials were similar in composition and nitriding history, the difference was assumed to be due to differences in density or porosity.
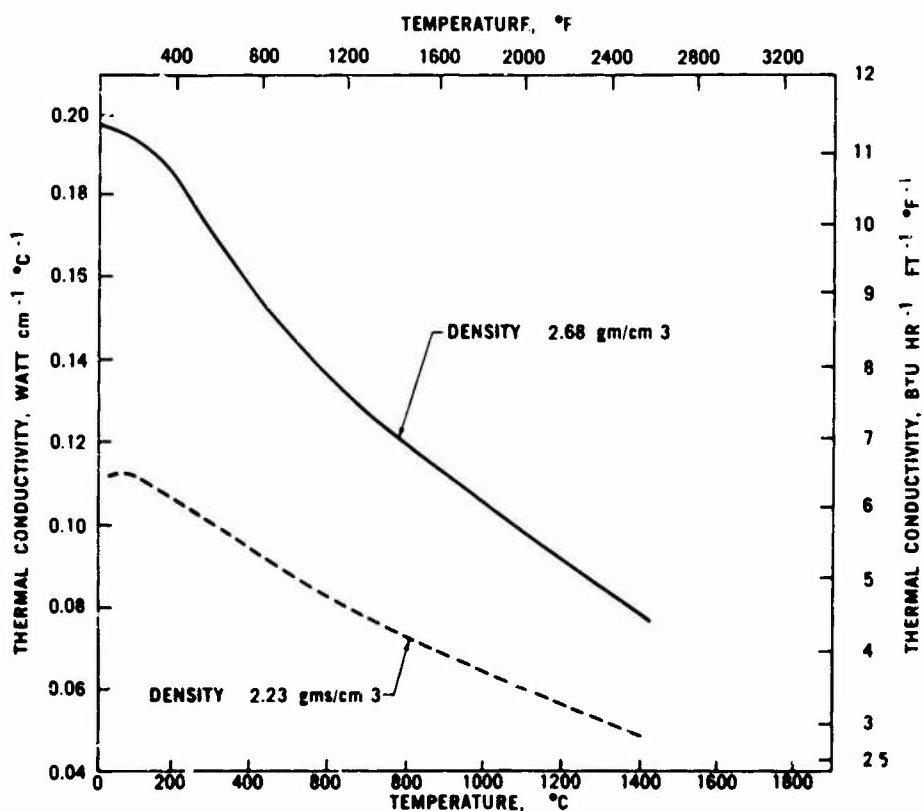
Figure 3.2.2-12 — Thermal Conductivity of Slip Cast RBSN
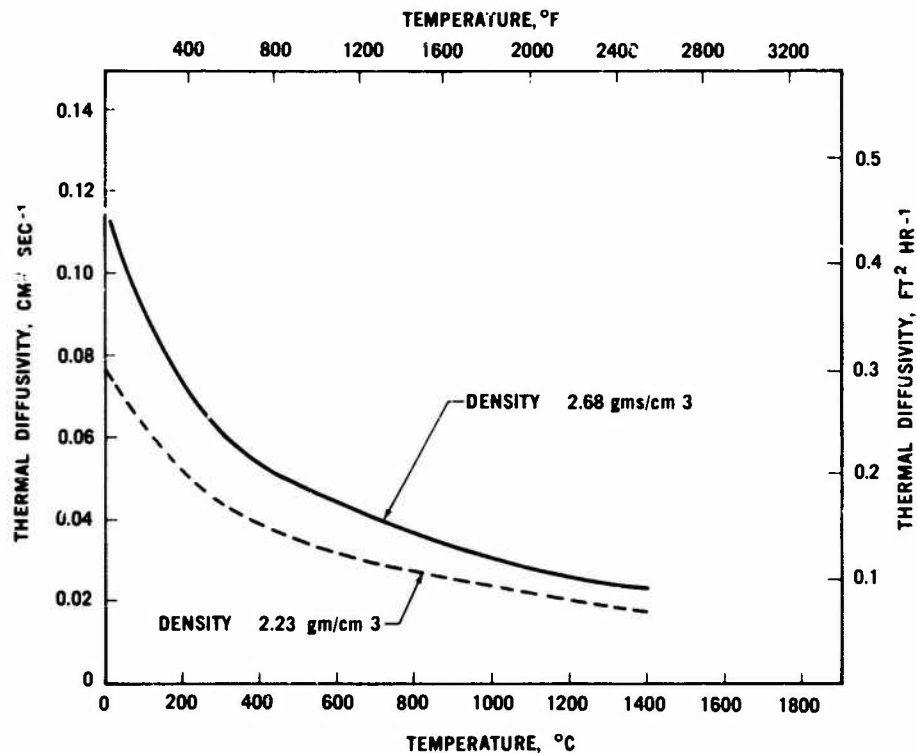
Figure 3.2.2-13 — Thermal Diffusivity of Slip Cast RBSN

Elastic Constants of Silicon Nitride

Longitudinal, Young's and shear modulus, along with Poisson's ratio, was determined for slip cast materials using the sonic method.[6] The results are shown in Figures 3.2.2-14 through 3.2.2-17 along with those for two hot pressed Si_3N_4 materials included for comparison.
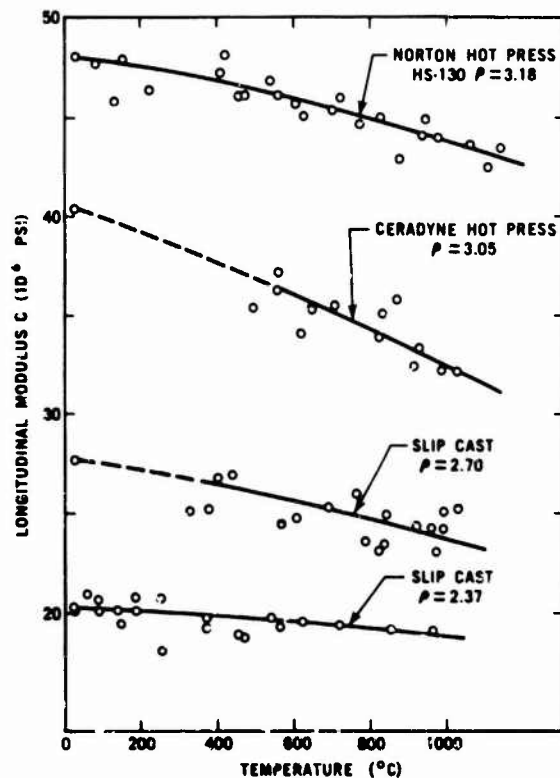

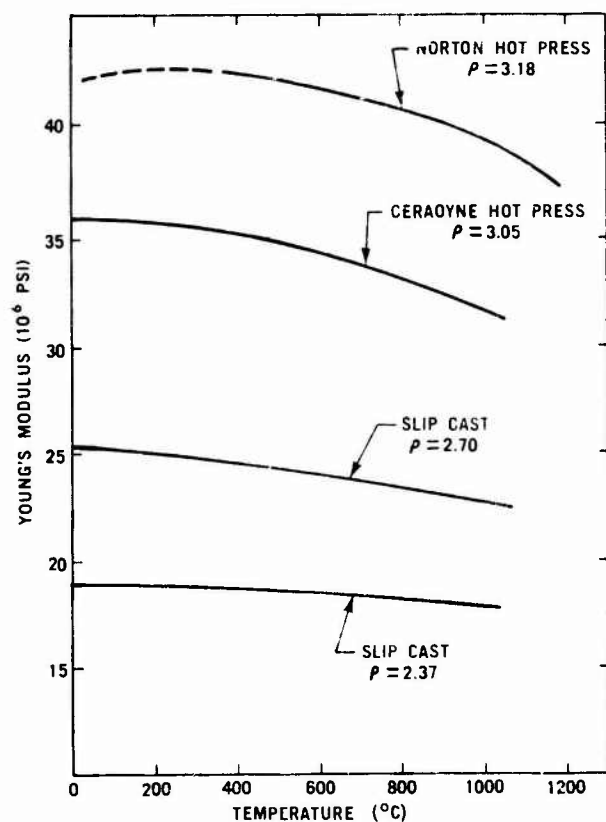Figure 3.2.2-14 — Longitudinal Elastic Modulus of Various Silicon Nitrides

Figure 3.2.2-15 — Young's Modulus of Various Silicon Nitrides
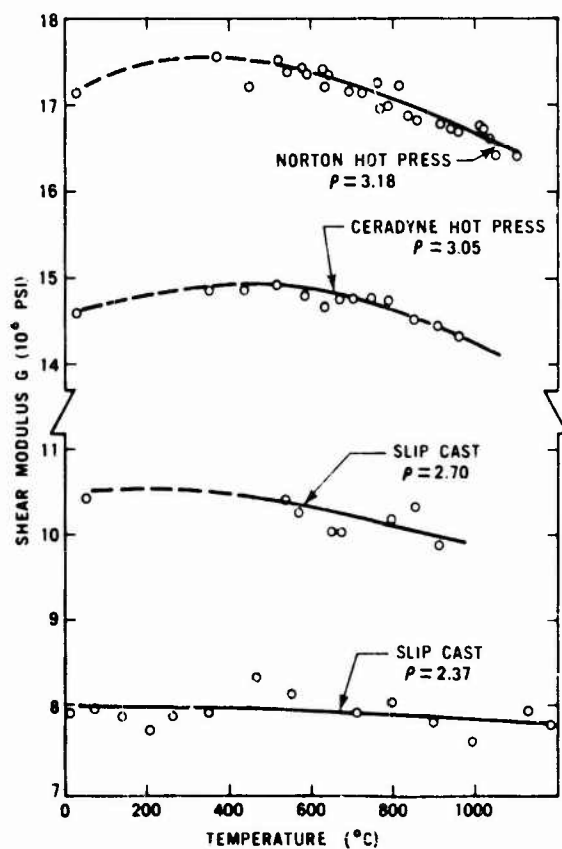
Figure 3.2.2-16 — Shear Modulus of Various Silicon Nitrides
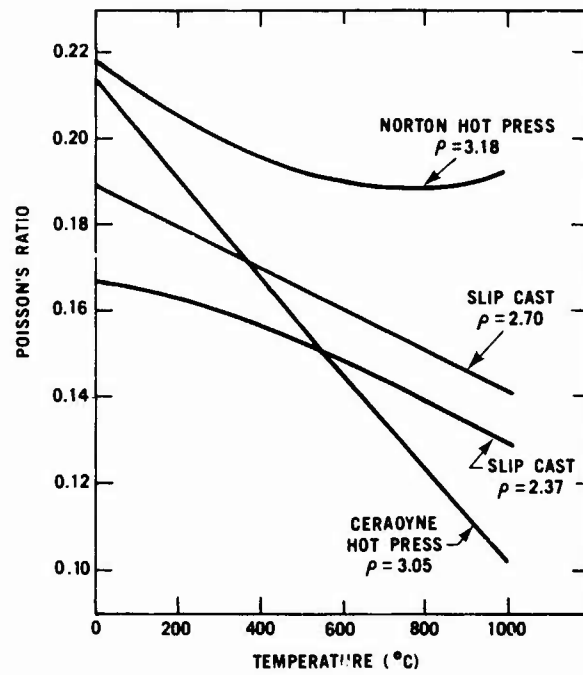
Figure 3.2.2-17 — Poisson's Ratio of Various Silicon Nitrides

3.2.3 HOT PRESSED SILICON NITRIDE

3.2.3.1 Introduction

At low nitrogen pressures and temperatures greater than 1800°C, silicon nitride (Si_3N_4) tends to readily dissociate. Traditional sintering techniques do not work at lower temperatures because of insufficient atomic mobility in Si_3N_4. Thus, Si_3N_4 is generally produced by reaction bonding or hot pressing.

Silicon nitride of theoretical density and having strength on the order of 100,000 psi can be produced by hot pressing. A densification aid liquifies during the simultaneous application of heat and pressure helping the Si_3N_4 powder to densify by a solution-reprecipitation process across the liquid grain boundaries. This grain boundary phase, which is vital to densification of the Si_3N_4 powder, represents a primary disadvantage of hot pressed silicon nitride (HPSN); this grain boundary phase softens or melts at elevated temperatures which deteriorates the strength of the HPSN, and, when stressed, causes creep and slow crack growth.

Silicon nitride of full density and high strength is required to endure the high operating stresses present at the hub of a turbine rotor. Thus, the major emphasis in the hot pressing area of this program was to develop a feasible technique for fabricating hubs for the duo-density Si_3N_4 turbine rotor (Section 4.3 of this report). Refinement of powder processing techniques was conducted in parallel with this effort. Late in the program, work was directed towards densification aids other than magnesium oxide (MgO), in the attempt to find an additive which would not decrease the strength of Si_3N_4 at elevated temperatures.

3.2.3.2 Material Development for Hot Pressing

Initial Research

After attempting many different fabrication techniques for rotors, efforts were directed towards a "duo-density" process. HPSN was used for the hub of the rotor where stresses were highest but where temperatures were low enough to minimize creep. Then, in one operation, the hub was hot pressed and bonded to a RBSN blade ring. Using RBSN placed constraints on the temperature, pressure, time and densification aid that could be used to form the rotor; e.g., pressures above 1,000 psi deformed the blade ring and cracked the blades. Consequently, the initial research in hot pressing was to study the bonding process and the effects of various pressing parameters on bond quality.

Ceramic components with simplified shapes (which simulated the rotor) were used during feasibility studies[1] (Figure 3.2.3-1). The rings were fabricated by cold pressing or slip casting silicon into shape, nitriding to form Si_3N_4, and then machining to the designed dimensions. The hubs were prepared by hot pressing α Si_3N_4, with a MgO additive, into a full density disk simulating the hub. The bond surfaces were machined to remove any oxide or reaction layer. A thin coating of lacquer containing Si_3N_4 and 1 w/o MgO was painted on the bond surfaces to enhance densification and fill small machining defects.

This duo-density shape was then hot pressed for one hour at 1775°C and 2,000 psi. After pressing, the bond quality appeared excellent (Figure 3.2.3-2).

Often, a severe reaction of the RBSN with the carbonaceous gases in the hot press environment occurred during hot pressing, with the formation of silicon carbide (SiC). The most effective solution to this problem was to line the hot press cavity with a Grafoil® or molybdenum foil barrier layer.

Bonding studies were conducted using disks of RBSN and HPSN two inches in diameter. As before, the bond surfaces were machined to remove any reaction layer and painted with a bond-promoting layer of Si_3N_4 and 0.5 w/o MgO in lacquer. Then, after bonding, the samples were characterized with respect to microstructure and strength. The strength measurements were conducted under three-point loading with the sample positioned so that the point of maximum tensile stress occurred at the joint.
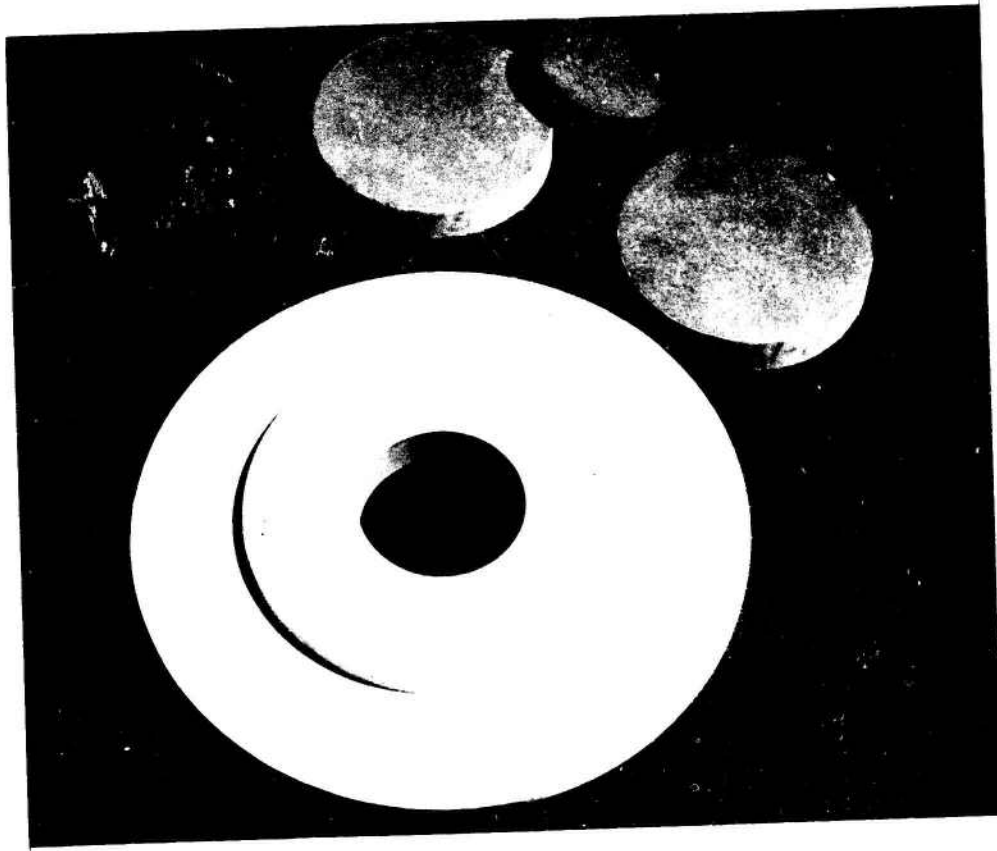
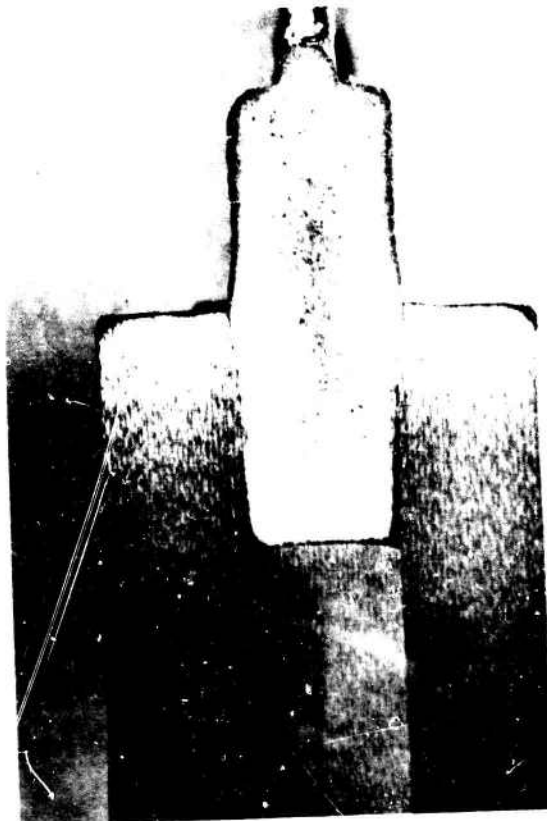Figure 3.2.3-1 — Press Bonded Duo Density Shape

Figure 3.2.3-2 — Sectioned Duo Density Shape

Strength of the samples ranged from 23,000 psi to 31,000 psi with no apparent correlation to bond quality. The location of the fractures was of greater importance than the strength of the material; in well bonded materials the fractures always occurred in the RBSN. This indicated that the bond region was not strength limiting.

Variables in Processing and Their Effects on HPSN

An evaluation of the variables affecting the quality of HPSN and an assessment of their relative importance was needed in order to accurately predict the properties and the reliability of rotors and to establish effective quality control procedures. A starting point was to determine the consistency of strength parameters from hub to hub and from area to area within individual hubs. The former was important in assessing the reproducibility of the hot pressing technique, the latter in deciding if separate strength parameters were necessary for each finite element in reliability analysis.

Five hubs were pressed from a Si_3N_4 + 2 w/o MgO powder; four were from the same powder milling batch and one was from a different batch. Test bars were cut as illustrated in Figure 3.2.3-3. Strength parameters of hubs from the same batch were fairly consistent; however, significant variations in strength existed in hubs from different batches.
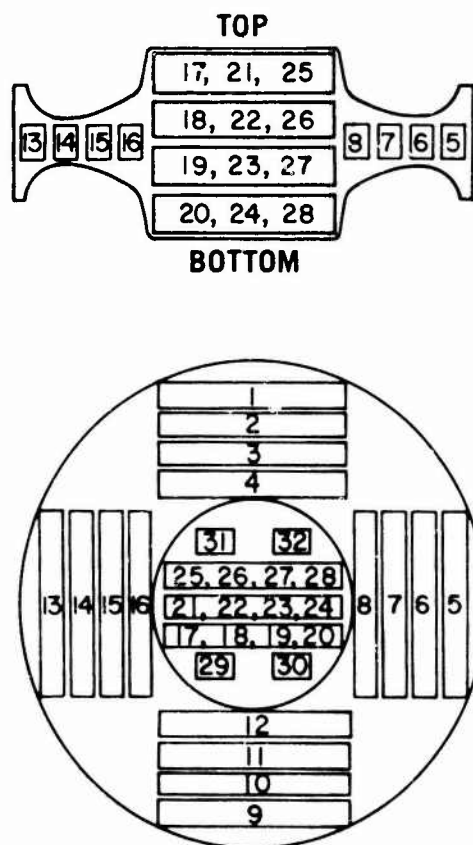

Figure 3.2.3-3 — Machining Plan for Test Bars Cut From Formed Rotor Hubs

Within any single hub there were no statistically significant variations in strength. This meant that a single set of strength parameters could be used for all the finite elements of the rotor in reliability analysis, with the precaution that the data would be applicable only to a particular batch of powder. From this work it became apparent that the method used in preparing powder batches played a significant role in determining the final properties of the HPSN.

In order to gain insight into the effects of powder preparation methods on HPSN, a parametric study was conducted to assess the following variables:

1) Purity of the material: Si_3N_4 powder as received versus powder passed through a magnetic separator and air classified to 50 microns or less
2) Hot pressing additive: 2 to 5 weight % MgO
3) Milling balls: tungsten carbide (WC) versus aluminum oxide (Al_2O_3)
4) Type of milling: dry versus wet in reagent grade absolute methanol
5) Milling time: 48 hours versus 72 hours
6) Hot press pressure: 500 to 5,000 psi.

Because the strength data might be influenced by subtle differences in machining quality of the test bars, two different machining shops were used to indicate if this variable affected the test results. Bars were tested in four-point bending at 1600°F (871°C) and 2200°F (1204°C); these temperatures were projected to be the maximum operating temperature at the bore and at the bond ring of the rotor, respectively.

Evaluation of results from a saturated fractional factorial analysis of the above variables showed that, within the conditions investigated:

1) Wet milling with Al_2O_3 balls produced low strength
2) No significant difference exists between milling with dry or wet WC and dry Al_2O_3 balls
3) High strengths resulted at pressures as low as 1,500 psi
4) Milling time had no significant effect
5) 5 weight % MgO was superior to 2 weight % MgO
6) Machining source had a significant effect

Using these findings, quality control procedures were established for powder processing with records kept of all the critical data characteristic of each Si_3N_4 batch used for hot pressing. Each new lot of Si_3N_4 powder and each lot of additive was characterized by emission spectroanalysis, particle size distribution, X-ray diffraction, B.E.T. surface area, and oxygen content (via neutron activation analysis). Amounts of Si_3N_4 powder, densification aid and methanol added to each batch were recorded, along with starting date, milling time, rpm and WC contamination level (this was calculated from the weight of the WC balls pre and post milling). After milling and screening, each batch was additionally characterized by particle size analysis. This data proved useful for tracing pressing problems, calculating hot press densities and locating milling problems; e.g., fast wearing WC balls.

AME CP-85 grade Si_3N_4 powder with a 5 weight % MgO additive was experimentally hot pressed to examine the effects of the hot pressing parameters on material quality. Temperatures were 1500°C to 1750°C, pressures were 1,000 psi to 5,000 psi and hold times were one hour to seven hours.

The design of the experiment allowed each parameter's effect to be independently studied at more than one level; e.g., temperature effects with other parameters held constant at 1,000 psi for three hours or at 2,500 psi for three hours. Hot pressed billets were evaluated by density, microstructure, X-ray analysis and four-point MOR at both room temperature and 2200°F.

Except for one billet pressed at 1,000 psi for three hours at 1500°C, all others were greater than 99% dense. Each parameter's effect on room temperature strength is displayed in Figures 3.2.3-4 through 3.2.3-6. Each symbol in the figure represents an average of five test bars.

Temperature during hot pressing appears to be the dominant factor influencing room temperature strength. Through the use of X-ray diffraction, the relationship between room temperature strength and temperature was identified as resulting from the conversion of α Si_3N_4 to β Si_3N_4 during hot pressing. As this conversion proceeds, a network of β Si_3N_4 needles develops; these interlocking needles are stronger than the α Si_3N_4 grains. Maxima in each curve, therefore, probably represent the completion of this conversion; decreases beyond maximum may represent grain growth.

Strength behavior at 2200°F as a function of pressing temperature displayed quite a different trend; strength steadily declined as temperature increased (Figure 3.2.3-7). Tentatively, this behavior was linked to the occurrence of a cellular network of fine porosity in some HPSN which gives billets a mottled appearance (Figure 3.2.3-8).
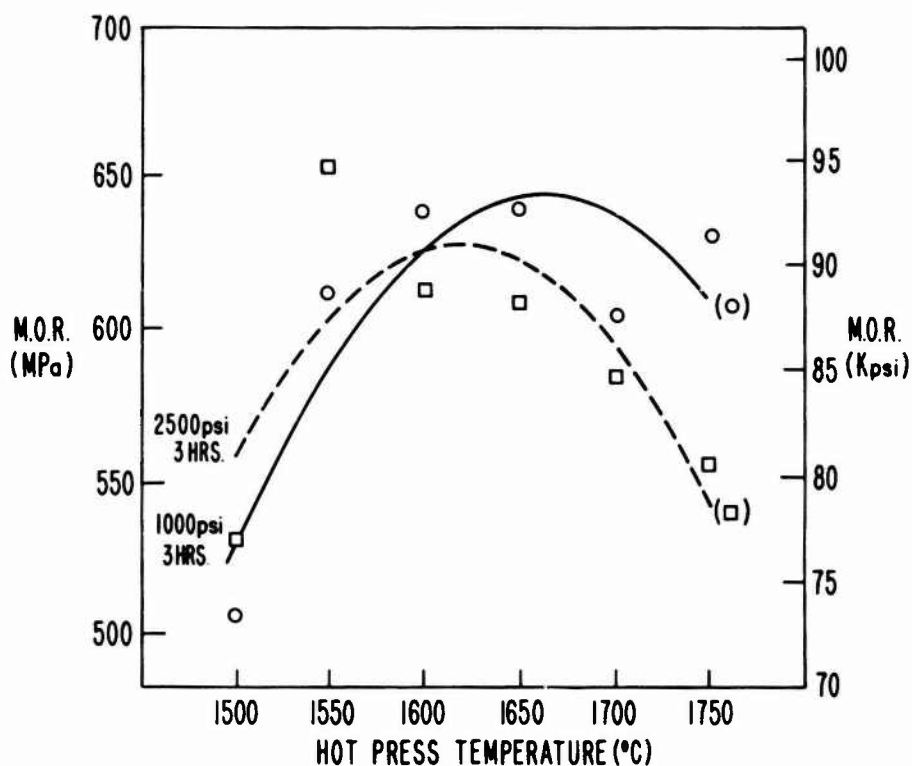
Figure 3.2.3-4 — Effect of Hot Pressing Temperature Upon Room
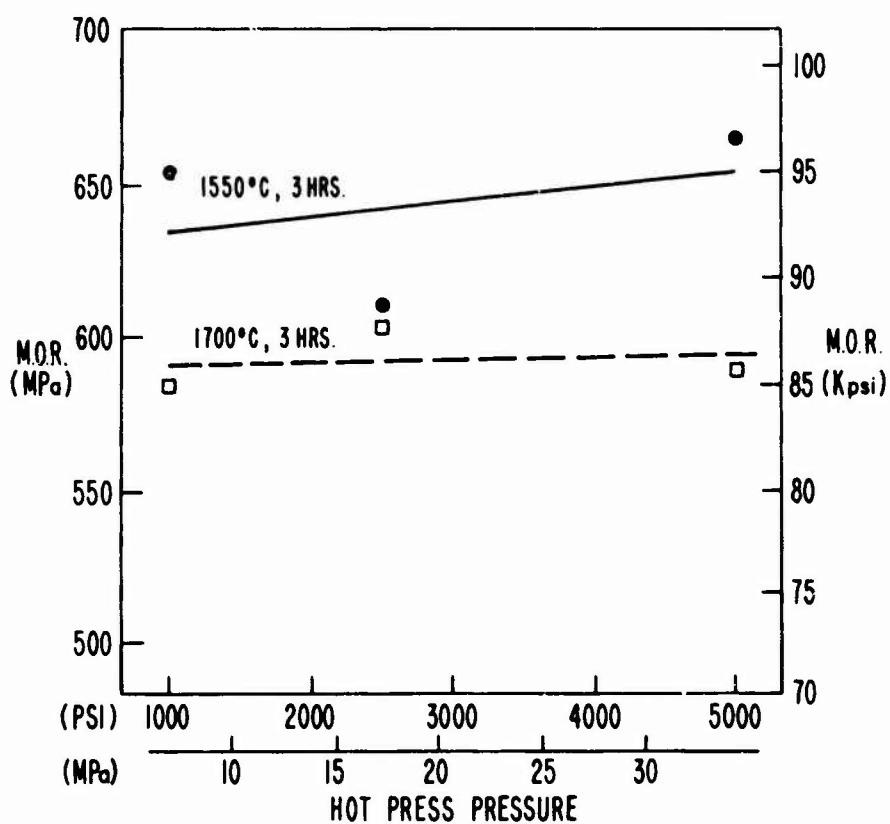Temperature Strength of HPSN

Figure 3.2.3-5 — Effect of Hot Pressing Pressure Upon Room
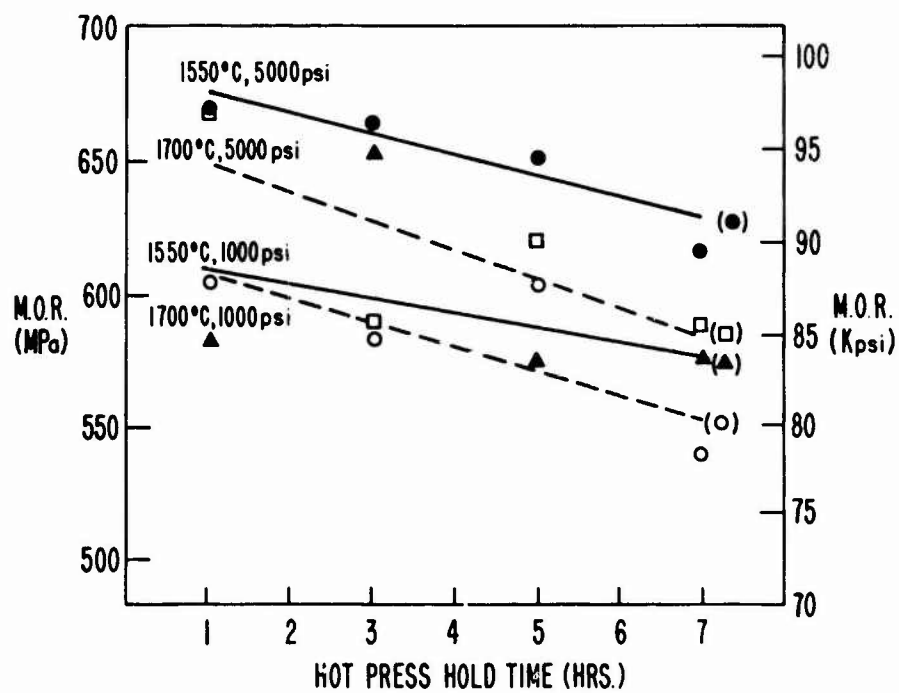Temperature Strength of HPSN

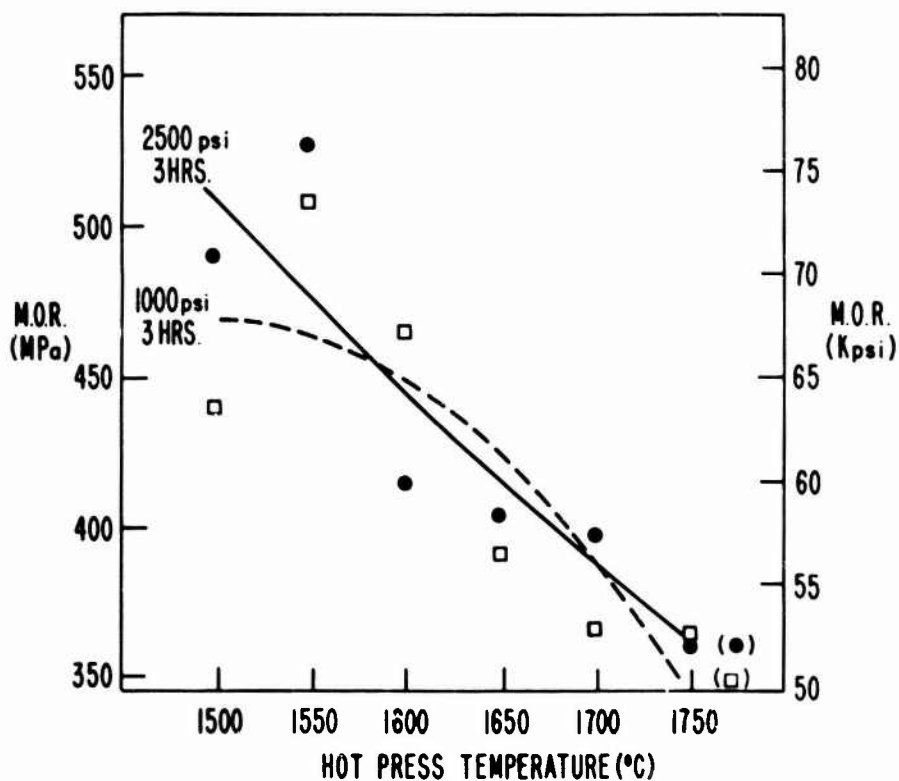Figure 3.2.3-6 — Effect of Hold Time Upon Room
Temperature Strength of HPSN

Figure 3.2.3-7 — Effect of Hot Pressing Temperature
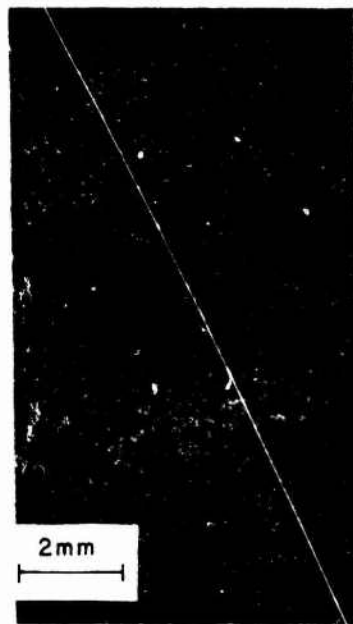Upon 2200°F Strength of HPSN

77

Figure 3.2.3-8 — Microstructure of HPSN Pressed at 1600°C, 1000 psi with a Three Hour Hold Time

Quantitative values were given to this effect by asking several people to assign test sections of each billet, based on its degree of mottling, to one of five groups. Group 1 was not mottled and Group 5 was badly mottled. The average group number resulting from five trials was termed the "appearance factor" for each pressing. This factor correlated well to the 2200°F strength tests but did not correlate to the room temperature tests (Figures 3.2.3-9 and 3.2.3-10). Figures 3.2.3-11 and 3.2.3-12 display the dependence of the 2200°F strength on hold time and pressure during hot pressing. Further work is required to better understand the causes of this mottling even though this study gave insight into the processing requirements for producing high strength hot pressed silicon nitride.
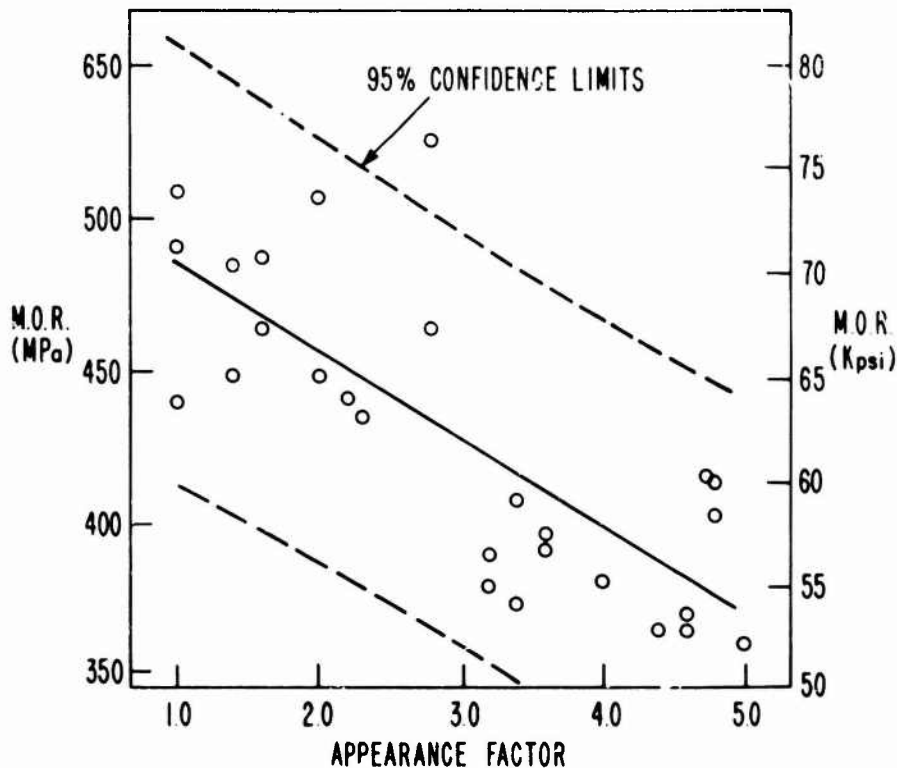

Figure 3.2.3-9 — Relationship Between Appearance Factor and 2200°F Strength of HPSN
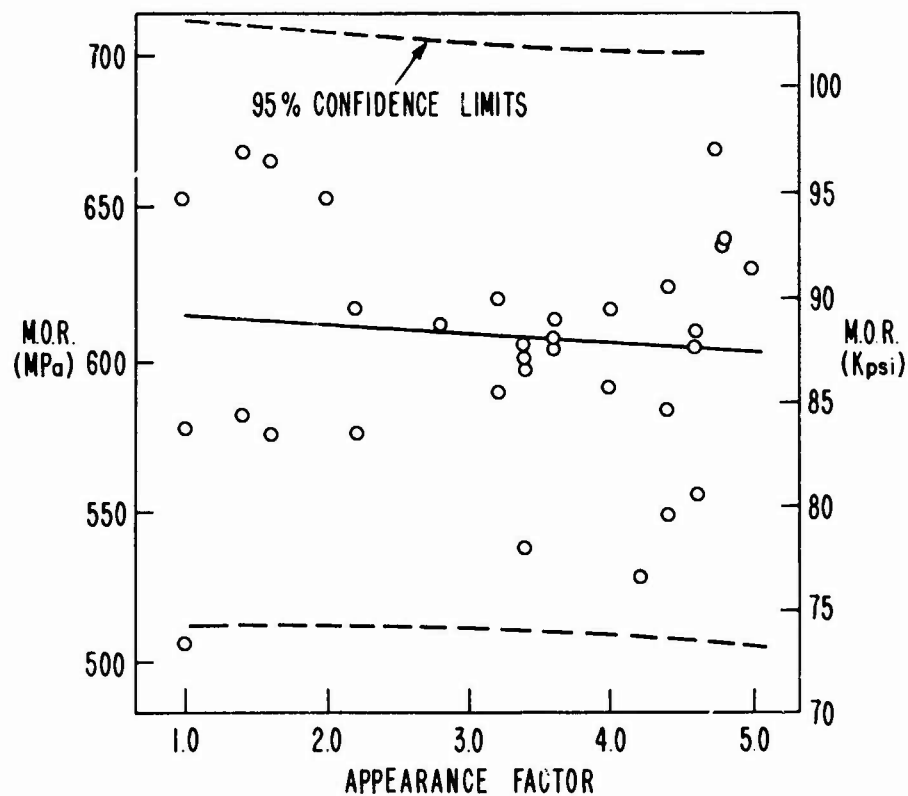
Figure 3.2.3-10 — Relationship Between Appearance Factor and Room Temperature Strength of HPSN
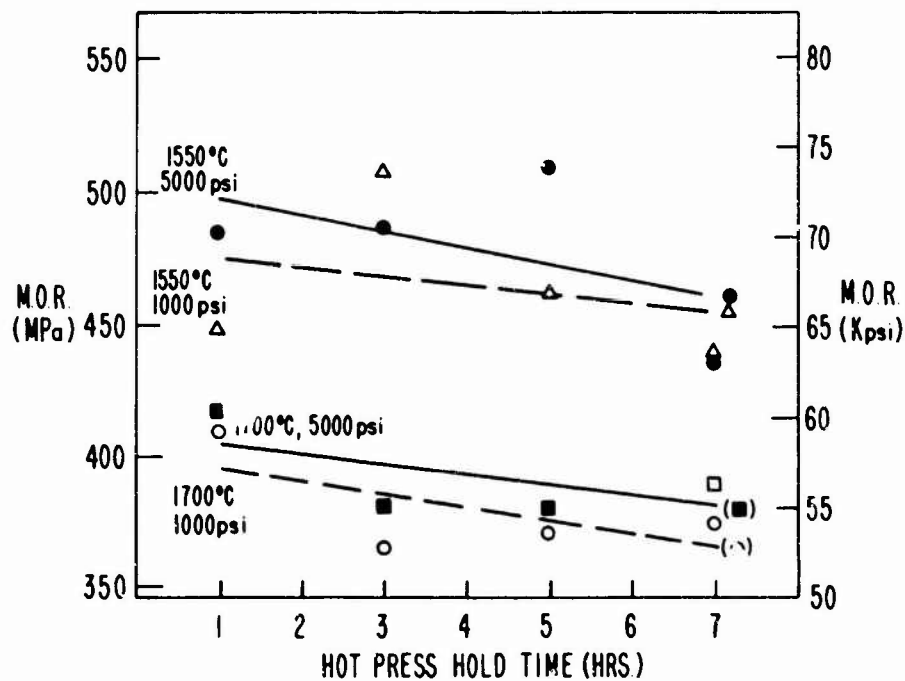

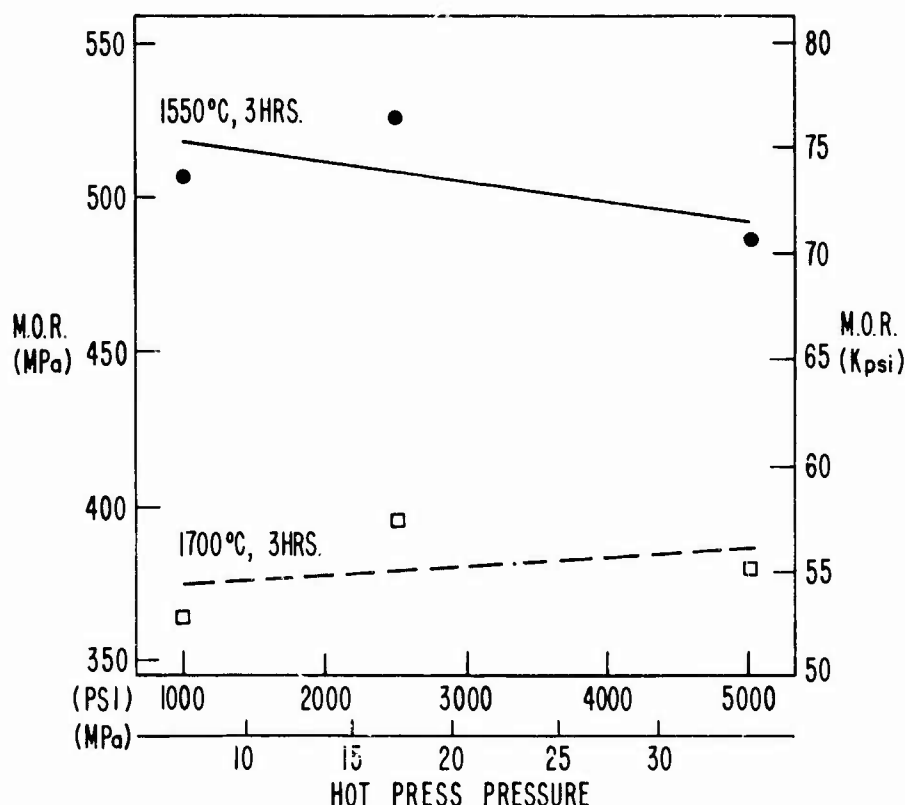Figure 3.2.3-11 — Effect of Hold Time Upon 2200°F. Strength of HPSN

Figure 3.2.3-12 — Effect of Hot Pressing Pressure Upon 2200°F Strength of HPSN

Improved Hot Pressed Silicon Nitride

The study of hot pressing parameters (time, temperature and pressure) demonstrated that silicon nitride could be strengthened through better fabrication techniques, although the grain boundary phase of magnesium silicate remained a limiting factor for strength at elevated temperatures. Consequently, two investigations were initiated to significantly improve the high temperature strength of silicon nitride by increasing the refractoriness of the grain boundary phase: first, by using a silicon nitride starting powder of higher purity; and second, by replacing the magnesium oxide (MgO) additive with other additives to promote densification.

For the first approach, six commercial grade silicon nitride powders, five with a high content of α Si_3N_4 and one that was amorphous, were obtained and analyzed (Table 3.2.3-1).

The weight percent of each major impurity, oxygen (O_2), iron (Fe), aluminum (Al), calcium (Ca) and magnesium (Mg), varied widely between powders. Batches of each powder with 2 wt. % and 5 wt. % MgO additions were milled in methanol with tungsten carbide (WC) balls, dried, broken up and passed through a 100 mesh screen prior to hot pressing. Two hot pressing conditions were used: 5,000 psi held for three hours at 1700°C and 1,000 psi held for three hours at 1700°C. The second set of conditions approximated those used during fabrication of duo-density rotor hubs. After pressing, the 2-5/8 inch diameter disks were removed from the graphite die, sandblasted and measured for density by Archimedes' principle. Test bars were diamond ground from the fully dense disks and tested for strength in four-point bending at both room temperature and 2200°F.

AME CP-85 was the baseline powder since it was in use for fabrication of duo-density rotor hubs. A summary of characteristic strengths at room temperature and 2200°F for each batch is summarized in Table 3.2.3-2. Other than the AME powder, none of the other powders reached high density at 1,000 psi, so no test data was obtained from this group.

TABLE 3.2.3-1

CHEMISTRY OF COMMERCIAL GRADE SILICON NITRIDE POWDER

	AME CP-85B	AME Hi-Purity	Starck	Annawerk	Sylvania SN 402	Sylvania SN 502
α-Si_3N_4*	84.7	~70	93.4	~80	0.5-1	~90
β-Si_3N_4*	14.3	~30	6.6	~20	Amorphous	~10
Si_3N_4O*	0.7	0.5-1	<0.5	0.5-1	0	0
Si(free)*	0.3	0.5-1	0	0.5-1	0	<0.5
O_1*	1.44	1.89	1.10	2.15	2.61	1.64
SiO_1*	0	0	<0.5	0	0	0
Fe**	0.88	0.35	0.02	1.40	<0.01	0.04
Al**	0.63	0.17	0.05	0.15	0.01	0.01
Mg**	0.01	0.01	0.02	0.10	<0.01	<0.01
Ca**	0.20	0.01	0.05	0.20	<0.01	<0.01
Ni**	0.03	<0.01	<0.01	0.02	<0.01	<0.01
Cr**	0.01	<0.01	0.02	0.01	<0.01	<0.01
Ti**	0.08	0.05	0.02	0.05	<0.005	<0.005
B**	0.0005	0.0005	<0.002	0.008	<0.0002	<0.0002
Si**				Base		

*By X-ray Analysis — weight percent
**By Emission Spectrographic Analysis — weight percent

TABLE 3.2.3-2

STRENGTH OF Si_3N_4
HOT PRESSED AT 5000 psi AND 1700°C WITH MgO ADDITIVE

Additive and Test Temperature	AME CP-85B	AME Hi-Purity	Starck	Annawerk	Sylvania SN 402	Sylvania SN 502
Room Temperature					Not tested, material	
Weight % MgO 2	101.7	94.8	88.5	80.6	was only	89.1
Weight % MgO 5	104.1	92.5	81.3	—	95-97% dense.	96.5
2200°F					No test	
Weight % MgO 2	62.7	48.4	44.4	26.6	bars cut.	56.6
Weight % MgO 5	68.0	55.4	44.3	—		39.8

★ Each value represents characteristic strength, Kpsi, based on five test bars.

All the hot pressed powder, with both the 2 and 5 weight percent MgO additions, had good strength at room temperature. The baseline AME CP-85B powder produced the strongest test bars at both room temperature and at 2200°F.

It is significant that powders of higher purity still lost strength at 2200°F; this indicated that this approach probably would not increase material strength at high temperatures. The disk pressed from Annawerk powder with a 2 weight % MgO additive showed a severe strength loss at 2200°F; this was probably due to the high Fe content (1.4%).

In the second approach, the literature was surveyed for likely additives and the following were selected for evaluation: 15 weight % zyttrite (Y$_2$O$_3$ stabilized ZrO$_2$), 5 weight % cerium oxide (CeO$_2$) and 8 weight % yttria (Y$_2$O$_3$). Batches were made for each additive and pressed at 5,000 psi and 1700°C for three hours. The same methods of evaluation were used as for the MgO additive batches. A summary of characteristic strengths at room temperature and 2200°F for each batch is summarized in Table 3.2.3-3.

TABLE 3.2.3-3

STRENGTH OF Si$_3$N$_4$ POWDERS HOT PRESSED WITH VARIOUS ADDITIVES

	AME CP-85B	AME Hi-Purity	Starck	Annawerk	Sylvania SN 402	Sylvania SN 502
Room Temperature					Not tested, due to	
15 Weight % Zyttrite	122.1	86.1	80.5	91.9	previous	66.1
5 Weight % CeO$_2$	118.8	96.2	+	119.6	difficulty in	+
8 Weight % Y$_2$O$_3$	103.6	‡	‡	94.8	producing dense samples	‡
2200°F					with MgO.	
15 Weight % Zyttrite	71.9	68.4	46.4	72.9		66.6
5 Weight % CeO$_2$	67.0	69.8	+	53.4		+
8 Weight % Y$_2$O$_3$	105.7	‡	‡	59.0☆		‡

★ Each value represents characteristic strength, Kpsi, based on five test bars.
☆ This value represents characteristic strength, Kpsi, based on seven test bars.
+ No pressing made.
‡ Material did not reach 99% density.

At both temperatures, the zyttrite additive improved the strength of the test bars more than the MgO additive; however, a strength loss was again observed at 2200°F. The strength results using zyttrite in the Annawerk powder is of particular interest as the loss of strength is much less severe than that observed using MgO. Probably the grain boundary phase formed with zyttrite can contain significant amounts of Fe (1.4%) without serious loss of refractoriness. The CeO$_2$ additive produced only a small improvement in high temperature strength; although the grain boundary phase appeared more tolerant of Fe than that formed by MgO. With the Y$_2$O$_3$ additive, full density was achieved only in the AME CP-85 and Annawerk powder. No strength losses at high temperature were observed in the AME CP-85 test bars. Later tests verified this observation.

In order to evaluate the possibility of forming rotor hubs from these improved materials, AME CP-85 Si$_3$N$_4$ powder was mixed with the various additives and pressed under 1,000 psi at 1700°C for three hours. These conditions were more representative of those used in production of duo-density rotors.

The percent of theoretical density produced with each additive was as follows: 5 weight % CeO$_2$ reached 98.9%; 15 weight % zyttrite reached 95.7%; and 8 weight % Y$_2$O$_3$ reached 91.6%. As each sample failed to reach full density, no test bars were evaluated.

3.2.3.3 Physical Property Characterization

Strength, elastic properties, and thermal expansion were determined for various compositions of hot pressed silicon nitride which were developed and utilized during this program.

The strength of the various materials was discussed earlier in Section 3.2.3.2. Elastic property measurements were performed on two compositions representing the range of densification additive used, namely 2% and 5% MgO. Curves of longitudinal modulus, Young's modulus, and shear modulus vs. temperature are shown in Figure 3.2.3-13 (2% MgO) and Figure 3.2.3-14 (5%, MgO). Measurements were made on Si$_3$N$_4$ test bars by a pulse-echo ultrasonic technique [3]. Young's modulus was calculated from measured values of longitudinal and shear moduli. A modest decrease in the various moduli is evident as MgO content increased from 2% to 5%.
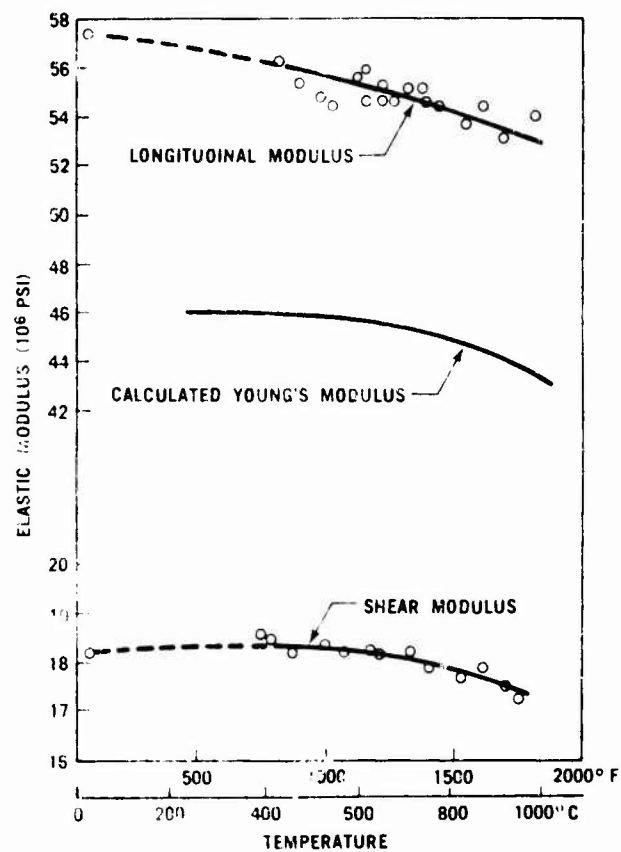
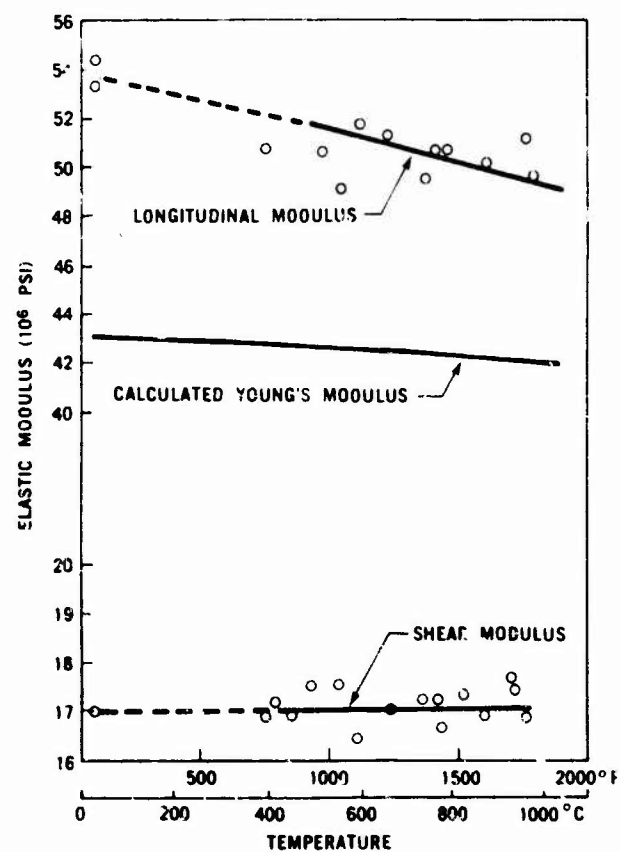Figure 3.2.3-13 — Elastic Moduli of Press Bonded 2% MgO HPSN

Figure 3.2.3-14 — Elastic Moduli of Press Bonded 5% MgO HPSN

Thermal expansion measurements were also performed on hot pressed Si_3N_4 materials of varying MgO content. Measurements were conducted on a differential dilatometer from room temperatures up to 900°C, and are shown in Figure 3.2.3-15. The expansion curve of Norton NC132 hot pressed Si_3N_4 is included as a reference point. This data reveals that increasing MgO content also slightly increases thermal expansion.
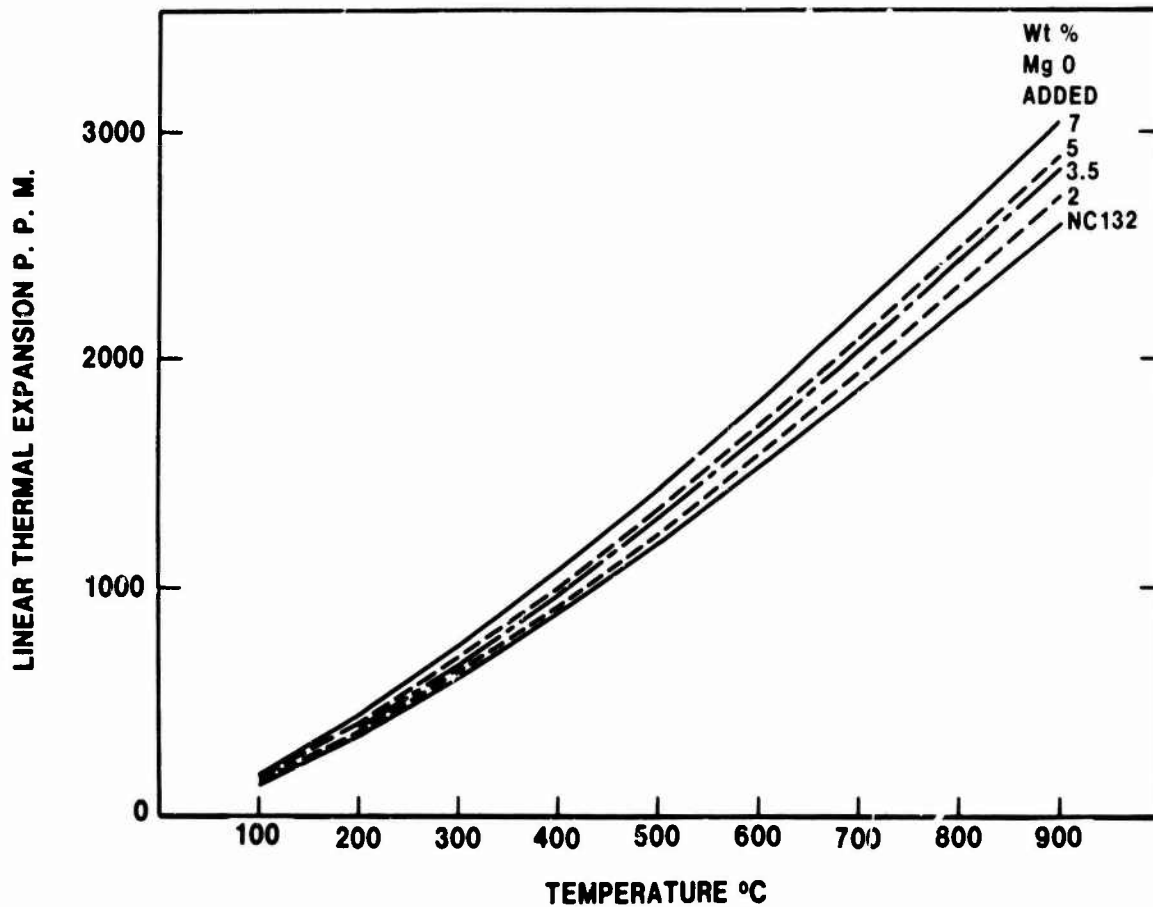
Figure 3.2.3-15 — Thermal Expansion Behavior of Several Grades of HPSN

3.2.4 MOLDED REACTION-BONDED SILICON CARBIDE

Early Work

Prior to this program, a process was developed in-house for molding and reaction sintering silicon carbide (SiC) to form a completely dense body.[64,65,66,67] The process involved the formation of an α-SiC filled, thermosetting plastic which was molded into complex shapes. Subsequent steps included carbonizing the plastic at high temperature in an inert atmosphere to yield a C-SiC composite and siliciding the composite at high temperature in a vacuum or controlled atmosphere to form a fully dense SiC-Si material. The final SiC-Si body had essentially the same dimensions as the initial molded shape within a tolerance of 1%.

At the beginning of this program, strengths of 40 to 50 Kpsi were measured, and numerous plastic-SiC ratios were investigated for improved moldability and microstructures. The moldability of the mixtures was studied by flow in a spiral mold. Several particle size distributions of the SiC filler were evaluated. Mercury porosimetry was used to classify the pore size distribution obtained after carbonization.

It was found that the amount of plastic, the amount of SiC, the SiC particle size and the particle size distribution all influenced the moldability of the mix and the ability to completely silicide thick sections. Close control of the siliciding atmosphere had permitted siliciding sections up to one inch thick.

Complex Turbine Parts

During 1974, about twenty-five stators were molded and the best of these were carbonized and silicided. Several were tested in the 10 light test as described in Section 4.4.3 of this report and in a modified turbine engine. A SiC stator has met the program goals of 175 hours at 1900°F and 25 hours at 2500°F without apparent damage.

In 1976 and 1977, about twenty-five one-piece rotors were formed. Difficulty was encountered in molding the thick hub section without apparent cracks. Holding pressure on the rotor for 10 to 30 minutes after forming improved the cracking situation and produced several rotors which were subsequently carbonized and silicided. Some rotors were destructively evaluated and found to be incompletely silicided in the hub area.

Microstructure and Properties

The microstructure developed is a summation of the starting materials and processing that occurs during the forming and sintering of SiC. For example, if one starts with 600 mesh SiC as the filler material for the thermosetting plastic, and carries out the processing as described above, a typical microstructure as seen in Figure 3.2.4-1 is observed.
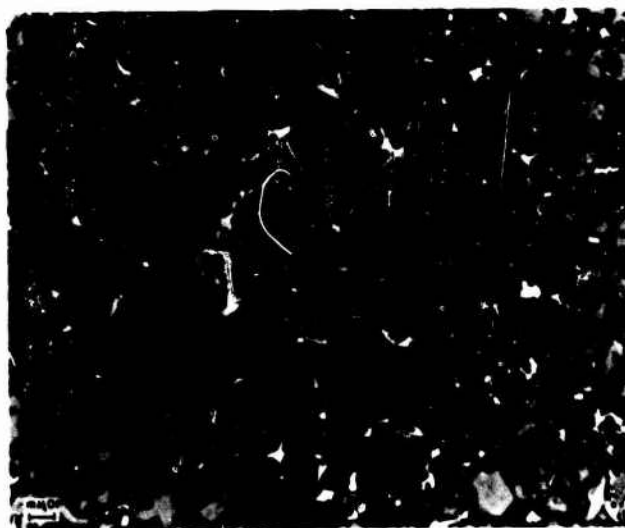

Figure 3.2.4-1 — Microstructures of Reaction Bonded Silicon Carbide

The original α-SiC particles are surrounded by a β-SiC envelope which forms from the reaction of Si and C during this siliciding process. The excess void volume is filled with the silicon phase, in amounts up to 10%, and produces a void-free solid material. Typical room temperature mechanical properties of the material so formed are given in Table 3.2.4-1 for round rods 0.25 inches in diameter tested in four-point bending.

TABLE 3.2.4-1

MECHANICAL PROPERTIES OF α-SiC-Si

Round Rods	Characteristic Strength	
	Kpsi	MPa
As-silicided	49	340
Ground	61	420
Ground and Polished	75	520

Individual strengths as high as 100 Kpsi (689 MPa) have been measured. As seen in Table 3.2.4-1, the strength is influenced by surface preparation. Research has been aimed at improving the strength of both as-silicided and ground materials since practical applications favor as-silicided surfaces for economic considerations. Strength has also been found to be a function of α-SiC particle size, as seen in Figure 3.2.4-2.
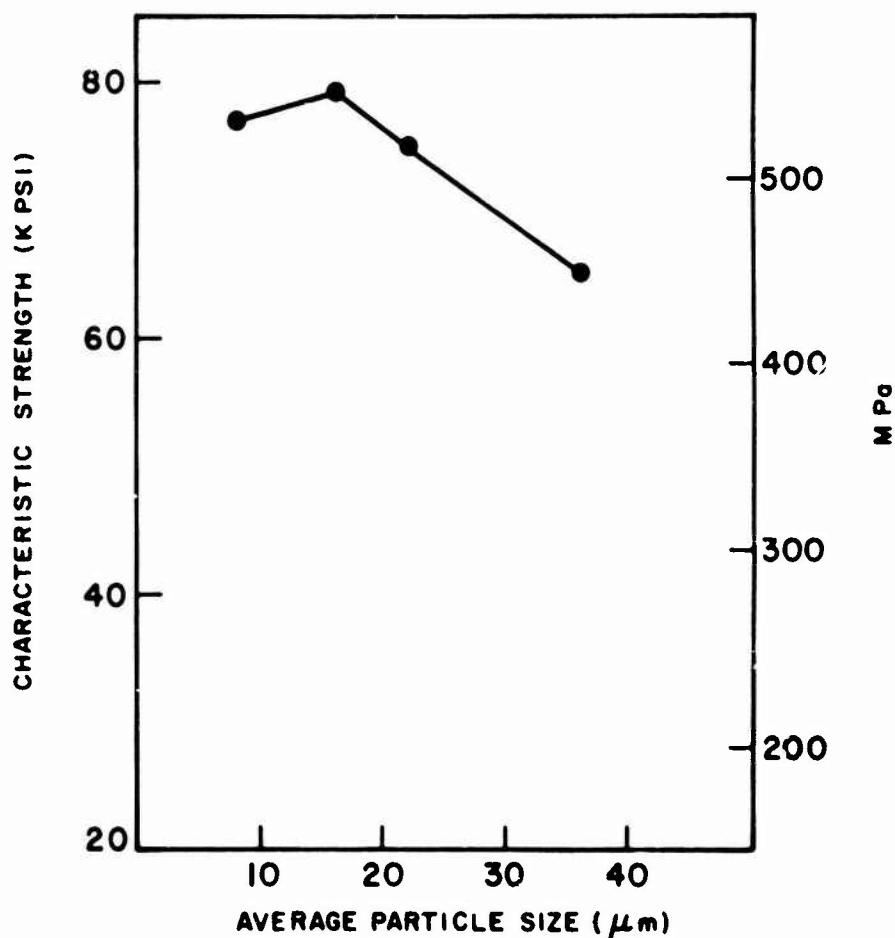

Figure 3.2.4-2 — Flexural Strength of Reaction Bonded Silicon Carbide as a Function of Initial α SiC Particle Size

Material with 16μ average particle size of SiC appears to be optimum at this time, with larger particle sizes yielding weaker materials and smaller particle sizes producing composites difficult to completely silicide.

Attempts to improve the strength of this material by uncanned hot isostatic pressing (HIP) were made and some improvements were measured. Samples which initially were 24 Kpsi in transverse bend strength were improved to 38 Kpsi by a HIP treatment at 1350°C for one hour with 30 Kpsi argon pressure. Another HIP treatment at 1450°C, which is above the melting point of silicon, was attempted. The higher temperature for one hour permitted significant silicon surface evaporation which produced a porous, weak surface. In this case the strength was decreased to 60% of its original value. Under the proper conditions of temperature and time, it may be possible to realize significant improvements in strength and strength consistency by the use of the HIP process.

3.3 TESTING AND EVALUATION

3.3.1 NON-DESTRUCTIVE EVALUATION

3.3.1.1 Introduction

During the decade of the seventies considerable attention was focused on the development of silicon nitride and silicon carbide as engineering materials. They were studied for application in utility, military and automotive turbine engines, and in diesel and Stirling engines. Even though considerable progress was made and actual components tested in turbine engines,[1-13] a key to the success of practical commercial use of ceramic materials is the development of effective non-destructive evaluation techniques for ceramic components.

It is well known that strength of a ceramic is a function of the size and type of flaws in the material; the smaller the flaws, the greater the strength. Many NDE techniques to detect minute Griffith-type inclusions and flaws in simple ceramic specimens (coupon shapes) have been investigated under government sponsorship[68,69]. These included conventional ultrasonics (45 MHz), very high frequency ultrasonics (250 MHz), neutron radiography, microfocus X-ray, image enhancement, microwaves, thermography, dye penetrants and photo-acoustic spectroscopy. Since this program was concerned with NDE of turbine components, some of these techniques were not sufficiently advanced for application to complex shapes within the program time frame.

Furthermore, experience with such complex shaped components has shown that first order quality problems resulted, not from Griffith-type flaws, but from relatively gross fabrication process flaws. Accordingly, the approach adopted was to seek NDE techniques which could detect gross fabrication flaws in a complex part. Without the presence of gross fabrication flaws, it was assumed that the size and distribution of Griffith-type flaws in a component was the same as in test specimens. Since the reliability of a component is predicted from test specimen data and probabilistic design techniques, eliminating components having gross fabrication flaws through NDE is essential to the attainment of predicted reliability.

A successful NDE technique for ceramic components should, therefore, meet two major criteria. It should have the capability to: 1) detect gross fabrication flaws to ensure that the material quality of the component is equal to that of the test specimens used to determine property data for design; and, 2) evaluate the quality of a complex shaped component in a practical manner.

Many NDE techniques were investigated during the course of this program. These spanned significant development efforts in some cases, notably ultrasonics and X-ray radiography, plus monitoring or evaluating NDE programs underway elsewhere. In assessing the latter, judgements were made mostly on the practicality and potential of the particular technique for locating relatively gross fabrication flaws in complex parts such as the duo-density Si_3N_4 rotor.

3.3.1.2 Radiography [1-13]

Radiography, in particular X-ray radiography, was found useful for the detection of gross flaws in molded gas turbine components[6,7] and other components of complex geometry. This NDE inspection technique also filled an important gap in the inspection of materials with high porosity. For example, defects in reaction bonded silicon nitride were difficult to detect using techniques such as ultrasonics because of impedance problems associated with porosity.[2]

An important tool used in the development of radiographic processes was the step block configuration, Figure 3.3.1-1. This configuration was used to optimize radiographic processes for the detection of flaws in the duo-density rotor. The step block was also used to evaluate both X-ray and xeroradiography where it was revealed that xeroradiography permitted a wider range of material thickness to be imaged than X-ray radiography.[4]

X-ray exposure parameters were established for HPSN. These parameters are shown in Table 3.3.1-1 for various material thicknesses. The sensitivity levels for several types of defects were also determined, and are illustrated in Table 3.3.1-2.
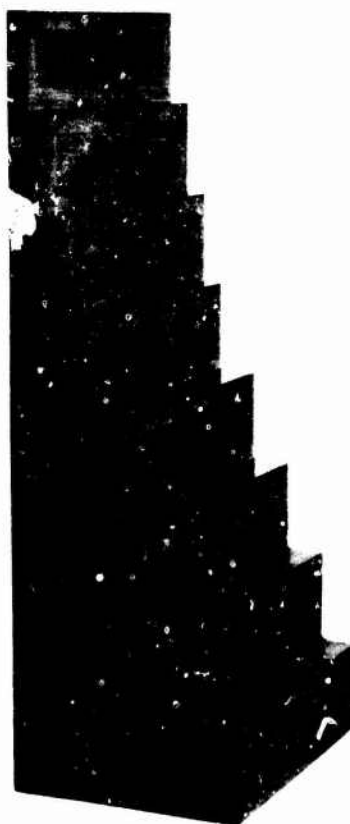
Figure 3.3.1-1 — Hot Pressed Silicon Nitride Radiographic Step Block Standard

Table 3.3.1-1

X-RAY EXPOSURE PARAMETERS FOR HOT-PRESSED Si_3N_4

Material Thickness mm	Exposure Time Minutes	Current mA	Voltage KV	Source To Film Distance cm	Film	Remarks
3	3.0	10	40	60	M	
6	6.0	10	40	60	M	
12	5.0	10	60	60	M	
14	6.0	10	60	60	M	
16	7.0	10	60	60	M	
27	2.5	10	100	60	M	
30	3.5	10	100	60	M	
1.5-3	3.0	10	40	60	ML*	Vacuum
3-10	5.0	10	60	60	ML	Vacuum
12-23	4.0	10	70	60	ML	Vacuum
12-26	4.0	10	84	60	ML	Vacuum
16-27	5.0	10	70	60	ML	Vacuum
16-24	5.0	10	84	60	ML	Vacuum

*Kodak type M-8 lead-pack film.

Table 3.3.1-2

DETECTION OF DEFECTS BY X-RADIOGRAPHY
(60-100 kV, 10 mA, 60 in. SOURCE DISTANCE)

Sensitivity

BN Filled Cavity	0.04 in.
Crack, Hole	0.03 in.
Steel Particle	0.007 in.
WC Particle	0.005 in.

Conventional X-ray radiography was an important in-process screening technique used in the molding of silicon nitride gas turbine stators and duo-density blade rings.[5,6,7] Gross flaws such as shrink cracks, voids, and high density inclusions were readily detected at the molding stage thus preventing further costly processing of the part. As such, X-ray radiography was used as one of the techniques to optimize molding parameters as development of higher density RBSN proceeded.

The most useful X-ray equipment utilized in this program was the Magnaflux Microfocus X-ray apparatus, Figures 3.3.1-2 and 3.3.1-3. This equipment was advantageous over conventional X-ray because its small focal spot of 0.05 millimeters permitted, 1) film focal distance of 3 inches, 2) direct magnification up to 36X, and 3) fine resolution and geometric sharpness. The resolution of this equipment can be seen in Figure 3.3.1-4 which illustrates a 1/8 inch RBSN coupon with a 2T hole size of 0.010 inches.
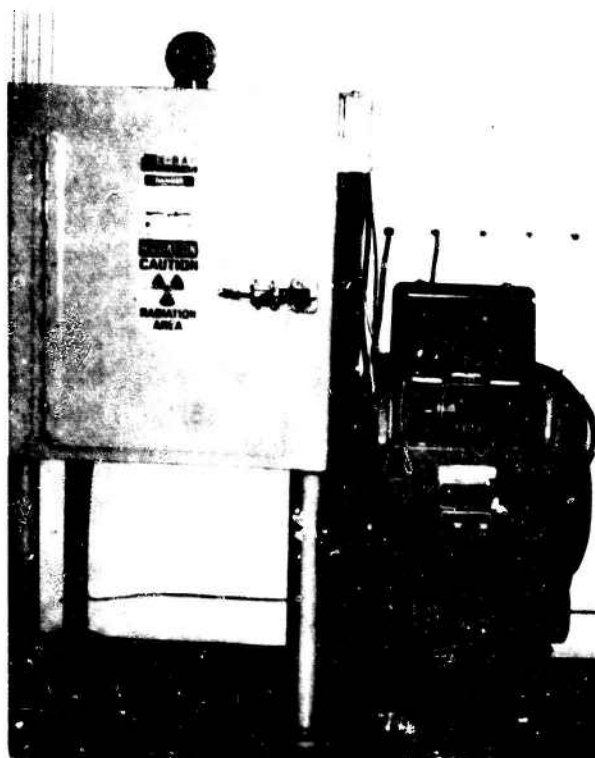
Figure 3.3.1-2 — Microfocus X-Ray Equipment

Figure 3.3.1-3 — Microfocus X-Ray Tube and Molded Blade Ring Positioned for Oblique Radiograph

4T (0.020")

2T (0.010")

8T (0.040")
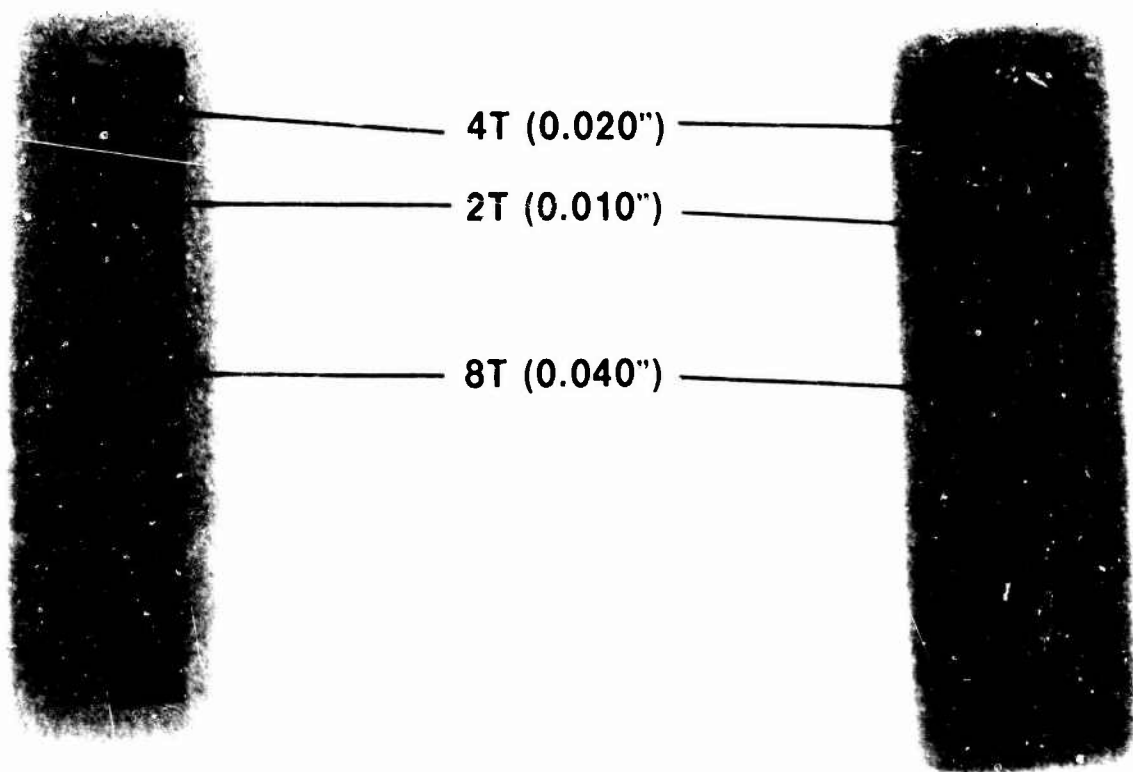
Figure 3.3.1-4 — Microfocus X-Ray of One-Eighth Inch Silicon Nitride Penetrameter

Techniques were also developed to make panoramic radiographs of circular components. Figure 3.3.1-5 is a close-up view of the panoramic tube head used, and Figure 3.3.1-6 shows the fixture design for obtaining panoramic radiographs.
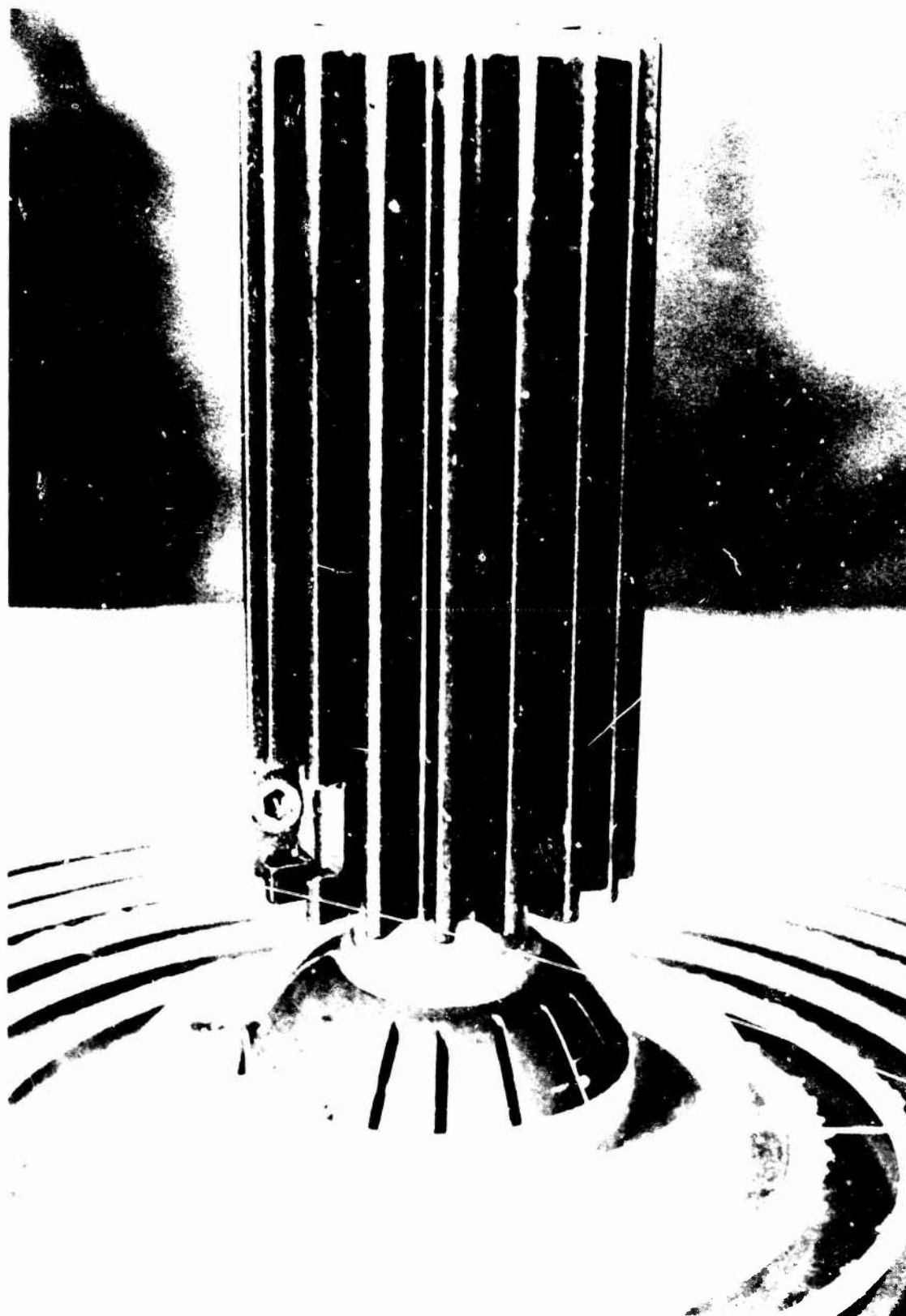

Figure 3.3.1-5 — Close-up View of Panoramic Microfocus X-Ray Tube Head
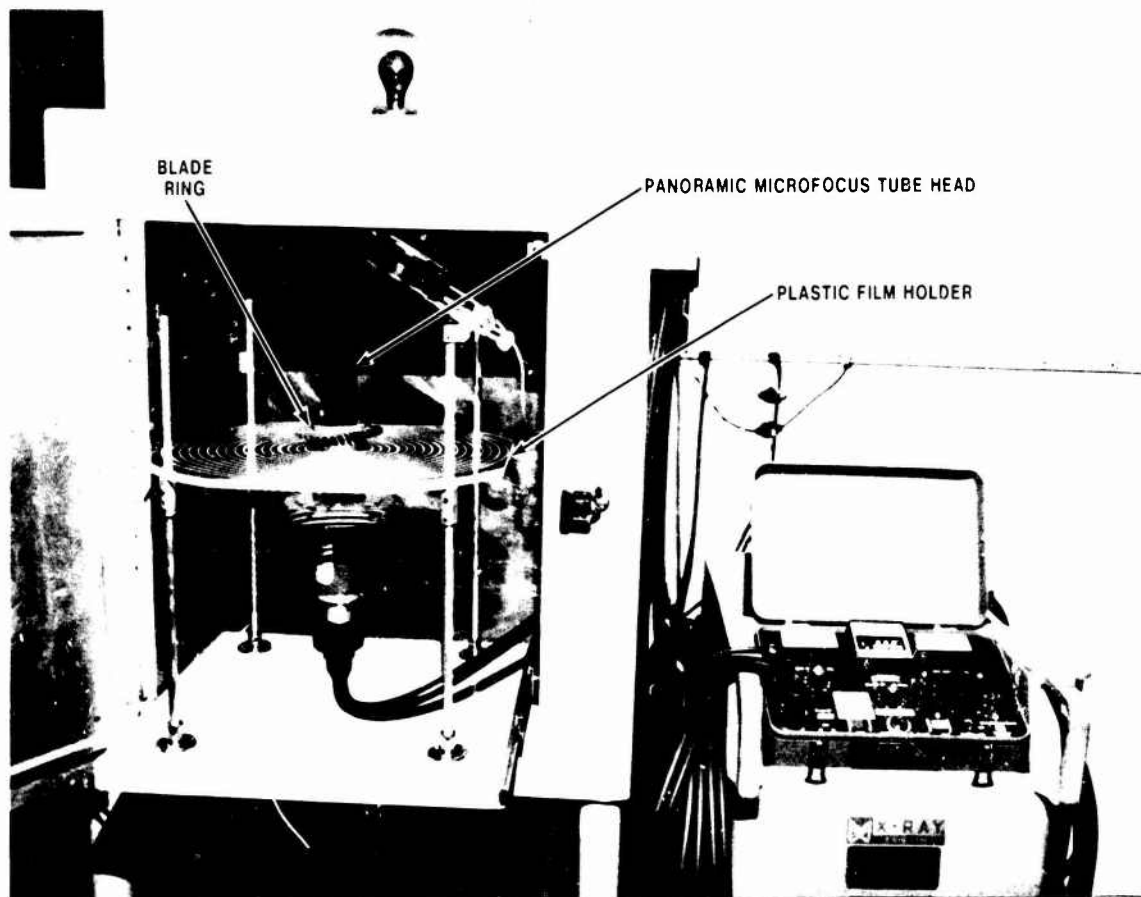
Figure 3.3.1-6 — Panoramic Microfocus Equipment and Fixture for Radial X-Ray

Summarizing radiography developments during this program, it has been established that X-ray is suitable for, 1) complex components, 2) void or cavity type defects 250 microns and larger, and 3) for components in the as-molded state.

3.3.1.3 Dye Penetrants[6,8]

Dye penetrants were found to be one of the more useful NDE tools for detecting flaws in complex shaped ceramic components. Zyglo penetrants were effective for high density nitrides and carbides, while a mixture of graphite and oil was found to be effective for gross flaw identification in white lithium aluminum silicate (LAS) ceramics.

Dye penetrants, however, were not found suitable for the porous ceramics such as RBSN. In these cases the open porosity of the material would retain the penetrant ca ing a "bleeding" action resulting in masking of the defect.

Whereas dye penetrants were found extremely useful for complex shapes, this method of NDE was restricted to surface flaw identification. Other disadvantages are limited sensitivity (approximately 125 microns) and the limitations associated with high volume and high speed examination of components.

3.3.1.4 Visual Inspection

Visual inspection using a microscope at low power magnifications (5X-30X) was used extensively for the identification of surface defects in complex shapes. This method of inspection is actually an integral part of dye penetrant inspection, but because of its suitability for defect identification in RBSN, visual inspection will be treated separately in this report.

93

It was pointed out previously that dye penetrants were unsuitable for RBSN due to porosity. A significant characteristic of flaws present in RBSN before nitriding is the secondary silicon nitride phase formation at the defect site. This secondary phase exhibits itself as a fibrous white material contrasted on the greyish background of RBSN, Figure 3.3.1-7. The flaw in Figure 3.3.1-7 has been designated as a planar flaw, and is one of the more difficult defects to detect in RBSN. Visual inspection had widespread usage in this program in the identification of these flaws if surface connected in RBSN stators, nose cones, blade rings, and other structural components. An adjunct and valuable addition to the visual inspection procedure was the use of the Circon Video System, Figure 3.3.1-8. This equipment with magnification capability of 20-200X permitted simultaneous inspection of a complex part by several people. The equipment consists of a TV camera, screen, and optical system. Fiber optics was the source of lighting. One very important aspect of this equipment was the reduction in inspector fatigue normally associated with visual inspection.

Visual inspection including use of the above is limited to surface defect detection, and to flaw identification greater than about ___ micron. In addition operator fatigue is normally an important, though somewhat intangible, factor affecting the thoroughness of results.

3.3.1.5   Ultrasonics[1-6]

Ultrasonic NDE was investigated as a technique with potential sensitivity to detecting subsurface flaws in ceramic polycrystalline materials. Cseveral techniques were developed for the detection of defects in LAS, HPSN, and RBSN (Retolt Magnaflux equipment with a frequency range of 0.5-15 MHz, Figure 3.3.1-9, was used for this work.

Figure 3.3.1-7 — Planar Type Defect Detected by Visual Inspection (37x)

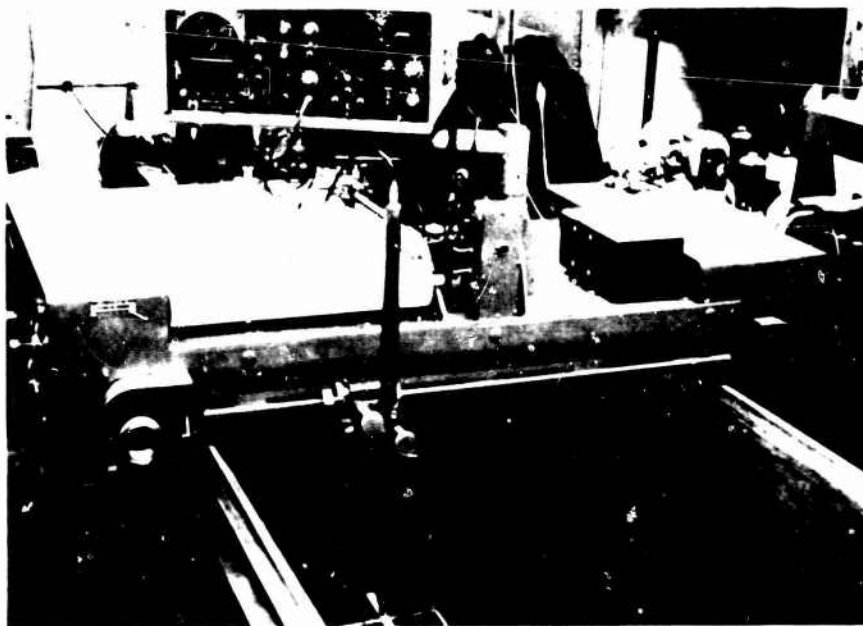Figure 3.3.1-8 — Circon Video Visual Inspection Equipment

Figure 3.3.1-9 — Ultrasonic Defect Detection System

Defects 60 microns in size[6], 5-60mm below the surface in HPSN, were detected using conventional ultrasonic procedures. In lower density materials, such as LAS, resolution was decreased.

An improved technique, computer-aided ultrasonics, was also investigated.[4,5,6] The results of this work revealed improved resolution over conventional ultrasonics.

Techniques[1,2] were developed to measure sonic velocities in both a longitudinal and transverse mode. These measurements were used to calculate dynamic modulus of elasticity. A secondary method for measuring sonic velocity was also developed.[3] This method introduces an elastic wave by electronic pulsation of the test specimen.

Relationships between sonic velocity of RBSN and density were established[7] (Figure 3.3.1-10). Density gradients were detected in LAS samples,[2] and material inhomogeneity was observed through sonic velocity gradients. It appeared that longitudinal velocity data, rather than dynamic modulus of elasticity data, was more useful in determining the level of material inhomogeneity.
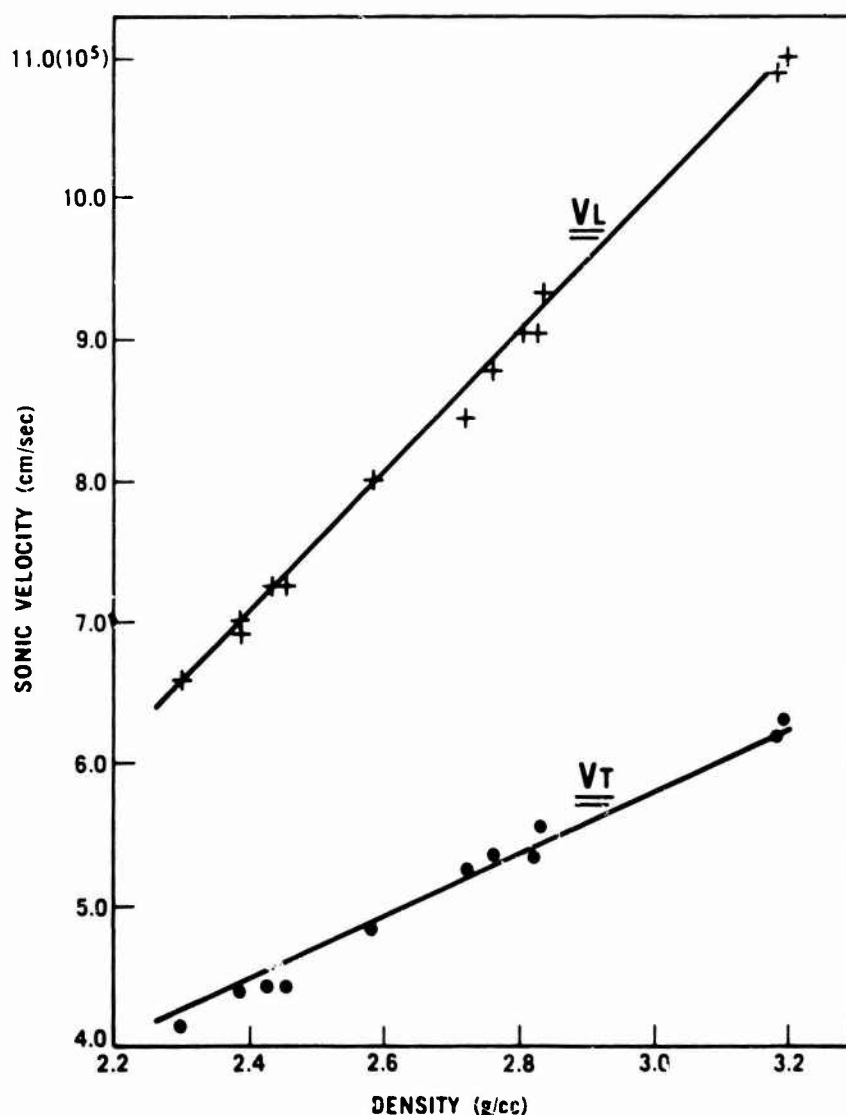
Figure 3.3.1-10 — Longitudinal (V$_L$) and Transverse (V$_T$) Sonic Velocity Vs. Density for Silicon Nitride

In summary, it was found that ultrasonic NDE was superior to other techniques in terms of resolution limits — approaching 25 microns. The technique, however, was mostly useful for simple shapes and low porosity materials. Considerable development effort would be required to develop transducer coupling techniques for a complex shape such as an airfoil.

3.3.1.6 Acoustic Emission

The effect of mechanical and thermal stress on the acoustic emissions (AE) of HPSN, RBSN, and LAS ceramics was studied.

Figure 3.3.1-11 shows the AE versus time response of prestressed LAS. This curve demonstrates the well-known Kaiser effect (defined as a lack of AE until a previous stress level is exceeded). Figure 3.3.1-11 also shows the AE response-to-stress signature as a precursor to failure. This suggests the use of AE as a proof testing technique to determine subcritical and critical crack growth.

10,000 —

≈ 1800 LBS.
FAILURE
(PRESTRESSED TO 1600 LBS.)

E SUM (1mv/IN.)

≈ 1600 LBS.

≈ 1400 LBS.

0

TIME (5 SEC./IN.)
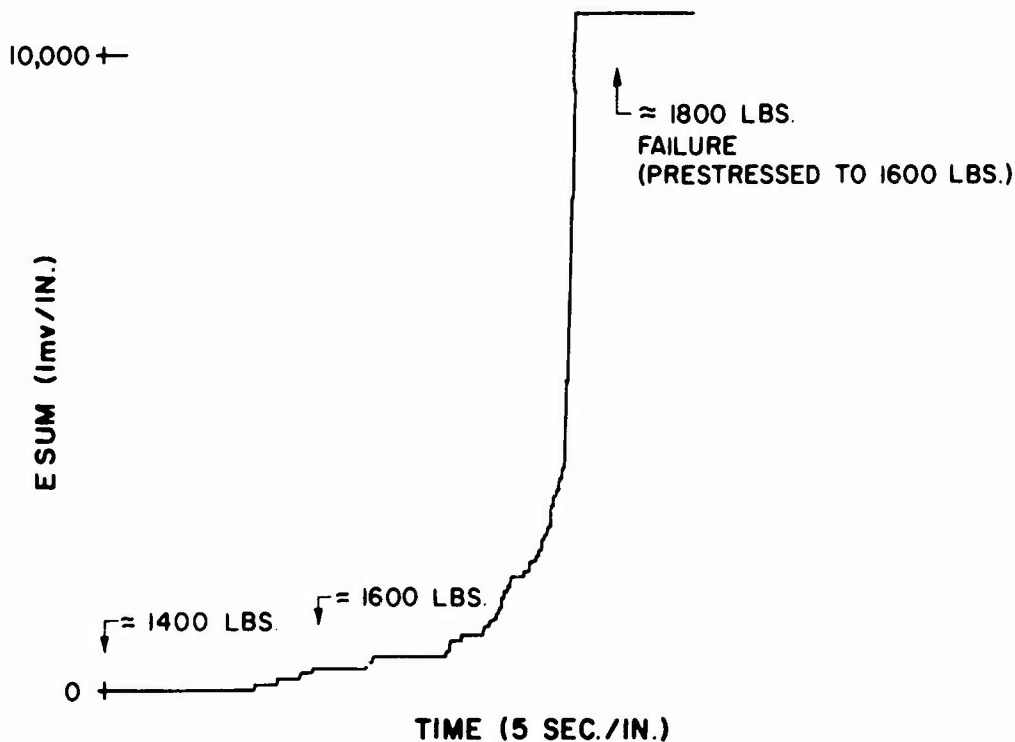
Figure 3.3.1-11 — Acoustic Emission Summation Vs. Time for Prestressed (to 1600 Pounds) Corning 9453 Lithium Aluminum Silicate

AE was also used to measure the effect of laser induced flaws in HPSN.[4] Relationships between MOR and AE were established for test samples with induced flaws.

The application of AE as a quality check of duo-density rotors and stators was investigated. [5,6] Figure 3.3.1-12 is a typical AE response of a low density RBSN second stage stator thermally damaged while subjected to an oxidation test. These data suggest the potential of AE as material quality checks and design selection.

Summarizing this work, it appears that the use of AE as an NDE tool has potential as a simple in-process screening technique. AE, however, was not reduced to practice mainly because of fixture-noise problems (when mechanical load testing), and wave guide — component interface noises (when thermal loading).

3.3.1.7 Other NDE Techniques

A number of other NDE techniques were studied during this program from the standpoint of monitoring outside program status or limited feasibility investigation. These techniques were Electrostatic, Electromagnetic, Holosonics, High Frequency Ultrasonics and Infrared Thermography.[11,12,13] In general, these techniques were not pursued in this program because they were receiving focused support in other programs and because of their long development time and expense for application to complex parts.
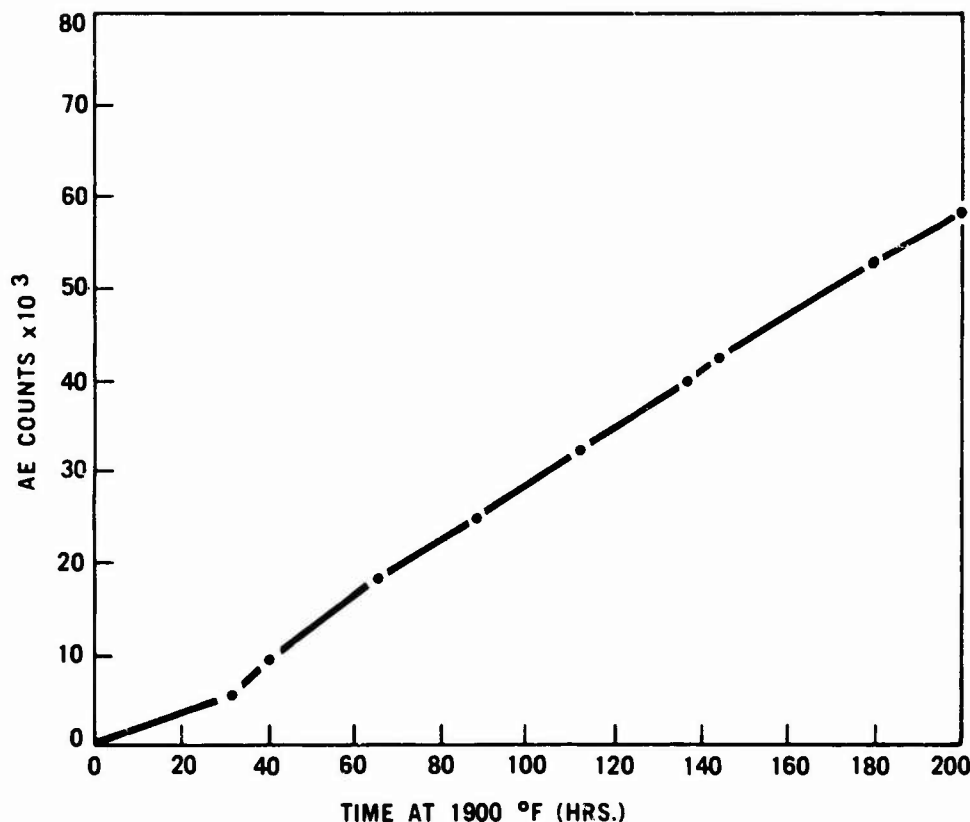
Figure 3.3.1-12 — Acoustic Emission Vs. Time for Severely Oxidized RBSN Stator (No Load)

3.3.1.8 NDE Techniques Selected for Use in This Program

For practical use in evaluating ceramic turbine components, selection of an NDE technique has generally been based on the following factors:

- size and type of flaw to be sought
- complexity of the component to be examined
- required examination time
- development time
- development cost

Perhaps the greatest limitation of most of the NDE techniques previously described is the difficulty of examining complex parts such as a duo-density rotor in a relatively timely and inexpensive manner. The more useful NDE techniques were, therefore, visual examination with a microscope, X-ray radiography and dye penetrants.

This selection was also made due to the occurrence of two specific types of gross flaws found in molded reaction-bonded silicon nitride; molding flaws and planar flaws. By comparison, other flaws, such as small inclusions, were not of immediate concern.

Visual Examination

Visual examination was the most widely used NDE technique. It was employed at seven process stages in the fabrication of duo-density rotors, for example. It was adaptable to most part shapes and was the only known method of detecting planar flaws on the airfoil of a rotor. Use of the micro-video imaging system greatly enhanced visual inspection by minimizing operator fatigue.

X-ray Radiography

X-ray radiography, using both conventional industrial and Magnaflux Microfocus X-ray equipment, was used primarily for inspecting molded components. This technique can detect molding flaws and cracks in the rim/disk area of rotor rings.

Sometimes flaws occur directly under blades in the rim of the blade ring. A Microfocus panoramic X-ray tube was used to develop techniques to assess quality in this area.[13] This tube enabled inspection of the entire rim circumference in one radial view. This Microfocus X-ray also enabled magnification to 36 X with a variable focal (50-500μ) tube.

Dye Penetrants

Dye penetrants were usually unsuitable for reaction-bonded silicon nitride; they were valuable for hot pressed materials where minimum porosity is present and dye bleeding from the pores does not mask flaws. They were particularly suitable for assessing the bond quality between reaction sintered and hot pressed silicon nitrides in duo-density rotors.

3.3.1.9 Future NDE Needs and Recommendations

Of the NDE techniques evaluated, ultrasonics was judged to have the greatest potential for detecting minimum size flaws. Several research projects demonstrated that ultrasonics could detect flaws as small as 25μ. However, ultrasonics is limited for the evaluation of complex shapes. A simple means of rapidly attaching or coupling the transducers to complex shapes is needed; future NDE funding should be directed to this specific end.

Of the gross fabrication flaws, the planar type in molded reaction-bonded silicon nitride blades was shown to be the most difficult to detect. Although visual inspection could sometimes detect this flaw in complex parts such as rotor blades, most of these passed undetected until later. This was true for both surface and subsurface planar flaws. An NDE technique recommended for future development which may resolve this problem and generally provide an inspection method for complex shapes is X-ray tomagraphy.

3.3.2 TESTING TECHNOLOGY

General purpose testing technology as applied to both materials and components was developed during the program. This technology, although developed specifically for a vehicular gas turbine, is applicable to other structural ceramic applications. This section of the report discusses evaluation methods, MOR Testing Technology and Ceramic Component Test Rigs.

3.3.2.1 Evaluation Methods

In the evaluation of the results of material property determination and component testing, the basis of strength and reliability analyses used to predict the probability of failure in ceramics was Weibull's statistical flaw theory and probability distribution[15,21] discussed in Section 3.1 of this report. Additionally, other statistical tools were developed for use with reliability prediction methods and in the analysis of experimental data.

Extensive literature surveys and Monte Carlo investigations resulted in selecting the maximum-likelihood method for estimating the parameters of the two-parameter Weibull distribution. This method provides the desirable properties for estimations which are exact for small sample sizes and yields a basis for hypothesis testing. A user-oriented timesharing computer program was developed.[13]

A second user-oriented timesharing computer program was developed to conduct an hypothesis test based on the Weibull distribution.[13] This program determines if a statistically significant difference exists between two Weibull distributions based on samples of the same size. This procedure may be used to monitor development of materials or components and to establish the presence of correlations between predicted and measured reliabilities.

A number of analytical techniques were employed during the course of the program for ceramic material evaluation. The microstructure, chemical and phase composition of ceramic materials were studied utilizing a variety of techniques including:

- optical microscopy with normal and polarized light
- scanning electron microscopy with nondispersive X-ray analysis
- transmission electron microscopy
- emission spectroscopy for chemical analysis
- neutron activation analysis for oxygen content
- quantitative X-ray diffraction for phase analysis

3.3.2.2 MOR Testing Technology

The development of materials and processes, in the early stages of this program, was on a steep learning curve. During this time, different size Modulus of Rupture (MOR) test bars and test fixtures were used which were tailored to satisfy the individual requirements of the particular material and/or process being developed.

Approximately mid-way through the program, the Army Materials and Mechanics Research Center proposed a "Military Standard for Test Methods for Structural Ceramics", which defined an 'A' size test bar as 1/8 x 1/4 x 1 inches loaded in four-point bending (3/8 top span, 3/4 bottom span). This standard was used throughout the remainder of the program. The test fixture utilized is shown in Figure 3.3.2-1. Room temperature MOR testing was conducted using heat-treated tool steel fixtures while elevated temperature testing required fixtures made of hot pressed silicon carbide. The cross-head speed for both room and elevated temperature evaluation of fast fracture strength was 0.020 inches/minute.
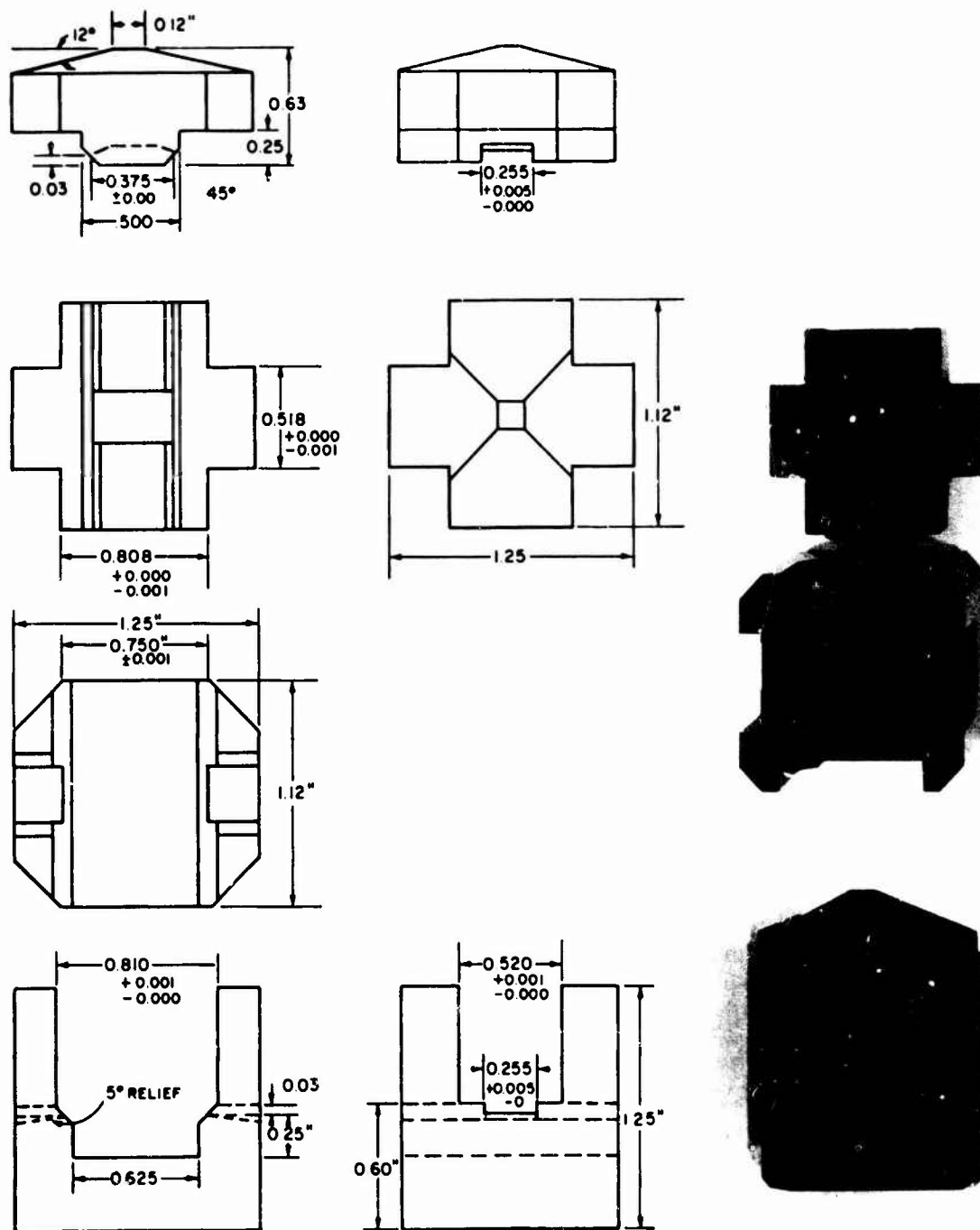
Figure 3.3.2-1 — Details of Self-Aligning Ceramic Fixture Used for MOR Testing

During the course of the program, some advantages and disadvantages of different shape MOR bars were evaluated as follows:

ROUND TEST BARS

Advantages	Disadvantages
• machined round bars eliminated edge chipping and associated edge failures particularly prevalent in silicon carbide	• as-cast or as-molded bars required locating "flash" line at neutral axis when testing
	• higher Hertzian contact stress
• eliminated extraneous stresses due to torsion effects on twisted bars	• lower volume of material subjected to peak bending stresses

RECTANGULAR OR SQUARE TEST BARS

Advantages	Disadvantages
• easy to locate "flash" line of as-cast or as-molded bars at neutral axis or in compression region	• more difficult to machine, edge chamfers/radii must be ground in longitudinal direction
• lower Hertzian contact stress	• extraneous stresses due to torsion effects on twisted bars or fixtures increases apparent scatter and decreases apparent strength of specimens
• higher volume of material subjected to peak bending stresses	

The higher Hertzian contact stresses in round versus rectangular test bars can be alleviated by: (1) increasing the radius of the knife edges in the test fixture, (2) increasing the test bar length and test span, or (3) utilizing three-point versus four-point bending.

The extraneous stresses due to torsion effects on twisted rectangular or square bars can be alleviated by: (1) diamond grinding the surfaces flat and parallel, or (2) utilizing test fixtures which float the loading points.

3.3.2.3 Ceramic Component Test Rigs

Testing of ceramic components played a major role in the program by providing feedback to the design, analysis, material and process development activities. As described in Section 2.4, Testing & Evaluation Approach, many test rigs were developed which would evaluate ceramic components, first individually and then in sets, by subjecting them to the various types of loading in separate tests. Table 3.3.2-1 shows the rigs utilized in evaluating the various ceramic components subjected to various types of loading. Generally, the more complex types of loading required more complex rigs and considerable effort was expended to devise simpler tests and rigs which would preserve the fracture surfaces intact to aid in failure analysis and corrective action in the fabrication and/or design processes.

TABLE 3.3.2-1

CERAMIC COMPONENT TEST RIGS

| | Ceramic Components Evaluated | | | | Types of Loading | | | | |
Test Rig	Combustor	Nose Cone & Shrouds	Rotor(s)	Stator(s)	Mechanical	Thermal Shock	Thermal Steady-State	Aero-dynamic	Vibratory
Stator Vane Bend				X	X				
Rotor Blade Bend			X		X				
Stator Outer Shroud Pressure				X	X				
Cold Spin			X		X				
Thermal Shock			X	X		X	X		
Rotor Disk Thermal Stress			X				X		
Combustor	X				X	X	X		
Light-Off Qualification	X	X		X	X	X	X	X	
Ceramic Structures	X	X		X	X		X	X	
2500°F Flowpath	X	X		X	X		X	X	
Hot Spin			X		X		X		
Turbine Rotor	X	X	X	X	X		X	X	X
Modified Engine	X	X	X	X	X	X	X	X	X

Rotor Blade and Stator Vane Bend Testing

The primary purpose for developing the rotor blade and stator vane bend tests was to monitor the effects of processing improvements and provide timely feedback to the fabrication efforts. However, a variety of other goals were accomplished which:

- provided the capability to correlate the analytical stress analysis model with strain gauged test results

- determined the existence of and quantified the effects of surface and subsurface flaws and determined the potential gain for unflawed components

- evaluated component strength at various stages in the fabrication process thereby identifying processing steps that affect component quality

- evaluated processing changes on component strength

- determined effects of thermal shocking and/or oxidation on component strength

- provided a means for proof testing of as-fabricated components prior to expensive and time-consuming machining and testing

- generally preserved fracture surfaces intact to allow complete fractographic analysis to pinpoint fracture origin and cause

The rotor blade bend test fixture[9,10,11], shown in Figure 3.3.2-2, subjected the airfoils to nearly pure bending with an inherent trace of torsion present due to the twisted geometry of the blade. The direction of loading shown in Figure 3.3.2-2 produced compressive stresses in the leading and trailing edges and tensile stresses at the back or convex side of the airfoil. Reversing the direction of the load produced tension at the leading and trailing edges and compression at the back. The maximum stresses for either load direction occurred at the base of the airfoils adjacent to the platform. The test fixture was designed such that both blade rings and duo-density turbine rotors in various stages of processing could be evaluated on the same equipment.

The stator vane load test [8,11,12] is shown in Figure 3.3.2-3. The leading and trailing edges and the back of the vanes were subjected to either tensile or compressive stresses depending on whether the front or back side of the inner shroud was employed as the load surface. In either case, the maximum stresses were produced at the vane root adjacent to the outer shroud. Initially, only destructive tests were conducted to evaluate fabrication processes. Later, stator vanes were proof tested prior to machining but this was time consuming as each of the 25 vanes had to be loaded individually, first from the front and then from the back. Accordingly, the test fixture shown in Figure 3.3.2-4 was designed and built. Each of the 25 vanes were simultaneously loaded by 25 independent hydraulically loaded pins thereby reducing the proof test time by a factor of 25.

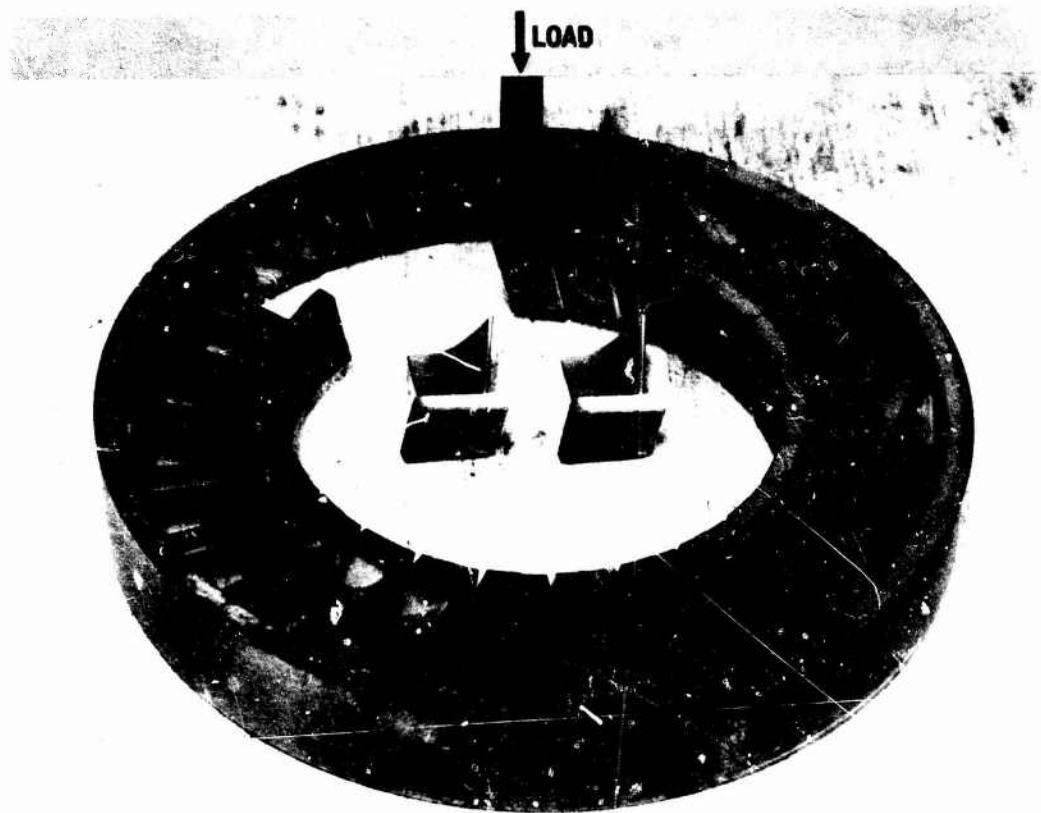Figure 3.3.2-2 — Rotor Blade Bend Test

Figure 3.3.2-3 — Stator Vane Bend Tend

Figure 3.3.2-4 — Stator Vane Bend Mechanical Test Fixture

Stator Outer Shroud Pressure Test

The stator outer shroud pressure test was developed primarily to screen stators for defects in the outer shroud prior to engine or rig testing.[11,12] The test fixture, shown in Figure 3.3.2-5, subjected the outer shroud to a tensile tangential stress by applying an internal hydraulic pressure. The stators were tested in the finish ground condition to include any detrimental effects due to surface finish or chipping. As shown, the stator was trapped between two flat plates and sealed at the shroud inside diameter with thin, flexible rubber lip seals. The stress level in the outer shroud was controlled by a pressure control valve on the hydraulic supply line and monitored by a gage reading internal pressure in the sealed cavity. Test results are presented in Section 4.4.3 of this report.
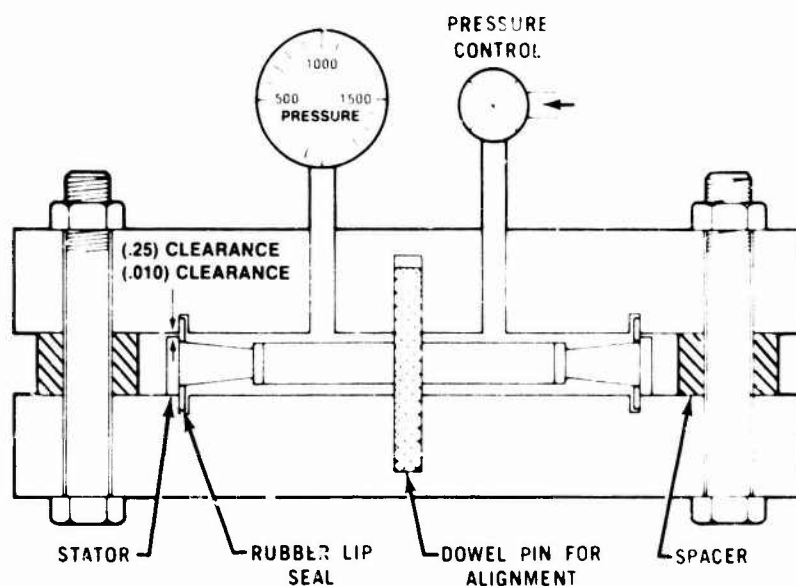
Figure 3.3.2-5 — Schematic View of Stator Outer Shroud Pressure Test Method

Cold Spin Testing

Cold spin testing was conducted in a vacuum spin pit shown schematically in Figure 3.3.2-6.[2-11] The test specimen was suspended in a vacuum chamber from an air turbine capable of achieving 100,000 rpm. Photographs could be taken at the instant of failure through a glass plate in the bottom of the vacuum chamber. The single frame camera could be replaced by a special 16mm high-speed (3,000 frames per second) motion picture unit to study time to failure. The failure detector shown in Figure 3.3.2-6, a ceramic burst ring painted with conducting epoxy, was later replaced by a cylindrical tube of 1.5 inch wide masking tape with several windings of thin copper wire. This triggering device was less expensive, easy to fabricate and allowed failed particles to escape thereby minimizing secondary damage to the remaining rotating blades.

The spin test facility was capable of testing simple ceramic hubs, segments of blade rings or complete blade rings bonded to a metal or ceramic hub with heat cured epoxy, and full duo-density ceramic turbine rotors.

Thermal Shock Test Rig

The thermal shock test rig was developed to screen candidate ceramic materials in simple bar form and evaluate changes in design and processing variations on stators and rotor blade rings.[3-9]

A schematic of the rig is shown in Figure 3.3.2-7. Up to eight samples could be clamped to the air actuated mechanically indexed rotary table. The cycle time could be varied from 0 to 4 minutes and table revolutions were recorded on a digital counter. Cooling air could be supplied to each of the eight samples to establish required thermal gradients by cooling the stator shrouds or rotor blade platforms.

Six stations supplied cool quench air which could be independently adjusted to control the downshock rate. Two mixing burners, using natural gas and oxygen, could be adjusted to a concentrated pencil flame or a more diffuse larger flame. An infrared sensing pyrometer and temperature recorder were used to set the burner and cooling air flows. Failures were automatically recorded as a step change in the recorded temperatures. Safety equipment monitored ultraviolet light from the flames and would shut off the gas and oxygen, if required.

CERAMIC TEST SPECIMEN

CERAMIC BURST RING

EPOXY CONDUCTING PAINT

TACHOMETER PICKUP

TURBINE AIR LINE

100,000 RPM AIR TURBINE

VACUUM LINE

LEADS TO FAILURE DETECTOR

VACUUM CHAMBER

GLASS PLATE

CAMERA

FAILURE DETECTOR

DUAL STROBE LAMPS

MIRROR

SPIN PIT

DIGITAL TACHOMETER

TURBINE PRESSURE

VACUUM GAUGE

THROTTLE

OPERATORS PANEL
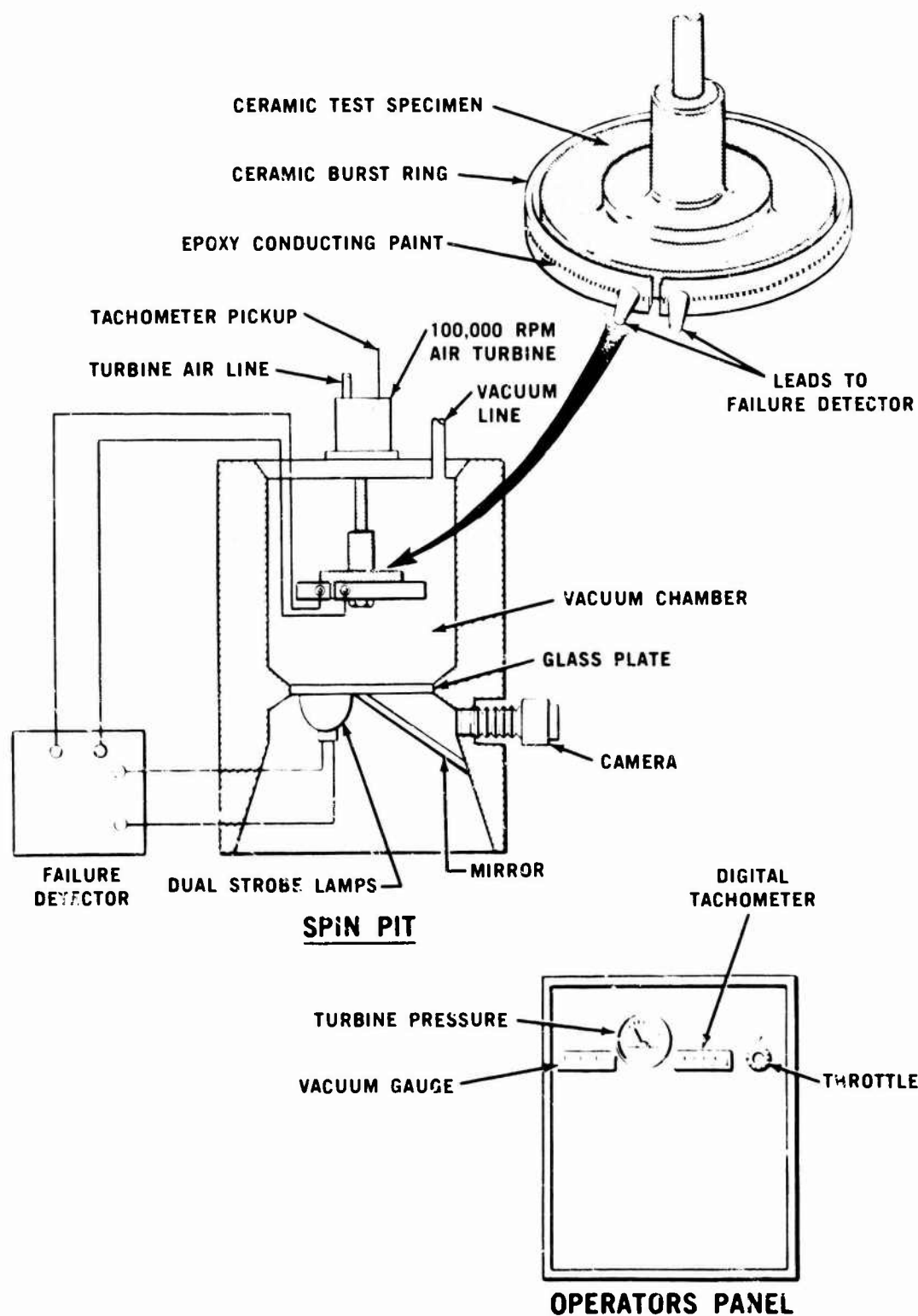
Figure 3.3.2-6 — Schematic View of Spin Pit
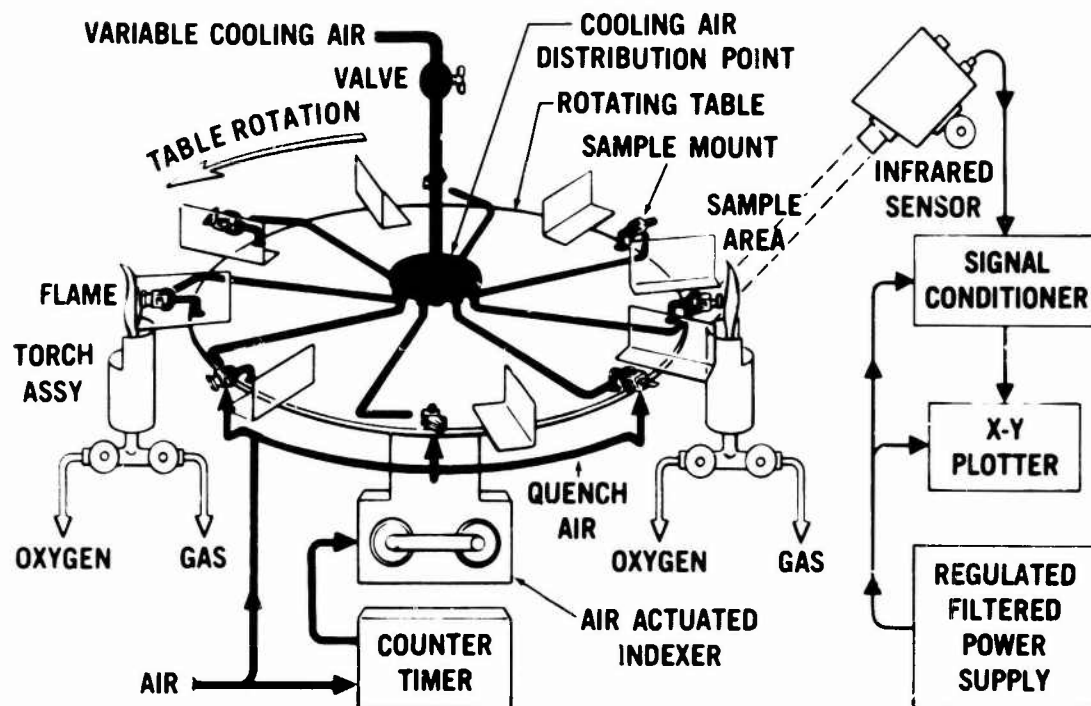
Figure 3.3.2-7 — Schematic View of Thermal Shock Test Rig

This type of test rig offered several advantages over more extensive engine testing as follows:

- a complete stator or blade ring was not necessary as segments from damaged components could be evaluated

- thermal gradients — both upshocks and downshocks — were adjustable and repeatable

- automated testing and failure recording

- design and process changes could be evaluated quickly

- fracture surfaces were preserved intact to expedite failure analysis

Rotor Disk Thermal Stress Rig

A test rig was designed and built which subjected the turbine rotor hub to a radial thermal gradient thereby producing a tensile stress in the bore of the disk.[9] The rig consisted of a cylindrical container in which a rotor was placed between two 1000 watt electrical heaters. The heaters raised the temperature of the blades and platform while the rotor bore was cooled by a tube delivering shop air. Thermocouples and strain gauges were to be used to monitor the disk temperatures and stresses. Although the rig was shown to be capable of fracturing the rotor and preserving the fracture surfaces intact, many problems were encountered attempting to fasten thermocouples and strain gauges to the ceramic turbine disk. Since these gauges were required to control the test, the effort was deemphasized.

Combustor Test Rig

The combustor test rig was developed to evaluate ceramic combustors independent of the other ceramic components in order to eliminate secondary damage as a result of combustor failures. The rig, shown in Figure 3.3.2-8, could operate at inlet temperatures from ambient to 1800°F, exit temperatures in excess of 2500°F and airflow rates up to two pounds per second. Facility air could be supplied at pressures of up to 65 psia and temperatures up to 1100°F. A secondary heater in the system would be utilized when inlet temperatures of 1100 to 1800°F were desired. The quartz window observation port, shown on the right in Figure 3.3.2-8, allowed visual inspection of the exterior of the ceramic combustor. The other observation port, shown on the left in Figure 3.3.2-8, provided visual observation of both the combustion process and the interior wall of the ceramic combustor.
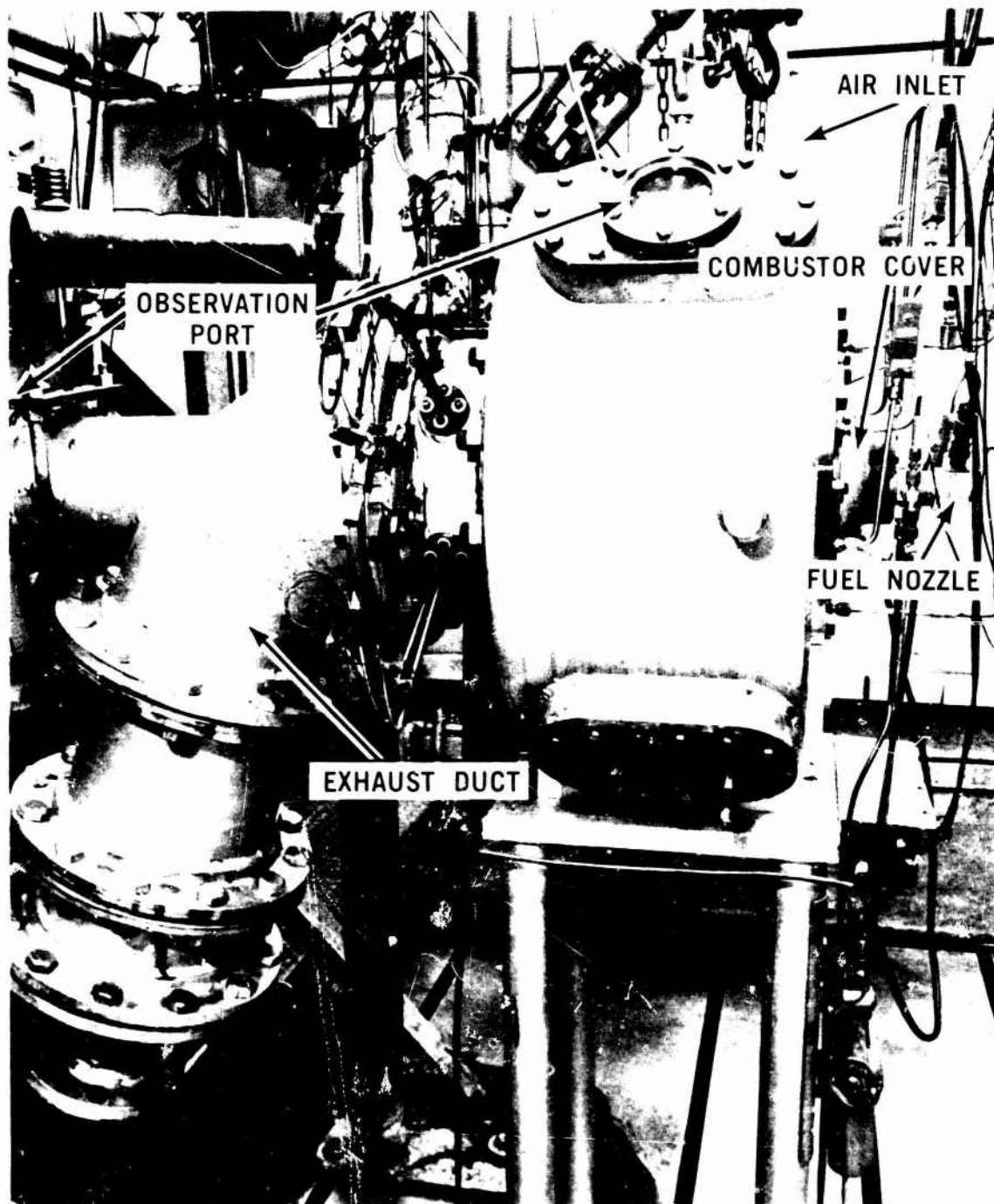
Figure 3.3.2-8 — Combustor Test Rig

Light-Off Qualification Test Rig

The light-off qualification test rig consisted of a complete engine assembly, less the turbine rotors, as shown in Figure 3.3.2-9. The stationary ceramic components to be qualified were installed in their normal position immediately downstream of the combustor. Engine speed and therefore airflow was controlled by a motoring dynamometer directly coupled to the engine output shaft. Thus, simulation of the engine thermal shock and aerodynamic loads on the stationary ceramic hot flowpath components could be achieved during engine start-up.
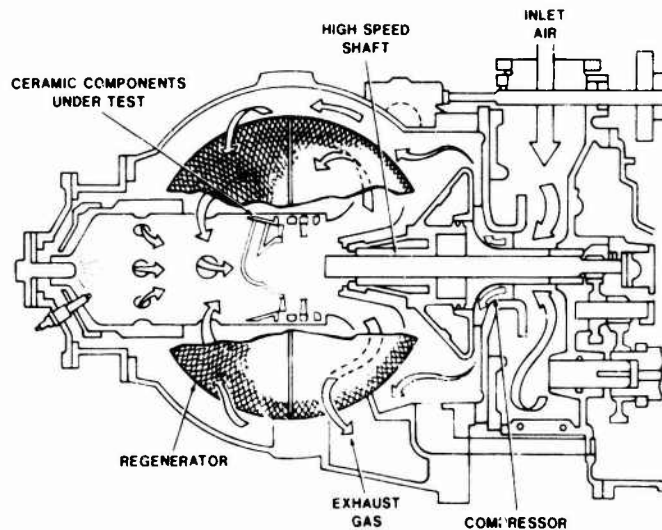
Figure 3.3.2-9 — Schematic Cross-Section View of Engine Simulator Test Rig Used for Light-Off Qualification Testing

A control system was developed which would detect light-off and accelerate the rig to idle speed while controlling the temperature to a predetermined schedule. Originally the light-off signal used in the control was detected by a fast response thermocouple; however, durability problems necessitated another approach. The test rig was fitted with a quartz window in the combustor assembly, as shown in Figure 3.3.2-10. A photoelectric cell was then sighted through the window to detect combustion. Figure 3.3.2-10 also shows an infrared sensor which could be used to determine the thermal response of different areas of the nose cone and first-stage stator. Test results are presented in Section 4.4.3 of this report.
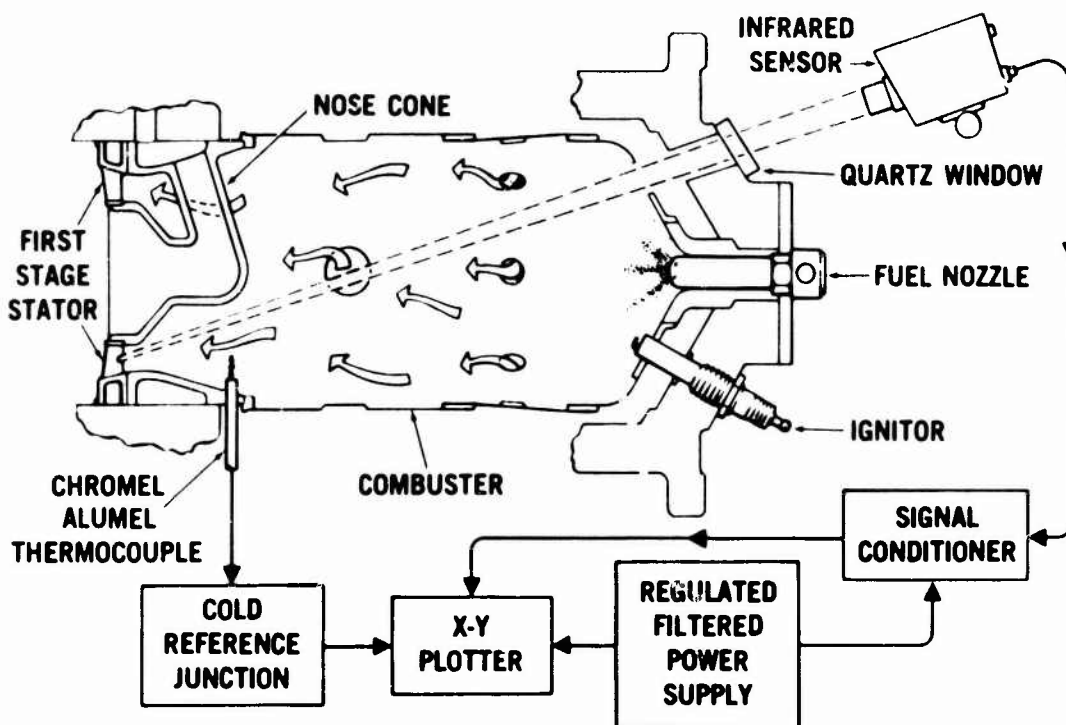
Figure 3.3.2-10 — Schematic View of Quartz Window Modification to Engine Simulator Test Rig

Ceramic Structures Test Rig

The ceramic structures test rig (Figure 3.3.2-11) was configured to evaluate the stationary ceramic flowpath components for steady-state durability over the complete range of engine airflows. The maximum temperature was restricted to 1930°F to prevent overtemperature of the two rotary regenerators. As shown in Figure 3.3.2-11, the high-speed shafting and compressor was replaced by an external air supply which could be manually adjusted along with the fuel supply to control airflows, temperatures and pressures. A variable speed electric motor was utilized to drive the regenerator system.
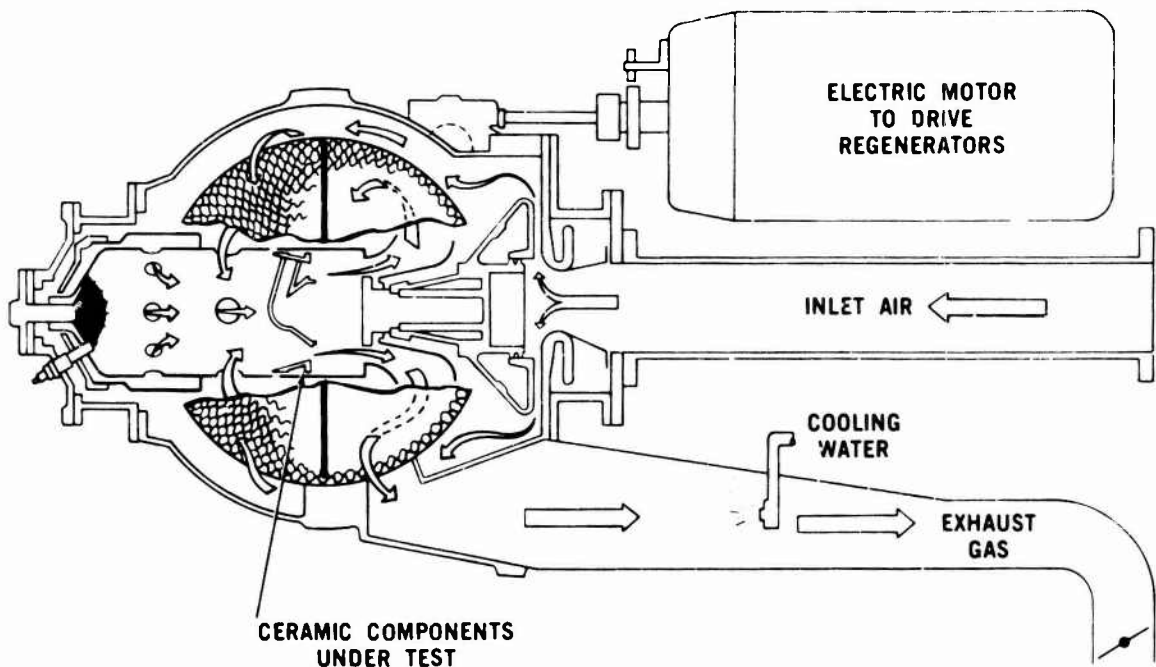
Figure 3.3.2-11 — Schematic Cross-Section View of Ceramic Structures Test Rig

2500°F Flowpath Test Rig

The 2500°F flowpath test rig was designed to evaluate the stationary ceramic flowpath components up to temperatures of 2500°F over the complete range of engine airflows. Figure 3.3.2-12 shows a cross-section of the rig, which consisted of an outer stainless steel shell and an inner ceramic flowpath, separated by high temperature insulation. The rig utilized a standard engine type combustor assembly operating with preheated, compressed air which was delivered from the test facility at temperatures up to 1100°F. Airflow, temperatures, and pressures could be manually controlled over the entire operating range via a series of valves. The hot exhaust gas was cooled with a water spray prior to dumping into the cell exhaust system. The combustor exit temperature was monitored by using thermocouples located at the inlet of the nose cone.

The stationary flowpath components could be tested one at a time, all together, or any combination thereof, by utilizing substitute ceramic spacers (except for a nose cone which was required for all testing). A rear observation port provided visual inspection of the components during testing.

Hot Spin Test Rig

The hot spin test rig was designed to quickly evaluate ceramic turbine rotors at temperature and speed with minimum cost. The principal features of the rig (Figure 3.3.2-13) were:
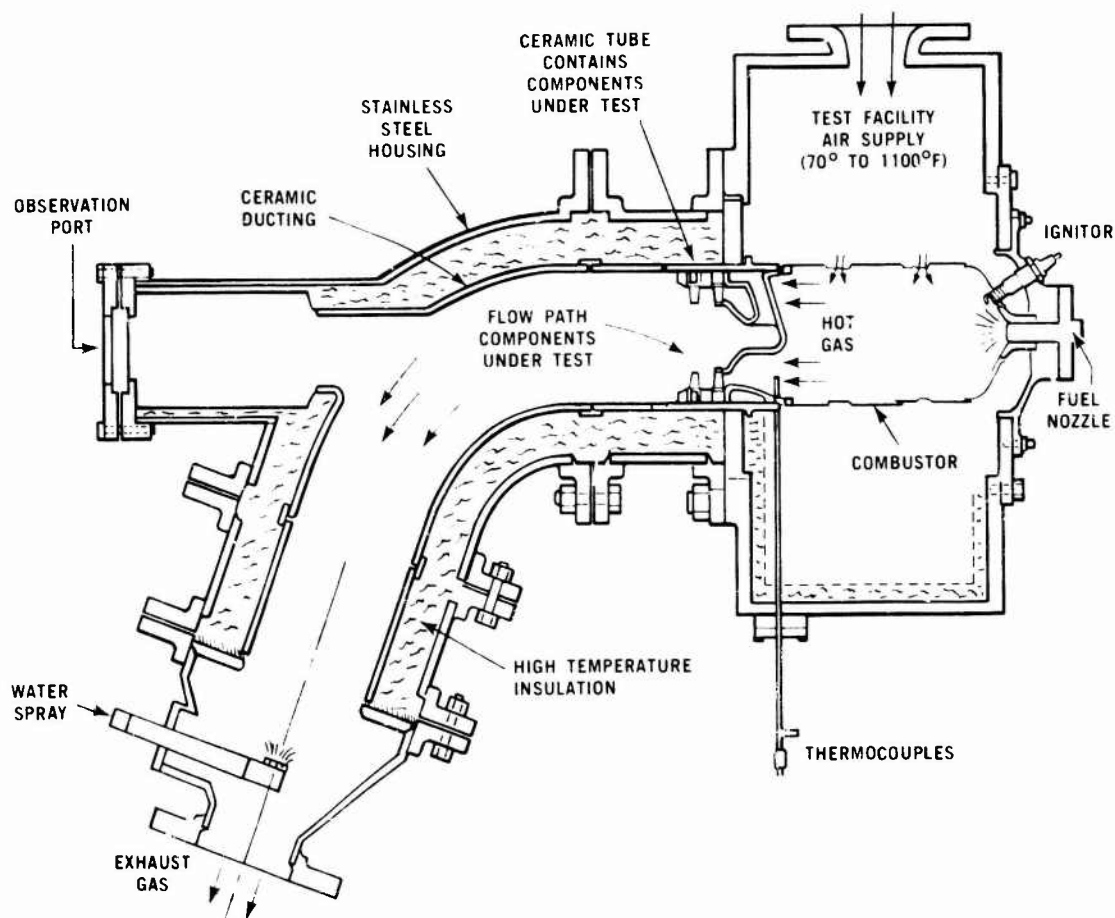
Figure 3.3.2-12 — Schematic Cross-Section View of 2500°F Flowpath Test Rig
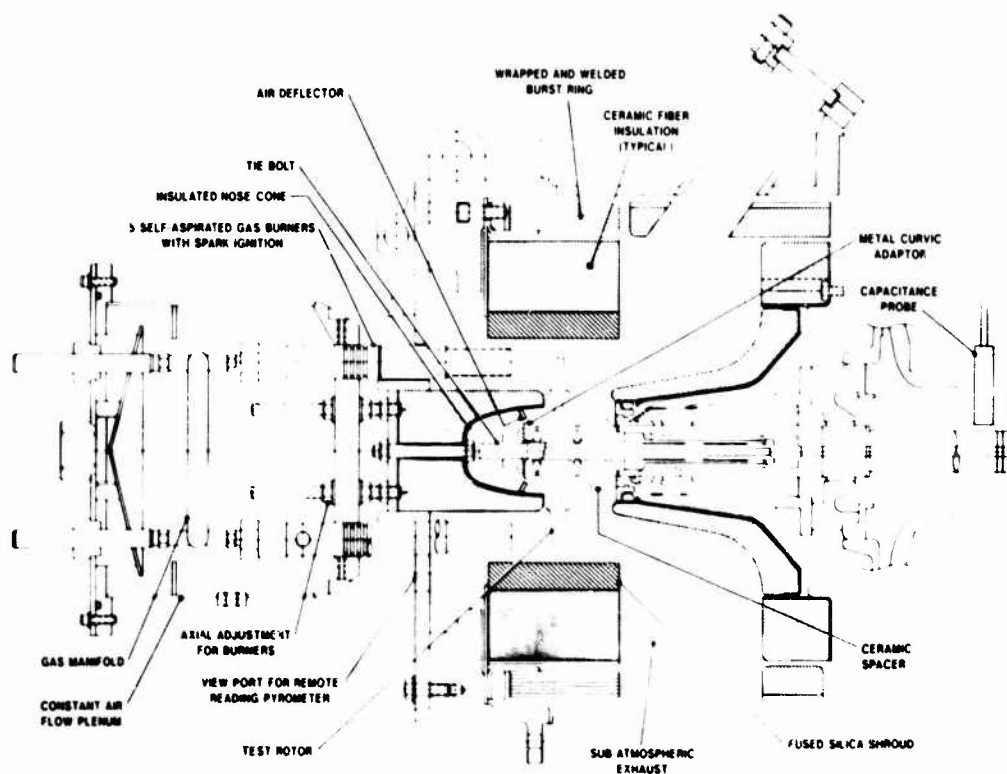
Figure 3.3.2-13 — Schematic Cross-Section View of Hot Spin Test Rig

- a single ceramic rotor could be tested

- no stationary ceramic flowpath components were required

- a simplified combustor was used

- containment of all failed rotors was achieved

- rotor hub and blade temperature measurement capability was provided

- automatic failure detection system was provided

- turn-around time after failure was minimized (about 1 week)

The simplified combustion system consisted of up to twelve stainless steel flame tubes attached to a mixing section from a commercially available propane burner and encased in a plenum supported by the air-cooled combustor cover. Thus, choked flow conditions in both the combustor air and fuel (propane) could be achieved while maintaining a constant air/fuel ratio regardless of the burner downstream pressure. This configuration eliminated earlier flame-out problems encountered during rapid accelerations with bladed rotors.

An Inconel X-750 spiral wound burst ring and high alumina ceramic fiber insulation was used to protect the main housing. A solid fused silica shroud ring eliminated earlier durability problems of erosion of the ceramic fiber insulation above the rotor blade tips.

The engine configuration curvic couplings and folded bolt arrangement were utilized to connect the test rotor to the high-speed shaft. Elimination of the compressor enabled the rotor and shaft to be built up and balanced outside the rig and installed in the rig without disassembly, thereby eliminating any uncertainty present in configurations which first balance the rotor and shaft, then remove the rotor during the assembly of the shaft into the rig. An air deflector was positioned inside the insulated nose cone to direct the rotor bolt cooling air exhaust over the metal curvic adaptor keeping it at an acceptable temperature level.

A capacitance probe which measured clearance of the high-speed shaft was utilized as a failure detector in the developed rig. This system replaced an earlier burst detector located above the rotor blade tips consisting of several closely spaced windings of 0.010 inch diameter platinum wire encased in insulating material, which exhibited durability problems.

The temperature of the ceramic rotor blades and hub could be monitored by a radiation pyrometer mounted on the test rig and sighted through either a front or rear viewport. Continuous recording on magnetic tape of the outputs of the radiation pyrometer, capacitance probe, speed, cooling airflows, etc., aided in failure analysis.

Turbine Rotor Test Rig

The design of the turbine rotor test rig, shown schematically in Figure 3.3.2-14, was similar to but less complex than the engine, although it used all of the hot flowpath components except for regenerators. The engine centrifugal compressor was utilized to absorb power and provide compressed air to cool the main housing of the test rig. The inlet air to the combustor was supplied by the facility, thereby allowing control of airflow and temperature independent of the rotational speed of the rig. As shown in Figure 3.3.2-14, the complete hot flowpath ceramic components, including the ceramic turbine rotors, could be subjected to the aerodynamic, thermodynamic and mechanical loading encountered in a complete engine. However, the time and expense to rebuild this rig after a rotor failure precluded extensive use of the rig; rotor development was conducted in the hot spin test rig.

Modified Engine Test Rig

For rotor testing, the engine was modified so that reduced blade height rotors and/or single turbine rotors could be tested at higher temperatures and lower speeds than planned for the two-stage, full blade height, turbine rotors. The modification reduced the regenerator inlet temperature to an acceptable level by diluting the hot gases exiting from the turbine with combustor inlet and/or compressor discharge air as shown in Figure 3.3.2-15.
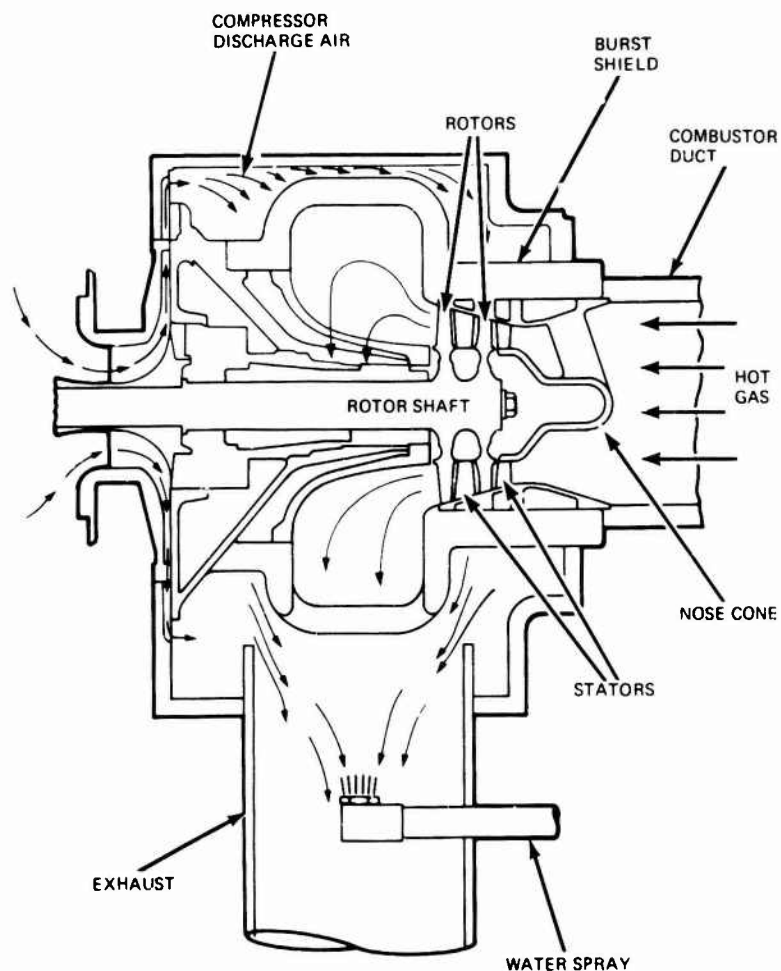
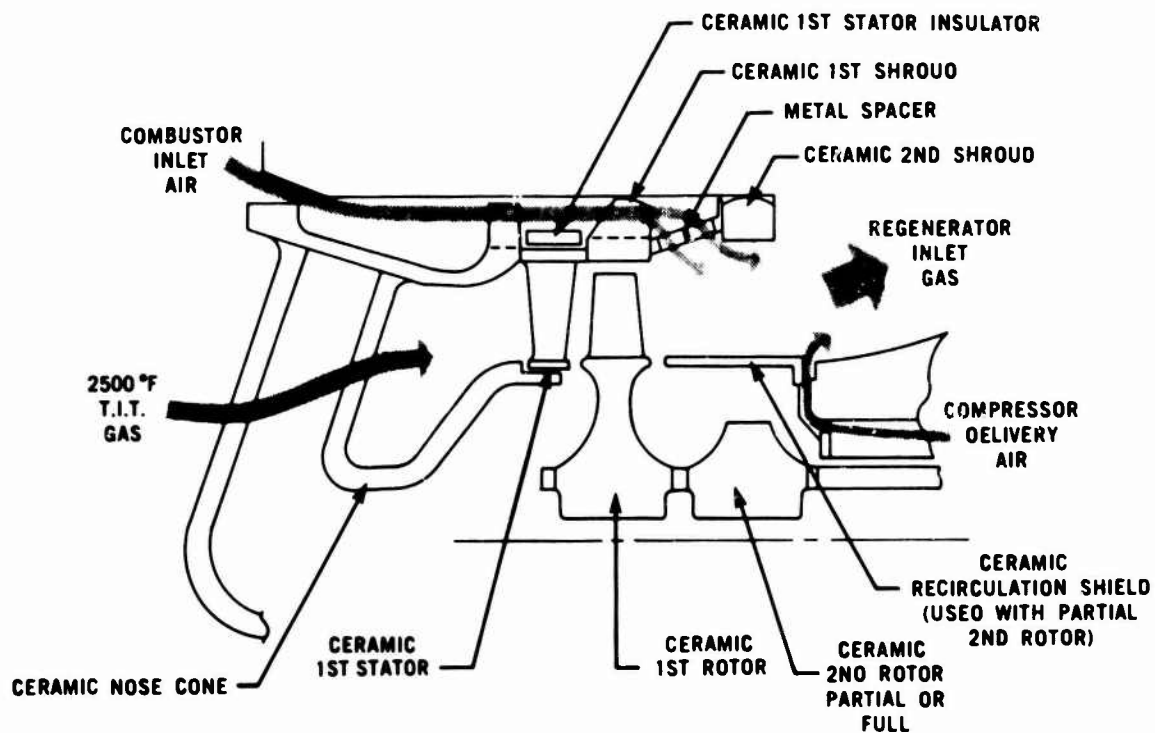Figure 3.3.2-14 — Schematic Cross-Section View of Turbine Rotor Test Rig

Figure 3.3.2-15 — Schematic Cross-Section View of Modified Engine Test Rig

4. COMPONENT DEVELOPMENT

4.1 INTRODUCTION

This section of the report deals specifically with the development of the ceramic components for the all-ceramic hot flowpath of Ford's experimental Model 820 vehicular turbine engine to meet the 200-hour 2500°F program objective. These components fall into two categories as follows:

- CERAMIC TURBINE ROTOR
- CERAMIC STATIONARY COMPONENTS
  - Stators
  - Nose Cone
  - Combustor
  - Rotor Tip Shrouds

Design, materials and processing, and testing and evaluation for each of these two component categories are reported in this section. Before that, however, the following subsections cover the overall turbine flowpath design iterations which influenced or were influenced by the ceramic components themselves. These flowpath design iterations thus provide a framework for the component development addressed in subsequent sections.

4.2 TURBINE FLOWPATH DESIGN ITERATIONS

The design of a turbine flowpath for an automotive gas turbine engine is an involved process of optimizing the relationships between turbine efficiency, low rotor inertia, and other limitations imposed by material properties and fabrication processes. Due to the practical limitations of the relatively small size of automotive turbines, penalties are unavoidable. These include blade blockage due to minimum trailing edge thicknesses, large blade tip running clearances as a percentage of blade height, and the low blade chord Reynold's number. This section summarizes the development of aerodynamic-ceramic installations on a program primarily concerned with establishing ceramic technology.

4.2.1 FLOWPATH DESIGN A

The initial flowpath design (Design A) was completed prior to initiation of this program. This design, shown in Figure 4.2.1-1, was made for a 2500°F turbine inlet temperature with ceramic stationary components and cooled metallic rotors. A ceramic nose cone with three hollow struts for the cooling air was included in the flowpath which were sized to pass 7% of the compressor air flow. The two-stage axial turbine was designed with a constant hub diameter and for a 55/45 work split between stages at 100% speed. The mean blade trailing edge thickness of 0.020 inch for the stator and 0.017 inch for the rotor were selected as desirable requirements. The first and second stage stators did not have tip shrouds, although aft platforms of each stator served as rotor tip shrouds. All other aspects of the design followed conventional procedures for metallic turbines with a "free-vortex" flow distribution. Efficiency estimates and off-design characteristics were estimated using a revised version of the well-known Ainley-Mathieson correlation[71,72].

4.2.2 FLOWPATH DESIGN B

Early in this program, Design A was modified to Design B[1], which provided for uncooled ceramic rotors by reducing the first stage stator chord, by re-staggering the stator blades for correct stage matching, smoothing the channel contours, and adding a tip shroud to the first stage stator. Reducing the first stage stator chord by cutting back the trailing edge increased the trailing edge thickness to 0.030 inch. Some limited cold testing of Design B turbine configuration showed that an overall efficiency of 80% was achieved on a total/static basis. Figure 4.2.2-1 shows a cross section of the flowpath of Design B. The second stage stator blades were cantilevered from their outer shroud which resulted in unacceptable running clearance requirements at the hub. Therefore, for aerodynamic as well as some mechanical and ceramic fabrication reasons, Design B was modified to Design C.
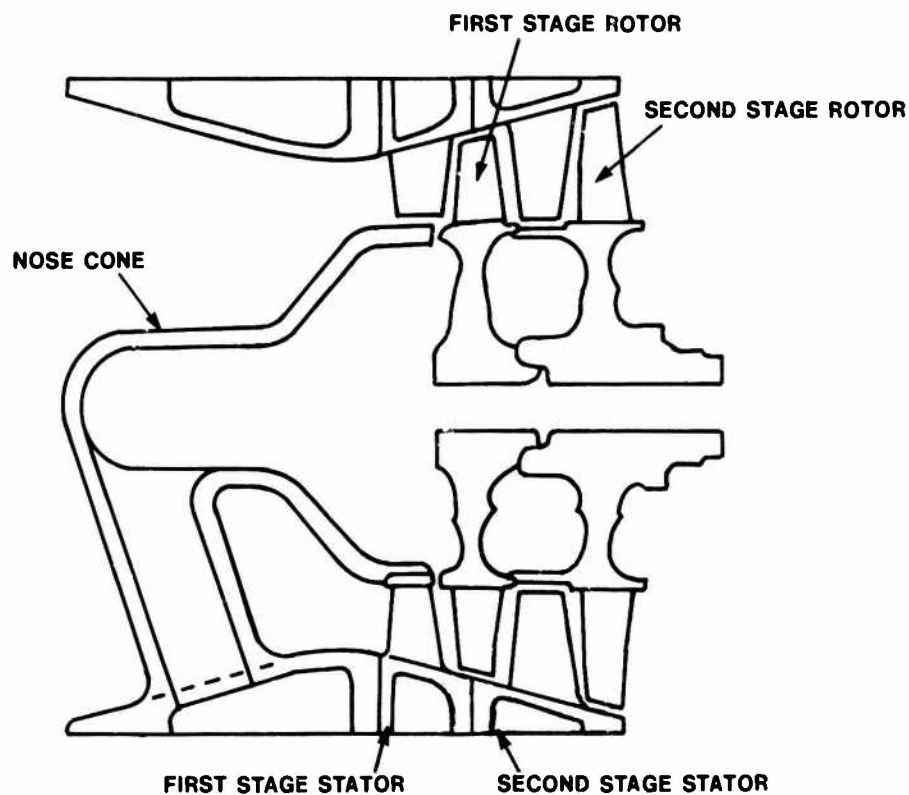
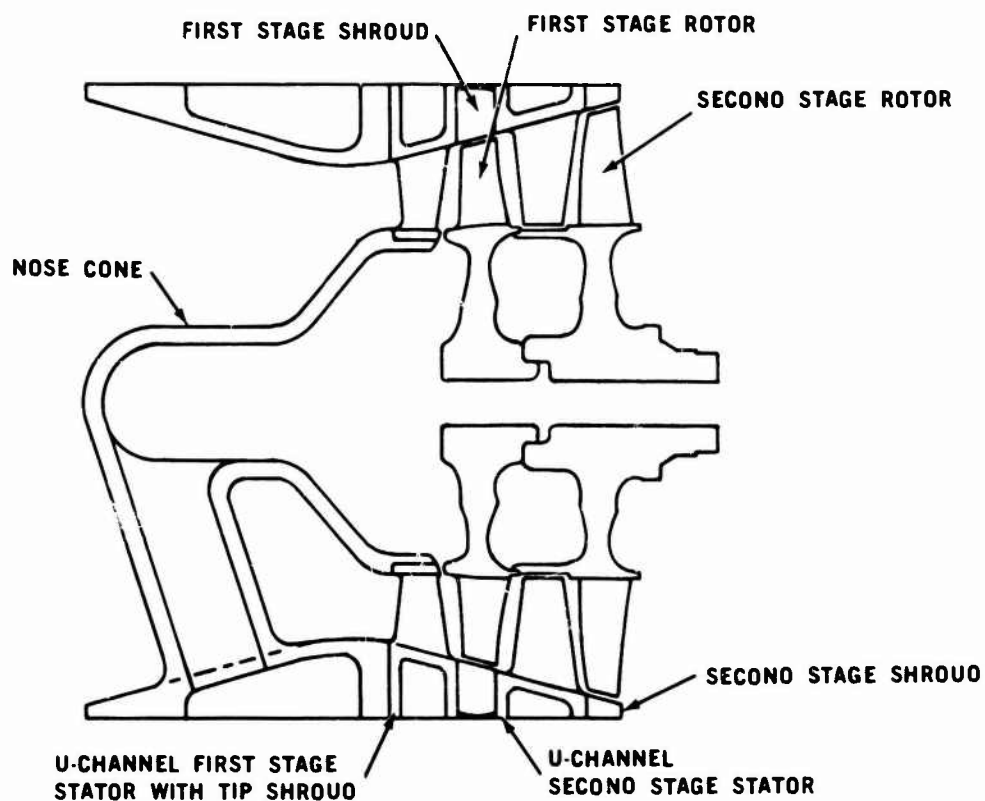Figure 4.1.1-1 — Schematic Cross-Section View of Design A Flowpath

Figure 4.2.2-1 — Schematic Cross-Section View of Design B Flowpath

4.2.3 FLOWPATH DESIGN C

The flowpath of Design C[3][5] is shown in Figure 4.2.3-1. The first stage stator channel shape was modified to provide parallel walls so that a one-piece molding from tooling with axial "draw" could potentially be used. The second stage stator was still of the segmented construction; however, an inner shroud was included to reduce the leakage across the stator. This modification eliminated the thin cylinder between the rotors which provided a mechanical improvement for the rotor.
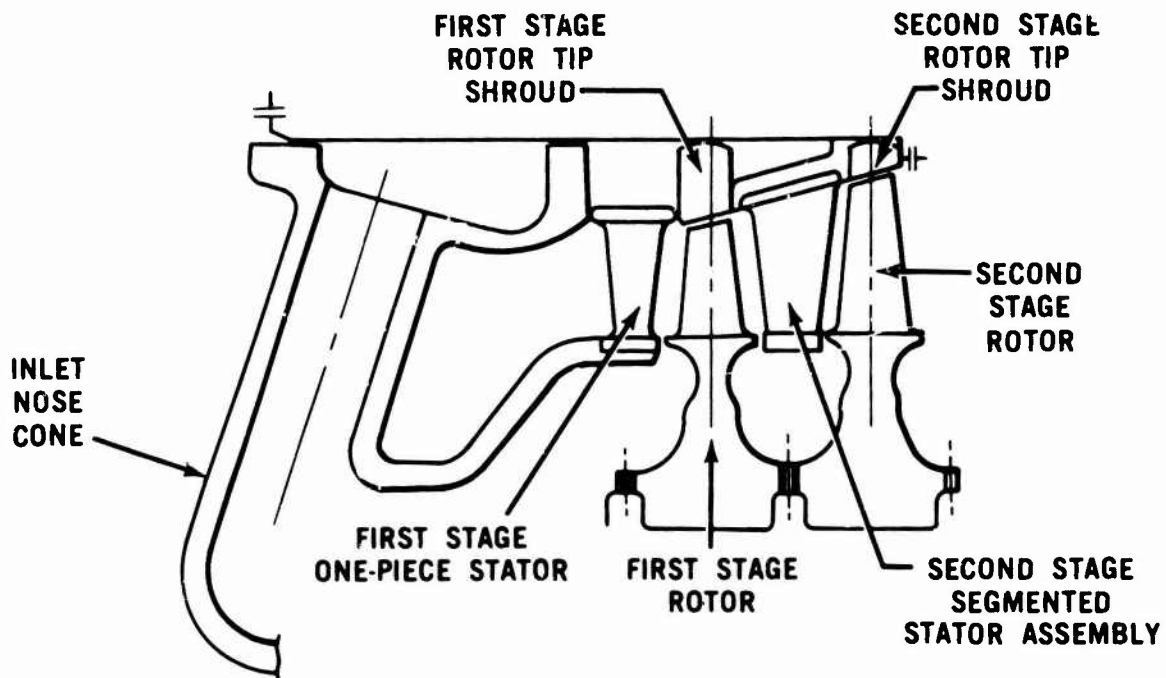
Figure 4.2.3-1 — Schematic Cross-Section View of Design C Flowpath

4.2.4 FLOWPATH DESIGN D

To eliminate fabrication problems with the segmented second stage stator and to reduce the number of fabricated parts in order to expedite ceramic turbine development, a further modification was made (Design D)[7] which featured a monolithic stator common to both stages and a rotor common to both stages. Stator aerodynamics were based upon the first stage Design C stator, while the rotor aerodynamics were based upon the Design C second stage rotor. As shown in Figure 4.2.4-1, Design D consists of identical stators in the first and second stage locations, and with the exception of the machined tip diameters, identical rotors in the first and second stage locations.

No aerodynamic testing of Design D was conducted; however, estimates of efficiency indicated that a loss of four percentage points would occur at maximum speed. A reduction in flow capacity of eight percentage points was also estimated.
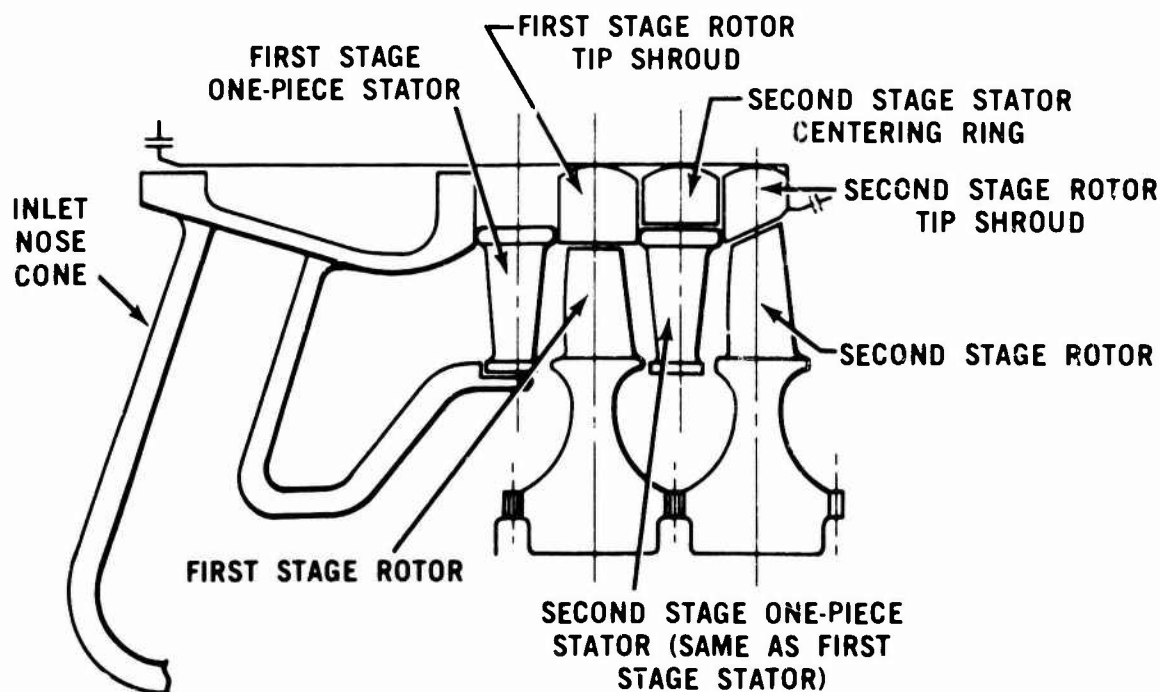
Figure 4.2.4-1 — Schematic Cross-Section View of Design D Flowpath

4.2.5 FLOWPATH DESIGN D′

The rotor blades of Design D were still of the "free-vortex" design. The associated twist of the blades resulted in bending and torsional stresses which were additive to the tensile centrifugal stresses. To reduce the maximum blade stresses and to improve fabrication, the rotor blading was redesigned to have non-twisted, radially and centriodally stacked airfoils. This new configuration was labeled D′(D prime)[8]. As before, the same rotor was used in both the first and second stage locations. The stationary components were unchanged from Design D. The cross-sectional flowpath of Design D′ is identical to that of Design D, shown in Figure 4.2.4-1.

The concept of radial or helical stacking requires that the camberlines of all radial sections be connected in a fixed relationship. For the parabolic camberlines used in this design, the result is a family of parabolas through a common origin whose ordinates are related through the ratio of the section radii. One implication of this in blade design is that once one camberline is fixed, e.g., the hub section, the camberlines at all other radial sections are fixed and variations of blade angles can only be achieved by "sliding" the blade section along the given camberline. However, in order to maintain centroidal stacking of the total blade, the amount of "sliding" possible is relatively small, thereby producing a blade with minimal hub-to-tip variation. Therefore, it was possible to achieve the large hub-to-tip variations of blade inlet angles necessary to match the flow leaving the unmodified stators.

The rotor blade was designed so that the maximum average centrifugal stress at 110% speed would be reduced from 21,000 psi (Design D) to 13,000 psi (Design D′). The trailing edge thickness varied linearly from 0.022 inch at the tip to 0.034 inch at the blade root to facilitate injection molding of the higher strength 2.7 gm/cm^3 density Si_3N_4 material.

As a consequence of the radial stacking and some high rotor incidence angles, the D′ Design was calculated to be 1.0 to 1.8 percentage points lower in efficiency than the D Design which it replaced.

This configuration minimized bending and torsional stresses while improving the blade cavity filling characteristics during the molding operation and permitting manufacture by radial draw tooling. No aerodynamic testing of Design D′ was conducted.

4.2.6 FLOWPATH DESIGN E

To assess the efficiency potential of a turbine designed with the experience gained and knowledge of ceramic constraints learned from this program, an analytical design was made aimed at achieving an improved efficiency turbine, Design E [9,10]. The design criteria used were based on assumptions of material and fabrication capabilities available or judged to be available at the conclusion of the program, as listed in Table 4.2.6-1.

TABLE 4.2.6-1

DESIGN CONSTRAINTS FOR DESIGN E Si_3N_4 TURBINES

● Compatibility with current engine cycle (i.e., speed, pressure level, mass flow, temperature)

Rotors
● Radially and centroidally stacked blades
● One-dimensional blade stress $\leq$18,000 psi tension
● Two-dimensional disk stress $\leq$30,000 psi tension
● Trailing edge thickness = 0.022 in. tip, 0.029 in. mean, 0.036 in. root
● Material density in blades of 2.7 gm/cm'
● Material density in hub of 3.2 gm/cm'
● Radial draw fabrication

Stators
● Axial draw fabrication
● Trailing edge thickness = 0.030 in.
● Strength requirement is less than that for rotors

Flowpath optimization was performed using an in-house computer program to calculate multistage turbine performance and gas properties at the intercomponent planes within the turbine. The overall aerodynamic flowpath is shown in Figure 4.2.6-1. As would be expected for best efficiency, the stators and rotors are not common for both stages as they were in Design D'. Design E efficiency was estimated to be 7.5 percentage points higher in total-to-total efficiency than the D' Design.

2.97" RAD

2.76" RAD

2.18" RAD

2.C7" RAD
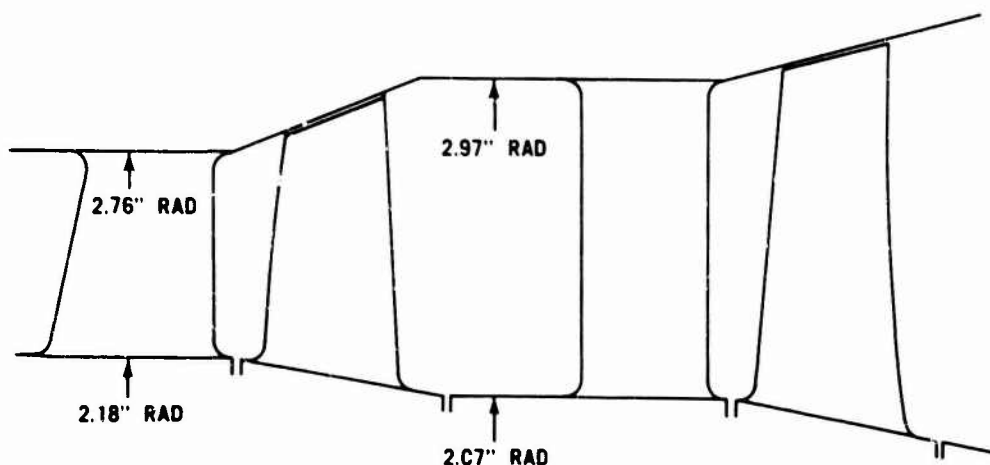
Figure 4.2.6-1 — Design E Aerodynamic Flowpath

The design of individual blade sections for both stator and rotor blades conformed, as closely as possible, to the criteria established in the flowpath optimization analysis. A basic two-dimensional analysis of the gas flow fields of both the rotors and stators was conducted using the NASA Computer Program TSONIC[73]. Both rotor and stator blades have parabolic camberlines. The camberlines were of a single family for each rotor which provided the radial blade stacking necessary to achieve low stress. The blade sections had their centroids radially stacked to reduce bending stresses. The stator blade designs permitted axial draw in molding, while the rotor designs allowed radial draw.

4.2.7 EFFECT OF INCREASED STAGING ON EFFICIENCY AND RELIABILITY

An analytical study[11,74] was conducted to evaluate the potential efficiency and reliability trade-offs between a two-stage and a three-stage axial turbine. Generally speaking, in adding a stage to a turbine, one anticipates a gain in aerodynamic efficiency for the same blade speed and pressure ratio. Alternatively, the speed may be reduced, the efficiency level maintained, and the reliability of each stage increased because of the lower stress levels associated with the reduced speed. This increase in reliability, however, will be counteracted to some degree by a reduction in reliability due to the addition of a third rotating component.

To quantitatively establish the relative efficiency/reliability advantages of the three-stage turbine, various flowpath configurations of both two- and three-stage turbines were analyzed in terms of aerodynamic efficiency at 70% speed and mechanical reliability at 100% speed. Simplified stress models of disks and blades were used for all configurations. The disks considered were equal in thickness to those currently fabricated. In the efficiency analysis, various aerodynamic quantities were investigated to assure that the final configurations were at a reasonable optimum while subject to common constraints.

The conditions assumed in the efficiency calculations are summarized in Table 4.2.7-1. Free-vortex designs were used rather than non-free-vortex helically stacked designs because of the ease of scanning different configurations with free-vortex techniques. Helically stacked non-free-vortex turbines were generally ≤1% lower in efficiency than the equivalent free-vortex designs.

TABLE 4.2.7-1

TURBINE AERODYNAMIC EFFICIENCY STUDY

Constant Parameters and Conditions
- Free-Vortex Design Turbines
- Negligible Stator Leakage
- Solidity, Trailing Edge Thickness, Tip Clearance, Number of Blades

Turbine Inlet Conditions
- At 70% Speed
  Inlet Temp. 2715°R; Exit Temp. 2300°R
  Airflow 0.92 pps; Inlet Press. 22.7 psia
  Total/Total Press. Ratio 2.21

Varied Parameters
- Rotational Speed; Nmax Varied From 100% to 81.6%.
- Flowpath Geometry
- Weight Flow
- Stage Work Split
- Annulus Areas
- Degree of Reaction; Stage Exit Swirl

For the three-stage turbine designs, different basic flowpath configurations were studied as shown in Figure 4.2.7-1, consisting of a constant tip diameter (flowpath C), a constant pitch line diameter (flowpath B) and a constant hub diameter (flowpath A).

The incremental total-to-total efficiency levels for various configurations and rotational speeds are shown in Figure 4.2.7-2 as a function of mean turbine blade speed squared. The relatively good correlation indicates that for the given gas conditions mean overall blade speed is the major factor of efficiency. The effect is independent of the variety of configurations and speeds used whether blade speed is varied by radius changes or rotational speed. All of the remaining items shown in Table 4.2.7-1, weight flow, stage work split, annulus area and stage exit swirl generally had small effects on efficiency.
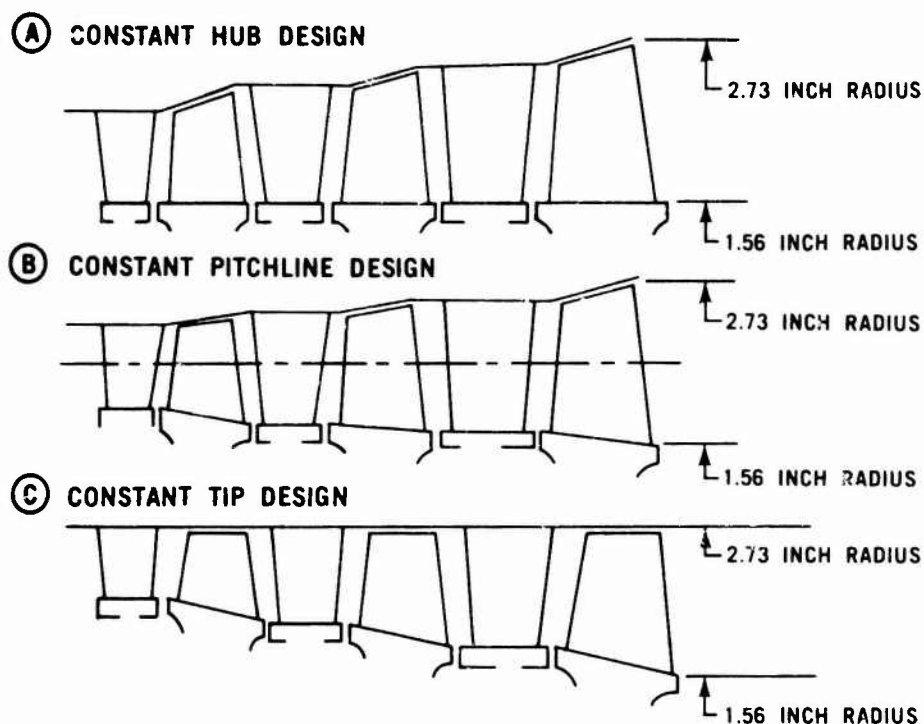
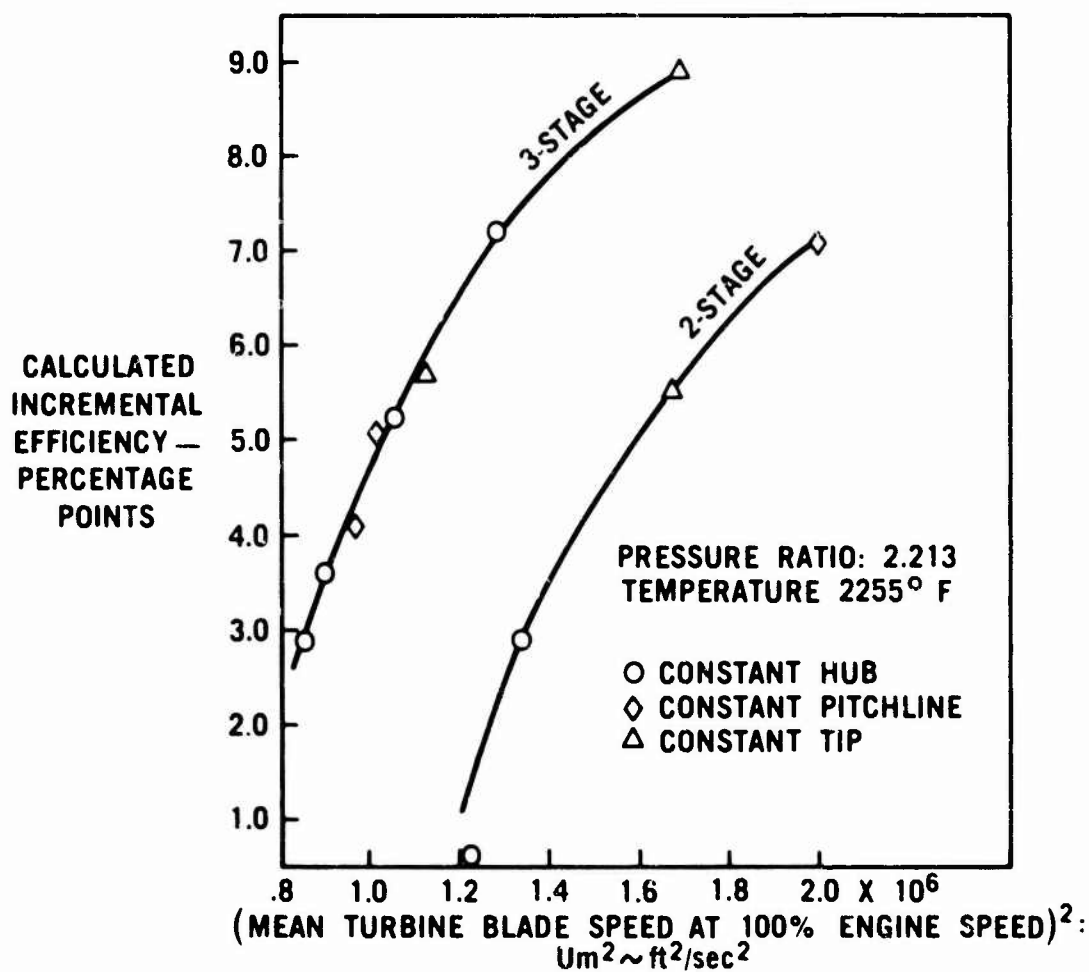Figure 4.2.7-1 — Three Stage Flowpath Configurations

Figure 4.2.7-2 — Comparative Total-to-Total Efficiency

As would be expected, the two-stage turbines have significantly lower efficiencies than the three-stage turbines for the speed range considered. Simplified stress models were constructed of both the blading and the disks in order to estimate the relative fast fracture mechanical reliability of the various two- and three-stage turbine configurations studied. The construction of the models was particularly oriented towards evaluating the effects of those variables, i.e., hub and tip diameters and rotational speed, which increase aerodynamic efficiency by increasing blade speed. The assumptions used in the stress models are summarized in Table 4.2.7-2; Figure 4.2.7-3 schematically shows the simplified model used. All stress analysis was done at the appropriate 100% speed level.

TABLE 4.2.7-2

TURBINE ROTOR STRESS ANALYSIS AND RELIABILITY MODEL

Disk Model
- D' First Stage Axisymmetric Finite Element Model
- Diameter Varied 3.1 Inches to 4.2 Inches
- Max Hub Thickness Maintained
- Common Temperature Boundary — All Stages
- Common Blade Number
- Speed 52,452 RPM to 64,240 RPM

Blade Model
- One-Dimensional Model
- Tip Diameter Varied
- Taper Ratio and Root Area Common to All Stages
- Blade Temperature Constant with Radius
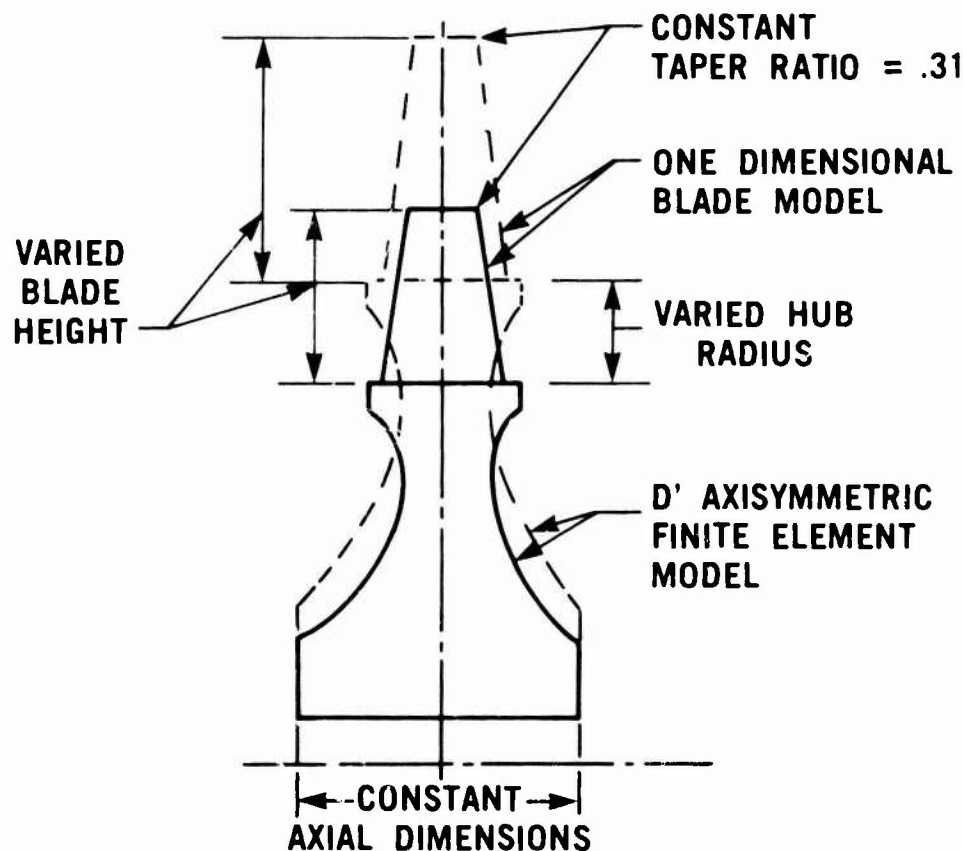
Figure 4.2.7-3 — Schematic View of Simplified Rotor Stress Model

123

The blade mechanical stress distribution was determined on a one-dimensional basis. Blades in each stage were assumed to have a constant temperature representative of typical relative gas temperatures for that stage. Weibull failure probability analyses were performed on the disks and blade models separately. Strength properties used are shown in Table 4.2.7-3, and represent typical property levels for silicon nitride materials available at time the study was made.

TABLE 4.2.7-3

STRENGTH PROPERTIES

	Temp °F	Weibull Slope m	MOR (psi)
2% Mg0 Hot-Pressed Si3N4	78	10	109,000
(Hub)	1700	10	95,000
	2100	10	78,000
	2300	10	63,000
	2500	10	42,000
5% Mg0 Press-Bonded Si3N4	78	10	90,000
(Bond Ring)	1700	10	81,900
	2100	10	65,700
	2300	10	52,200
	2500	10	33,300
Injection-Molded Si3N4	78	11.1	36,300
(Blades and Platform)	1700	16.2	33,300
	2100	13.3	31,900
	2300	9.5	33,000
	2500	12.1	31,900

Figure 4.2.7-4 presents the fast fracture probability of failure for the various flowpath configurations and rotational speeds studied, plotted as a function of overall turbine mean blade speed squared, the same parameter as used in Figure 4.2.7-2 for aerodynamic efficiency. The greater reliability at a given mean blade speed of the two-stage over the three-stage is to be expected because of the extra rotating component in the three-stage design. It should be pointed out that the absolute level of the curves is a strong function of the particular material properties and wheel and blade geometry used. It is felt that apparent correlation of probability of failure with mean blade speed over the limited range studied is attributable in some degree to the fact that, for the disk and blade geometries, and material strength properties assumed, the rotors were basically disk strength-limited. That is, the numerical reliability of the disks was in general lower than the blades and was therefore controlling.

This preliminary study showed that a ceramic three-stage turbine is an attractive alternative to the current two-stage design due to greater reliability and efficiency. It was shown that, for the same overall level of efficiency, a three-stage turbine would have significantly higher reliability operating at 50,000 rpm than a two-stage design operating at 64,000 rpm. Alternately, at equal levels of mechanical reliability, a three-stage turbine can be expected to have a 3 to 5 percentage point efficiency gain relative to a two-stage turbine.
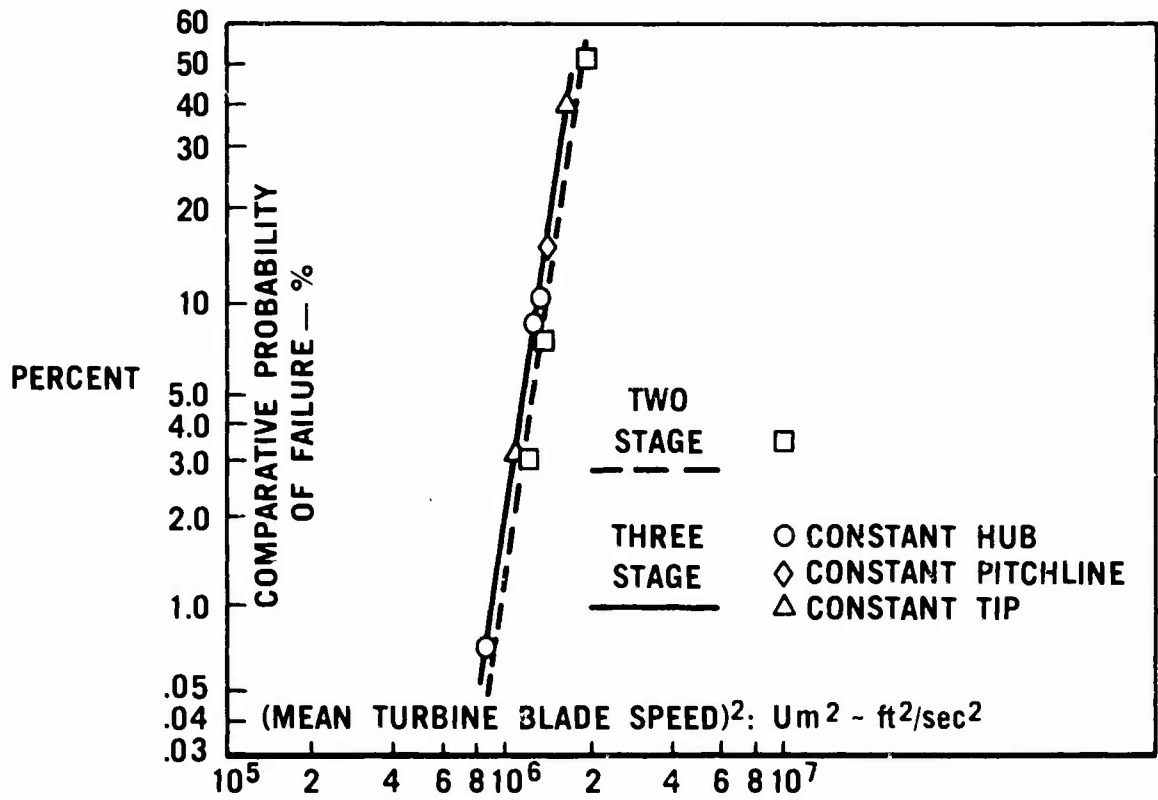
Figure 4.2.7-4 — Rotor Fast Fracture Probability of Failure

4.3 CERAMIC ROTORS

4.3.1 DESIGN

4.3.1.1 Design A

As indicated in Section 4.2, the initial flowpath design (Design A) was completed before initiation of this program and was based on a cooled metal rotor. Also prior to this program, in-house design studies and experiments had been conducted on a hybrid rotor comprising ceramic blades and a superalloy hub. From these studies, it was concluded that: (i) a strong ceramic such as hot pressed silicon nitride would be required for the blade root due to high stresses in the attachment area, (ii) the metal hub design will be fairly bulky causing an excessive overall rotor inertia (NOTE: low rotor inertia is important for automotive applications), and (iii) the metal hub had to be cooled, thus, aggravating efficiency and cost. As a result of these earlier studies, it was decided to investigate an all-ceramic rotor for the Model 820 engine hot flowpath, designated Design B.

4.3.1.2 Design B

Preliminary designs were conceived for first- and second-stage Design B all-ceramic rotors, at that time using codes generaly applicable to metal rotors. Preliminary thermal and centrifugal stresses were calculated using physical properties of either a fully dense silicon nitride material or a fully dense silicon carbide material.

These stresses were calculated for assumed extreme transient start-up and acceleration conditions and for the maximum steady-state condition as shown in Figure 4.3.1-1 and Figure 4.3.1-2. While these preliminary rotor designs did not consider how the part would be made, they were the first step to define part geometry with respect to stresses indicating that both fully dense silicon nitride and silicon carbide could be considered candidate rotor materials.
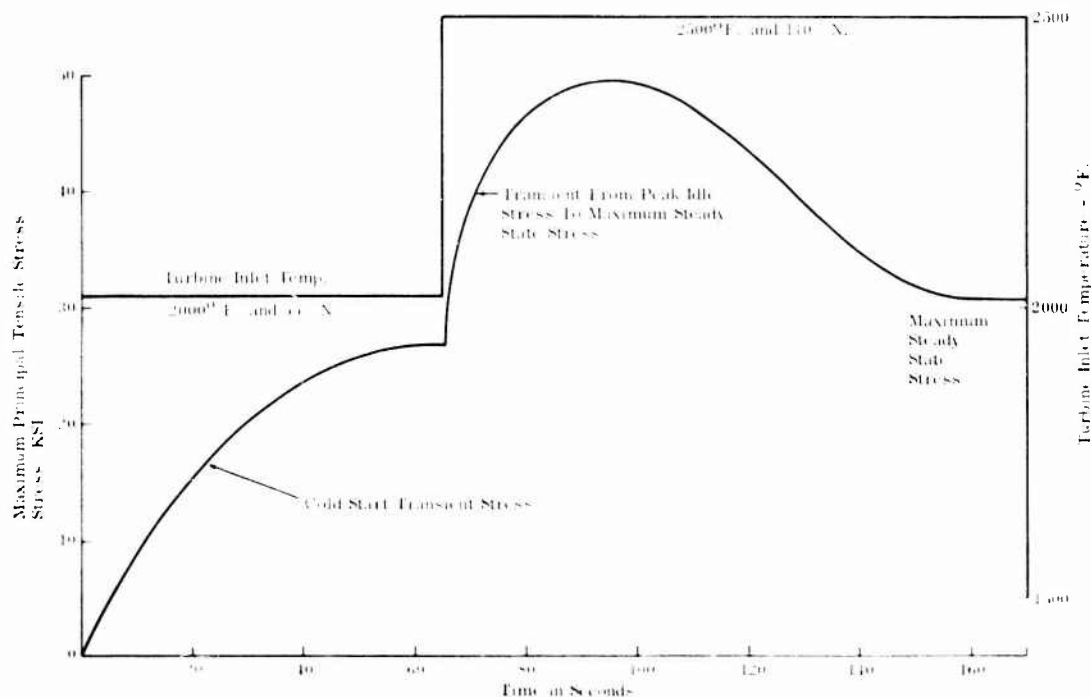
Figure 4.3.1-1 — Effect of Assumed Engine Operating Conditions
Upon Dense Silicon Nitride Rotor Disk Stresses
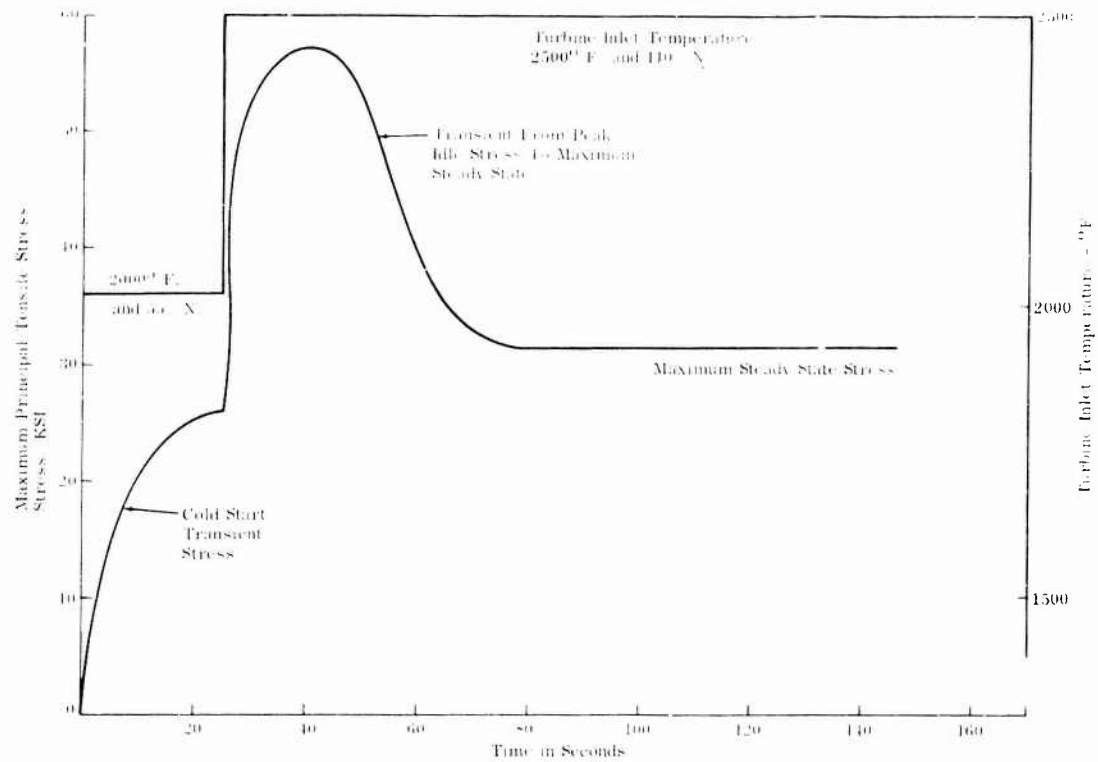
Figure 4.3.1-2 — Effect of Assumed Engine Operating Conditions Upon Dense Silicon Carbide Rotor Disk Stresses

A very important design problem was how to attach the ceramic rotors to the metal shaft. Such an attachment needed to allow for thermal mismatch yet maintain concentricity of mating parts and the ability to transmit torque. Several designs of cooled folded bolts were conceived and investigated leading to the hollow folded bolt shown in Figure 4.3.1-3. Another important feature of this attachment was the actual part-to-part interface. For this, a special 15-tooth half-barrel curvic coupling was designed and some experimental ceramic-to-metal specimens were made such as shown in Figure 4.3.1-4.
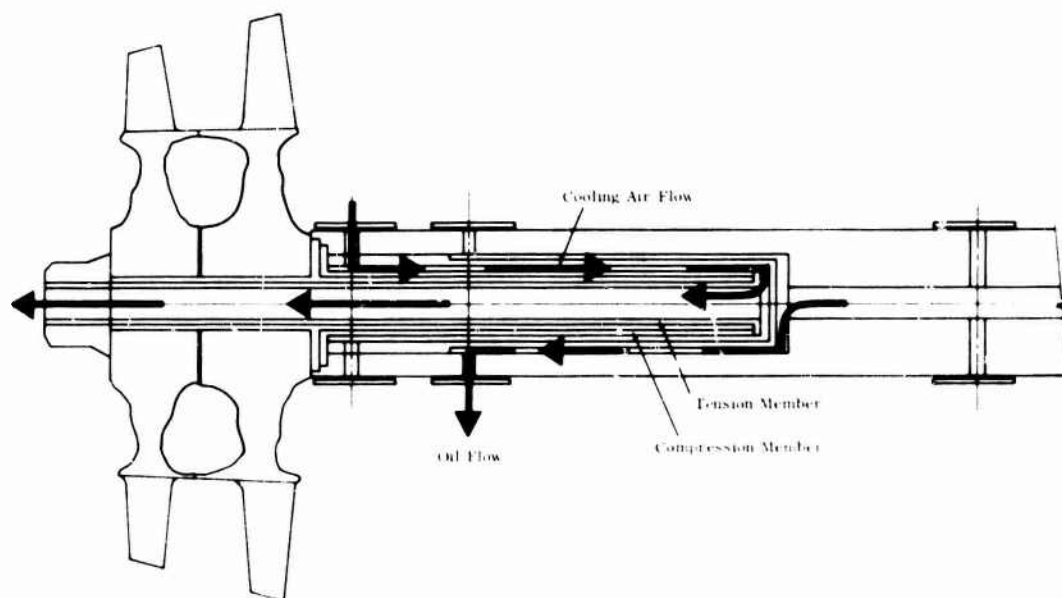
Figure 4.3.1-3 — Schematic View of Hollow Folded Bolt

Figure 4.3.1-4 — Ceramic (Left), Meta. (Right) Curvic Coupling Set

4.3.1.3 Design C

As can be seen from Figure 4.2.2-1 shown earlier, the Design B rotors included wide platforms at their rim which provided the inner wall of the flowpath. The Design C rotor configuration eliminated this platform connection as indicated in Figure 4.3.1-5 which also shows the finalized ceramic rotor attachment and special tooling designed to install the attachment with a controlled bolt pretension. Finite element, two-dimensional stress analyses and failure probabilities, using Weibull's weakest link
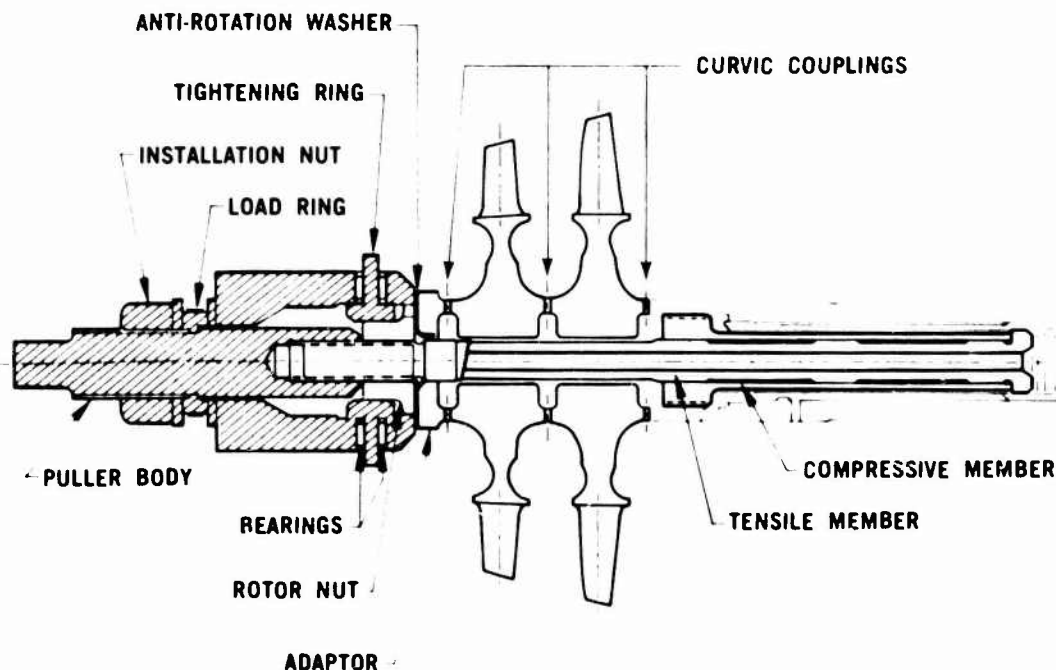
Figure 4.3.1-5 — Schematic View of Design C Turbine Rotor-Shaft Assembly Showing Installation Tool

theory, were computed for Design C rotors for various operating conditions confirming that hot pressed silicon nitride was a candidate rotor material with respect to mechanical properties.

Because of the continual difficulty in trying to fabricate a complete hot pressed silicon nitride rotor and in light of successful experiments to bond hot pressed silicon nitride to reaction-bonded silicon nitride, a duo-density rotor was conceived. In this, as shown schematically in Figure 4.3.1-6, a blade ring of injection-molded reaction-bonded silicon nitride is bonded to a hub of hot pressed silicon nitride. In addition to fabrication advantages, this concept was considered favorable since the more creep-resistant blade material suited the high temperature, relatively low stress conditions of the blade whereas the hub material suited the lower temperature, higher stress conditions of the hub.
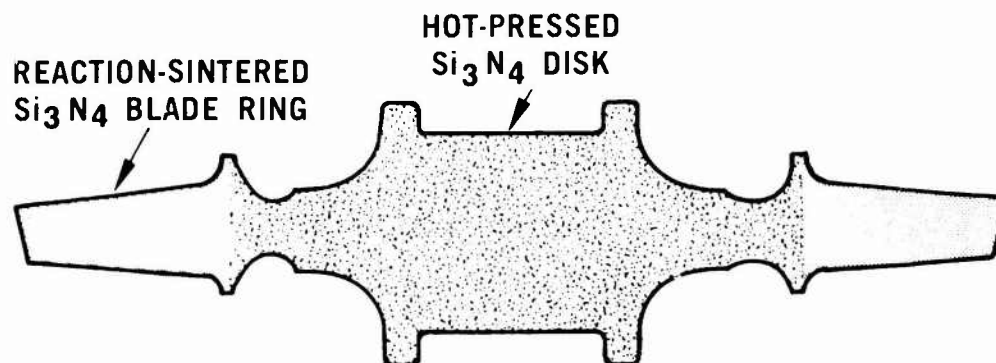
Figure 4.3.1-6 — Conceptual View of Silicon Nitride Duo Density Turbine Rotor

4.3.1.4 Designs D and D'

To provide a more intense effort on rotor development, the ceramic flowpath configuration was modified from Design C to Design D as shown in Figure 4.2.4-1 shown earlier. This modified flowpath used one basic rotor configuration for both first and second stages. The rotor disk design was refined to have a symmetrical profile common to both first and second stages. A three-dimensional computer model of the blade and platform was prepared (see Figure 4.3.1-7) and heat transfer coefficients calculated around the blades and in the cavity between the first- and second-stage rotors for various operating conditions.
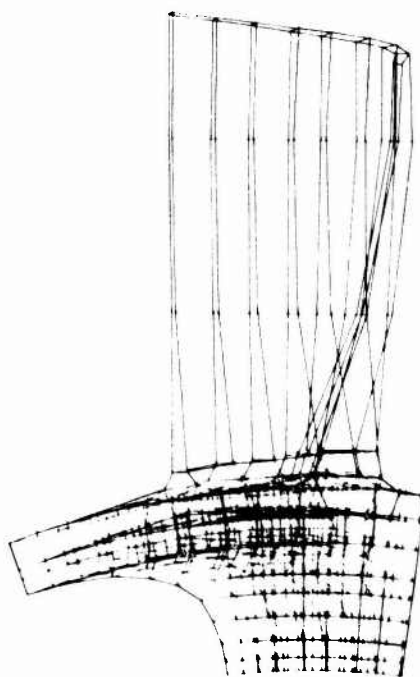
Figure 4.3.1-7 — Front View of Three Dimensional Model of Rotor Blade, Platform, and Disk Position Extending to the Throat Region

129

A three-dimensional stress study of the blade and platform revealed that the blade was not optimized for minimal stresses which were considered necessary, especially in a duo-density rotor configuration where the blade material has only moderate strength. Accordingly, using the 3-D computer codes, the rotor blade was redesigned for no twist and for radial stacking to minimize bending and torsional stresses. This rotor redesign was known as Design D'. Calculated maximum principal tensile stresses for the full-speed operating condition for an unwrapped blade surface are shown in Figure 4.3.1-8.
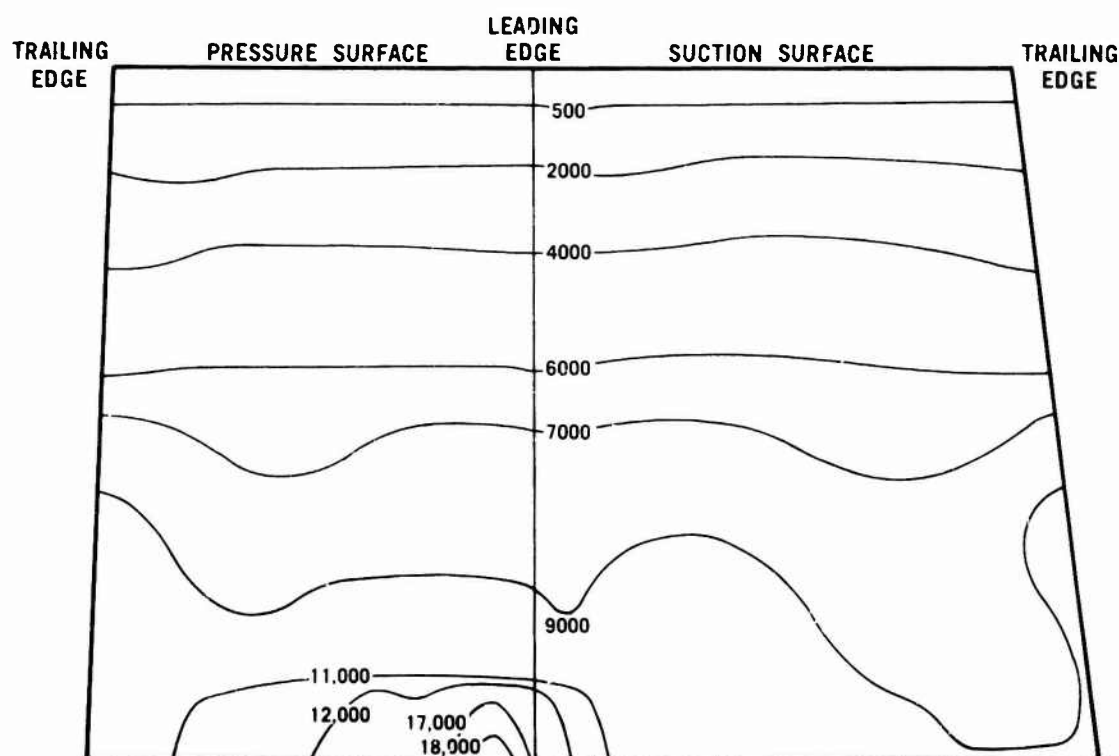
Figure 4.3.1-8 — Contour Map of Principal Tensile Surface Stresses (psi) of Rotor Blade at 2500°F T.I.T. and 100% Speed

Preliminary techniques for predicting lifetime reliability (see Section 3.1 of this report) were used to re-examine the disk profile of the Design D' rotor which, up to this point, had been designed on the basis of fast fracture. Disk contour modifications were investigated within the constraints of retaining the hot pressed hub blank and the rotor attachment hardware; this allowed for machining changes to the disk profile. Computer models of the disk were prepared (Figure 4.3.1-9) with the ability of varying the throat thickness from the original 0.300 inches. Design D' rotor time-dependent reliability was calculated for up to 25 hours, which was the initial durability goal of the rotor at full speed, maximum temperature conditions. It must be emphasized that time-dependent material properties used in these calculations were, at this stage, extremely preliminary and the analytical technique itself had not been verified. Table 4.3.1-1 shows the calculated 25-hour reliability and, interestingly, shows that a 0.400 inches thickness throat has better 25-hour reliability yet worse fast fracture reliability than the 0.300 inches throat configuration. The 0.480 inches throat shows a somewhat lower reliability but nonetheless was selected for the planned rotor hot spin testing program because of: (i) the very preliminary nature of the analytical techniques and material properties to predict time-dependent reliability, (ii) the ability to start hot spin testing with the thick throat and then, if deemed necessary re-machine rotors to a lesser throat dimension, and (iii) all calculations had assumed purely elastic behavior; any plastic behavior would tend to favor a thicker throat. Figure 4.3.1-10 shows maximum principal tensile stress contours for the 0.480 inch thick rotor disk for the full speed, 2500°F turbine inlet temperature condition. This was the configuration of the six duo-density rotors hot spin tested in this program.
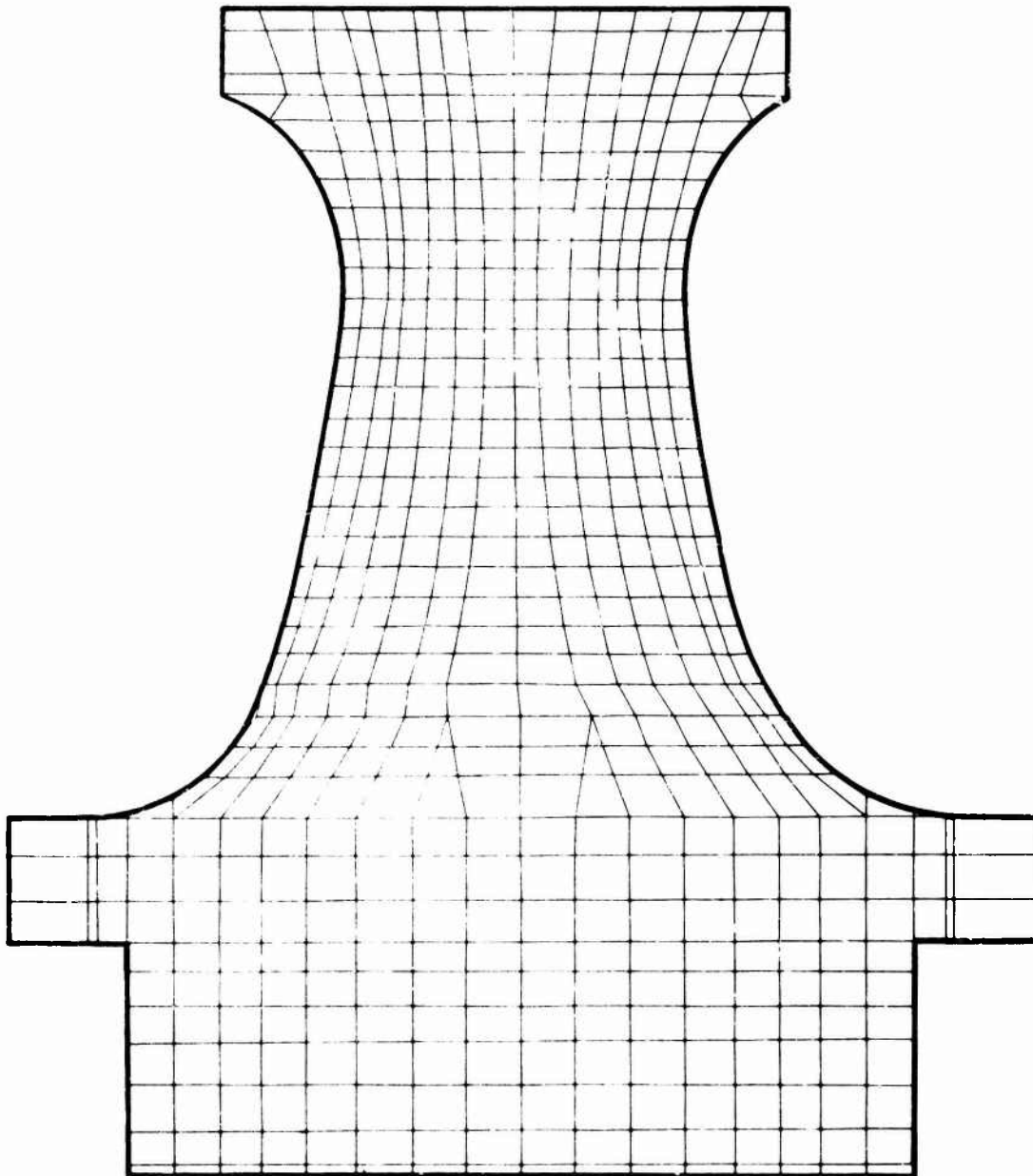
Figure 4.3.1-9 — Rotor Disk Model, 0.400 Inch Throat

TABLE 4.3.1-1

FAST FRACTURE AND TIME DEPENDENT RELIABILITY ESTIMATES FOR THE
FIRST STAGE TURBINE DISK (EXCLUDING BLADES) AT 2500°F TIT AND 100% SPEED

Throat Thickness (Inches)	SCG Threshold Temperature(+) °C, °F	Reliability (Fast Fracture)	Reliability (Time Dependent, SCG) (25 Hours)	Critical SCG Disk Region
.300	770°, 1420°	.99787	.29156	Throat
.400	770°, 1420°	.99647	.82042	Throat
.480	770°, 1420°	.98986	.60986	Bore

(+): Threshold temperature for a loading rate of 1 MPa/min. (8.7 ksi/hr.) on the "A" size MOR test bar.

131
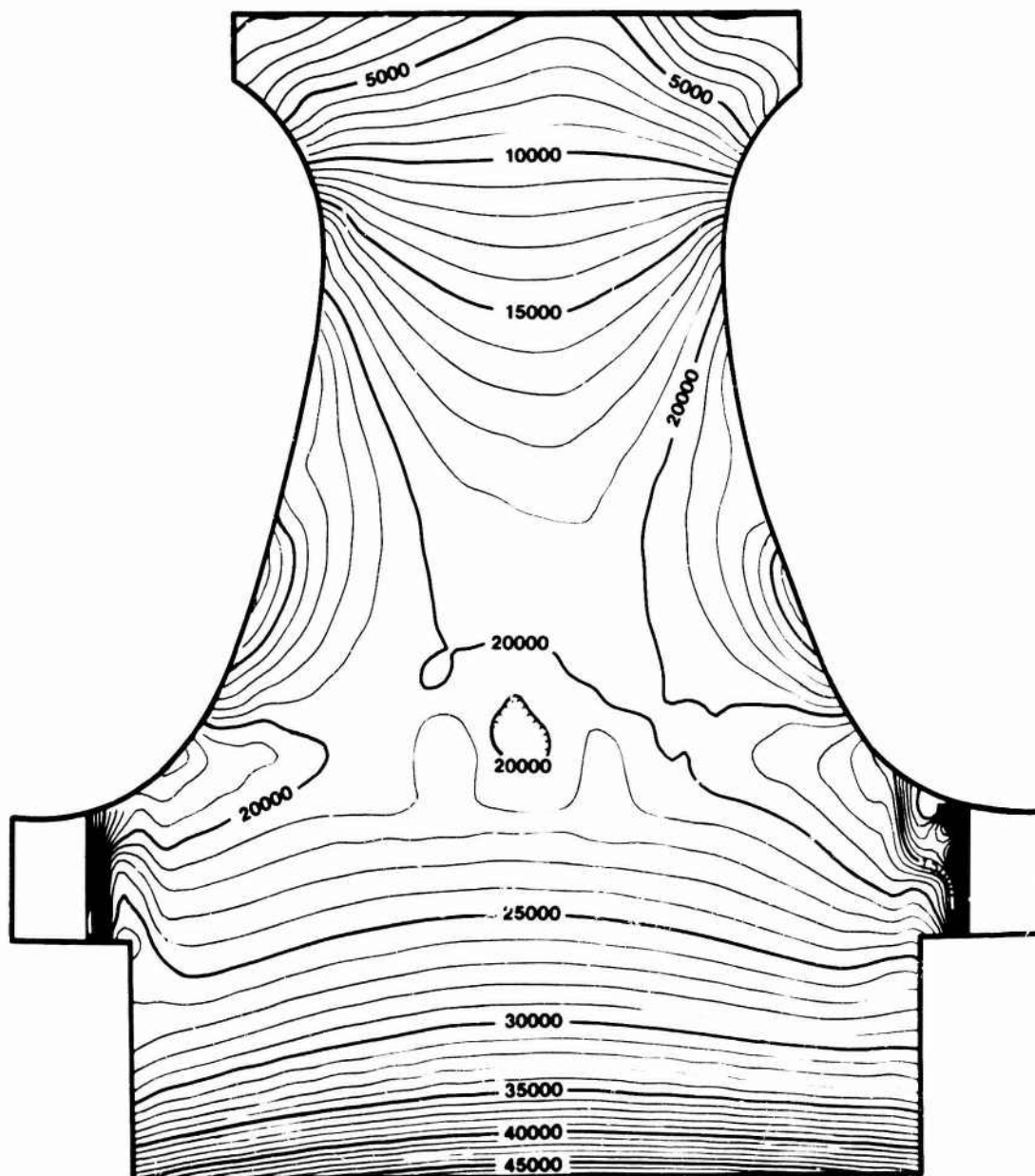
Figure 4.3.1-10 — Maximum Principal Tensile Stresses (psi) for Rotor Disk, 0.480 Inch Throat, at 2500°F T.I.T. and 100% Speed

4.3.2 CERAMIC ROTOR MATERIALS AND PROCESSING

4.3.2.1 Introduction

A variety of approaches for the fabrication of ceramic turbine rotors were conceived and evaluated and reported in detail in semi-annual progress reports[1-7]. Since fully dense silicon nitride or silicon carbide appeared to be the most attractive candidates from design aspects (Section 4.3.1), initial approaches involved these materials. During work on these approaches, the duo-density approach was conceived and development work was initiated. As progress was made, this duo-density approach became progressively more attractive in terms of possibly providing all-ceramic turbine rotors capable of meeting program goals while still meeting the time and funding constraints of the program. The latter factor was paramount in the exercise of judgment as to whether to terminate a specific fabrication approach or to continue to expend time and money in its development. Therefore, while some of the rotor fabrication approaches were considered to be promising, extensive additional effort was required for success. In terms of both time and funding, such effort could not be continued within the program constraints and work was therefore terminated, sometimes reluctantly.

4.3.2.2 Exploration of Rotor Fabrication Methods

Several rotor fabrication methods were conceived and evaluated both in-house and through various firms having technical expertise in the specific processes of interest. These approaches are discussed in the remainder of this section.

'Welded' Hot Pressed Si₃N₄ Rotor

The Norton Company conducted development work on a proposed approach to fabricate a monolithic rotor which would be made up of 36 individual hot pressed Si_3N_4 rotor blades with wedge-shaped roots to be assembled into a suitable fixture and, with the addition of more Si_3N_4 powder, re-hot pressed or 'welded' into a complete monolithic rotor.

Much of the program effort was expended in attempting to produce the small airfoil section to the required shape. While formed hot-pressed blades approximating airfoils were produced, as illustrated in Figure 4.3.2-1, it was not possible to produce the blades to print. In particular, it was difficult to obtain thin tips and trailing edges, especially while avoiding reaction with the graphite hot pressing die materials.

Figure 4.3.2-1 — Hot Pressed Silicon Nitride Turbine Blade

A group of wedge-shaped root sections were fabricated and are shown in Figure 4.3.2-2 as assembled in a simulated 'welding' fixture. The problem of maintaining proper stacking and alignment during the 'welding' process was also recognized and, along with the difficulties in hot pressing the airfoil shape, caused this effort to be terminated. Even if the problems could be solved, this approach appeared economically unattractive for other than production of a few rotors for evaluation purposes.
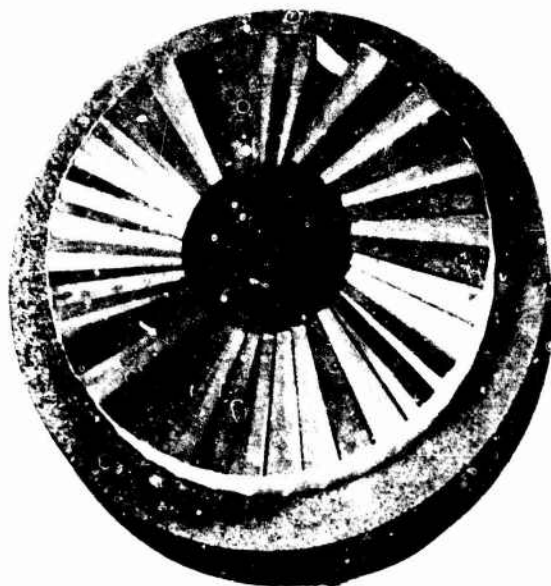

Figure 4.3.2-2 — Simulated Blade Welding Assembly Fixture

Pseudo-Isostatic Hot Pressed Si_3N_4 Rotor

Another technique for assembling a rotor from a group of segments was conceived and evaluated in-house. Pie-shaped RBSN segments, comprising an airfoil blade and a root section as shown in Figure 4.3.2-3, were fabricated by injection molding. Note that the root section approximates the hub configuration and extends to the bore of the rotor. After nitriding, 36 of these segments were assembled into another injection-molding tool, Figure 4.3.2-4, and the remainder of the hub region was injected, which served to bond the segments into a complete rotor. Following a second nitriding operation to nitride this latest material, the part was ready for the densification step.

Figure 4.3.2-3 — Molded RBSN Rotor Segment
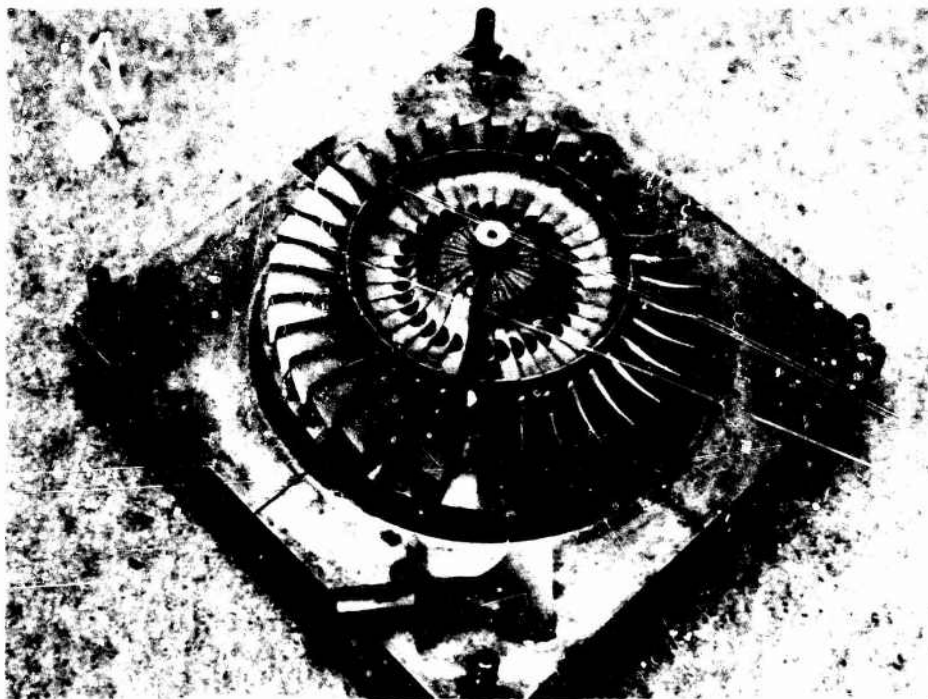
Figure 4.3.2-4 — Assembly of Molded Rotor Blades

Pseudo-isostatic conditions were attempted in a conventional graphite hot press, having a cylindrical body and round top and button punches. The rotor was packed into the center of a bed of powder, and heat and pressure applied to achieve densification. If the proper powder could be developed, it was expected to act in a similar means to a liquid medium and permit equal pressure to be applied to all sections of the complex-shaped rotor for densification. Some experiments in densifying AME Si_3N_4 powder containing 2% MgO produced test bars of 3.19 g/cc density and a three-point MOR strength of 95,000 psi, indicating that the process was at least capable of providing high-strength material.

Considerable effort was expended in studying the nitridation of the injection-molded silicon in order to produce nitrided material high in the α phase, which was necessary to produce high-strength HPSN. Methods were found which resulted in RBSN having such a high α phase [1,2]. The addition of the MgO densification aid was also studied via adding MgO to the silicon powder before molding and by impregnating the final RBSN rotor assembly with soluble magnesium-containing salts.[1,2]

Various grades of graphite were evaluated as the pseudo-isostatic medium, with best results observed with the use of graphite flakes. A number of rotors were assembled and subjected to the densification process. A major problem of non-uniform flow of the graphite powder under pressure was never solved. This non-uniform flow caused deformation and fracture of the thin rotor blades.[2,3]

A secondary problem caused by the graphite was a severe surface chemical reaction with the Si_3N_4 forming SiC, resulting in very low material strength. Boron nitride powder was substituted for the graphite powder which solved the reaction problem. However, the BN did not behave any more like a fluid than did the graphite, so the distortion and cracking problem remained unsolved. The BN also densified to a high degree during the hot pressing cycle and was very difficult to remove from around the vanes. A number of attempts were made to use graphite inserts between the blades which greatly reduced but did not solve the deformation problem.[3]

Due to these rather substantial problems, further work on this approach was terminated. The basic approach is attractive if monolithic rotors could be fabricated, eliminating the need to form and assemble individual segments, and, most importantly, if the ideal pseudo-isostatic medium could be found. Further research in this area may be worthwhile.

Hot Pressing of Si₃N₄ Rotor Using 'Conformable Tooling'

Another approach to forming a monolithic rotor of dense silicon nitride was proposed by the Joseph Lucas Company in the U.K. The rotor would be assembled, prior to hot pressing, from 36 individual oversized blade sections formed by injection molding using α phase Si_3N_4 powder. Two hub-halves, formed by cold pressing the same Si_3N_4 powder were then added to the assembly as shown in Figure 4.3.2-5. The rotor assembly was then densified and bonded by a hot pressing operation; the direction of applied load is noted in Figure 4.3.2-5.
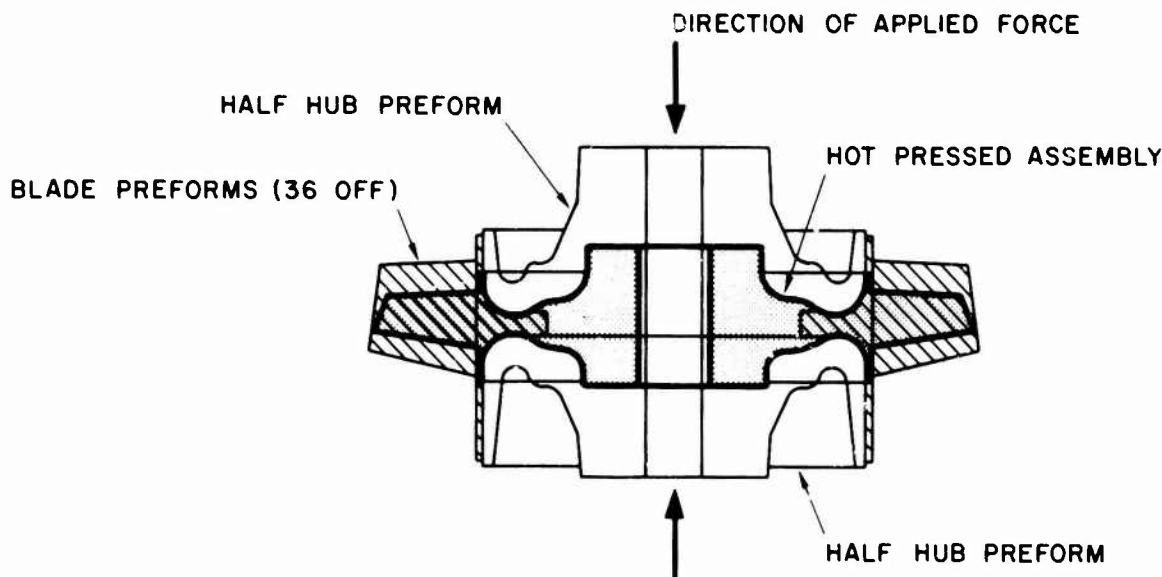
Figure 4.3.2-5 — 'Conformable Tooling' Rotor Assembly Concept

The unique aspect of this concept was the use of 'conformable' tooling instead of conventional graphite components for the hot pressing dies. While the nature of the materials used to make the 'conformable' tooling remain proprietary with Lucas, the concept called for the tooling to densify under load and temperature to the same degree and at the same rate as the Si_3N_4 rotor component, thus in principle providing quasi-isostatic loading to the rotor.

A number of trials were made at Lucas, which did result in densification of the Si_3N_4 material to 3.08 g/cc (97% T.D.). However, extreme distortion and fracture of the blades was noted in every case. Two views of one of these unsuccessful trials are shown in Figure 4.3.2-6. Most of the blades have been fractured, while the remaining blades exhibit severe distortion. This trial was made with a flat disk-shaped hub simulating the actual contoured hub design. The change in volume during densification exceeded 2:1, since the pre-forms were of low density.

Since it appeared that the results of the 'conformable' tooling concept were not promising, and much additional time would be needed to reach the feasibility stage, this work was terminated.

Chemically Vapor Deposited Silicon Carbide Rotor

A unique forming method with capability for accurate fabrication of complex shapes like turbine rotors is Chemical Vapor Deposition (CVD). Various gases can be combined at high temperature to produce compounds which are deposited slowly upon a substrate to form a dense structure of high purity material. Prior work at Energy Research Corporation on CVD silicon carbide had demonstrated bend strengths of over 100,000 psi on small test samples, and had also demonstrated that small airfoil shapes could be deposited inside of a female mold[1] A program was initiated with this firm to develop the technology for fabrication of CVD SiC rotor blade rings, with the intention of developing attachment methods to SiC rotor hubs, had satisfactory blade rings been developed.
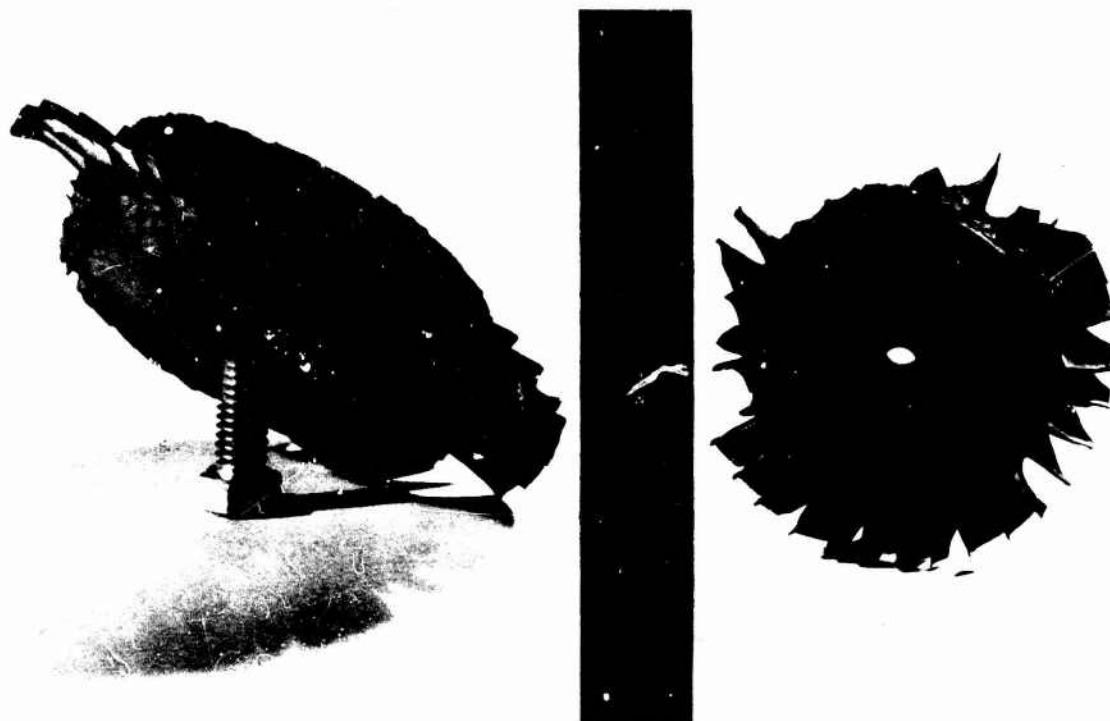
Figure 4.3.2-6 — Results of Unsuccessful Assembly Trial Using the 'Conformable Tooling' Approach

Much of the early work on this approach was spent on mold development.[2,3] Two types of molds were selected for evaluation. One type was a silica-zirconia ceramic mold, formed by conventional investment mold techniques over a wax pattern. Silicon carbide deposited on this mold surface was severely weakened by oxygen contamination from the mold. Thin barrier coatings of tungsten were applied to the ceramic molds, but resulted in only slight improvement in quality of the deposited SiC. The second mold type to be evaluated was formed by coating a beryllium copper pattern with CVD tungsten. The beryllium copper was subsequently removed by acid leaching, leaving a very thin tungsten mold, as illustrated in Figure 4.3.2-7. Due to the decreased mass of this thinner mold, as compared to the ceramic mold, temperature gradients during deposition were immediately reduced and better quality SiC with no apparent contamination from the mold resulted. Process development, therefore, proceeded using this type of mold.
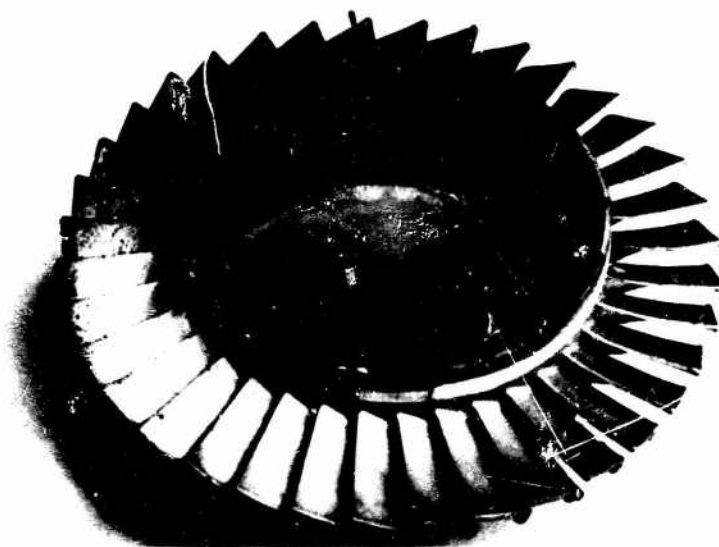
Figure 4.3.2-7 — Tungsten Mold

Deposition parameters evaluated included temperature distribution within the mold, concentration of reactant gases within the carrier gas, flow rate of the gas mixture, deposition time and temperatures. A number of CVD SiC blade rings were produced and delivered by Energy Research for evaluation. A group of four such blade rings is shown in Figure 4.3.2-8. All of the blade rings showed evidence of severe residual stress, as noted by spalling of chunks of material, at times accompanied by considerable energy release.
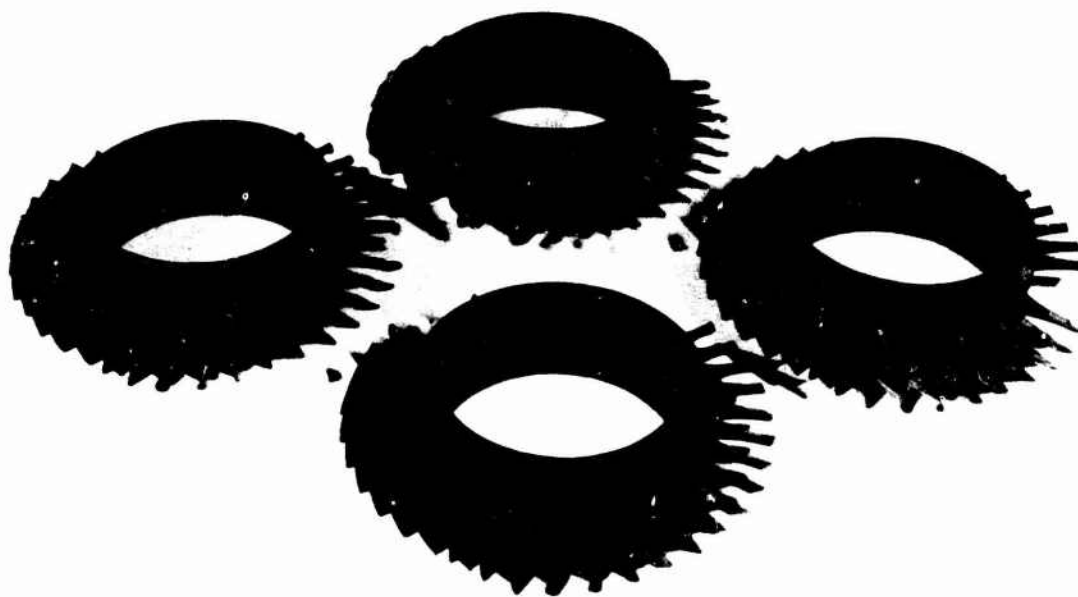
Figure 4.3.2-8 — CVD Silicon Carbide Rotor Blade Rings

Three of these rings were evaluated by spin testing, resulting in blade failures at 13,260, 11,360 and 16,590 rpm, respectively; these speeds were estimated to produce stresses of 2,000-3,000 psi.

Another problem was observed in studying the material produced. Figure 4.3.2-9 is an electron micrograph taken at 7100X of a corner section, showing the orientation effect of growth upon two mold surfaces at a right angle to each other, with a resulting diagonal junction plane. Large columnar crystal growth was also observed in studying the microstructure of the CVD SiC, which is deleterious to the attainment of high strength.

At this point in time in the program, it appeared that development of a high-strength SiC blade ring made by the CVD process would require more time than was available in order to meet program objectives, so this work was terminated. However, further work is recommended to attempt to solve the problems encountered.

Machined Rotors

Techniques were evaluated which appeared plausible for machining of complete turbine rotors from billets of hot pressed Si_3N_4 and SiC. Such machining was never seriously considered as a practical means for production of rotors, but could possibly have been useful for fabricating a few rotors for evaluation to check out material properties, design methodology and rotor testing. Two techniques were evaluated, ultrasonic machining and electronic discharge machining (EDM). Ultrasonic machining appeared feasible for both Si_3N_4 and SiC, but only hot pressed SiC had adequate electrical conductivity to permit EDM. Therefore, ultrasonic machining was investigated for hot pressed Si_3N_4 and electric discharge machining was investigated for hot pressed SiC.

Figure 4.3.2-9 — Microstructure of CVD Silicon Carbide at Joint of Two Adjacent Areas (7100X)

Ultrasonic impact grinding, used to make turbine rotors from hot pressed silicon nitride, employed a non-rotating tool oscillating at high frequencies (20 KHZ) and small amplitudes (0.002 in.). The tool, shown in Figure 4.3.2-10, was sprayed with an abrasive slurry of 200 grit boron carbide which was drawn under and through the tool by vacuum. End-cutting of constant cross section airfoils, the first step in this process, was achieved as shown in Figure 4.3.2-11. However, the rotor blades, designed to provide optimal aerodynamic performance, required twisted, tapered airfoils. The second step in this process was to convert the constant airfoil shapes into the required twisted, tapered shapes by a combination of side and end-cutting modes. These attempts were unsuccessful as they resulted in breakage of the airfoils and the tools. This, combined with the excessive cutting time (40 minutes/constant section airfoil) and tool wear (1 part tool to 3 parts silicon nitride), resulted in the suspension of further effort on this approach, although ultrasonic machining of Si_3N_4 has since been used successfully for simpler shapes.

A program was carried out to investigate the feasibility of electric discharge machining a turbine rotor from a hot pressed billet of dense silicon carbide. A cutting rate of 0.206 cubic inches per hour with a tool wear-to-material removal rate of 1 to 9 was achieved on one grade of Ceradyne hot pressed silicon carbide. However, a rough surface finish and a preponderance of surface cracks resulted in reducing the strength of the material by about 50%. This, combined with breakage of thin airfoil sections, caused this effort to be suspended.

Conclusion

As noted, a number of approaches for the fabrication of small axial turbine rotors were investigated in the early stages of this program. Several of these approaches were dropped when enough information had been obtained to permit judgment that they would not be successful within the program timing. Of these approaches, pseudo-isostatic densification and CVD forming appeared feasible given extensive additional effort.

One final factor which entered into the judgment to stop further work on the fabrication approaches described in this section was the increasing attractiveness of a new fabrication approach called "duodensity Si_3N_4 rotor." A description of the development of this process occupies the balance of this section of the report.

Figure 4.3.2-10 — Ultrasonic Tool for Machining Constant Thickness Blade Positions
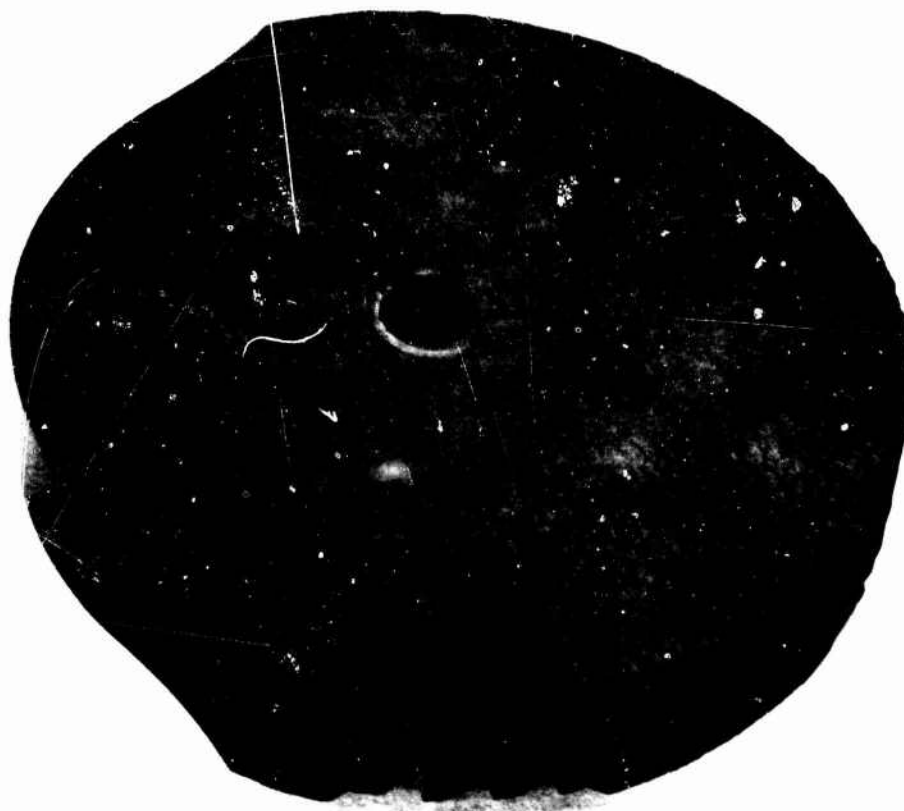

Figure 4.3.2-11 — Constant Section Blades Ultrasonically Machined in HPSN Disk

4.3.2.3 Duo-Density Silicon Nitride Turbine Rotor Fabrication

Introduction

As noted in the previous section, a number of rotor fabrication approaches were conceived, developed, evaluated and finally terminated because they were unable to provide monolithic all-ceramic turbine rotors within program timing constraints. These investigations, along with some successful early experiments in bonding of hot pressed Si_3N_4 to reaction-bonded Si_3N_4, led to the conception of the duo-density Si_3N_4 rotor, which appeared compatible with known ceramic forming processes, even though further development was required.

The design concept, illustrated earlier in Figure 4.3.1-6, makes best use of the high strength of hot pressed silicon nitride for the rotor hub region, where operating stresses are highest. Also, operating temperatures are lower in the hub region than in the blades, which helps to circumvent the loss in strength at high temperatures of the HPSN. Another conceptual advantage is the rather simple shape of the hub, which appeared possible to form by the hot pressing process which is limited by its inability to form complex shapes.

The very complex-shaped rotor blade ring can be readily fabricated from injection-molded RBSN to near net shapes. While the strength of RBSN is much lower that that of HPSN, the operating stresses in the blade ring are also much lower than in the hub, which favors the use of RBSN. Another advantage of using RBSN for the blades was its good strength retention at the high operating temperatures of the blades.

The duo-density concept therefore appeared to be logical considering the maximum utilization of the advantages of the two materials while minimizing weaknesses. The remainder of this section will be devoted to a discussion of development of fabrication techniques for the components and the development of the hot press bonding assembly method for the duo-density rotor.

Blade Ring Fabrication

By the time the duo-density rotor had been conceived, an improved RBSN material with a density of 2.55 g/cm³ had been developed. The duo-density rotor required the molding of monolithic rotor blade rings using this material, as shown in Figure 4.3.2-12.
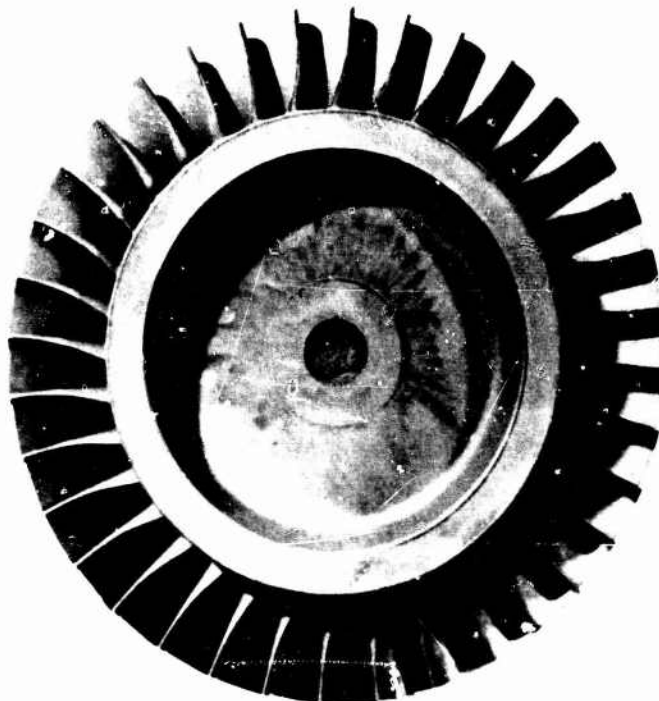
Figure 4.3.2-12 — As-Molded Blade Ring for the Duo Density Rotor

These first generation rotor blade rings were fabricated on a 450-ton Reed Prentice injection molder with horizontal clamp. The tooling was formed from hardened steel; a scroll mechanism actuated the blade inserts. Due to the blade geometry, a compound angle of withdrawal was required in this tool; i.e., the inserts moved up and out on an incline as the die was opened. The material was injected through a central gate, as illustrated in Figure 4.3.2-13. A view of the tool in the open position is shown in Figure 4.3.2-14.
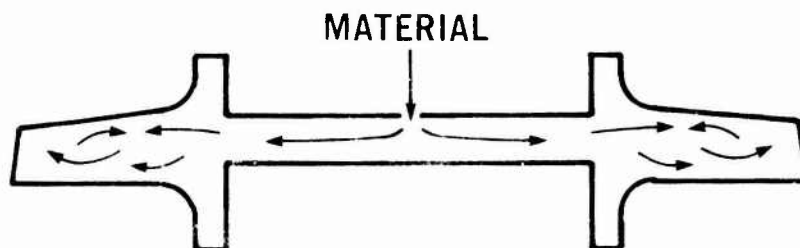
MATERIAL

Figure 4.3.2-13 — Schematic View of Material Flow in Blade Ring Molding Tool
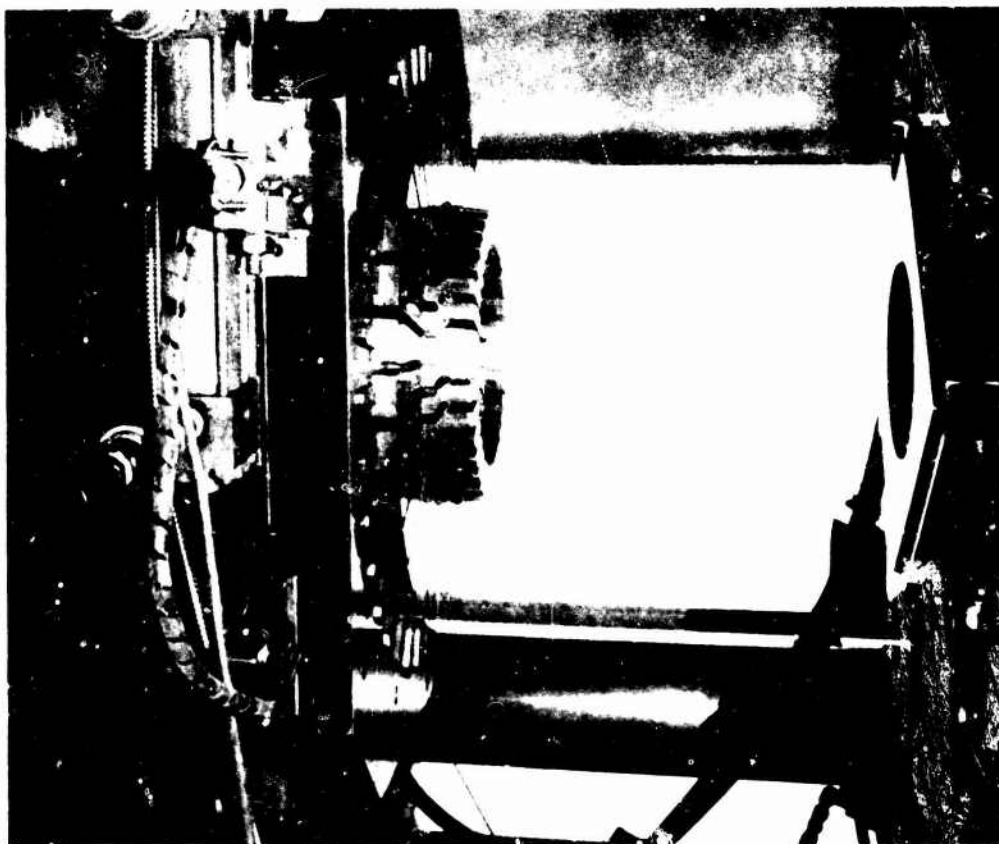
Figure 4.3.2-14 — Rotor Blade Ring Injection Molding Tool Mounted in Molding Machine

Figure 4.3.2-13 also illustrates the material flowpaths through the tool. Blade quality was low due to the compound angle of withdrawal of the inserts and a knit line which resulted at the trailing edge of the blade. Erratic test performance resulted from the blades cracking.[3] The next phase of development addressed this problem and others which had appeared during this preliminary development. They were:

1) The molding process possessed no accurate controls on time, temperature or pressure, the major variables of injection molding.

2) There was no control of die cooling, although heat was available when required.
3) Die actuation was manual, inherently slow, and required a complete cycle of close, stop, and open before the constraining blade inserts could be released from the blades; this prevented flexible variation of time and temperature.
4) There was no provision to acquire pressure and temperature data from within the tool cavity.

A second generation of rotor tooling and modifications to existing molding equipment corrected those deficiencies noted in the earlier equipment and enabled fabrication of higher quality rotors.[4]

The second generation rotor, Design D', was lower in stress and more uniform in cross-sectional area than the previous design,[5] as discussed in Section 4.3.1.4. By changing the blade configuration, an axial, unidirectional pull of the blade-forming inserts was provided. Sometimes the inserts stuck to the blades, which often caused the blades to crack when the inserts were axially pulled out. Delaying the pull on every other insert and polishing the surface to 1μ RMS eliminated this cracking.

Since the component could not be allowed to shrink while constrained within the tool, hydraulic actuation was employed to increase the opening speed of the tool to allow removal of the inserts as quickly as possible. Cooling passages were added to the tool to improve temperature control within the die. By upgrading the temperature controllers, both the machine and die temperature control was improved. Vacuum capability was added to the machine to allow reproducible venting of the die. Before this, material tended to plug the normal vents; i.e., those small enough to prevent flash formation. The vacuum system was designed to remain free of contaminants and was provided with a closed loop control to prevent molding when vacuum was not drawn. A new material with a nitrided density of 2.7 g/cm^3 and characteristic strength of 35-40 KSI, discussed in Section 3.2.1, had a lower 'green' strength than the previously used 2.55 g/cm^3 material.[6] The yield of higher density rotors was increased by the addition of an automatic spray of mold release, even when using the material with weaker 'green' strength.

A solid state control system was built to improve control of the molding process.[7] This allowed accurate timing of all sequences and the removal of inserts based upon component temperature. It interfaced with two strip chart recorders and a flow control device to regulate the injection rate of material into the die.[8] Additional data was acquired by an oscilloscope which traced cavity pressure versus ram position, as shown in Figure 4.3.2-15.
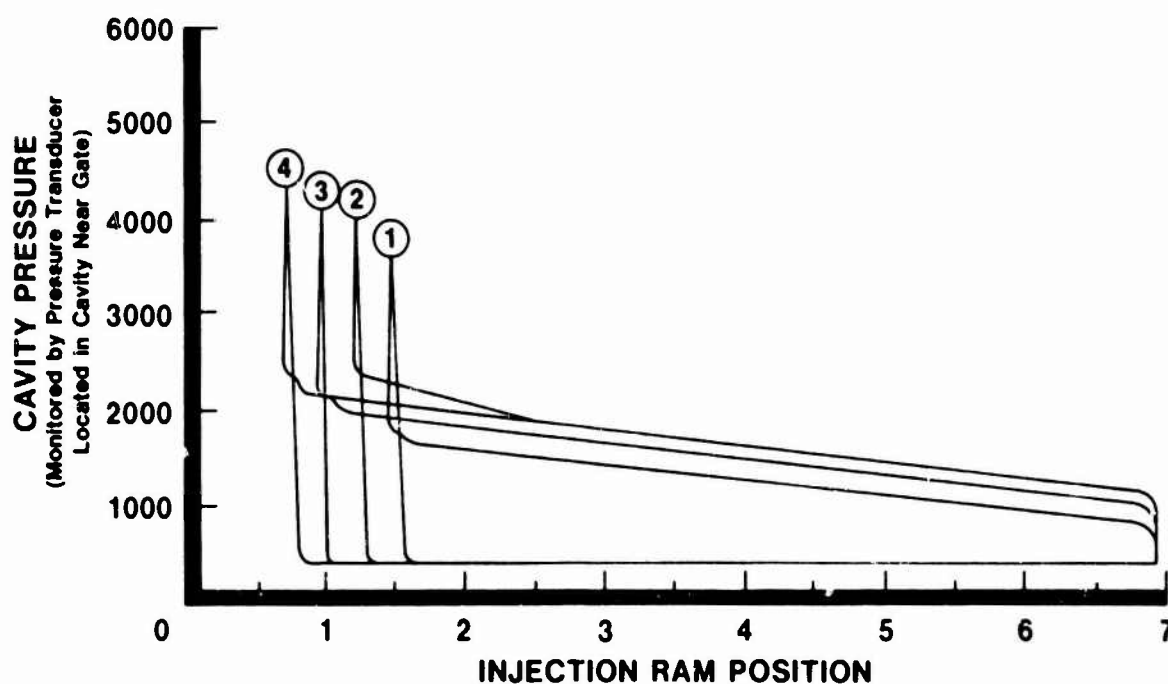

Figure 4.3.2-15 — Typical Profile of Cavity Pressure Vs. Ram Position

Several parametric studies were performed using this molding system to identify those parameters required for molding high quality rotor blade rings.[9] In general, high injection rates and low holding pressures were needed to mold blade rings free of voids and cracks. During this period, typical flaws were voids, cracks and inclusions.

By premixing the molding material under vacuum and carefully controlling flow into the die, voids were reduced.[9] Cracks were eliminated by controlling the mold pressure[9] and by minimizing deflection of the tool during injection.[10]

Inclusions were eliminated by more thoroughly premixing the material and elevating the nozzle temperature.[11] As a result of these changes in the molding process, the yield of rotor blade rings having no visible flaws in as-molded parts steadily increased during the course of the program, as noted in Figure 4.3.2-16.
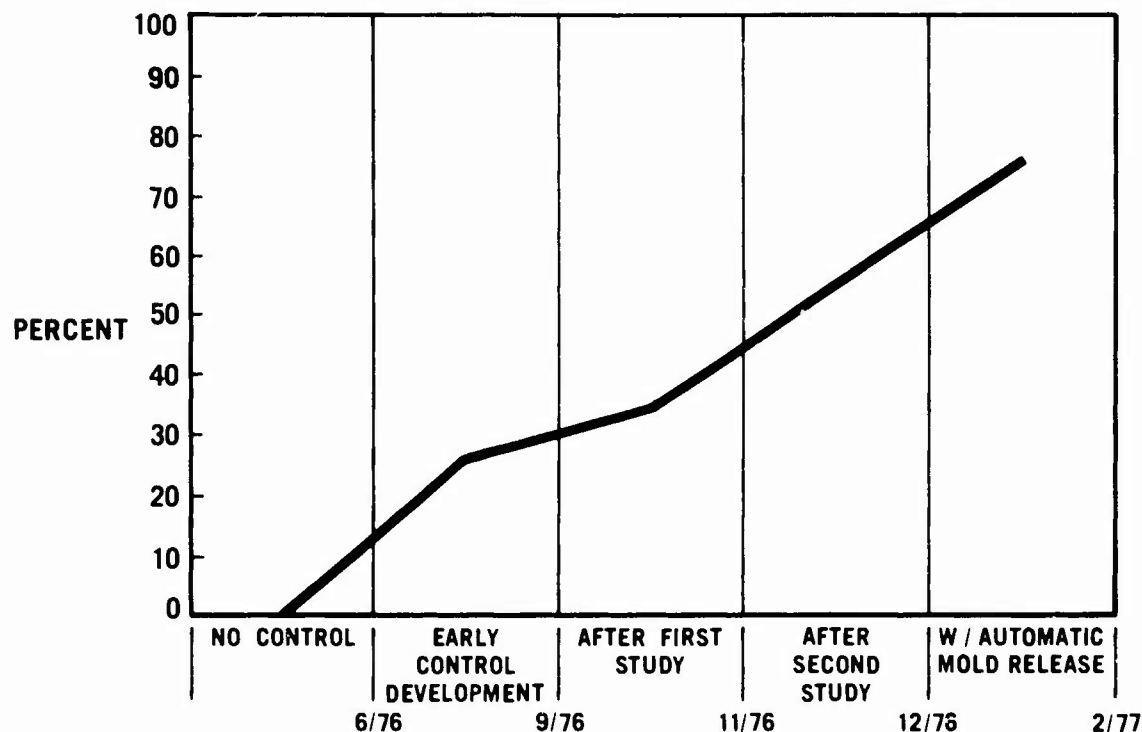
Figure 4.3.2-16 — Improvement in Quality of Rotor Blade Rings Vs. Time

In order to mold high quality rotors, accurate control of all process parameters is essential. The compressibility, non-Newtonian flow and low 'green' strength of ceramic molding compounds makes process control and data analysis difficult. However, with the application of the latest electronic controls, process control was improved to produce large numbers of high quality molded blade rings required for the duo-density rotor development program.

Blade Fill

Early work in press bonding a rotor blade ring to a hub, as discussed in the next section, showed that the entire rim of a blade ring needed support, particularly between the blades, to avoid deformation and cracking of the blades and rim when pressure was applied. A number of different support systems were tested.[1,2,3] and although some of them significantly reduced deformation and cracking, only one was found capable of providing sufficient support for a good bond between rim and hub while allowing no damage to the blades or rotor rim. This was a slip cast double blade fill technique which also allowed easy removal of the assembly after the press bonding operation. A description of the process follows.[4]

Silicon nitride blade rings, after machining and inspection, were dipped in a boron nitride/methylethyl ketone slurry. The boron nitride served as a lubricant for subsequent blade fill removal and as a barrier material which prevented bonding between the blade ring and blade fill during the nitriding step.

The first blade fill operation consisted of manufacturing the removable inserts between the rotor blades, as shown in Figure 4.3.2-17. The boron nitride coated rotor blade ring, with its trailing edge down, was placed into a contoured plaster block, shown in Figure 4.3.2-18. A concentric silastic rubber ring with access holes to each blade cavity was press fitted over the leading edge contour of the blade ring; this masked the leading and trailing edges of the blades. The independent casting cavities were formed by placing a plaster ring over the outside of the rotor blade ring. Once the above assembly was completed, a silicon metal slip was introduced centrifugally into the cavities through the access holes in the rubber ring. When casting was complete, the fixtures were removed and the rotor blade ring with the cast inserts was dried.
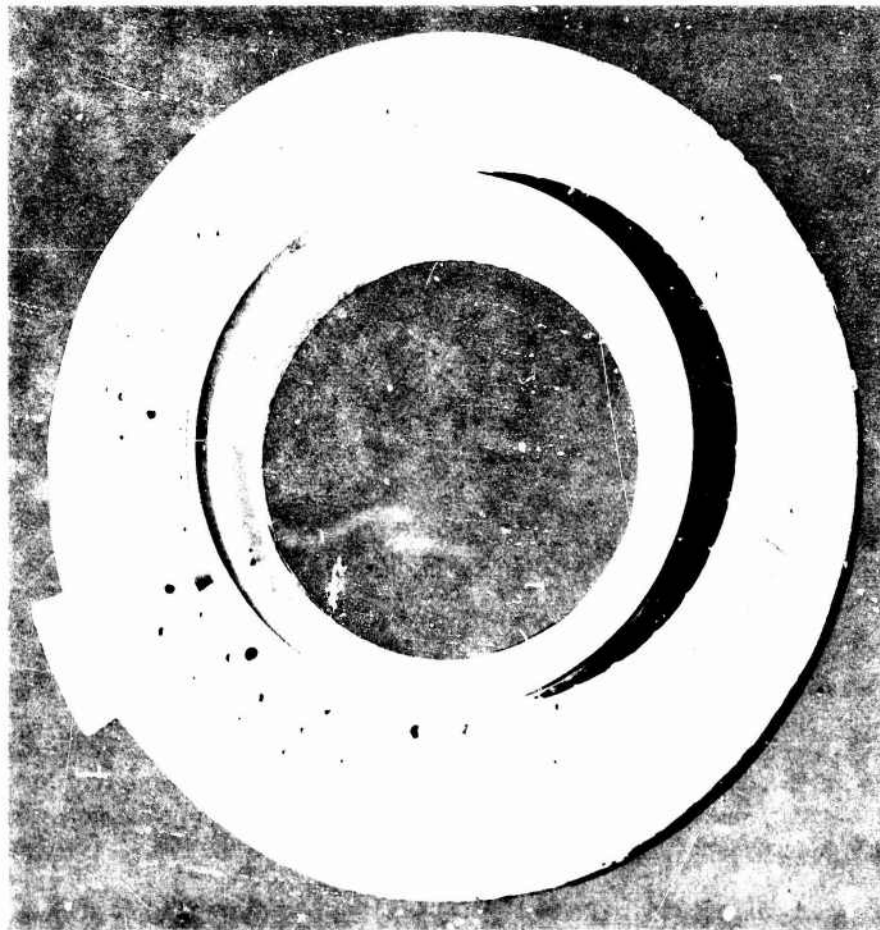
Figure 4.3.2-17 — Blade Ring Showing First Blade Fill
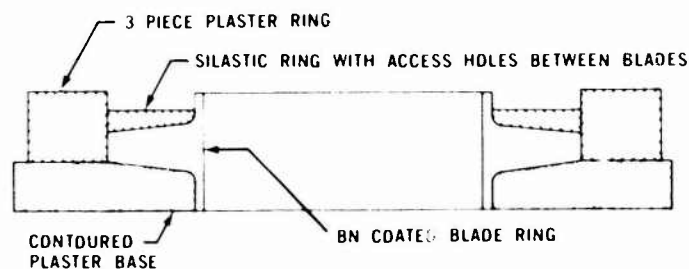
Figure 4.3.2-18 — Schematic View of First Blade Fill Operation

145

The second blade fill operation was initiated by applying another coating of boron nitride to this assembly. Once the coating had dried, the assembly was centered in a graphite retaining ring on a plaster block. A low density silicon metal slip was introduced into the cavity which encased the first blade fill assembly. After being allowed to dry, the entire assembly was nitrided using the standard demand system cycle, then diamond ground to its final dimensions prior to press bonding, as illustrated in Figure 4.3.2-19.

Figure 4.3.2-19 — Completed Blade-Filled Rotor Prior to Press Bonding

After the press-bonding operation, the blade fills were removed with care to avoid damage to the encapsulated blade ring. A 300-watt CO_2 laser was then used to make a circumferential cut 0.100" deep around the second or outer blade fill, as shown in Figure 4.3.2-20. A series of four to six radial cuts 0.250" deep were then made along the top and bottom surfaces, shown in Figure 4.3.2-21, with the laser beam. The pie-shaped segments of the outer blade fill were easily removed from the rotor assembly which, in turn, allowed removal of the individual inserts between the blades.

Controlling the boron nitride thickness appeared to be a critical step in this process. If the boron nitride was too thick in the rim region, the rim was deformed until the compressed boron nitride either supported the rim or the rim fractured. But, if the boron nitride was too thin, the blade ring bonded to the blade fill during the nitriding process which made removal of the blade fill impossible. A thick layer of boron nitride was desirable on the airfoils so that small motions of the blades were accommodated without fractures. The coating thicknesses found to be effective are shown in Figure 4.3.2-22. The thin sections range from 0.001" to 0.003", while the thick sections from 0.005" to 0.010".

Controlling the density of each blade fill was also important. Low density blade fills were easily cracked and compressed during hot pressing, which damaged the blades. When the density was too high, the blade fill did not nitride completely, and the free silicon exuded during nitridation and bonded the assembly together. The slip presently in use contains five weight percent of silicon nitride powder. This lowers the cast density and still provides nitrided densities in the range of 2.55 to 2.65 g/cm³.[7]

OUTER BLADE FILL

POINT OF
CONTACT OF
LASER BEAM

ROTARY TABLE
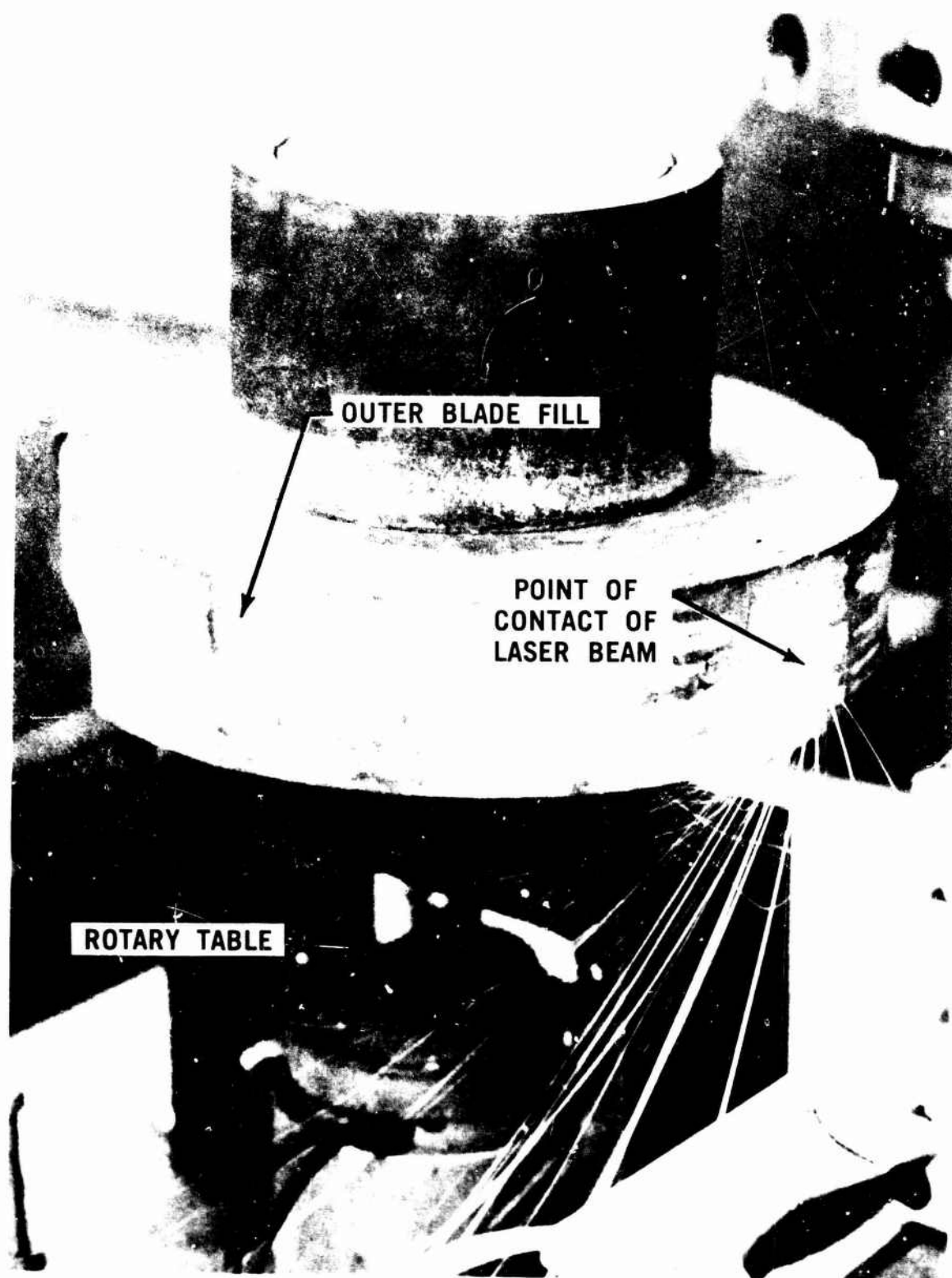
Figure 4.3.2-20 — Circumferential Cutting of Outer Blade Fill with CO_2 Laser
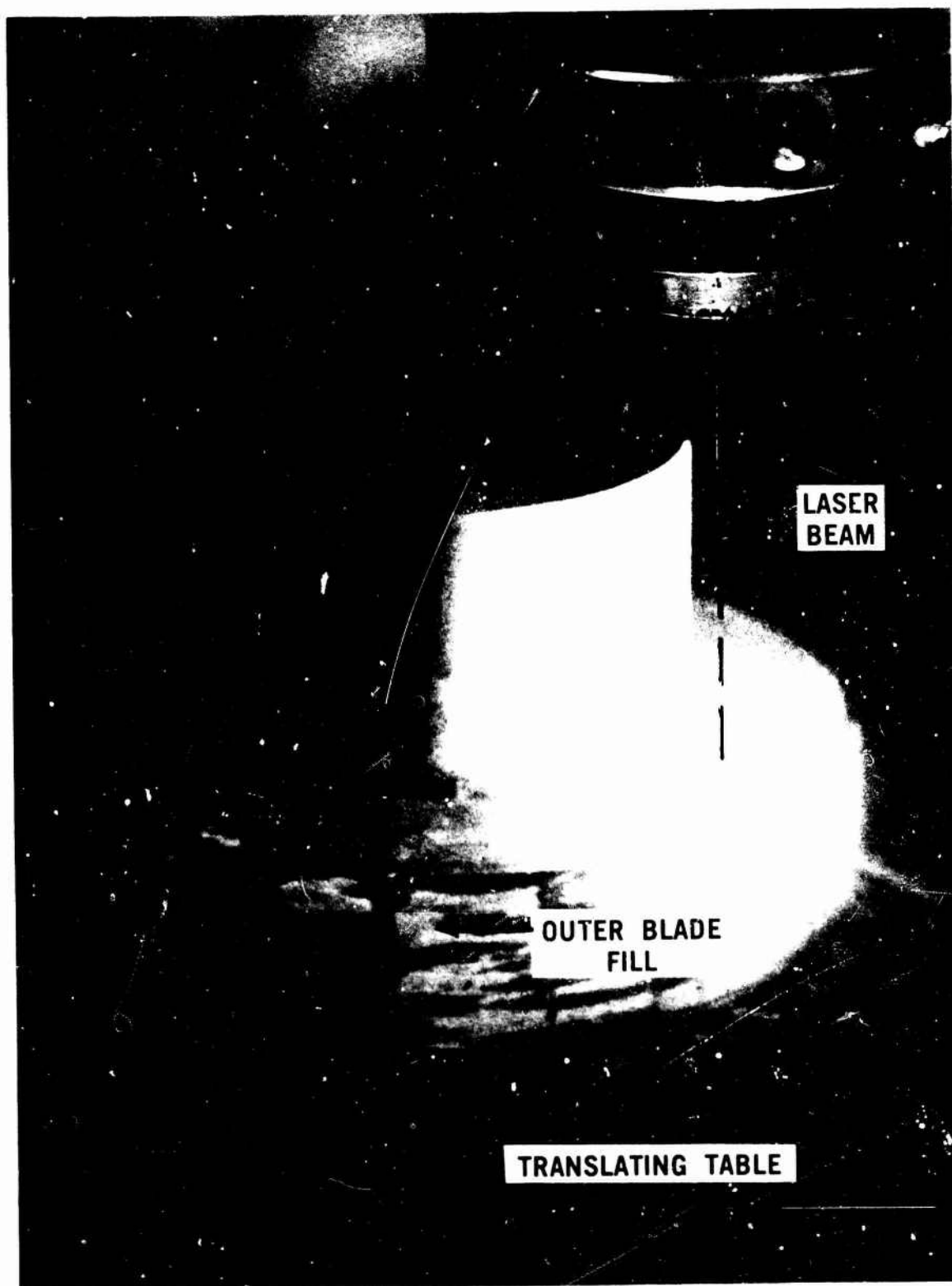
Figure 4.3.2-21 — Radial Cutting of Outer Blade Fill with CO_2 Laser

BORON NITRIDE THICKNESS
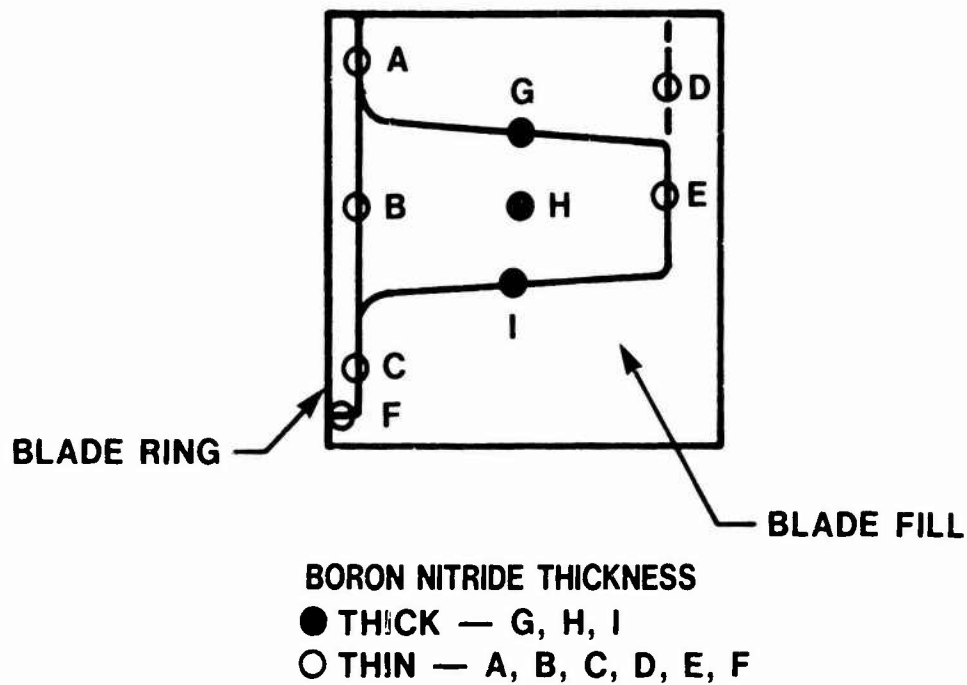● THICK — G, H, I
○ THIN — A, B, C, D, E, F

Figure 4.3.2-22 — Schematic View of Blade Filled Blade Ring Showing Boron Nitride Layers

Hub Fabrication and Bonding

In the fabrication of duo-density silicon nitride turbine rotors, the hot press bonding step forms and bonds the dense hot pressed silicon nitride hub to the reaction-sintered silicon nitride blade ring. Early concepts[2-6] utilized hot pressed hubs pre-fabricated in a separate hot pressing operation prior to bonding to the blade ring. Figure 4.3.2-23 shows the first concept employed in early 1973.
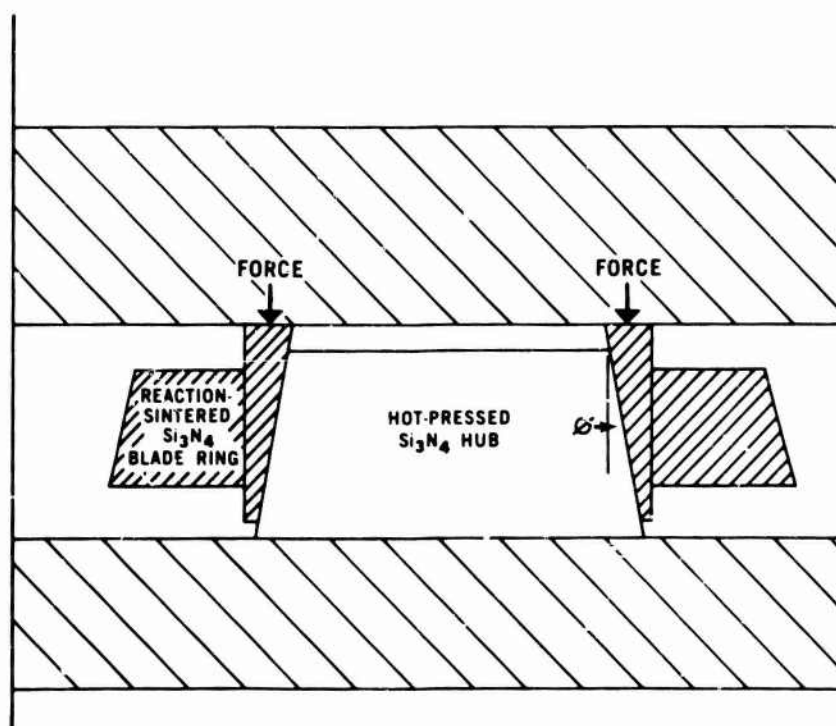
Figure 4.3.2-23 — Schematic View of Duo Density Rotor Fabrication Concept Using Tapered HPSN Hub

The blade ring did not bond to the hub at pressures up to 1,000 psi while higher pressures fractured the blade ring rim.[4] The graphite tooling was redesigned to support the blade ring above and below the blades, as shown in Figure 4.3.2-24, to prevent axial cracking of the blade ring rim. Although bonding of the pre-fabricated hub to the reaction-sintered blade ring did occur in several cases and axial rim cracking was reduced, there was considerable cracking and tearing of the blades as shown in Figure 4.3.2-25.
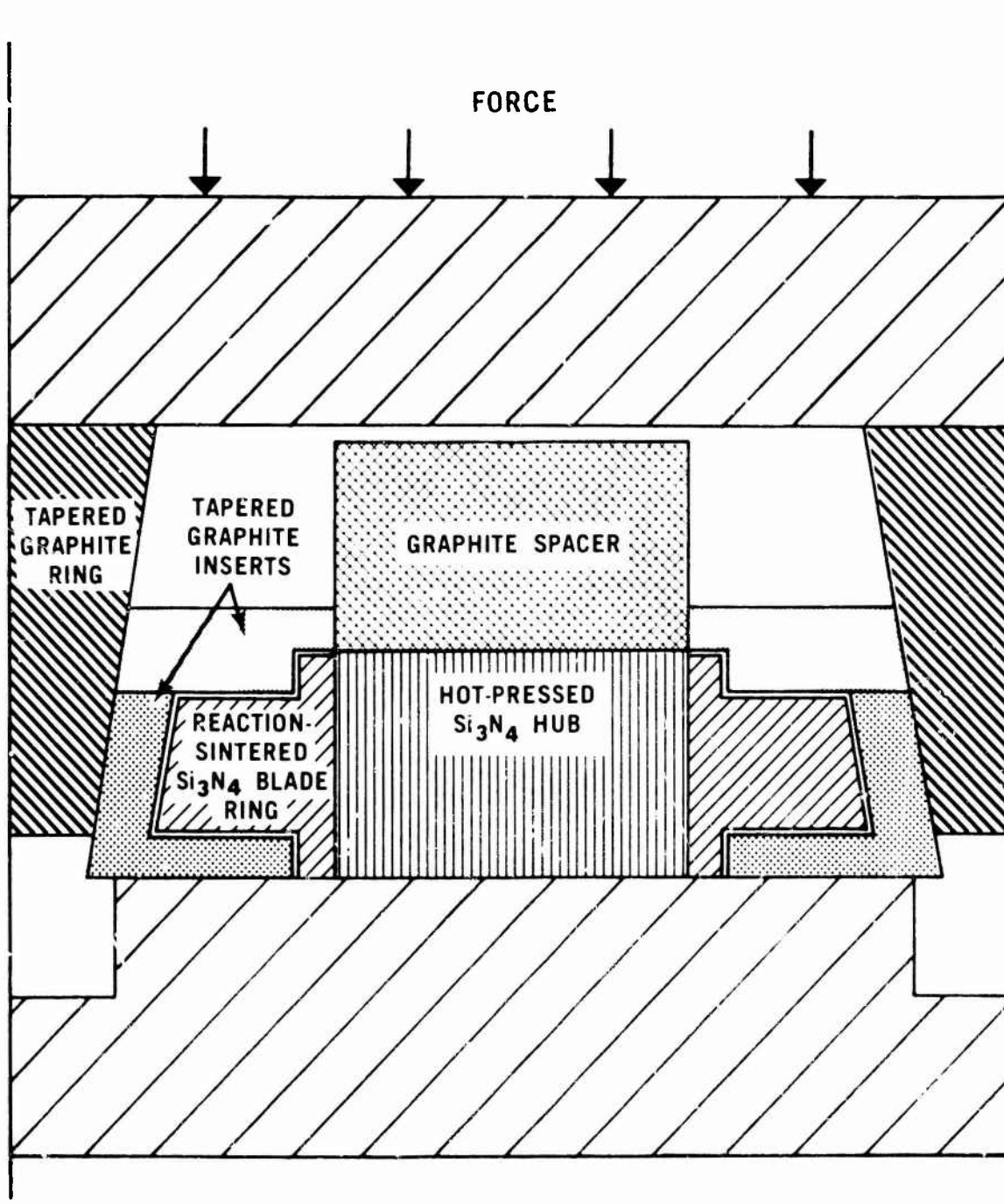
Figure 4.3.2-24 — Schematic View of Duo Density Rotor Fabrication Concept Using Graphite Blade Support and Graphite Wedges

Figure 4.3.2-25 — Schematic View of Press Bonded Duo Density Rotor Fabrication
Concept Illustrating Deformation and Blade Ring Cracking

It was apparent that the blade ring rim must be supported not only above and below but also in between the blades. This was accomplished by the blade filling process described in the previous section of this report. Lack of independent pressure controls for the blade ring and the hub produced or resulted in variations in bonding and restraint pressures which caused breakage of the rim and inconsistent bonding between the rim and the hub.[5] A redesign of the graphite tooling and the loading system of the bonding assembly, shown in Figure 4.3.2-26, allowed independent control of the applied pressures to the outside graphite wedge and the inside hot pressed hub.[6]

This figure also shows a fully contoured hub hot pressed to shape at 4,000 psi prior to the press bonding step. Bonding at the outer extremities of the rim was of only fair to poor quality while the bond produced near the blade centerline was much better. Axial and circumferential rim cracking and accompanying blade cracking still persisted to such an extent that no good quality rotors were produced. The hot press bonding tool was altered to enable simultaneous hot pressing and hot press bonding of the silicon nitride hub to the blade ring, as shown in Figure 4.3.2-27,[7] to improve bonding over the entire interface. However, blade and rim cracking still occurred. Additionally, inconsistent densification of the attachment region of the hot pressed hub resulted. Increasing the hot pressing pressure to achieve complete densification of the hub fractured the blades. A few rotors of very poor quality with less than half the blades remaining were tested. Both the blade cracking and attachment region densification problems were solved with the introduction of the three-piece concept shown in Figure 4.3.2-28.[10]

The pre-formed hub was hot pressed at high pressure, 4,000-5,000 psi, in a separate operation to densify the attachment region. Due to the smaller area bonding ring, the forces applied to the system were reduced during the bonding operation; this greatly reduced the incidence of blade and rim cracking. Several rotors free of blade and rim cracks were produced for testing but insufficient densification of the bonding ring and poor blade ring bonding were problems, as shown in Figure 4.3.2-29.
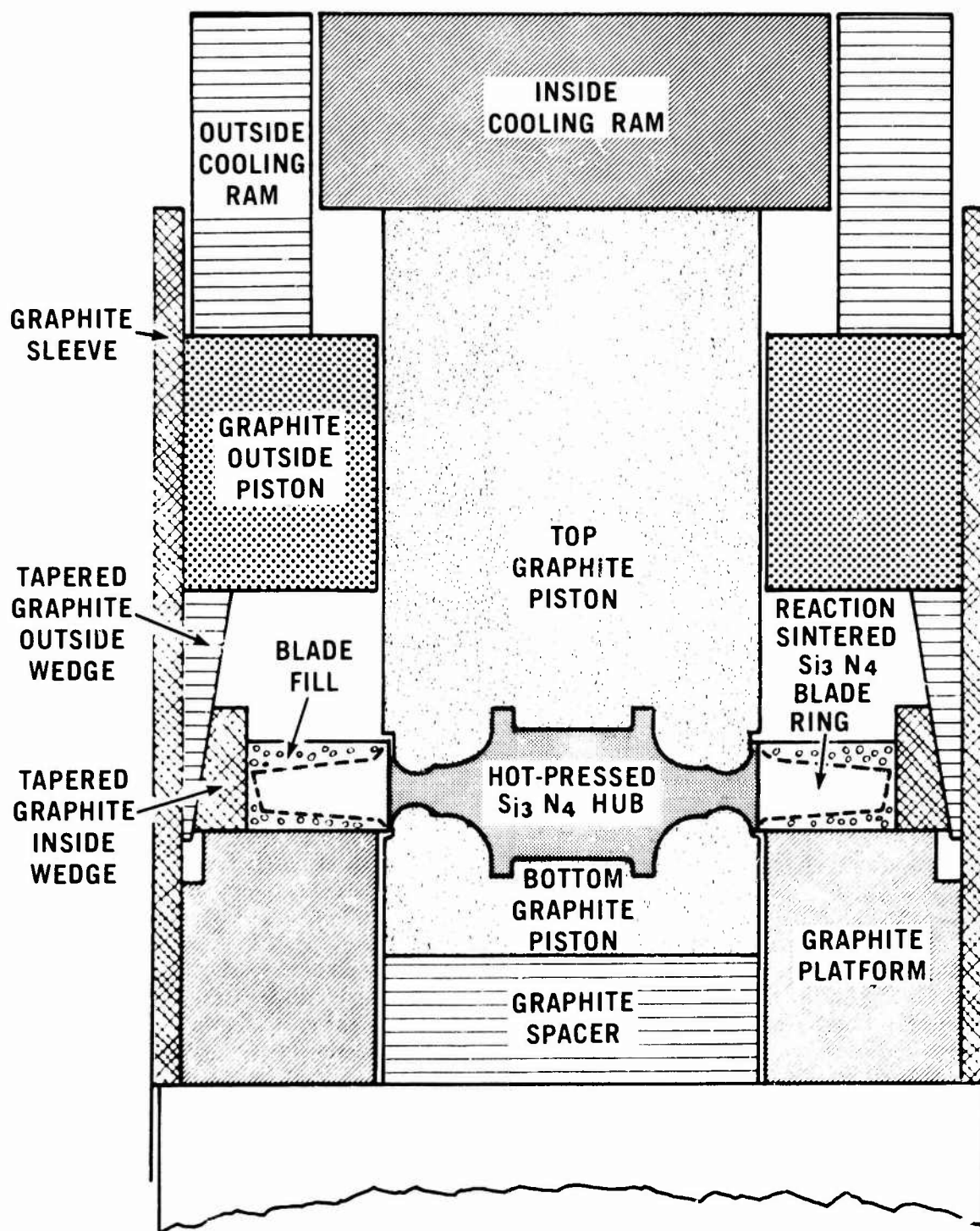
Figure 4.3.2-26 — Schematic View of Press Bonded Duo Density Rotor Fabrication
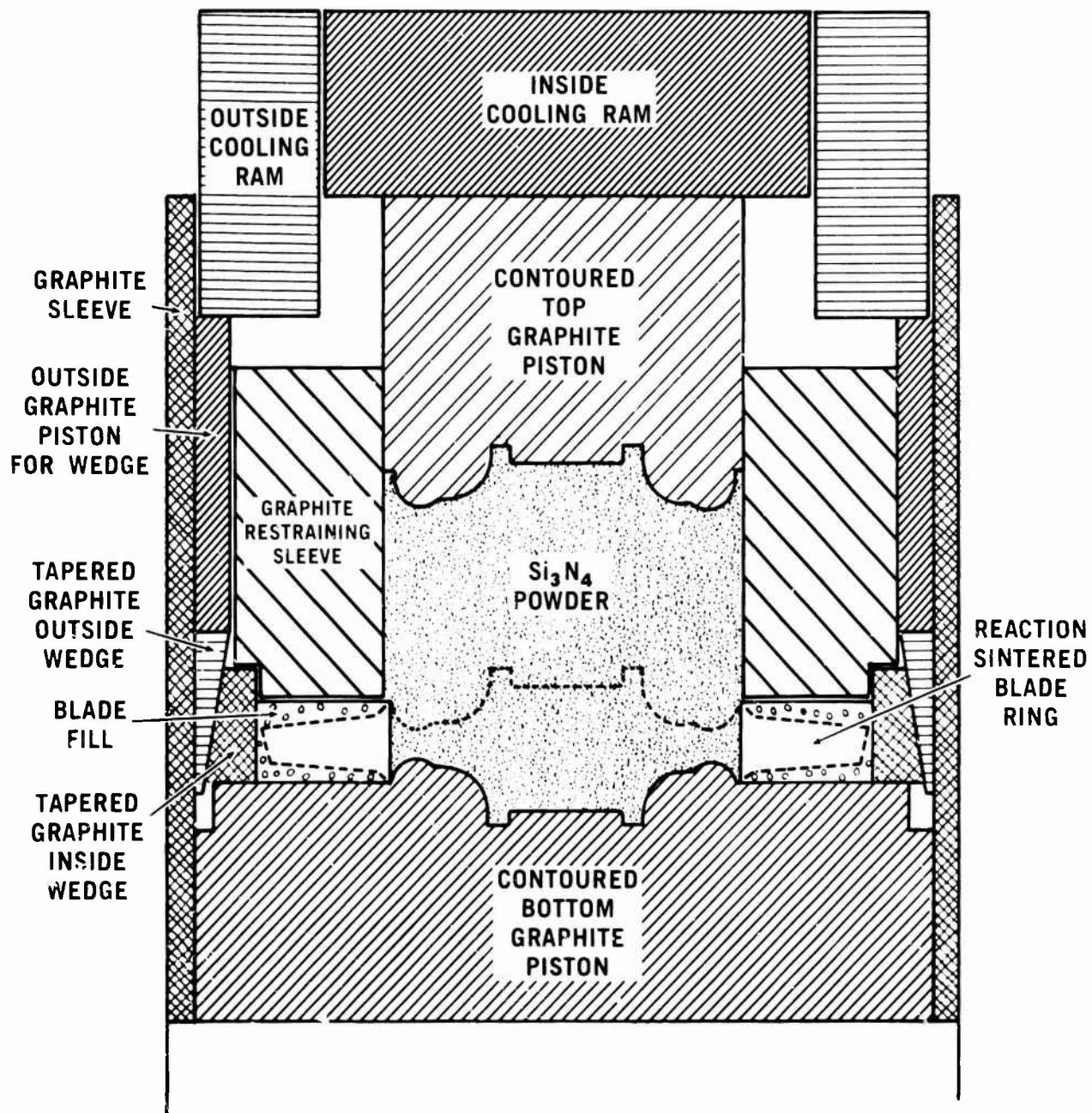Concept Illustrating Method of Applying Independent Pressures

Figure 4.3.2-27 — Schematic View of Press Bonded Duo Density Rotor Fabrication
Concept Illustrating Method of Simultaneously Forming the Contoured
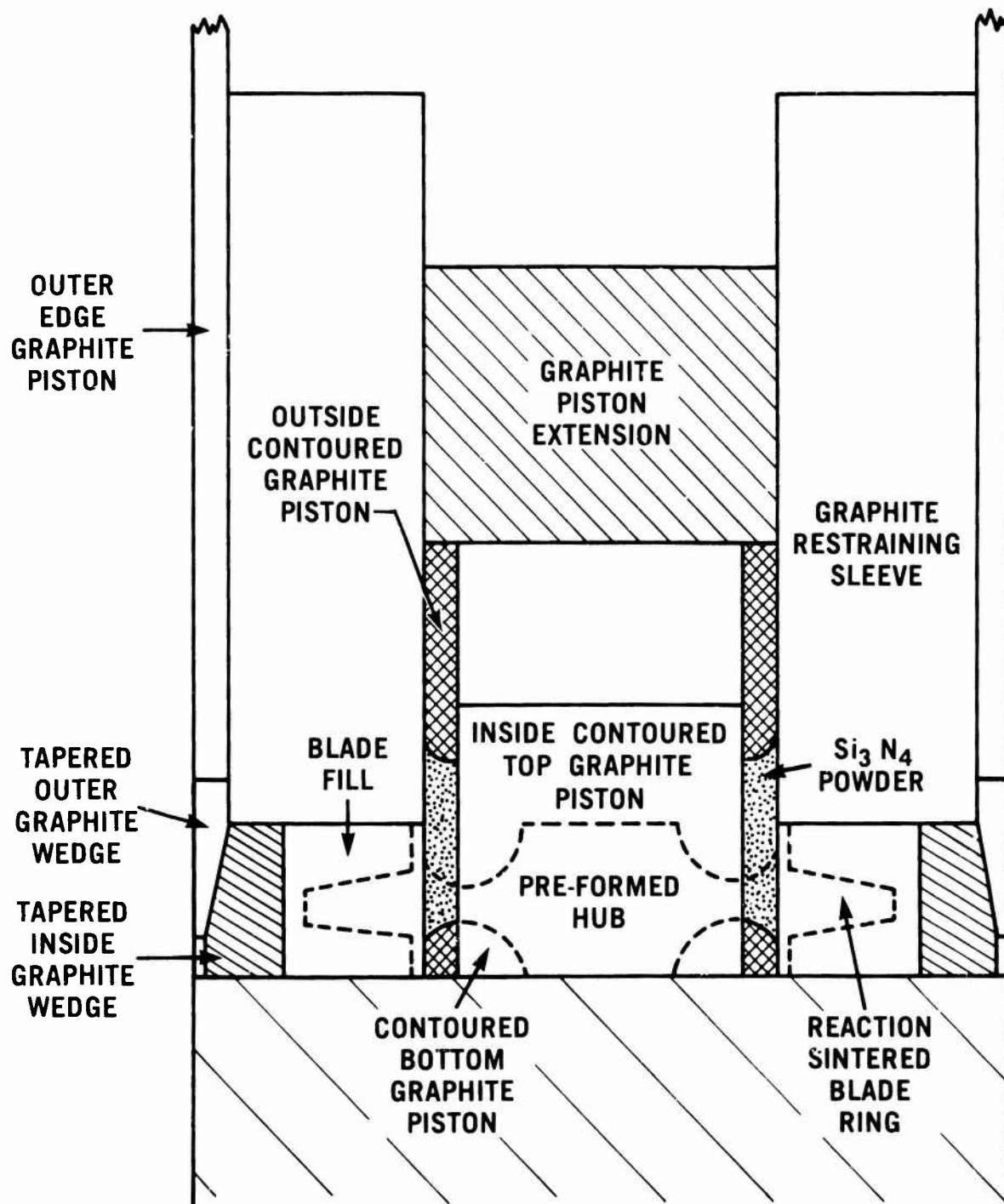Hub and Bonding of Hub and Blade Ring

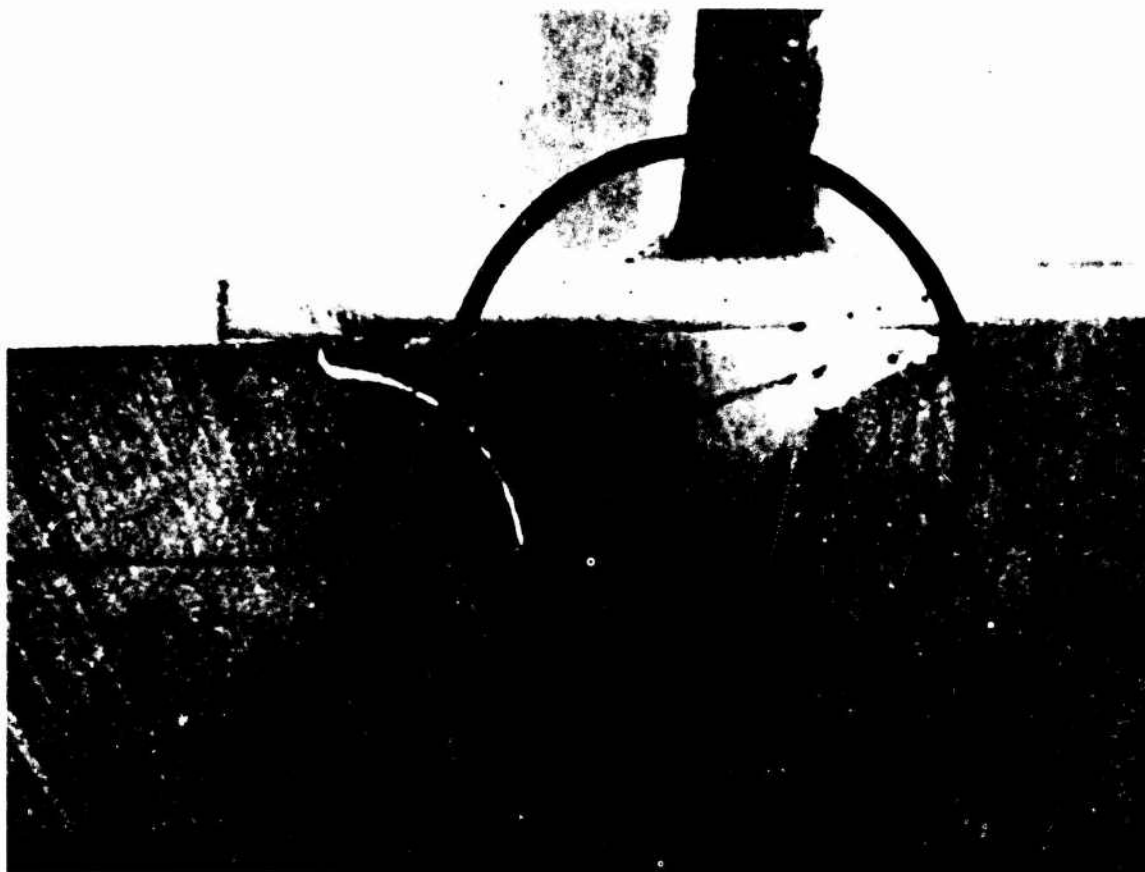Figure 4.3.2-28 — Schematic View of Press Bonded Duo Density Rotor Fabrication Concept Illustrating Three Piece Method

Figure 4.3.2-29 — View of Sectioned Press Bonded Three Piece Duo Density Rotor Illustrating Poor Quality Bonding

Modifying the bottom contoured piston and using cold pressed preforms were tried but the densification problem persisted.[10] During the work on this densification problem another problem appeared. Test bars cut from several three-piece rotors showed that the hot pressed to hot pressed bond strength varied from 18% to 98% of the parent material.[11] This problem was confirmed by low speed bond joint failures in hot spin testing.

The results of a separate hot pressed silicon nitride study on pressing parameters revealed that high-strength material could be produced at low pressures in flat sided disks.[11] Therefore, a simplified two-piece design was introduced which enabled densification of the silicon nitride powder at low hot-pressing pressures (1,000 psi) and eliminated the troublesome bond joint between the hot pressed materials, as shown in Figure 4.3.2-30.

Twenty-four simplified two-piece trials were made with pressures ranging from 500 to 2,000 psi. Rim or blade cracking occurred on most rotors to some degree. These problems were minimized at 1,000 psi with 1,000 pounds wedge restraining load. Five of the twelve rotors produced under these conditions exhibited no rim cracks and three or fewer blade cracks. Although a few cracked blades were removed prior to hot spin or engine testing, the rotors performed reasonably well as described later in this report.[12]

The major problem areas with this and earlier concepts were blade cracking and inconsistent blade ring rim distortion and cracking. Two changes to the process were made during a separate DOE-supported program [13] which resulted in a major improvement in blade and rim quality and much more consistent results. The blade filling process was modified to provide more accurate control of the boron nitride thickness (the barrier material) which resulted in more uniform support for the blades and rim. In addition, the graphite tooling was redesigned to provide more consistent wedge action by eliminating the frictional drag loads on the outer wedge piston.[12] Forty-six simplified two-piece duo-

density turbine rotors were hot pressed with controlled boron nitride thickness and modified outer wedge cylinder design at standard conditions of three hours at 1,000 psi and 1715°C with a 3.5 weight % magnesium oxide densification additive in the silicon nitride powder. Seventy percent of these rotors were free of hot pressing induced flaws.[13]
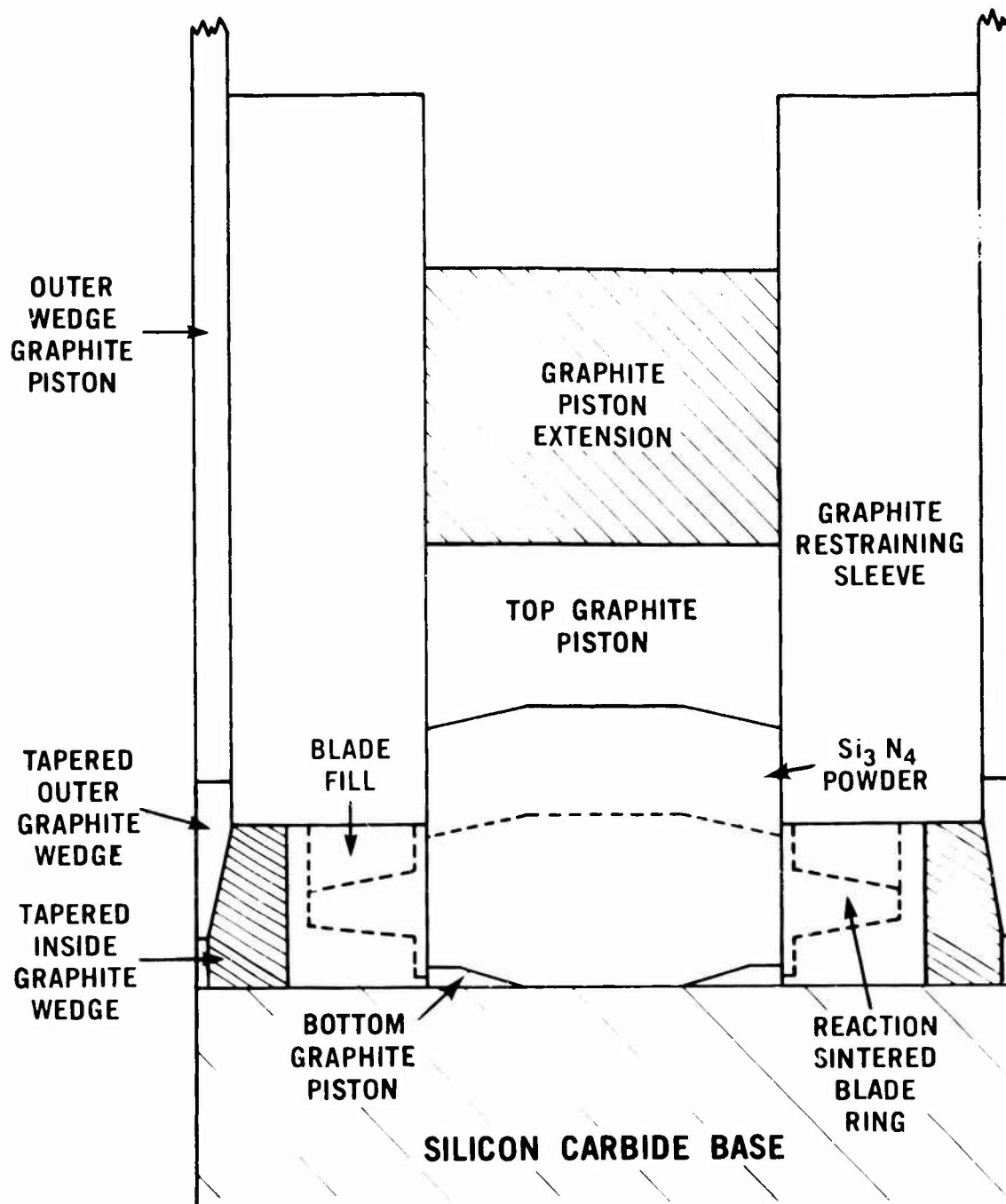

OUTER WEDGE GRAPHITE PISTON

GRAPHITE PISTON EXTENSION

GRAPHITE RESTRAINING SLEEVE

TOP GRAPHITE PISTON

TAPERED OUTER GRAPHITE WEDGE

BLADE FILL

$Si_3 N_4$ **POWDER**

TAPERED INSIDE GRAPHITE WEDGE

BOTTOM GRAPHITE PISTON

REACTION SINTERED BLADE RING

SILICON CARBIDE BASE

Figure 4.3.2-30 — Schematic View of Hot Press Bonding Assembly Illustrating Simplified Two Piece Duo Density Rotor Concept

A number of hot pressings, incorporating improvements discussed in this Section and having improved blade-fill (as discussed in the preceding Section), produced a number of press-bonded duo-density rotors which were free of blade and rim cracks.

Finish Machining

The laser and electron beam proved to be very effective in removing ceramic stock rapidly, but the high thermal shock induced by these methods was too severe for their consideration as possible

finishing operations. However, using a laser to cut slots in the expendable blade fill material used in the fabrication of the duo-density rotor was very successful, as discussed earlier.

Ultrasonic impact grinding and diamond grinding were identified early in the program as the two methods most likely to result in successful finish machining of a ceramic rotor. Both of these techniques could remove material stock from the difficult to machine hot pressed materials. The ultrasonic method was superior in machining certain complex shapes such as non-circular holes. Diamond grinding, however, proved to be the best technique in almost all of the more conventional machining operations. Diamond grinding was selected as the principal technique for finish machining duo-density rotors, primarily due to in-house and vendor experience in diamond grinding

Early duo-density rotors contained a HPSN hub with disc contours, center bore and curvic coupling recesses pressed roughly to shape so that finish machining was minimal. The introduction of the simplified hot pressing of rotors consisting of a solid hub with no contours required considerable finish machining through diamond grinding.[12]

Use of a plated form diamond grinding wheel was an essential part of the rotor development process because the grinding form was easily changed to follow design modifications. Precision grinding wheel forms were required to grind the curvic coupling teeth because the plated diamond grinding wheel could not be dressed during machining.

Approximately forty hours were spent in finish grinding of each duo-density rotor; this included polishing the rotor and grinding the curvic coupling and hand grinding to the desired radii at each curvic edge and removal of any notches, chips or other surface defects on the rest of the rotor.

To minimize the effect of machining damage, all ground surfaces of the duo-density rotors were polished, except for blade tips and curvic coupling teeth.

Twenty-five duo-density rotors were finish machined by these techniques and selected for hot testing. A picture of a finished duo-density rotor is shown in Figure 4.3.2-31.
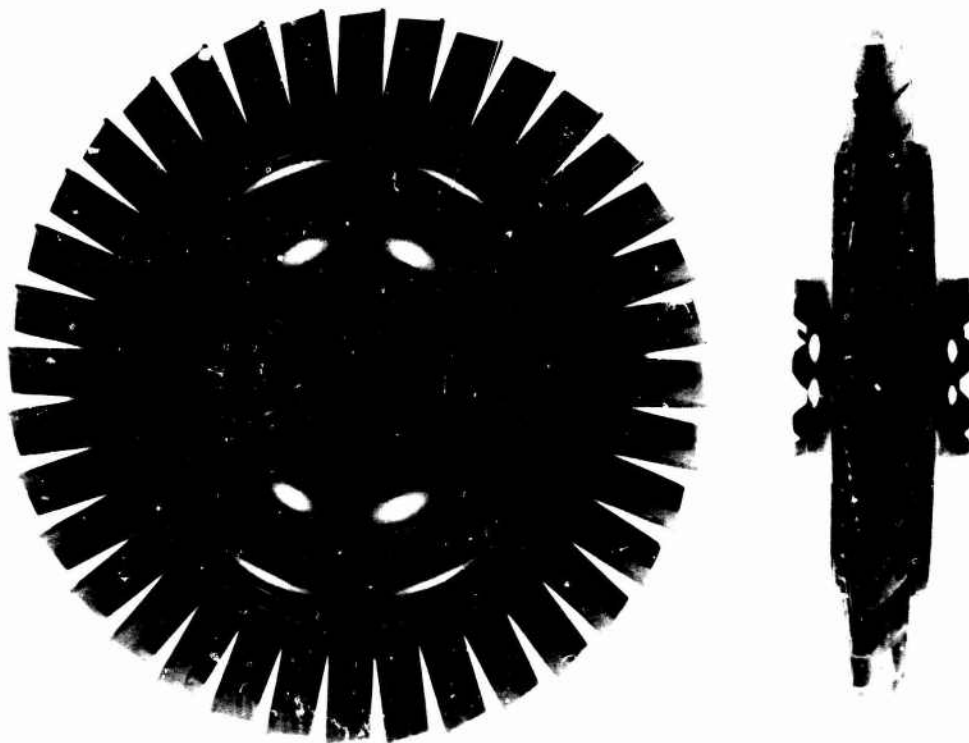
Figure 4.3.2-31 — Finished Duo Density Rotor Ready for Testing

4.3.3 ROTOR TESTING AND EVALUATION

4.3.3.1 Introduction

Testing and evaluation of duo-density Si_3N_4 turbine rotors was conducted using several procedures and testing techniques as discussed earlier in Section 3.3.2.3. A vacuum spin pit, operating at room temperature, was utilized to destructively evaluate rotor blades, hubs, various ceramic test disks, and alternate rotor concepts. It was also used as a proof test to qualify duo-density rotors for hot testing. A rotor blade bend test, was developed and applied for loading individual blades to failure, and provided useful information on material strength and defects in a rapid fashion for use in material and process improvement activities. Rotors which had been qualified in the vacuum spin pit were subsequently hot tested in a unique Hot Spin Test Rig, which simulated the thermal conditions of a gas turbine engine but featured rapid and inexpensive turnaround between tests in the event of a rotor burst. Duo-density rotor testing was also performed in the 820 turbine engine, in conjunction with an all-ceramic flowpath. The remainder of this Section will discuss the procedures and results in more detail for each of the test methods.

4.3.3.2 Cold Spin Testing

The vacuum spin pit (VSP), shown earlier in Figure 3.3.2-6, consists of a vacuum chamber, a high speed air turbine, a failure detector, a photographic mechanism and an operator panel. The test specimen is suspended from the air turbine in the vacuum chamber. Vacuum is required to reduce aerodynamic resistance on the test specimen. A photograph is taken as a particle of the failing specimen breaks an electrical circuit surrounding the test component, which activates the failure detector.

The data obtained from these tests were compiled and used as feedback for material and process improvements to the component. This data was also used by the design engineers to evaluate the unique design techniques which had to be developed for ceramics.

In all of the VSP tests, efforts were made to carefully prepare the test sample prior to testing. In preparing rotor blades for testing, care was taken not to cause any extraneous damage to the blade such as may occur during handling or machining. The blades were all visually inspected prior to testing to insure that flaws were not induced during the test sample preparation. In preparing rotors and rotor hubs for testing, the same machining procedures were used as would be used in the fabrication of a duo-density rotor. The same dimensional tolerances were specified along with the same surface finishes, diamond grit size, machining feeds, etc. In all cases, the same non-destructive evaluation techniques were applied to the test specimens. All components were visually inspected; rotor hubs were also examined using fluorescent dye penetrants.

Rotor Blade Cold Spin Testing

Spin pit testing of rotor blades was conducted in three separate phases. The first phase involved testing individual blade segments cemented to a metal or ceramic disk. The second phase involved whole blade rings cemented to hubs, and the third phase utilized complete duo-density rotors.

Early emphasis was placed on epoxy bonding of blade segments to hubs because this technique required a minimal amount of test material and promised rapid feedback for the fabrication development. Further, it could provide data from which statistical projections could be made to predict the eventual performance of the finished rotor. However, two problems developed which restricted utilization of this testing technique. The first problem encountered was that of securing a statistically significant quantity of material which would be representative of the current state of rotor development (material, design and fabrication changes were being made on a continual basis as part of the iterative fabrication process).

The second problem, which developed as improvements in blade fabrication were made, was that of insufficient bond strength. As the rotor blades became stronger, the predominant failure mode became that of epoxy bond failure.

The second phase of vacuum spin pit testing of rotor blades involved complete blade rings bonded to ceramic or metal hubs. It was determined that the strength requirements of the bonding material were considerably lower for complete blade rings than for individual blade segments. Several attempts were made to bond blade rings to metal hubs using solid one-part epoxy paste. This system proved to be successful and several blade rings were tested using this method. However, since it was determined that a degradation in blade strength[12] occurred during the press-bonding operation, it was decided to focus on spin testing of complete duo-density rotors.

For the third phase of rotor testing, four duo-density rotors were selected to determine the blade failure speed distribution. These rotors were thought to be representative of rotors suitable for hot spin testing.

Two rotors had all 36 blades present prior to testing. The other two had 25 blades and 5 blades prior to testing, and had been rejected from the hot test program for lack of blades. In each of the four rotor tests, careful inspection of the rotor blades was conducted prior to testing. All internal voids recorded prior to press-bonding and all detectable surface flaws were noted. Thirty-seven separate tests were conducted to complete the series. Failure speeds ranged from 38,440 rpm to 96,900 rpm. One hundred and two blades were tested which resulted in eighty-three blade failures and nineteen blades lost as a result of hub failure.

Of the eighty-three blade failures, forty-three blades contained either surface or internal flaws. Significantly, in each test where failure occurred below 90,000 rpm, one or more blades contained gross fabrication flaws which it is believed led to failure; in each test above 90,000 rpm, there were no visually detectable flaws associated with failure. Some known flaws, e.g., rim I.D. voids, apparently did not contribute to blade failure whereas other types of flaws, e.g. blade planar flaws, did correlate with failure. It was noted that the largest flaw found during these tests caused blade failure to occur at the lowest speed.

Combining all of the blade data, including suspensions and failures associated with flaws, resulted in a Weibull characteristic speed of 97,000 rpm with a slope of 6.0.

It was concluded from these tests that: (1) better NDE techniques are required to detect blade flaws which result in blade failure, and (2) improvements are required in the fabrication process to eliminate these gross defects. Both of these problems are addressed in reference twelve.

Rotor Qualification Spin Testing

The vacuum spin pit was also used extensively for pre-hot test evaluation of rotors. The qualification speed selected for cold testing was ten percent above the intended hot test speed. For most rotors this was 55,000 rpm (50,000 rpm hot test) or 70,000 rpm (64,240 rpm hot). The standard procedure for rotor qualification testing was to mount the test rotor in a reuseable arbor, which was balanced by adjusting screws in two planes. Next the arbor was secured in the vacuum spin pit and photographed in the stationary position. The rotor was accelerated until either a failure occurred or the qualification speed reached. Failure was detected by breaking the continuity of an electrical circuit which automatically recorded the failure speed. This switch also activated a strobelight and photographed the rotor burst. These photographs were used in determining the initial cause of failure.

Typically, in attempting a qualification test, one or more rotor blades would fail prior to reaching the qualification speed. Blade failures which occurred below 90,000 rpm were generally related to gross internal or surface defects.[13] As a result of this determination, it became standard procedure to remove all blades with known flaws which would be expected to fail during the qualification tests.

Table 4.3.3-1 lists a summary of rotors which were subjected to the vacuum spin pit qualification test. Thirty-six duo-density rotor qualification tests were conducted of which twenty-three passed the intended qualification speed. As may be seen, normally several blades would be lost during qualification testing. A determination would be made at the conclusion of the test as to the suitability of proceeding with the pending hot test based on the number of blades remaining.

TABLE 4.3.3-1

VACUUM SPIN PIT ROTOR
QUALIFICATION TEST RESULTS

Rotor Number	Speed RPM	Results
1195	45,380	Lost blade chip
	55,200	Rotor qualified
1211	55,000	Lost 4 blades at maximum speed, Rotor qualified
1213	63,620	Lost blade chip
	65,000	Rotor qualified
1231	55,000	Rotor qualified
1256	31,150	Lost one blade
	55,130	Rotor qualified
1287	44,760	Lost blade chip
	55,000	Rotor qualified
1294	65,640	Lost 1-1/2 blades
	70,580	Rotor qualified
1296	55,040	Rotor qualified
1298	55,220	Rotor qualified
1309	52,720	Lost 1-1/2 blades
	55,030	Rotor qualified
1324	64,000	Lost 1 blade
	69,480	Lost 1 blade, damaged 3 adjacent, Rotor qualified
1306	16,770	Rim chipping
	55,000	Rotor qualified
1304	55,000	Rotor qualified
1368	55,000	Rotor qualified
1389	41,500	Rim chipping
	55,000	Rotor qualified
1392	64,260	Lost 2 blades
	66,800	Lost 7 blades
	66,120	Lost 1 blade
	70,000	Rotor qualified
1382	49,750	Rim chipped
	63,780	Lost 2 blades
	67,690	Lost 2 blades
	70,000	Rotor qualified
1384	20,920	Lost 2 blades
	48,880	Lost 1-1/2 blades
	54,370	Lost 1-1/2 blades
	56,460	Lost 1 blade
	69,540	Lost 4-1/2 blades
	70,000	Rotor qualified

TABLE 4.3.3-1 (Continued)

VACUUM SPIN PIT ROTOR
QUALIFICATION TEST RESULTS

Rotor Number	Speed RPM	Results
1326	1,000	Lost 8 blades
	55,880	Lost 24 blades
1312	70,000	Rotor qualified
1342	36,620	Lost 6 blades
	67,670	Bond failure
1355	61,460	Lost all blades
1360	65,580	Hub failure
1329	26,700	Lost 2 blades
	57,650	Lost 2 blades
	64,550	Lost 1 blade
	70,000	Rotor qualified
1349	21,120	Lost 2 partial blades
	27,270	Lost 2 partial blades
	30,110	Lost 1 partial blade
1338	21,850	Lost platform chip
	48,780	Lost 2 blades
	63,460	Lost 7 blades
	70,000	Rotor qualified
1352	51,020	Lost all blades
1357	63,240	Lost 6 blades
	69,870	Lost 4 blades
	70,000	Rotor qualified
1364	61,990	Lost 3 blades
	68,980	Lost 4 blades
	70,000	Rotor qualified
1395	57,890	Lost 1 blade
	68,530	Lost 2 blades
	67,780	Lost 1 blade
	70,000	Rotor qualified
1379	65,570	Lost 2 blades
	69,500	Lost all blades — bond failure
1387	63,710	Lost 1 blade
	65,660	Lost 1 blade
	66,050	Lost 1 blade
	67,590	Hub failure
1377	32,960	Lost 2 blades
	64,320	Lost 1 blade
	66,010	Lost half of remaining blades
1373	66,710	Lost 29 blades

TABLE 4.3.3-1 (Continued)

VACUUM SPIN PIT ROTOR
QUALIFICATION TEST RESULTS

Rotor Number	Speed RPM	Results
t363	3,160	Lost t blade
	28,250	Lost 8 blades
	53,790	Lost 1 blade
	61,380	Lost 1 blade
	63,790	Lost 5 blades
1386	37,890	Lost 6 blades
	42,600	Lost 3 blades
	53,980	Lost 2 blades
	65,420	Lost 10 blades

4.3.3.3 Rotor Blade Bend Testing

A method was devised to rapidly evaluate rotor blades individually by applying a constant rate mechanical bending load. Two test fixtures, one for Design D blades and the second for Design D' blades, were devised for use on an Instron Test Machine. The D' blade bend test fixture was shown earlier in Figure 3.3.2-2. The purpose of this test was to evaluate manufacturing variations and the effects of processing on the component strength as compared to the more fundamental material strength as measured by MOR bar tests.

One of processing parameters evaluated by the blade bend test method was that of the effects of 4% H_2 in the nitriding atmosphere vs. 100% N_2. The strength of eight blade rings from the 4% H_2 nitridings tested consistently higher than the 100% N_2 blade rings.[11] This test confirmed the decision to introduce the hydrogen into subsequent nitridings.

The blade bend test became a quality control tool as a means of rapidly evaluating the quality of blade rings produced in a given nitriding cycle. For example, all blade rings nitrided in other than 4% H_2 were removed from further processing as a result of this test.[12] However, it was apparent that the blade bend test by itself was not sufficient to completely characterize the strength of the final product, the duo-density rotor.

This led to an investigation [12] of the effects on blade strength of the hot pressing cycle used in the fabrication of the duo-density rotor. It was discovered that a significant degradation occurred as a result of press-bonding. For example, a series of blade rings from a given nitriding cycle were tested "as nitrided" and compared to blades tested from the same nitriding after hot-press bonding. These results are summarized below:

Table 4.3.3-2

EFFECT OF PRESS BONDING UPON ROTOR BLADE STRENGTH

Nitriding Number	As Nitrided		After Hot Pressing		% Change	
	Weibull Slope	Characteristic Load*-Pounds	Weibull Slope	Characteristic Load*-Pounds	Weibull Slope	Characteristic Load
48	9.1	89.9	6.9	77.0	−24	−14
67	11.2	85.7	6.8	53.0	−39	−38
78	9.2	79.1	15.1	61.6	+64	−22

*Load at 63.2% failure.

The results were shown to be statistically different. However, later in the program it was determined that an additional parameter was significant, that being the difference in center support of a solid rotor versus an unsupported center blade ring.[13] As expected, the unsupported blade rings failed at lower characteristic loads than the supported blade rings. Therefore the actual change in characteristic load as a result of hot pressing would be in all probability something higher than reported in Table 4.3.3-2. It was also concluded that no degrading effect was observed as a result of the blade filling operation.

4.3.3.4 Turbine Rotor Hot Rig Testing

Introduction

When a ceramic turbine rotor fails catastrophically in an engine, or a high temperature turbine rotor test rig, extensive damage can occur to other ceramic and metal components and rebuilding requires considerable time. To minimize time spent in testing and loss of ceramic parts, a hot spin test rig (HSTR) was designed for use in ceramic rotor development as discussed in Section 3.3.2.3. It had considerably fewer parts than an engine, yet simulated mechanical and thermal loads and, after a rotor failed, could be rebuilt quickly.

Hot Spin Test Rig (HSTR)

Results of durability testing, completed in the present configuration of the HSTR, are summarized in Tables 4.3.3-3 and 4.3.3-4. The duo-density rotors tested were made of press bonded hot pressed silicon nitride.

25-Hour Durability Tests

TABLE 4.3.3-3

25-HOUR DUO-DENSITY CERAMIC ROTOR DURABILITY TESTS

Rotor Serial Number	Blade Ring Serial Number	Number of Blades During Test	Rim Temperature (°F)	Speed (RPM)	Audible Indications of Cracking on Disassembly	Zyglo Indications After Disassembly
1324	2032	27	1800	50,000	Yes	s
1287	2045	27	1800	50,900	Yes	Yes
1294	1794	31	1800	50,000	Yes	No
1306	2033	35-1/2	1800	50,000	No	No

Table 4.3.3-3 displays the results of four successfully completed 25-hour durability tests at steady state conditions of 50,000 RPM and rotor rim temperature of 1800°F. Rotor and blade ring serial numbers are shown for identification. When necessary, flawed blades were removed during balancing of the rotor and shaft assembly. The number of blades on the test rotors shown in Table 4.3.3-3 varied from 27 to 35-1/2 out of 36 possible.

The durability test start-up and shut-down schedule is shown in Figure 4.3.3-1. After the completion of these tests, the rotors were disassembled from the shaft. Indications of cracking were audible in three cases when the tie bolt load was released. In two of these cases the cracks were found with zyglo techniques. The rotor curvic teeth on the upstream side cracked where the rotor mated with the metal curvic adaptor. Tests conducted to solve this problem are discussed later.
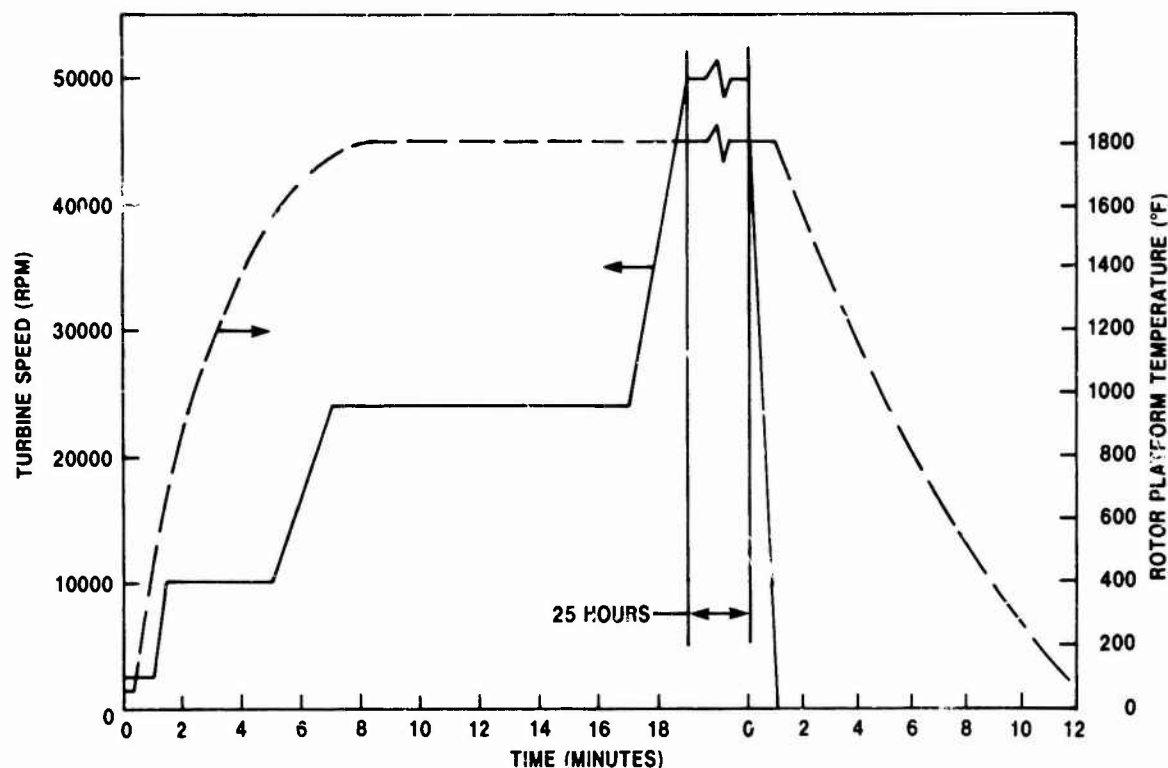
Figure 4.3.3-1 — Twenty-Five Hour Durability Test Schedule

200-Hour Durability Test

Table 4.3.3-4 displays the results of a successfully completed 200-hour durability test conducted on rotor 1306, the rotor which had given no audible indications of cracking after the 25-hour test.

TABLE 4.3.3-4

200-HOUR TEST
ROTOR 1306

Rim Temperature (°F)	Speed (%)	Turbine Speed (RPM)	Time at Speed (%)	Time at Speed (Hours)	Cumulative Time (Hours)
1800	100	50,000	12	25	25
1800	86.5	43,250	5	10	35
1800	77.5	38,750	5	10	45
1800	69	34,500	7	14	59
1800	59	29,500	25	50	109
1800	55	27,500	46	91	209

The data in Table 4.3.3-4 include the 25 hours at 50,000 rpm (100% speed) shown in Table 4.3.3-3. The remaining 175 hours of testing was continuous.

Beginning at 86.5% speed (43,250 rpm), the rotor speed was reduced to the next lower level upon completion of the planned time at each speed. A rim temperature of 1800°F was maintained during these speed changes. Shutdown after 200 hours occurred without problems and the blades and hub of

164

hub of rotor 1306 were without visible evidence of distress, as shown in Figure 4.3.3-2. However, when the bolt load was released for disassembly, indications of cracking were audible. Three curvic teeth were found broken. One of these is shown in Figure 4.3.3-3 and is typical of the breakage observed on other rotors.

Figure 4.3.3-2 — Rotor 1306 Before Testing

Figure 4.3.3-3 — Cracked Curvic Region of Rotor 1306 After Testing

Tests to Solve the Cracking Problem

The function of the metal curvic adapter is to pilot the tie bolt with respect to the rotor and shaft so that the assembly will remain in balance. Calculations showed that a small clearance, to accommodate differences in thermal expansion, between the metal tie bolt and a ceramic washer would satisfy balance requirements by keeping the tie bolt concentric to the rotor and shaft, as shown in Figure 4.3.3-4.

CERAMIC HUB

CERAMIC SPACER
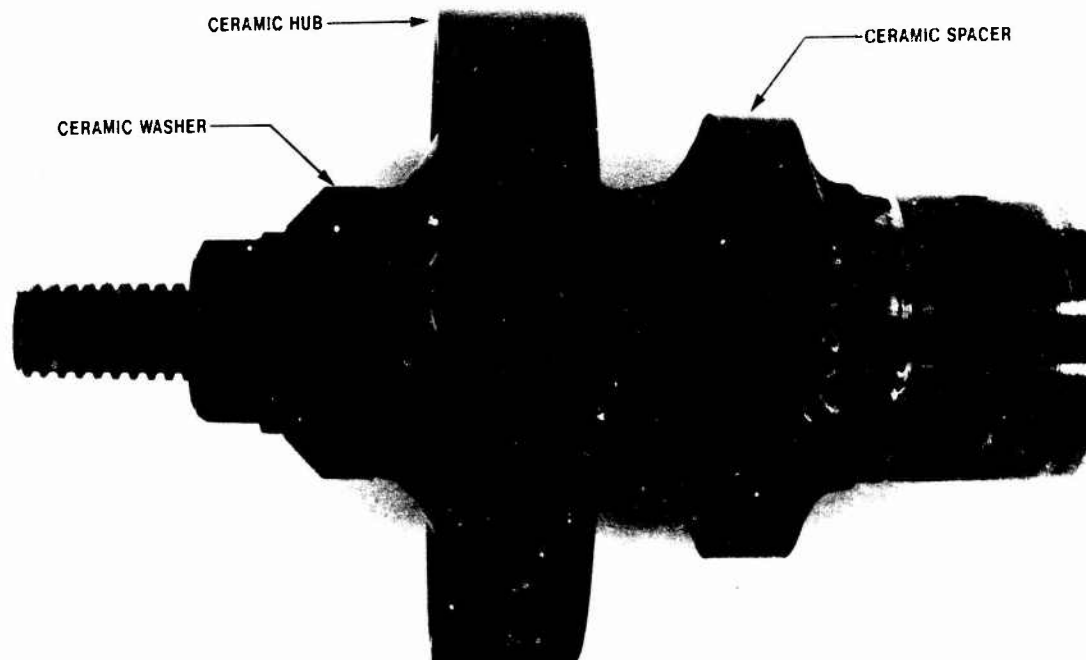
CERAMIC WASHER

Figure 4.3.3-4 — Assembly Showing Ceramic Washer

This first idea, a ceramic washer adjacent to a nut which was gold-plated to provide a solid lubricant, allowed relative motion to accommodate thermal expansion differences. After passing a one-hour test at room temperature and 64,240 RPM, this assembly was hot tested at 1800°F rim temperature where it failed at 61,000 RPM while under acceleration. The cause of this failure remains unknown, although the ceramic washer itself remained intact. Even though this idea had merit, no further tests were conducted due to a lack of suitable test hardware.

The ideal tooth-bearing pattern of the metal curvic adapters is rectangular. Examination of adapters used in testing the rotors always showed a tooth-bearing pattern that was trapezoidal, even though the bearing pattern of the curvic couplings was close to the rectangular ideal, as shown in Figure 4.3.3-5. The trapezoidal pattern was suspected of indicating a condition that placed excessive stresses on the ceramic curvic teeth. Additionally, it was noted that the clamping forces from the nut and the rotor were not in line radially on the metal curvic adaptor. This caused a disking effect on the adapter which accounted for the trapezoidal pattern. Further evidence in favor of the misaligned clamping forces being the source of the cracking problem was that the tooth patterns remained rectangular and no tooth cracking occurred at the rotor-to-spacer and at the spacer-to-shaft curvic couplings. Two different backup washers were designed to correct the trapezoidal pattern by aligning the forces on the metal curvic adaptor to eliminate the disking. A cross section of the first design, which was piloted on the bolt is shown in Figure 4.3.3-6.

The second design was lighter in weight than the first and was piloted on the rotor nut. These washers were tested at a rim temperature of 1800°F using hubs to minimize the possibility of failure. The hub with the first design failed at 46,400 rpm while that with the second design failed at 49,800 rpm. Both failures occurred during acceleration to 64,240 rpm. Since both failures were initiated in the hubs at the curvic teeth-metal curvic adaptor interface at about the same conditions, it was concluded that the backup washer worsened the situation. One possible reason was that the additional stiffness provided by the washer interfered with the relative motion at the ceramic-to-metal interface which increased stresses in the ceramic to the point of premature failure.

CONTACT DEPTH

TYPICAL SATISFACTORY CONTACT PATTERN

UNSATISFACTORY CONTACT PATTERN — BRIDGED BEARING

UNSATISFACTORY CONTACT PATTERN — EXTREME END CONTACT

NARROW PATTERN
HIGH ON TOOTH

UNSATISFACTORY CONTACT PATTERN — PRESSURE ANGLE MISMATCH

PATTERN HEAVY
ON ONE SIDE

UNSATISFACTORY CONTACT PATTERN — EXCESSIVE CHAMFER
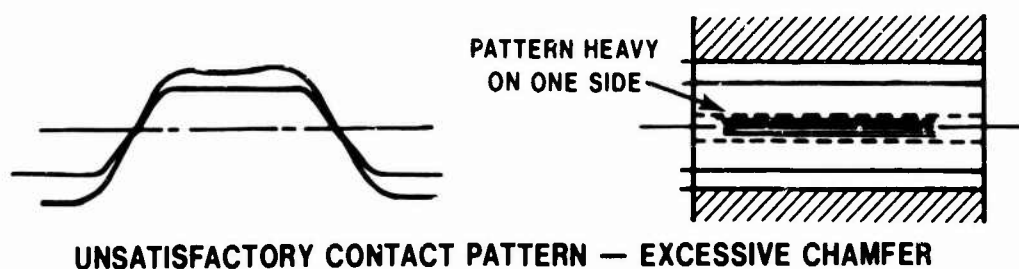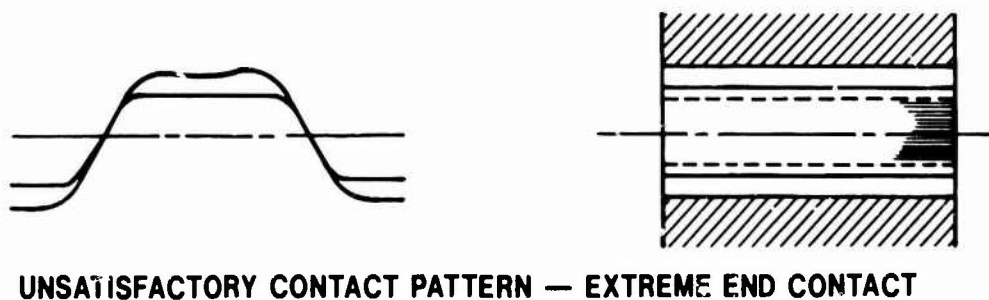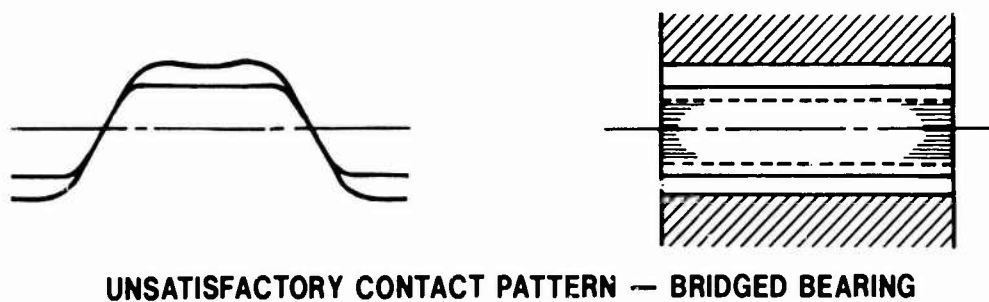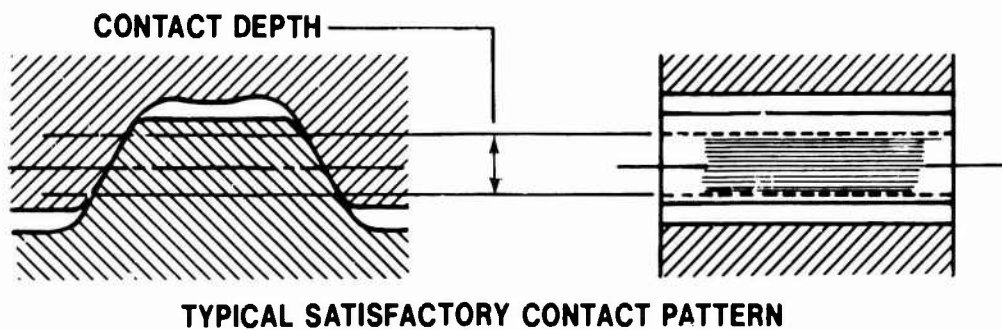
Figure 4.3.3-5 — Curvic Coupling Tooth Contact Patterns
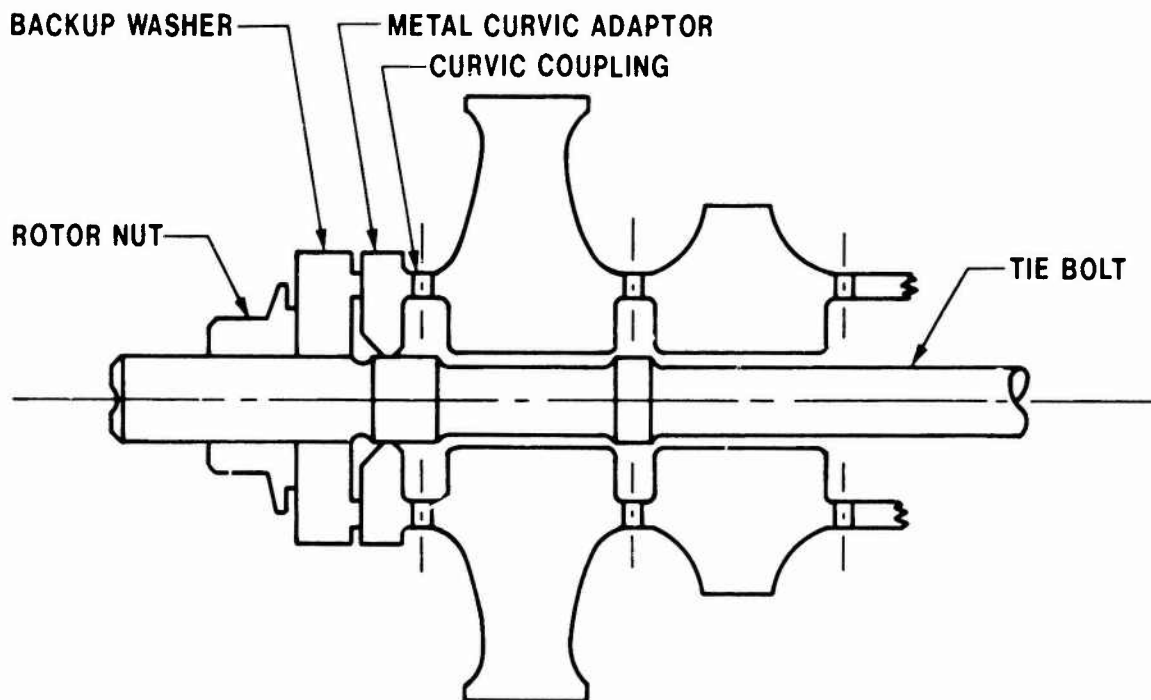
Figure 4.3.3-6 — Assembly Sketch Showing Washer Design Piloted on Bolt

Calculations showed that the tie bolt load could safely be reduced from 4,700 pounds to 2,500 pounds. This proportionally reduced the stress levels in the curvic teeth. The 4,700 pound load had stretched the metal tie bolt so that its spring rate accommodated the difference in thermal expansion between itself and the ceramic rotors. Beginning with tests of rotor 1382, the tie bolt load was reduced to 2,500 pounds.

High Speed Tests

The next program objective was to test a rotor for 25 hours at 64,240 rpm and a rim temperature of 1800°F. A series of tests, summarized in Table 4.3.3-7, was conducted using the schedule shown in Figure 4.3.3-1 except that the maximum speed was 64,240 rpm.

TABLE 4.3.3-7

64,240 RPM SPEED TESTS

Rotor Serial Number	Blade Ring Serial Number	Number of Blades During Hot Test	Rim Temperature (°F)	Speed (RPM)	Time (Hours)	Remarks
1312	2142	28	1800	64,240	1 3/4	Flame tube fell into rotor causing failure
1329	2274	24	1800	52,800	—	Complete rotor failure
1357	2317	19	1800	57,100	—	Complete rotor failure
1364	2336	24	1800	55,400	—	Complete rotor failure
1382	1323	29 1/2	1800	23,000	—	Blade/rim spalling
1392	2371	23	1800	10,000	—	Blade/rim spalling
1395	2353	25	1800	60,600	—	Complete rotor failure

Only rotor 1312 successfully reached 64,240 rpm. It was destroyed when a flame tube vibrated loose, worked forward and struck it. Four rotors failed during acceleration from 50,000 rpm to 64,240 rpm. The most likely causes of failure were hub bursts. Two rotors failed at relatively low speeds due to blade and blade ring spalling, as shown in Figure 4.3.3-7. Spalling may be a thermal stress problem caused by the rim going into compression as it is heated relative to the hub. A Weibull plot of rotor performance, excluding those failed by spalling, is displayed in Figure 4.3.3-8. The rotor which attained 64,240 rpm and the rotors which attained 50,000 rpm, as shown in Table 4.3.3-7 are included as suspensions.

Figure 4.3.3-7 — Example of Rotor Rim Spalling
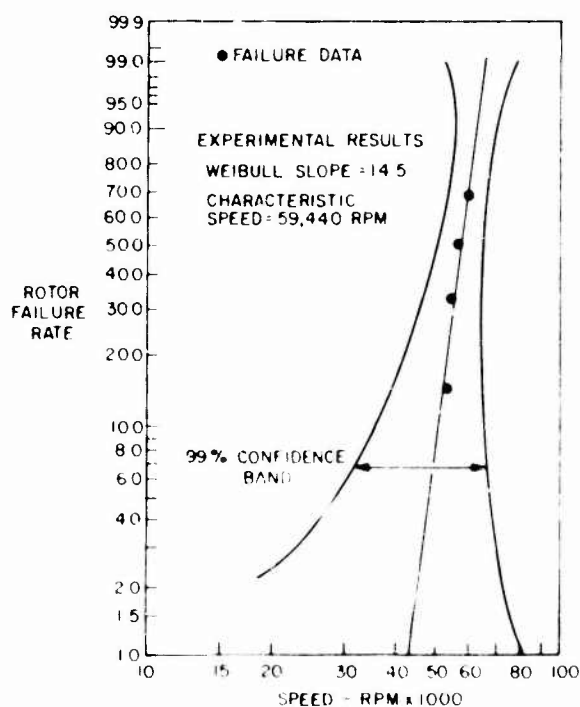
Figure 4.3.3-8 — Weibull Plot of Rotor Performance

169

Examining the data collected during these tests demonstrated a low probability of attaining the 64,000 rpm objective. Therefore, the test program was modified to investigate rotor operation at lower speeds and higher rim temperatures. As shown in Table 4.3.3-8, the objective was to test rotors for 25 hours at 50,000 rpm at the rim temperatures shown.

TABLE 4.3.3-8

HIGHER TEMPERATURE TESTS

Rotor Serial Number	Blade Ring Serial Number	Number of Blades During Hot Test	Rim Temperature (°F)	Speed (RPM)	Time (Hours)	Remarks
1338	2297	17	2200	30,000	1	
			2200	38,750	1	
			2200	43,250	1	
			2200	50,000	1/4	Failure
1384	2233	19	2000	24,000	1	
			2000	30,000	2/3	
			2000	34,400		Failure
1292	2036	35½	2000	50,000	25	OK

Rotor 1338 reached 50,000 rpm at 2200°F but failed, probably due to slow crack growth, after fifteen minutes. After this test, the rim temperature was reduced to 2000°F. Rotor 1384 failed at 34,400 rpm during acceleration from 30,000 rpm. Rotor 1292 was successful and sustained a 25-hour durability run at 50,000 rpm with a rim temperature of 2000°F. At this condition, burner flame temperatures of 3000°F and maximum blade temperatures of 2400°F were measured.

4.3.3.5 Turbine Rotor Engine Testing

Introduction

Engine testing of ceramic rotors was an unprecedented engineering endeavor in which the main difficulties stemmed from the high temperature environment of the ceramic engine and the catastrophic failures characteristic of ceramic parts. High temperatures made instrumentation difficult and expensive. The total failure of ceramic parts left few clues as to initiation of fracture.

Early in the program, tests were conducted on imperfect rotors to gain experience and to quickly identify problem areas. Testing was done at low speeds and temperatures. These parameters were increased as better rotors became available and confidence in the hardware increased.

A major problem was the rotor mounting design. This metal-to-ceramic interface was responsible for one of the two rotor failures incurred during the program, was implicated in the other failure and was a limiting factor in other successful tests.

Rotor Mounting Design

All ceramic rotors tested in engines were mounted to the engine shaft and to each other through face splines called curvic couplings, as shown in Figure 4.3.3-9. Rig tests, run before the start of engine testing, revealed a problem with the metal-to-ceramic interface designs; e.g., the coupling between the curvic adaptor and the first rotor. Different rates of thermal expansion and high coefficients of friction caused failures in the ceramic curvic coupling during thermal cycling.

Commercial lubricants [Nickle Ease, Molykote 321, Electro Film 1000X and Borekote] were tested on sample ceramic curvic couplings against the curvic adaptor shown in Figure 4.3.3-10. They were cycled through loads and temperatures shown in Figure 4.3.3-11 in an Instron test machine equipped with a furnace. Nickle Ease, with its graphite particles, caused problems in the balancing of rotor

assemblies. Molykote 321 worked well in balancing and was used in tests of rotors 716 and 717. Its low temperature capability limited its useful life in engine tests so it was replaced by Electro Film 1000X. A surface hardening treatment called Borekote was also tried but rejected because of a metallurgical incompatibility with the curvic adaptor material. All these lubricants had upper temperature limits of 800°F-1000°F and were marginal in that respect because of the high temperatures existing around the curvic adaptor during engine tests.
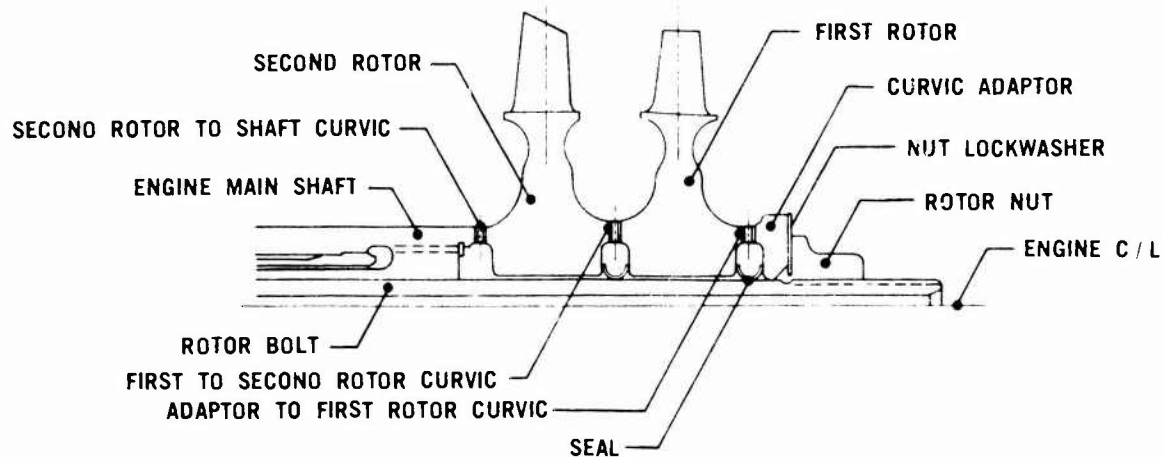
Figure 4.3.3-9 — Illustration of Rotor-Shaft Assembly
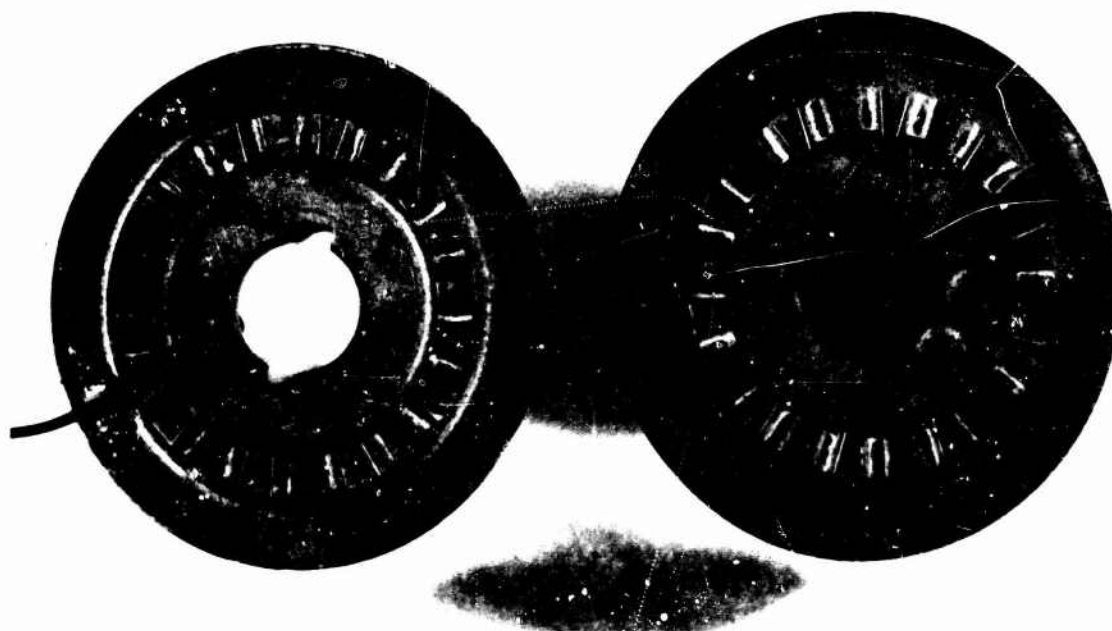
Figure 4.3.3-10 — Electro Film 1000x Lubricant After Three Test Cycles
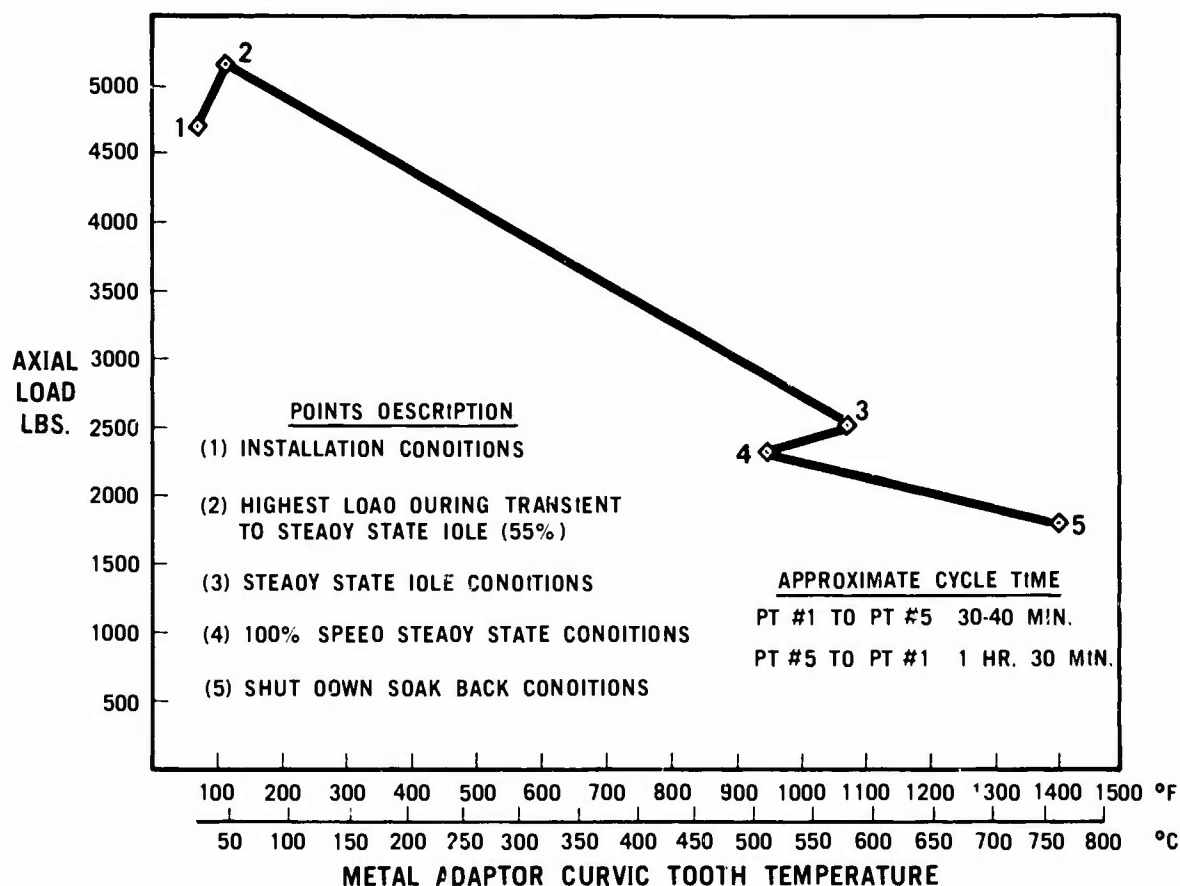
Figure 4.3.3-11 — Thermal-Load Cycle Schedule for Curvic Tooth Lubrication Tests

Tests of gold plate (0.0002 inches thick) on the metal curvic teeth proved most successful. Gold plate was used in the final three engine tests. Measurements of the gas temperatures around the curvic adaptor in the 2500°F turbine inlet temperature (TIT) tests of rotor 1195 disclosed that the temperature limit of the gold and the adaptor metal were being exceeded. Tests at 2200°F TIT were successful. A modification to the engine reduced the ambient conditions around the adaptor to 1100°F, so that a follow-up test at 2500°F TIT was totally successful.

Engine Tests of Ceramic Rotors

The following rotor tests are described in the order of their occurrence. Rotors 716 and 717 were the very first rotors tested in an engine.

Rotors 716 and 717 — These two duo-density rotors had blades cut down to 10% of full length. They were tested in a standard engine with the folded bolt mountings.[1,2,4,5,8] Molykote 321 was used on the curvic couplings as a lubricant. The test was conducted at 32,000 rpm and 2000°F TIT for forty minutes.[10] Post test inspections found that the rotors were in good condition but that the folded bolt had been overheated and permanently stretched. The bolt cooling system was modified to allow external control of the bolt temperature through the use of shop air. This modified system was used in subsequent engine tests.

Rotor 709 — Like rotors 716 and 717, 709 was a duo-density rotor. It had 10 blades which were 90% of full length. It was tested in a modified engine, as shown in Figure 4.3.3-12, to 2500°F TIT which allowed unheated air to bypass the single turbine and cool the exhaust to protect downstream regenerator cores and other hardware from excessively high temperatures.
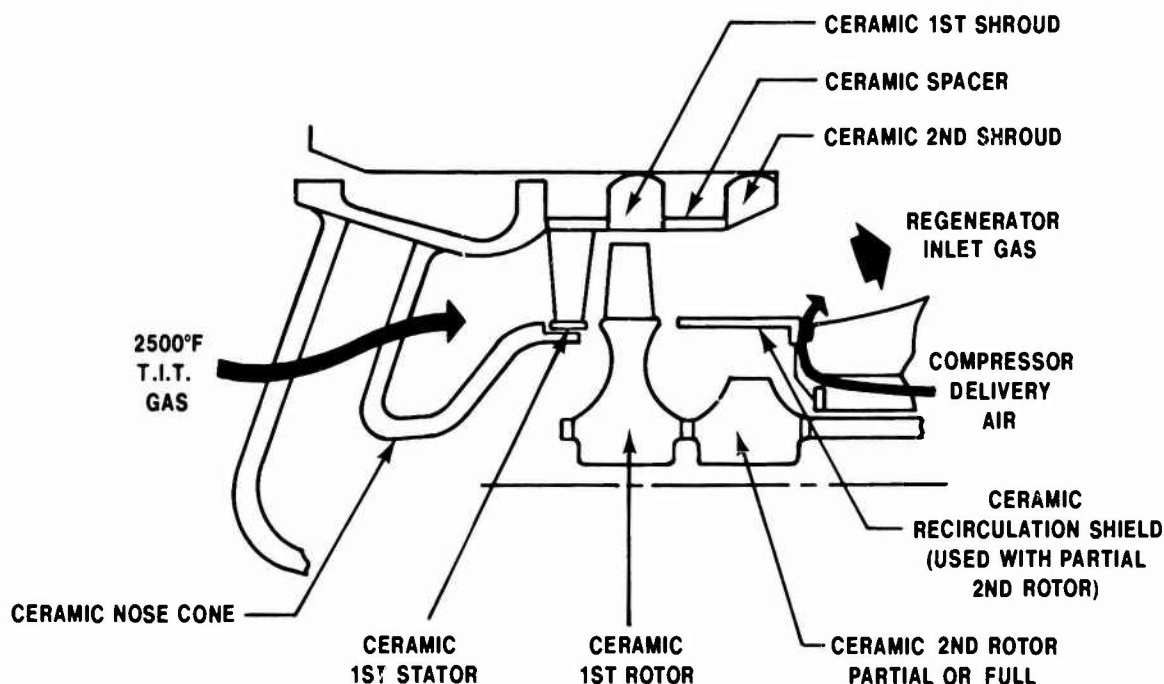
Figure 4.3.3-12 — Schematic View of Cross-Section of Modified Engine Flowpath

The rotor was run in two separate tests. The first was stopped at 52,800 rpm by a test cell problem while the engine was being accelerated to 100% speed. The second test ended in a rotor failure after 2.4 minutes while the rotor was being thermally stabilized at 2200°F TIT and 50,000 rpm. Rotor 709 was not a high quality rotor, thus the fact that it reached 52,800 rpm without failing was encouraging. This second test also proved out the modified bolt cooling system and the bypass air technique.[10]

Rotor 1195 — 1195 was a rotor with 27-1/2 blades 98% of full length and was the first to be run with the gold plating on the curvic adaptor and the rotor shaft curvic teeth. The air bypass system in the engine was changed so that the combustor inlet air was not routed around the rotor, as shown in Figure 4.3.3-12. This rotor had enough blades to reduce the exhaust temperature so that the regenerator cores would not be overheated.

This rotor was run in two tests. The first was a steady state ten-hour durability test at 45,000 rpm and 2200-2300°F TIT, and was completed without incident.[12] Rotating parts are shown in Figure 4.3.3-13 and a post test photograph of the rotor is shown in Figure 4.3.3-14. The capability of the rotor had not been exceeded, thus, a question still stood concerning the ultimate strength of rotors like 1195. Therefore, this rotor was tested further at 50,000 rpm and 2200-2300°F TIT for an additional 25 hours, again without failure.

At the end of the 25-hour run the TIT was raised to 2500°F and the rotor run at 50,000 rpm for an additional 1 hour and 54 minutes. During this portion of the test, thermocouples in the area of the curvic adaptor, as shown in Figure 4.3.3-15, indicated an ambient temperature of 1900°F. This high temperature had softened the adapter metal and removed the thin gold plating so that during the shutdown procedure the rotor failed, as shown in Figure 4.3.3-16. It was concluded from examination of the components that sticking of the curvic teeth had started the failure. A design aimed at ducting bolt cooling exhaust air at 700°F over the adaptor was initiated and used in the last engine rotor test of the program.
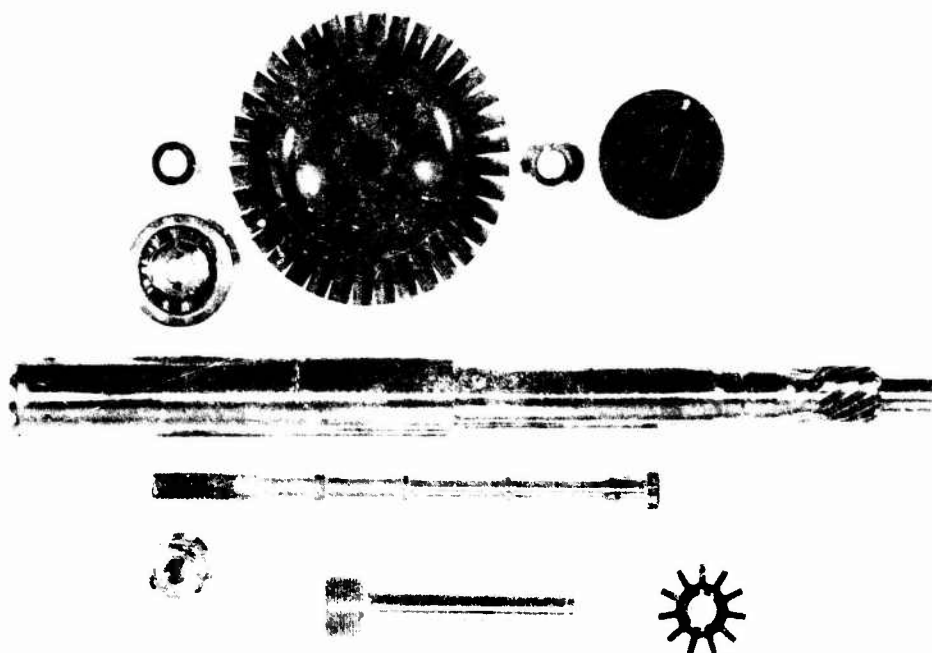
Figure 4.3.3-13 — Ceramic Rotor Number 1195, Attachment Hardware, and Main Shaft
(Defective Blades Were Removed Before Assembly and Test)
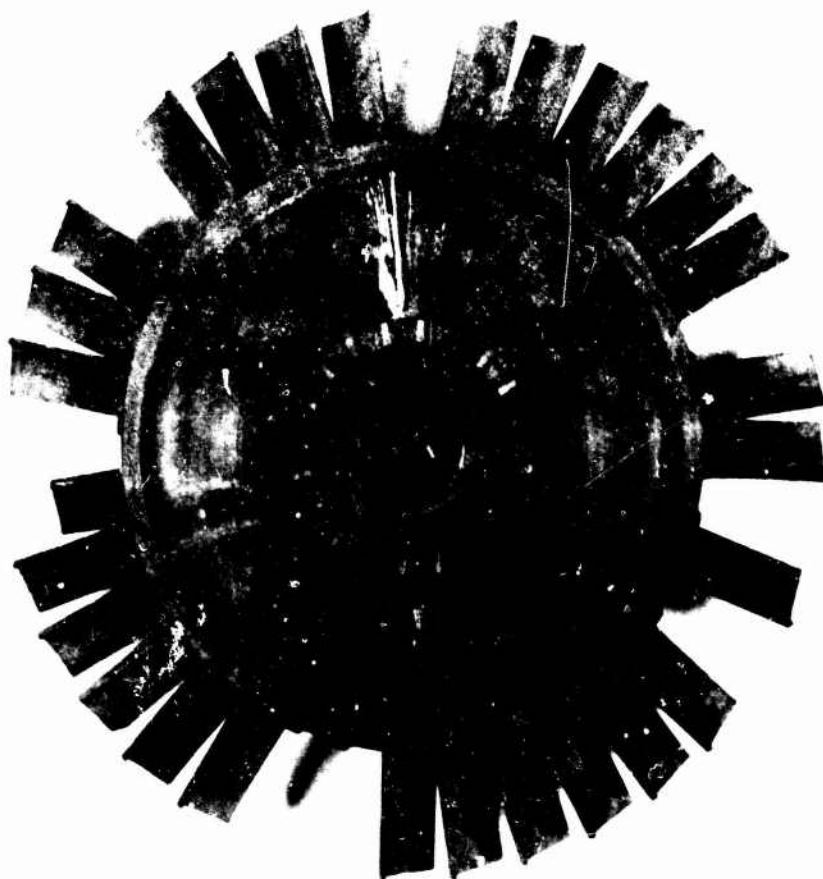
Figure 4.3.3-14 — Rotor 1195 After Ten Hour Run

	DESIGN TEMPERATURE F	ACTUAL TEMPERATURE F
1	1530	1900
2	1150	1880
3	—	1100
4	—	980

GAS FLOW

THERMOCOUPLES

ROTOR #1195

HIGH TEMPERATURE PROBLEM AREA

METAL CURVIC ADAPTER

DESIGN TEMPERATURE 1060 F
ACTUAL TEMPERATURE 1850 F
(ESTIMATED FROM HARDNESS DATA)
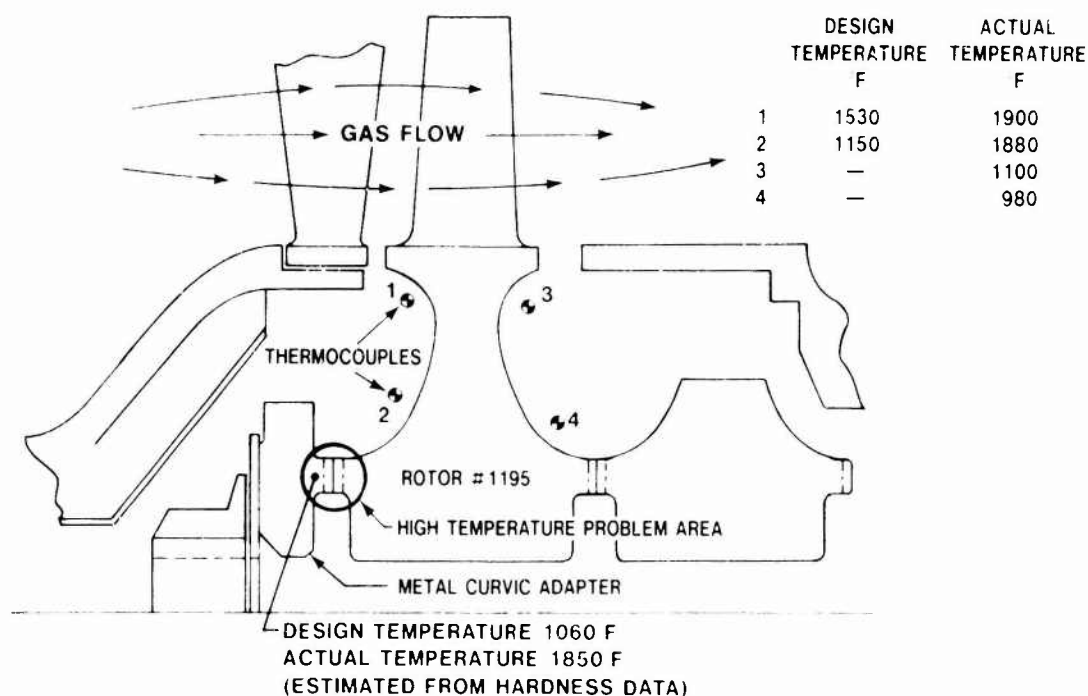
Figure 4.3.3-15 — Cross-Section of Rotor Number 1195 Showing Temperatures Measured
During Testing

Figure 4.3.3-16 — Hub of Rotor Number 1195 Reconstructed
After Failure During Shutdown

Rotor 1324   This last rotor tested was very similar to 1195 but had 26-1 2 blades rather than 27-1 2. The cone was modified with a small steel shield on the inside of the nose cone which ducted the 700 F bolt discharge air over the adaptor. Some clearances in the flowpath were reduced to control circulation of the 2500 F gas into the adaptor area. The adaptor was also reduced in diameter.[13] These modifications were proven out in a forty minute test of rotor 1324 at 40,000 rpm and 2500 F TIT. The run was totally successful. The temperature at the curvic adaptor, which had previously reached as high as 1900 F, reached a maximum of 1100 F during this test. Post test inspection revealed no problems. The gold plating in the adaptor was bright and the adaptor was of the same hardness as before the tests.

4.4 CERAMIC STATIONARY COMPONENTS

4.4.1 DESIGN

4.4.1.1 Design A

As indicated in Section 4.2, the initial flowpath design (Design A) was completed before initiation of this program and was based on ceramic stationary components and a cooled metal rotor. The stationary ceramic components comprised first and second stage stators, a turbine inlet nose cone and a can-type combustor as shown schematically in Figure 2.t of this report. Each stator comprised a bonded assembly of individually injection-molded RBSN vanes as shown in Figure 4.4.1-1; also, each incorporated its respective rotor tip shroud as an integral part of the stator assembly. An assembled stator is shown in Figure 4.4.1-2.
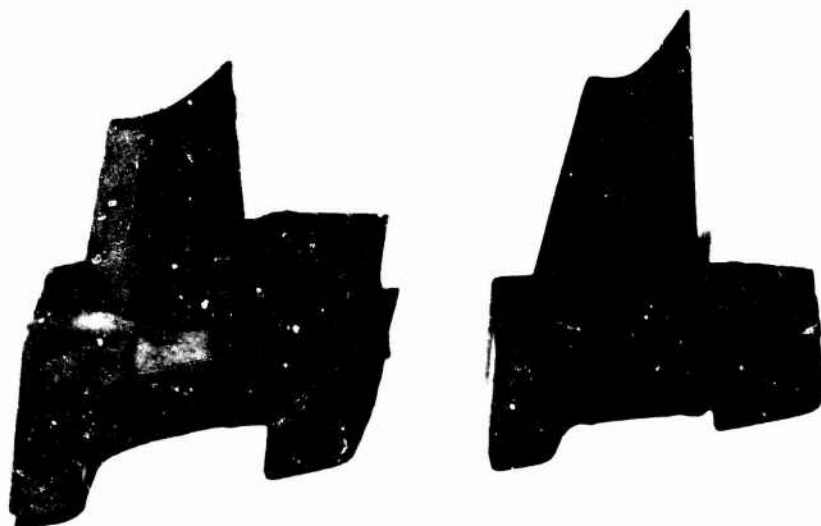
Figure 4.4.1-1 — Molded RBSN Design A Stator Segments Left — First Stage, Right — Second Stage
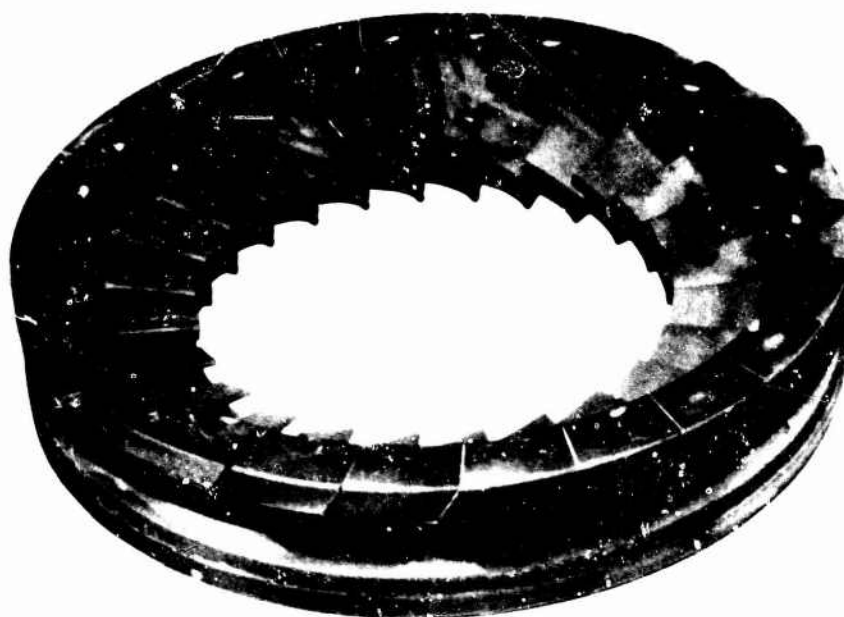
Figure 4.4.1-2 — Bonded Assembly of First Stage Design A RBSN Stator Segments

The ceramic nose cone was designed for one-piece molding and incorporated three hollow struts for transmitting cooling air as initially planned to the cooled metal rotor. The ceramic combustor was essentially a can-type combustor where the "can" was a ceramic tube with appropriate primary and secondary cooling holes; the combustor dome was designed for metal (Hastalloy X) with appropriate primary air cooling to allow for 2500°F turbine inlet operation. The metal dome facilitated cut-and-try design changes generally found necessary in optimizing light-off conditions.

4.4.1.2 Design B

Thermal shock testing of stators revealed vane failures due to a greater thermal inertia mismatch between the vane and vane base than had been anticipated. As a result, the stator was modified to Design 'B' where the rotor shroud was separated from the stator to lighten the mass (and thermal inertia) of the vane base. Individual Design B stator vanes are shown in Figure 4.4.1-3.
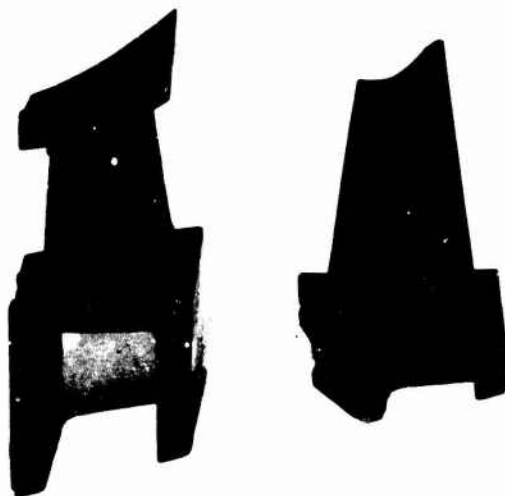
Figure 4.4.1-3 — Molded RBSN Design B Stator Segments; Left — First Stage, Right — Second Stage

A number of cases were analyzed to match up the nose cone and first stage stator for Design B as shown in Figure 4.4.1-4. Configuration D was selected and calculated nose cone stresses are shown in Figure 4.4.1-5. A nose cone of this configuration, as molded, was shown earlier in Figure 3.2.1-9.

Separate rotor shrouds were required with Design B and these were designed as simple rings with a single radial gap to interrupt hoop continuity and accommodate thermal mismatch. The Design B ceramic combustor tube shown in Figure 4.4.1-6 was essentially the same as Design A.

4.4.1.3 Design C

Engine and thermal shock testing of first stage Design B stators revealed a vane mid-span cracking problem due to unanticipated hot spots and associated thermal gradients. This led to narrowing of the vane chord, designated Design C, which solved the vane mid-span cracking problem. Despite the bonding of vanes into a stator assembly, there was a notch effect between vanes which caused cracking of the outer shroud. To solve this, tooling for a one-piece Design C stator was designed and built. Testing of nose cones revealed circumferential and axial cracking problems which led to a preslotted, scalloped, Design C configuration.

Though the combustor design remained unchanged, several grades of slip cast Si_3N_4 and recrystallized SiC were evaluated and shown to be unsuitable due to cracking resulting from unanticipated hot spots. "Refel" reaction-bonded SiC combustors, on the other hand, survived rig testing, establishing this material as a leading ceramic for combustors.

Design of the rotor tip shrouds also remained unchanged though durability problems were resolved by changing from cold pressed RBSN to slip cast RBSN material. Figure 4.4.1-7 shows a picture of the first and second stage rotor tip shrouds.
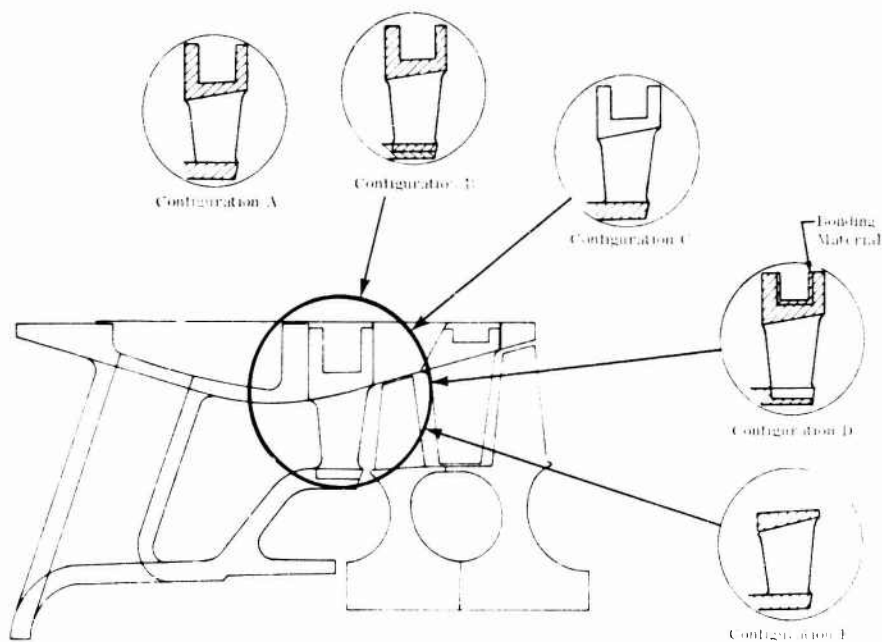
Figure 4.4.1-4 — Design B First Stage Stator — Nose Cone Configurations Which Were Analyzed
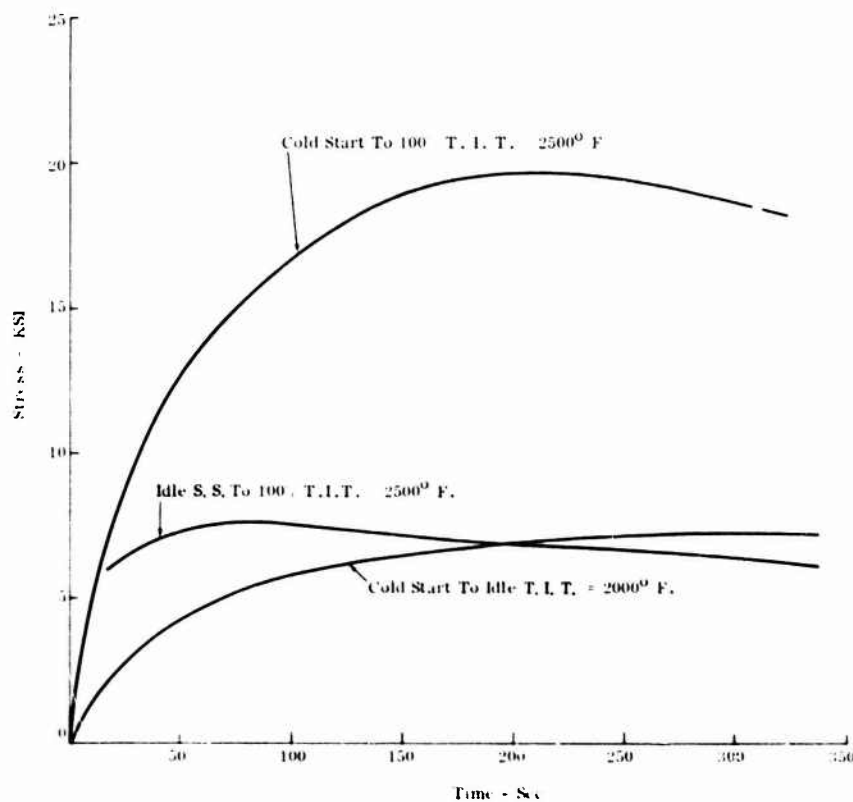
Figure 4.4.1-5 — Maximum Tensile Stresses in Design B Nose Cone Matched with Stator Configurations 'D' Over Several Transient Cycles

Figure 4.4.1-6 — Ceramic Combustor Tube
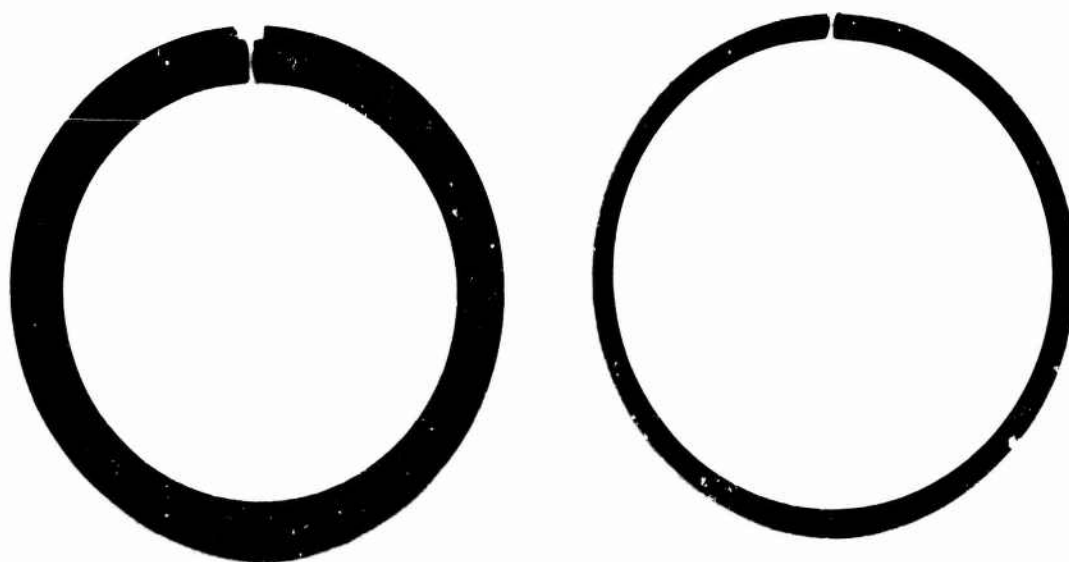
Figure 4.4.1-7 — Slip Cast RBSN Rotor Tip Shrouds Left — First Stage, Right — Second Stage

179

4.4.1.4 Designs D and D'

As indicated in Section 4.2, the Design D and D' flowpaths were the same with respect to the stationary components and utilized one-piece first stage Design C stators for both first and second stage locations. This stator design remained essentially unchanged through the remainder of the program though there were ongoing material and process improvements which continued to improve stator integrity.

The Design D nose cone was essentially the same as the Design C nose cone and incorporated the pre-slotting and scalloping as shown in Figure 4.4.1-8.

Figure 4.4.1-8 — Design D Injection Molded RBSN Nose Cone

Both thin and thick wall ceramic combustors were designed for the Design D flowpath; the thinner was predicted to have lower thermal stresses though higher mechanical stresses. Each configuration passed qualification testing.

The Design D rotor tip shrouds were the same as Design C although they incorporated a post-fabrication heat treatment to stabilize the material and solve an earlier operational problem of dimensional instability. Design D (or D' in the case of the stationary components) was the final configuration of stationary components in this program and was the configuration of components which met the program durability objectives.

4.4.2 MATERIALS AND PROCESSING

4.4.2.1 Introduction

Structural ceramic components were fabricated from RBSN by both injection molding and slip casting forming processes. The development of these RBSN materials was discussed in Section 3.2 of this report. During the course of the structural component fabrication effort, improved materials were adopted as rapidly as their respective development permitted.

The major emphasis in the material and processing efforts was placed upon component quality and reproducibility. The importance of feedback from screening, testing evaluations, and engine testing cannot be overemphasized. Once a component quality or durability problem had been discovered and identified through these tests, then meaningful action could be taken to identify the causes of — and develop solutions to — the specific problems. Component fabrication activities are summarized in the following sections.

4.4.2.2 Ceramic Stators

Silicon nitride stators were initially fabricated by the injection molding of individual segments which were then assembled into rings. Figure 4.4.1-1 shown earlier illustrates the first and second stage segments as molded in the Design A configuration. The assembly into rings was accomplished by placing the individual segments into a fixture containing piloting surfaces to accurately locate the ring. While held in this fixture another injection molding operation formed a complete ring of material in the U-shaped base channel, resulting in a one-piece accurately formed stator. Figure 4.4.1-2 shown earlier illustrates a completed ring, with the base channel partially filled with the material molded during the assembly operation.

While some stator assemblies were fabricated by this procedure and improvements resulted, rig and engine testing revealed that the bond joints were not reliable. A number of failures occurred at the joints, as noted in Section 4.4.4.4 of this report. In addition, this process was slow and laborious, producing many parts with obviously unsatisfactory bonding.

A subsequent effort involved development of tooling and processing to fabricate the Design D first stage stator as a one-piece injection-molded part. Each half of the tool contained the cavity to form one half of the airfoil. The stationary tool section formed the outer shroud and the moveable section formed the inner shroud. Formation of the inner shroud required a gap between each tip shroud segment. A collapsible core with wedge-shaped inserts at the midpoint between each vane provided the molded-in gap. As the moveable section retracted from the stationary section, the collapsible core moved inward as the tool went into the eject mode.

Temperature control was critical in using the one shot tooling. Correct temperature balance minimized molding flaws such as entrapped gas, shrinkage cracks, and fold and knit lines. Temperature balance was also required to hold the component on the moveable portion of the tool during ejection of the molded component. A slight shrinkage retained the component on the desired tool section until it was removed by the ejector system.

A one-piece first stage Si_3N_4 stator is shown in Figure 4.4.2-1. All vanes have a free gap at the tip shroud. Tip shroud gaps and concentricity of the part do not change during the binder burnout and nitriding processes.

In an effort to eliminate cold shut and internal void problems, several gating configurations were evaluated. Gating the material into the tool using a sprue bushing with 25 gates yielded 25 well defined knit lines. Changing to a 5 runner gate reduced the well defined knit lines to 5 and eliminated the other 20 knit lines. A single runner gate with a reduced area at the cavity entrance yielded a component having no knit lines. The mechanism which controlled knit line formation seemed to relate to the shear forces put into the material during injection. Greater shear forces yielded a more homogeneous part, although mold release was a problem due to increased surface abrasion during injection of the entire shot through one vane cavity.
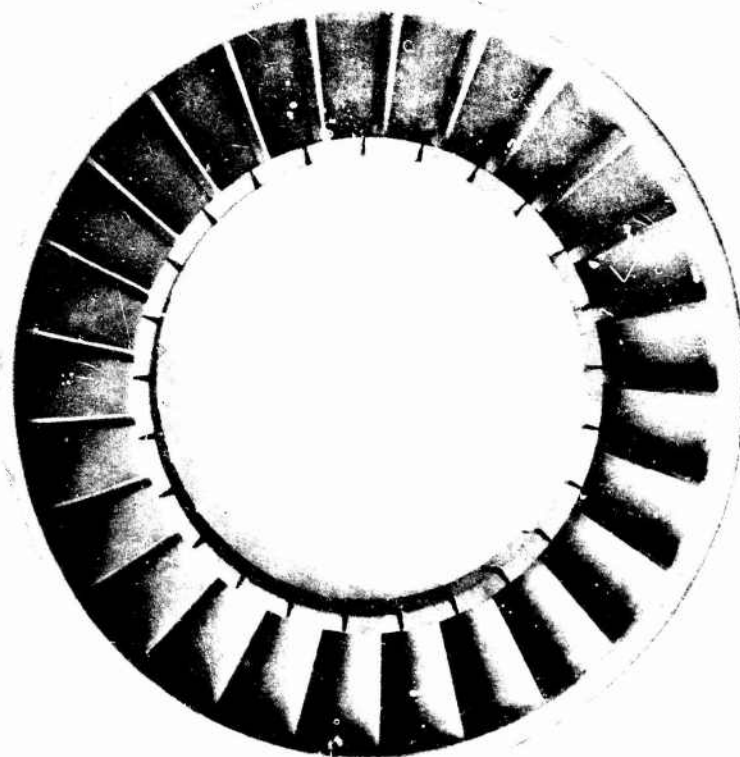
Figure 4.4.2-1 — One Piece Design D Injection Molded RBSN Stator

Cracking of the stator at the fillet radius between the inner shroud and vane during molding was caused by slight misalignment (0.005 inches) during die opening. To correct this misalignment, new linear ball bearings were installed on die guide pins. This change alone did not entirely eliminate the problem. A stripper plate and an extractor plate were added to push and pull the stator from the die prior to the point where misalignment damage occurred. This decreased the sensitivity of the die to misalignment, and crack-free components have been molded since these modifications were made.

A considerable number of one-piece RBSN stators were molded and processed during this program. Section 4.4.4.4 of this report discusses subsequent engine and rig test results.

4.4.2.3 Ceramic Nose Cones

In the 820 gas turbine engine, the air inlet nose cone was located ahead of the first stage stator. In this position it was subjected to the full temperature of the combustor exit gas and the thermal gradients present on engine shutdown. Therefore, the nose cone was fabricated from materials which had a high resistance to thermal shock; i.e., silicon carbide and silicon nitride. An example of a reaction-bonded silicon nitride nose cone was shown earlier in Figure 4.4.1-8.

Because the initial nose cones had relatively simple shapes, they were fabricated using a slip casting technique which also provided a short lead time. However, as the need for nose cones increased and slip cast components failed to perform adequately, injection molding was investigated as a possible fabrication method. The initial slip cast components were formed from Norton Crystar silicon carbide and consisted of an inner body cemented to an outer shell. Failures were encountered through the cemented joints and from thermal shock of the outer shell.

Tooling was procured to mold a monolithic nose cone of RBSN. The tool was made of hardened tool steel with withdrawable slides and core pins which formed the outer diameter and the hollow struts. Inner inserts were used to form the inside surface of the nose cone. Each molding shot required hand installation of these inserts. After withdrawal of the molded component from the tool, the inserts were removed by hand. Modifications to test component shape variations were done by machining a nose cone blank in the pre-fired state.

Temperature control was added to the tooling to relieve cracking problems. Shrinkage cracking was eliminated and cracking during removal of the hand inserts was minimized by removing the nose cone from the tool at the proper temperature.

Voids were found to result from poor tool sealing during injection of the molding mixture. Higher packing and holding pressures to squeeze out entrapped gas bubbles were made possible by auxiliary hydraulic cylinders which produced higher clamp loads on the tool slide. These cylinders also provided faster die insert removal which allowed improved control of shrinkage cracking in the strut area of the nose cone. The nose cones produced by this technique exhibited cracking in the bell area, caused by an overpacking condition. Hold pressure was reduced, which succeeded in eliminating this crack. Reducing the hold pressure also eliminated the overpacking and cracking upon die opening.

4.4.2.4 Ceramic Tip Shrouds

Rotor shroud rings were bands with a single radial gap interrupting their continuity, as shown earlier in Figure 4.4.1-7. The gap was provided to relieve stresses generated by thermal expansion during engine operation.

These rings were made initially from reaction-bonded silicon nitride fabricated using a cold-pressing process. A granular batch consisting of silicon powder and various binders was cold pressed at a pressure of 10,000 psi into cylindrical blanks approximately 1 inch thick. After burnout of the binders, the fragile silicon blanks were pre-nitrided to give them some strength, then machined into shroud rings. After machining, the shroud rings were nitrided. Shroud rings fabricated in this manner typically had densities of 2.2 gm/cm^3 and strengths on the order of 12,000 psi (measured in four-point bending). However, it was found that shroud rings made in this manner had a tendency to crack during engine operation.

In order to obtain higher strengths in the shroud rings, a slip casting method of fabrication was developed. In this process, the silicon metal powder was first ball milled to a mean particle size of 4.0 to 5.5μ. Then, a casting slip was prepared from the milled powder, distilled water and various deflocculating agents. This slip was then cast into plaster molds to form six inch high hollow cylinders. The cylinders were sliced into rings, nitrided, then diamond machined to final dimensions.

Shroud rings were fabricated by this method with densities from 2.35 to 2.75 gm/cm^3, and strengths in four-point bending ranging from 24,000 to 40,000 psi. These slip cast shroud rings did not crack during engine testing. However, it was found that their diameter decreased as a function of hot time in the engine.

In order to identify the possible causes for this dimensional change, a number of different slip compositions were tested. The impurity level of the silicon powder was the principle variable. Iron and calcium impurities were deliberately added in the form of Fe_2O_3 and CaF_2 as nitriding aids to promote the conversion of silicon metal to silicon nitride. To assess component stability, shroud rings were placed inside close-fitting rings of a lithium-aluminum-silicate material and heated to 1900°F for varying periods of time. After firing, the shroud rings were measured and any dimensional changes recorded. The results of these tests are displayed in Figure 4.4.2-2.

The dimensional stability of the material was significantly improved through the use of nitriding additives, particularly Fe_2O_3. This increased stability may have been due to a more complete conversion of silicon to silicon nitride. Although analysis by X-ray diffraction shows no residual silicon in any of the samples, it must be remembered that such analysis cannot detect concentrations below 0.5%. Subsequent photomicrographs of polished sections showed some unreacted silicon in the samples containing no additives. The greater instability of the materials at higher concentrations of calcium parallels the results obtained in creep measurements of both reaction-sintered and hot pressed silicon nitride.
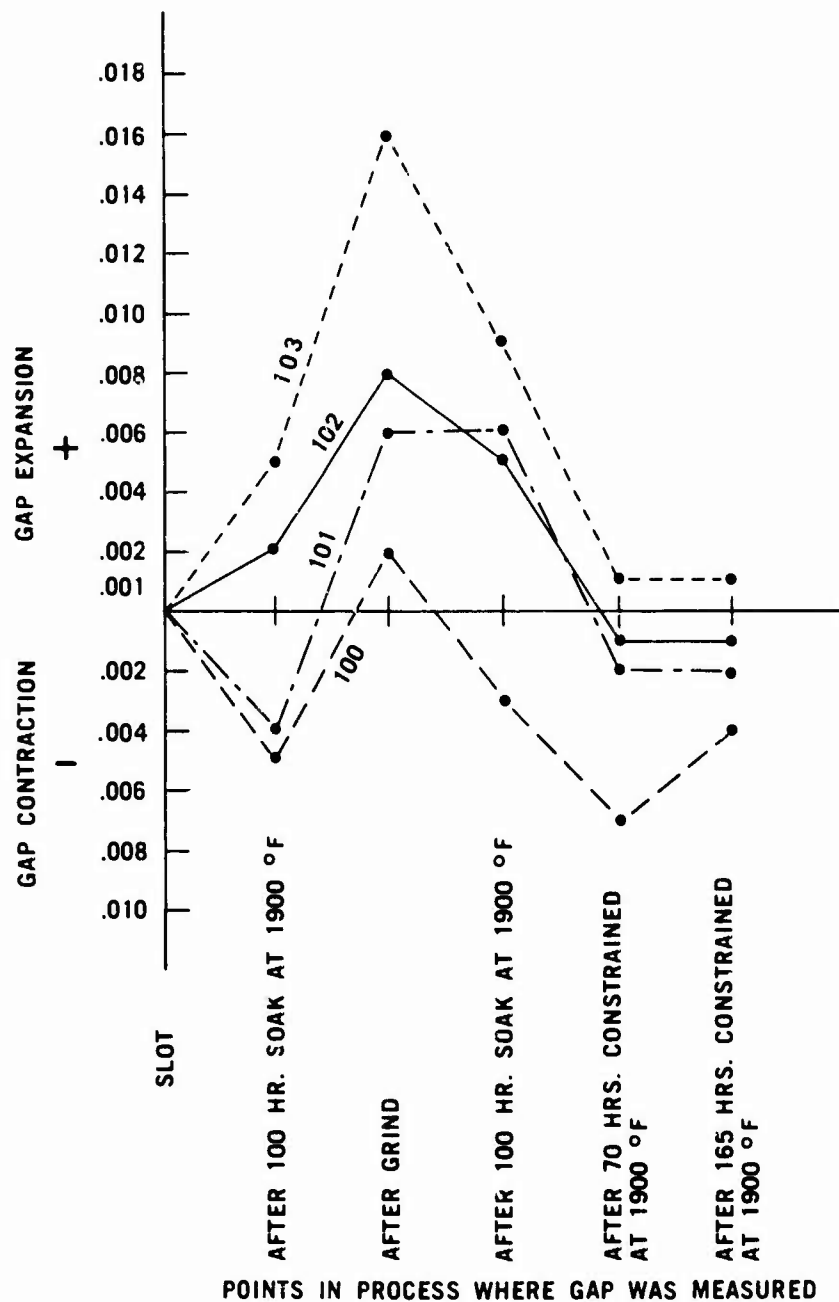
Figure 4.4.2-2 — Gap Changes in Slip Cast RBSN Shroud Rings at
Various Stages of Heat Treatment

Rotor shroud rings containing 1% and 3% Fe_2O_3 were further tested for periods up to 450 hours. After the first 10 hours there were no further dimensional changes. Engine testing of these shroud rings showed an improvement in performance. Further testing established a 3% Fe_2O_3 additive composition as the optimum, which is the material used throughout the remainder of this program.

4.4.3 SCREENING TEST RESULTS

Screening tests were used throughout the program to monitor the improvement in component quality as material changes and fabrication process changes were being made, and to perform component quality evaluations prior to extensive rig/engine test programs. Three specific screening tests were developed and used to verify the structural integrity of the ceramic stationary hot flowpath components. The tests, which are described in Section 3.3.2 of this report, are identified as the light-off qualification test, the stator vane bend test, and the stator outer shroud pressure test. Use of these screening tests proved to be a valuable means of assuring that the best available components would be used in engine durability evaluations.

4.4.3.1 Light-off Qualification Testing (L/O QT)

At the beginning of the program the L/O QT specified 25 simulated engine starts with the temperature limited to 1800°F and a hold time of 45 seconds. The first light was from room temperature and all succeeding lights from 1200°F, simulating a hot engine restart. As component quality improved, the severity of the test was increased by lowering the restart temperature: first to 1000°F, then to 500°F.

The majority of failures observed in the L/O QT were stator vane failure, believed to be due to thermal gradients between the vane and shroud. The thermal response of several points on the vane were obtained in a series of tests and shown in Figures 4.4.3-1 and 4.4.3-2. In addition to providing data for correlation with a thermal stress analysis being conducted, the data indicated that the 45 second hold time was longer than required to reach steady state conditions.
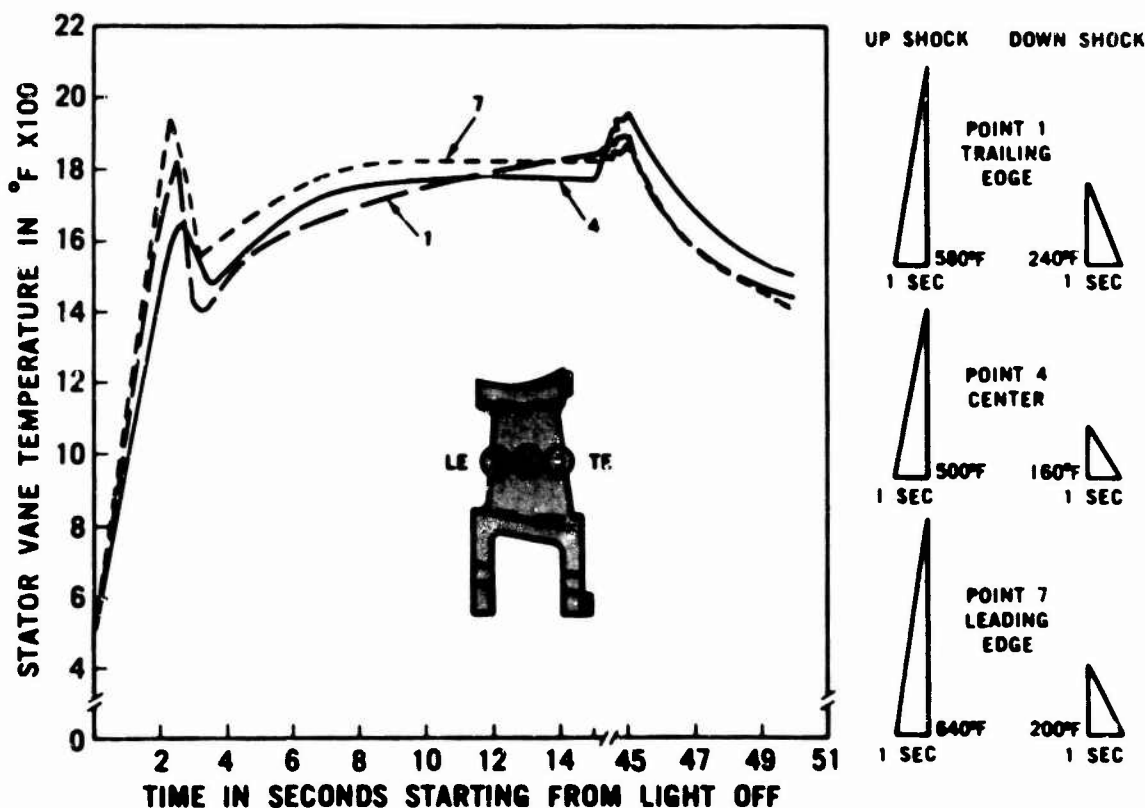
Figure 4.4.3-1 — Heating and Cooling Behavior of First Stage RBSN Design B Stator Vanes in Light-Off Qualification Testing From 500°F Start
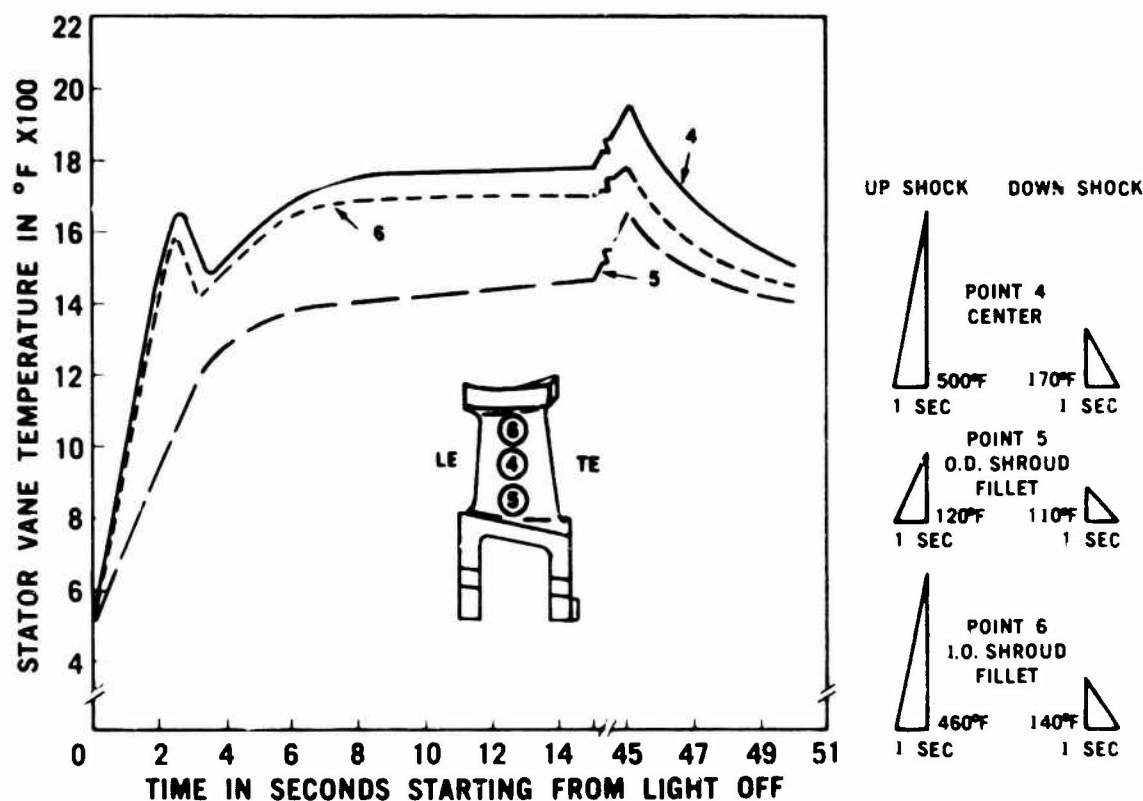
Figure 4.4.3-2 — Heating and Cooling Behavior of First Stage RBSN Design B Stator Vanes in Light-Off Qualification Testing From 500°F Start

The final version of the L/O QT sequence was established when the engine operating conditions for the duty cycle were defined. A ten light sequence was adopted as shown in Table 4.4.3-1. The light-off and hold temperature was increased to 1930°F, corresponding to engine design conditions. Although the number of lights were reduced, the thermal shock severity was increased by running each cycle from a cold light-off condition. The hold time at idle speed was modified to expose the hot flowpath components to a wider range of thermal environments. The hold time for the first five lights was reduced to 30 seconds since earlier tests showed this to be adequate for temperature (and therefore stress) stabilization in the stator vanes. A hold time of 60 seconds was established for the next four lights to accommodate the slower thermal response of the more massive stator outer shroud and rotor tip shrouds. A 300 second hold was used for the last cycle to insure full thermal equilibrium conditions of the nose cone. Typical light-off and cool down transients for the 10 light test are shown in Figures 4.4.3-3 and 4.4.3-4.

4.4.3.2 Stator Vane Bend Testing (VBT)

The VBT was used to mechanically stress stator vanes and screen out components containing flaws which were likely to cause failure by thermal shock in the L/O QT. The VBT was an outgrowth of a simple test devised to monitor the effects of processing improvements associated with the fabrication of one-piece ceramic stators, and is described in Section 3.3.2 of this report.

All the vanes from several stators which had undergone the L/O QT were loaded to failure in the VBT. Two of the stators had also accumulated significant durability test time. The resulting failure distributions are shown in Figure 4.4.3-5, and the data indicated that vanes capable of loads greater than 4-5 pounds would survive light-offs. Further, inspection of the fracture surfaces revealed that flaw-free vanes were typically capable of loads greater than 10 pounds. Therefore, an initial VBT proof load level of 10 pounds was chosen.

Nine 2.7 g/cc density RBSN stators were bend tested at the 10 pound level from the leading and trailing directions. Of the eight stators that survived, two sustained failures during the 10 light L/O QT. Vane bend failure load data was obtained from this last group of stators and each fracture surface inspected and classified as flawed or flaw-free. The two groups of data are presented in Figures 4.4.3-6 and 4.4.3-7.

TABLE 4.4.3-1

FLOWPATH QUALIFICATION TEST SCHEDULE

Number of Light	Light-Off Temperatures*, °F	Hold Time at 1930°F Seconds
1	70	30
2-5	150	30
6-9	150	60
10	150	300
10 Total Lights		420 Sec. at 1930°F

*Forced cooling used between lights to achieve these temperatures.
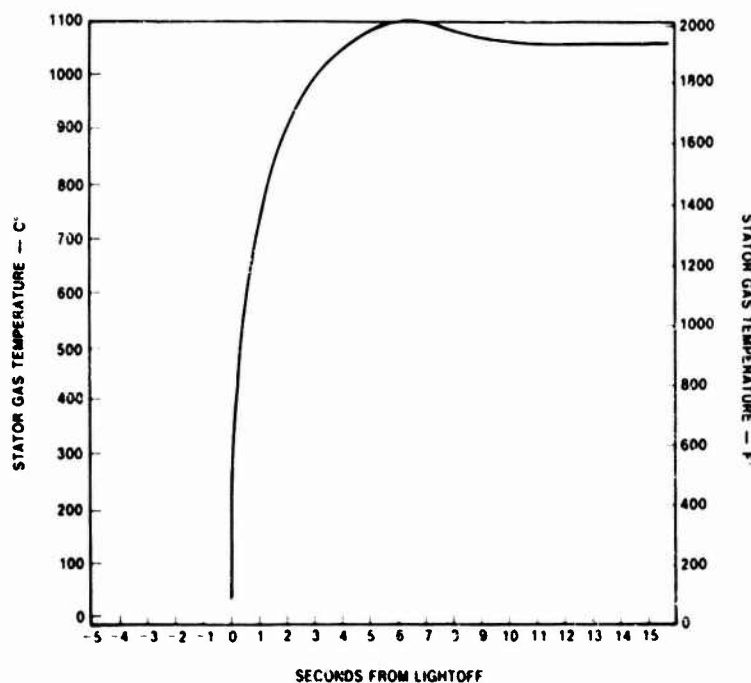
Figure 4.4.3-3 — Typical Light-Off Test Heat-Up Transient
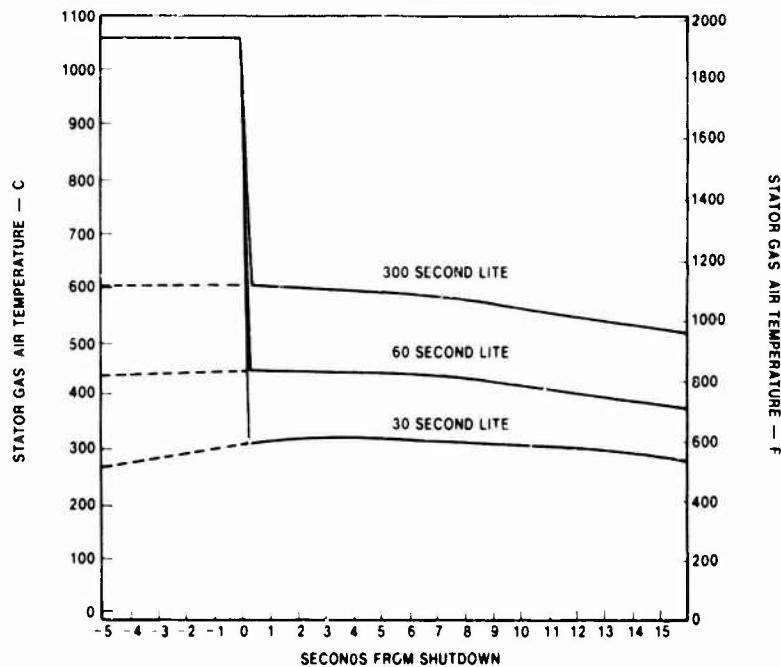
Figure 4.4.3-4 — Typical Light-Off Test Cool-Down Transient
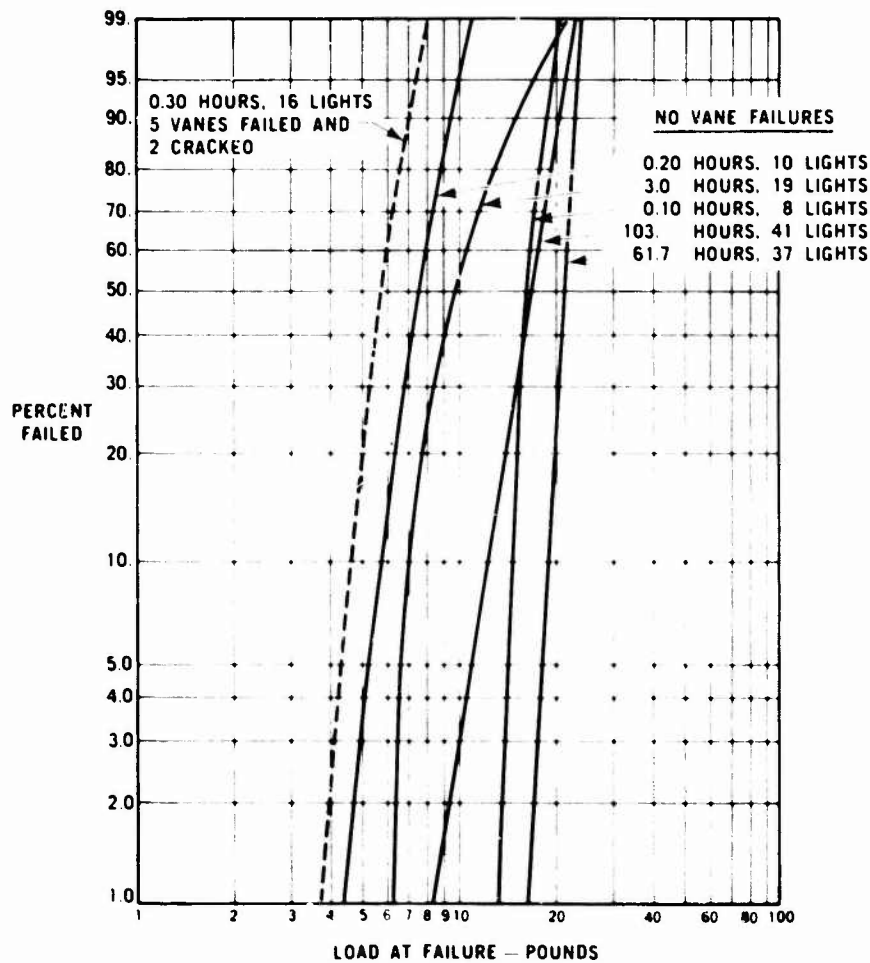
Figure 4.4.3-5 — Weibull Distribution of Vane Failure Loads for One Piece Design C
Stators Which Were Previously Engine Tested
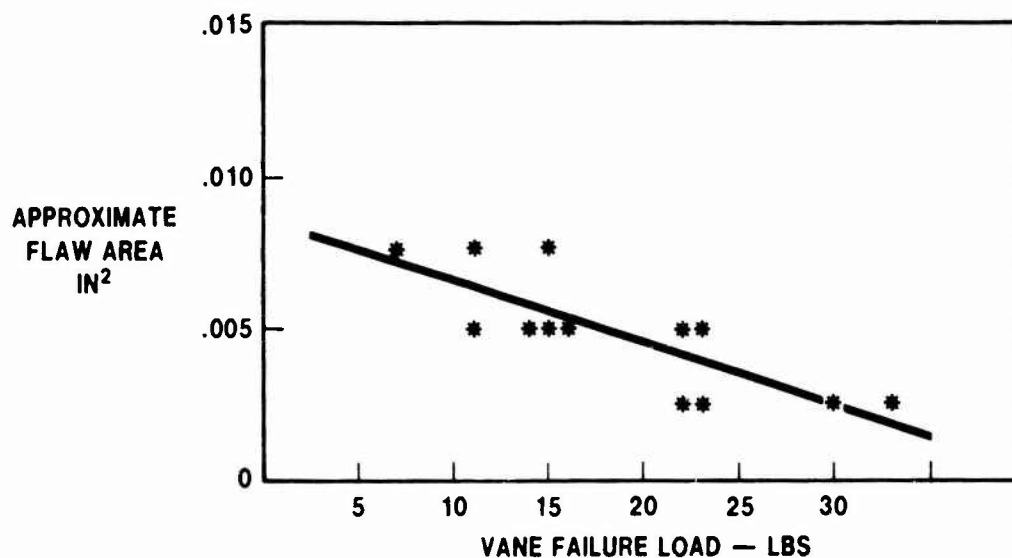
Figure 4.4.3-6 — Flaw Size Vs. Vane Failure Load for One Piece Design D Stators
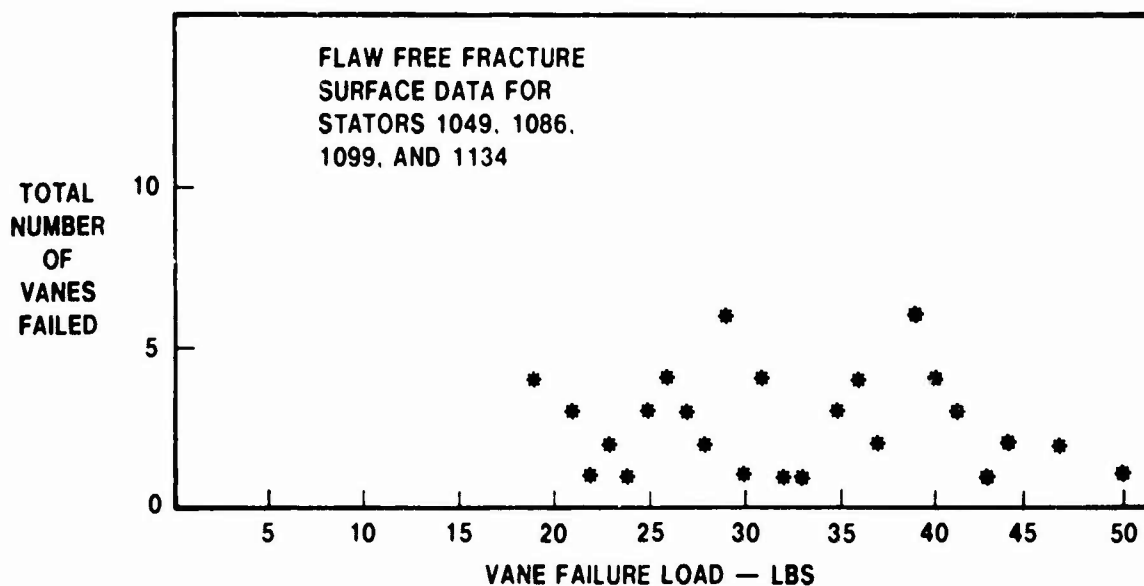
Figure 4.4.3-7 — Distribution of Vane Failure Loads for Unflawed Vanes, One Piece Design D Stators

In reviewing the vane load capability it was noted that the majority of the vanes (66 out of 77) successfully withstood an applied load greater than 19 pounds. The VBT proof load level was therefore increased to 19 pounds to enhance screening of poor quality vanes without jeopardizing good quality components.

At the conclusion of this program, 7 new 2.7 g/cc density RBSN stators were available for VBT screening. All were subjected to the 19 pound load test. Vane failures occurred in three stators. Five of the seven stators (3 which passed the VBT and 2 which had each lost 2 vanes) were processed through the 10 light test. Three of these survived the L/O QT without vane failures.

Survival of a stator in the 19 pound VBT would not guarantee that the stator would pass the L/O QT. However, the VBT provided reasonable assurance that vanes with large interior flaws or critical leading and trailing edge flaws could be screened out of the system.

189

4.4.3.3 Stator Outer Shroud Pressure Testing (SPT)

The SPT, described in Section 3.3.2 of this report, was devised to stress the stator outer shroud to a level sufficient to screen out those stators containing internal defects which could initiate failures in engine testing. Although loss of stator vanes was the dominant failure mode in the L/O QT and engine durability tests, some outer shroud failures were encountered. The failures generally occurred through internal fabrication flaws or voids which acted as stress raisers. A thermal stress analysis indicated that the maximum transient thermal tensile stress in the shroud was approximately 2,000 psi and in the tangential direction.

As in the case of the VBT, it was necessary to establish an appropriate screening stress level. The minimum level would be that determined by the thermal stress analysis (i.e., 2,000 psi). In order to obtain an upper bound, several good quality 2.55 g/cc density RBSN stators were tested to failure. Weibull analysis of the results indicated a characteristic strength of 11,000 psi with a Weibull modulus of 7.6.

The initial SPT screening stress level was established at the minimum value as determined by the stress analysis. Twelve stators were screened at the 2,000 psi level without failure. However, three of these failed through the outer shroud in the 10 light L/O QT. The screening stress level was increased to 4,000 psi; still significantly below the characteristic strength obtained earlier. One of three stators failed at this level. The two remaining stators successfully completed the L/O QT. Although the increased proof stress level resulted in improved survival rate in the L/O QT, the validity of this level cannot be clearly established without additional test results.

4.4.4 ENGINE & RIG TESTING RESULTS

4.4.4.1 Introduction

The stationary ceramic components shown in Figure 4.4.4-1 represent how the combustor, the nose cone, the two stator stages and the two rotor tip shrouds look now. They look considerably different than those produced at the beginning of the program. This section of the report shows how the design, materials, and development activities interacted to bring each component from its initial configuration to its present much more successful configuration.
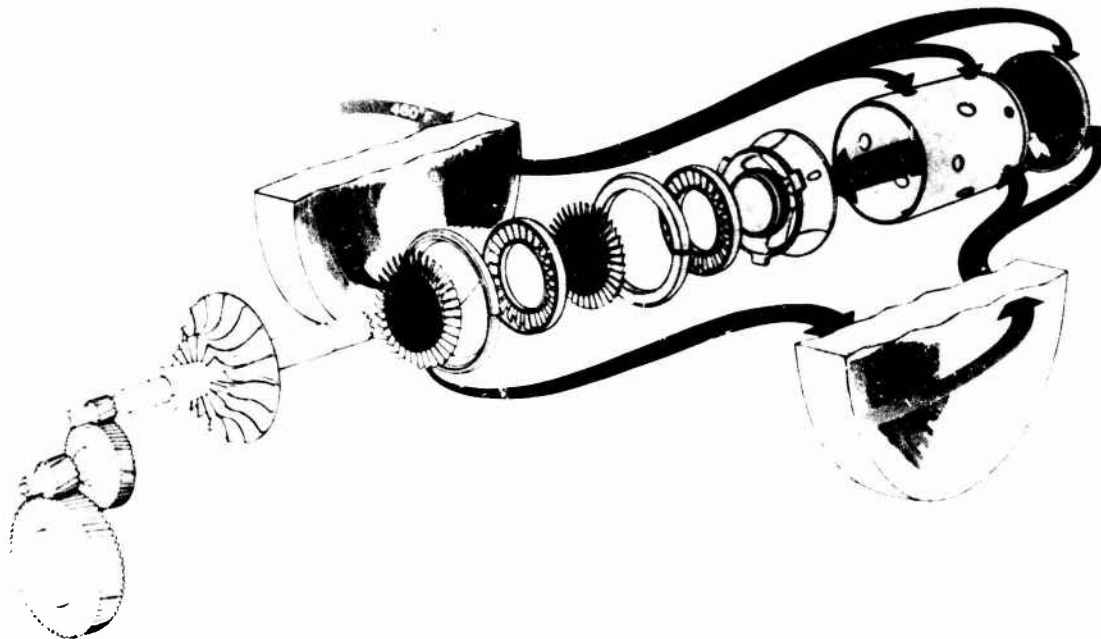
Figure 4.4.4-1 — Ceramic Flowpath

These stationary ceramic components were subjected to varying environments over the engine operating duty cycle, as shown in Figure 4.4.4-2. The engine turbine inlet temperature (TIT) schedule consisted of 175 hours at 1930°F from 55% to 90% speed and 25 hours at 2500°F at 100% speed. Typical turbine inlet temperatures during start-ups and shutdowns are displayed in Figure 4.4.4-3.

DAILY DUTY CYCLE SCHEDULE
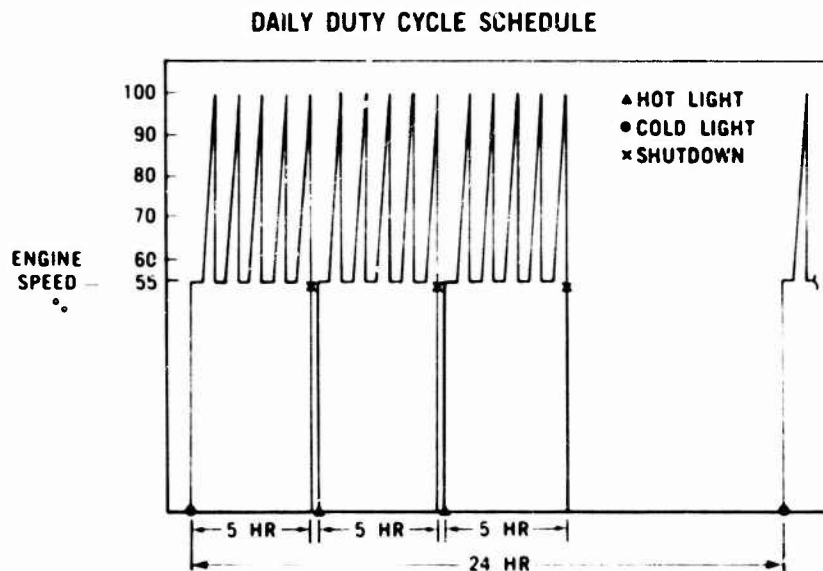
Figure 4.4.4-2 — Engine Durability Duty Cycle

191
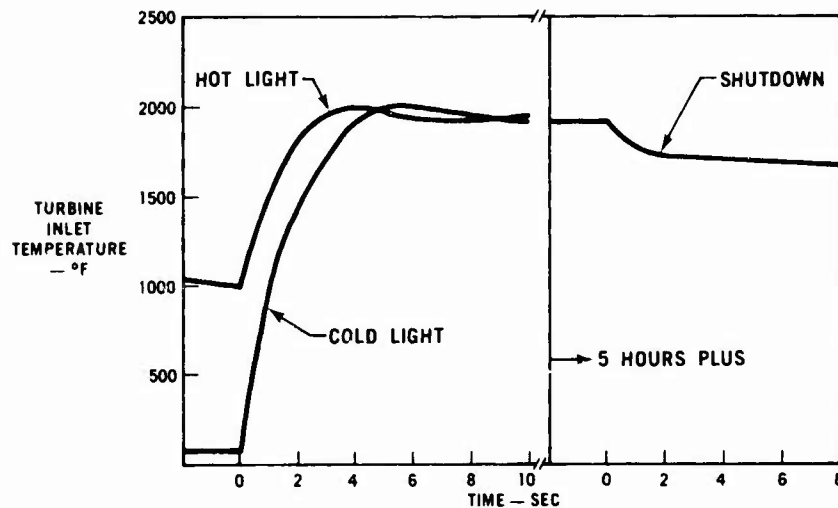
Figure 4.4.4-3 — Typical Engine Turbine Inlet Temperature Transients

For convenience in the development of these stationary ceramic flowpath components, a test and evaluation philosophy was established which separated the complex duty cycle into three types of testing. The components were tested and evaluated for the most part, under the following controlled conditions:

1. 1930°F — Steady state
   — Static testing (without turbine rotors)
   — Dynamic testing (with turbine rotors)

2. 2500°F — Steady state
   — Static testing
   — Dynamic testing

3. Cyclic — Transient
   — A sequence of light-off, acceleration to 55% speed and shutdown.

Initially all parts were subjected to ten transient cycles. This was followed by static steady state testing of 175 hours at 1930°F and 25 hours at 2500°F. This fulfilled the goal of the stationary component development effort.

4.4.4.2 Ceramic Combustor Testing

The ceramic combustor progressed through two iterations. The first iteration converted it from a test rig to an engine configuration and the second iteration reduced its operating thermal stresses by a reduction in wall thickness. Specific configurations, pertinent design and materials features, and development data used as a basis for progressing to a subsequent configuration are detailed in Figure 4.4.4-4, with references which contain more detailed data.

For the original combustor-design configuration, a variety of materials were evaluated, including silicon nitride, fused silica, silicon carbide, mullite, silicon carbide-coated graphite, and aluminum nitride. Each material was tested in the Ceramic Combustor Test Rig. During this initial evaluation phase, the most successful material was Refel silicon carbide.

The first iteration simply converted the test rig design to the engine design. Although one Refel silicon carbide combustor of this configuration completed 200 hours of duty cycle operation (including 25 hours at 2500°F), a number of components failed to survive a ten hour qualification test. A design analysis indicated that the steady state thermal stresses would be reduced by 40% with a material thickness reduction. The second iteration reflects this change.

192

CERAMIC COMBUSTOR DEVELOPMENT
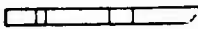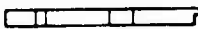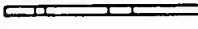
CONFIGURATION/MODIFICATION	DEVELOPMENTAL RESULTS
• ORIGINAL DESIGN	• TEST RESULTS
— TEST RIG DESIGN HAS REAR CONICAL MOUNTING CONFIGURATION	— REFEL SiC PARTS DEMONSTRATE ENCOURAGING RESULTS (4)
• FIRST ITERATION	• TEST RESULTS
— ENGINE DESIGN (THICK WALL CONFIGURATION)	— 200 HOUR DURABILITY ACHIEVED (25 HOURS AT 2500°F) (6, 7, 8, 9, 10)
	• DESIGN ANALYSIS
	— THERMAL STRESS ANALYSIS INDICATES THIN WALL CONFIGURATION REDUCES STEADY-STATE STRESSES
• SECOND ITERATION	• TEST RESULTS
— ENGINE DESIGN (THIN WALL CONFIGURATION)	— 100% SUCCESS THROUGH 10 HOUR QUALIFICATION TEST (9, 10)

Figure 4.4.4-4 — Ceramic Combustor Development

Test results on the thin wall Refel silicon carbide configuration verified the design analysis. All combustors tested successfully survived a 10-hour screening test. In addition, two combustors completed the 200 hour goal without incident.

4.4.4.3 Ceramic Nose Cone Testing

The ceramic nose cone progressed through four major iterations during its development. Specific configuration, pertinent design and material features, and resulting development data used as a basis for progressing to a subsequent configuration, are detailed in Figure 4.4.4-5.

The original design contained a number of specific features worth noting. The outer shroud was a solid shell with four thermocouple holes located near the front lip. At the rear of the outer shroud was a heavy solid ring called the rear flange. Three radial struts connected the outer shroud to a body called the inner bell. The inner bell was a shell with a tubular section in the center. Initial nose cones were fabricated by injection molding of 2.2 g/cm³ density RBSN.

Testing of this design produced axial outer shroud cracks, usually through the thermocouple holes. In addition, the inner bell cracked circumferentially, usually at the inner bell tube-to-inner bell junction. Fabrication studies noted that low density areas were present in the outer shroud front lip and rear flange sections. A design analysis confirmed high stresses were present in the inner bell tubular section junction and also indicated the possibility of adverse thermal gradients in the thicker front lip and rear flange areas.

The first nose cone iteration was designed utilizing this information. It had these modifications: 1) the rear flange was scalloped to reduce its mass, the front lip was cut back, and the four thermocouple holes removed; both these changes resulted in a more uniform thickness outer shroud; 2) the outer shroud was slotted axially in three places, spaced equally between each strut; 3) based on design analysis results, the tubular inner bell section was removed.

This nose cone was also fabricated in the 2.2 g/cm³ density RBSN material. Testing produced the following results: 1) occasional outer shroud cracks occurred; 2) axial inner bell rear lip cracks, a new mode of failure, was observed; 3) data indicated that the 2.2 g/cm³ density material RBSN was prone to severe loss in strength due to oxidation. An assessment of the inner bell rear lip axial cracks revealed that a change in the insulation configuration had occurred when the tubular section was removed. Additional insulation had been added which changed the thermal conditions in the area of the thin rear lip. This added insulation was subsequently cut back.

The second nose cone iteration reflected major changes, not all due to the prior development data. This configuration, now fabricated in 2.55 g/cm³ density RBSN, incorporated three thermocouple

holes. The reintroduction of these holes was necessary because of problems encountered with upstream hardware adaptation. Axially slotting the outer shroud appeared to be a benefit so this feature was maintained. These slots were oriented to pass through the three thermocouple holes. The insulation configuration was modified as noted earlier.
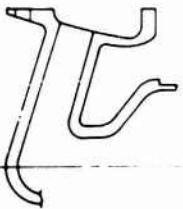
CERAMIC NOSE CONE DEVELOPMENT
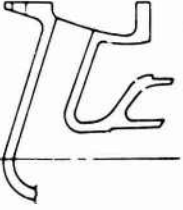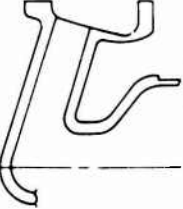
CONFIGURATION/MODIFICATION	DEVELOPMENTAL RESULTS
• ORIGINAL DESIGN	• TEST RESULTS:
— CONTINUOUS OUTER SHROUD	— OUTER SHROUD AXIAL CRACK (2)
— (4) THERMOCOUPLE HOLES	— INNER BELL CIRCUMFERENTIAL CRACKS (2)
— CONTINUOUS REAR FLANGE	• FABRICATION RESULTS
— INNER BELL TUBE	— POROSITY IN REAR FLANGE SECTION AND OUTER SHROUD FRONT LIP SECTION (5)
— 2.2 g/cc DENSITY INJECTION MOLDED REACTION BONDED SILICON NITRIDE (RBSN) (1)	• DESIGN ANALYSIS:
	— CONFIRMS HIGH STRESS AT INNER BELL TUBE TO INNER BELL JUNCTION (1)
• FIRST ITERATION	• TEST RESULTS:
CUT BACK CONTINUOUS OUTER SHROUD FRONT LIP AND ELIMINATED T/C HOLES (4)	— OCCASIONAL OUTER SHROUD CRACKS (2, 3, 4)
— SCALLOPED REAR FLANGE TO REDUCE MASS AND GRADIENTS (4)	— AXIAL INNER BELL REAR LIP CRACKS
— AXIALLY SLOTTED OUTER SHROUD — THREE PLACES EQUALLY SPACED (4, 5)	• FABRICATION RESULTS:
	— POOR QUALITY CONTROL (5)
— REMOVED INNER BELL TUBE AND MODIFIED INSULATION CONFIGURATION (3)	— 2.2 g/cc DENSITY MATERIAL PRONE TO HIGH OXIDATION (7).
— 2.2 g/cc DENSITY INJECTION MOLDED RBSN	
• SECOND ITERATION	• TEST RESULTS
— 2.55 g/cc DENSITY INJECTION MOLDED RBSN (8)	— REAR FLANGE SLOT-TO-SLOT CRACKS IN REDUCED AREA SECTION (9)
— (3) T/C HOLES REQUIRED (9)	— INSULATION MODIFICATIONS DIMINISHED AXIAL INNER BELL CRACK (9)
— AXIALLY SLOTTED SHROUD THRU (3) T/C HOLES (9)	— BEND TESTS OF REDUCED AREA REAR FLANGE SECTION INDICATE POSSIBLE REDUCTION IN LOAD CARRYING CAPACITY (9)
— MODIFIED INSULATION CONFIGURATION (9)	• FABRICATION RESULTS
	— TOOLING CONTROLS IMPROVE QUALITY CONTROL
• THIRD ITERATION	• TEST RESULTS
— 2.7 g/cc DENSITY INJECTION MOLDED RBSN (9)	— EVALUATION NOT COMPLETE
— FLOWPATH CONTOUR IMPROVED AERODYNAMICALLY (10)	• FABRICATION RESULTS
— ANGLED OUTER SHROUD SLOTS TO INCREASE LOAD CARRYING CAPACITY (9)	— MOLDING PARAMETERS NOT OPTIMIZED FOR 2.7 g/cc DENSITY MATERIAL

Figure 4.4.4-5 — Ceramic Nose Cone Development

Testing identified another problem. Rear flange slot-to-slot cracks occurred in the reduced area section. Prior slot orientation was at 120° intervals, so it was recommended that the new slots be angled to approach equal segments at the rear flange. No longer was axial bell lip cracking a problem, since the insulation modification had diminished this mode of failure. In the fabrication area, development of injection molding process controls improved component quality.

The third iteration is the present nose cone configuration. The recommended slot angling was achieved. These components were now being fabricated in 2.7 g/cm³ density RBSN. No rear flange failures occurred. Two components of this configuration successfully reached the 200-hour program durability goal.

4.4.4.4 Ceramic Stator Testing

The first stage stator progressed through four major iterations during its development. Specifics of the first stage iterations are detailed in Figure 4.4.4-6. A major effort was expended in developing the stator and demonstrates the required interactions between design, materials, and testing activities.

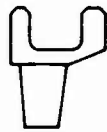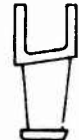**CERAMIC FIRST STAGE STATOR DEVELOPMENT**

	CONFIGURATION/MODIFICATION	DEVELOPMENTAL RESULTS
	• ORIGINAL DESIGN	• TEST RESULTS:
	— (25) SEGMENTS OF 2.2 g/cc INJECTION MOLDED RBSN (1)	— OUTER SHROUD SEGMENT BOND JOINT FAILURES (1)
	— INTEGRAL FIRST STAGE SHROUD	— VANE ROOT THERMAL CRACKS (1)
	— AERODYNAMIC CLEARANCE AT STATOR ID (TO NOSE CONE)	• FABRICATION RESULTS:
		SEGMENT BONDING MATERIAL LOW DENSITY AND LOW STRENGTH (1)
		• DESIGN ANALYSIS
		THERMAL SHOCK RIG TESTS OF VANE SEGMENTS CONFIRM SHROUD MASS TO VANE MASS THERMAL MISMATCH (1)
	• FIRST ITERATION	• TEST RESULTS:
	— SHROUD MASS REDUCED TO MORE CLOSELY MATCH VANE THERMAL RESPONSE (1ST TIP SHROUD SEPARATE PART) (1)	— OUTER SHROUD SEGMENT BOND JOINT FAILURES (2)
		— VANE THERMAL FAILURES MOVED TO MIDSPAN REGION (3)
	— INNER SHROUD ADDED TO DIMINISH AERODYNAMIC LEAKAGE (1)	— CUT BACK TRAILING EDGE VIRTUALLY ELIMINATES VANE MIDSPAN CRACKING (3, 4)
	• SECOND ITERATION	• TEST RESULTS:
	— REDESIGNED VANE TO CUTBACK CONFIGURATION (4)	— OUTER SHROUD SEGMENT BOND JOINT FAILURES (4, 5)
	— NEW SEGMENT INJECTION MOLDING TOOLING AND IMPROVED SEGMENT ASSEMBLY FIXTURE (3)	• FABRICATION RESULTS:
		— ONE PIECE TOOLING DESIGNED TO ELIMINATE SEGMENTED CONFIGURATION (5)
	THIRD ITERATION	TEST RESULTS:
	— ONE-PIECE INJECTION MOLDED PART (6)	— OUTER SHROUD CRACKING POSSIBLY FUNCTION OF RATE OF OXIDATION
	— 2.55 g/cc DENSITY RBSN (7)	FABRICATION RESULTS: — EARLY 2.7 g/cc DENSITY MATERIAL DATA INDICATES LOWER OXIDATION RATE (10)
	FOURTH ITERATION	TEST RESULTS:
	— 2.7 g/cc DENSITY RBSN (9)	— EVALUATION NOT COMPLETE
	— EXPANDED PRE-ENGINE TEST QUALIFICATION	FABRICATION RESULTS:
		— MOLDING PARAMETERS NOT OPTIMIZED FOR 2.7 g/cc DENSITY MATERIAL

Figure 4.4.4-6 — Ceramic First Stage Stator Development

The original configuration was an assembly of 25 segments, each of which contained a portion of the first stage tip shroud. The initial material used was 2.2 g/cm^3 density injection-molded RBSN. Two major test results were experienced: 1) failures occurred at the segment joints, and; 2) thermal cracks occurred at the vane root junction with the massive outer shroud. Thermal shock rig tests of vane segments confirmed a thermal mismatch at the vane root section.

The first iteration attempted to resolve the vane cracking problem through redesign. The first stage shroud section was removed and the outer shroud redesigned to more closely match the thermal response of the vane. The addition of an inner shroud of segmented configuration was done for aerodynamic reasons. Although bond joint failures were repeated, the vane thermal cracking was altered in that the vane cracking moved to midspan. Decreasing the vane span by removing material from the trailing edge, which also thickened the trailing edge, eliminated this cracking.

The second iteration incorporated this vane modification as a permanent change. Tooling modifications to optimize segment assembly were unsuccessful as failures in the segment bond joint persisted. Thus, one-piece tooling was designed to eliminate the segmented configuration.

The third iteration combined the one-piece design with a higher density 2.55 g/cm³ RBSN. This combination resulted in a major improvement in part life, but fabrication of such a complex part required considerable development. Outer shroud cracking was diminished but not eliminated. Oxidation of the stators, evidenced by measuring weight gain, appeared to be related to part life. As materials and processes improved, the rate of oxidation (weight gain) decreased. The weight gain of 2.55 g/cm³ density stators is summarized in Figure 4.4.4-7. As can be seen, some variation in weight gain still existed. Two stators, 948 and 954, exhibited very little oxidation and survived 175 hours at 1930°F without failure. After this test, stator 948 survived an additional 25 hours at 2500°F.
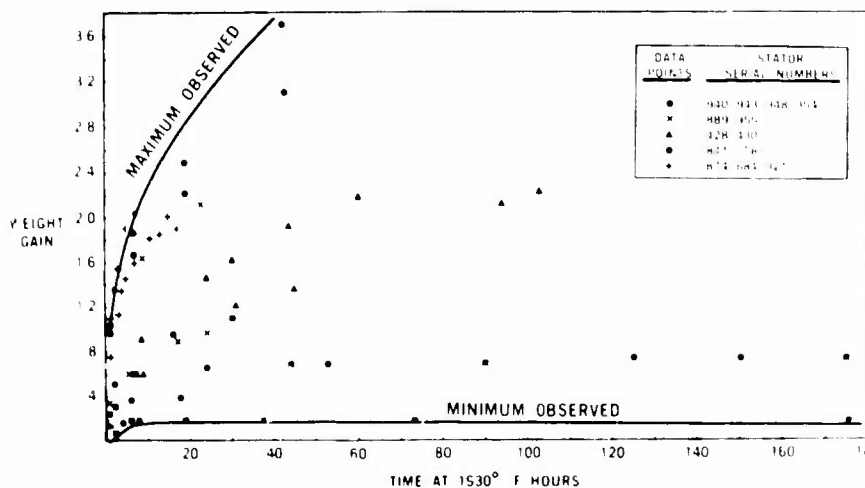
Figure 4.4.4-7 — Weight Gain Vs. Engine Test Time at 1930°F for 2.55 g/cc Density RBSN Stators

The fourth iteration involved combining the one-piece configuration with a major material improvement, 2.7 g/cm³ density RBSN. Molding developments and processing developments helped to make these parts more consistent. Fourth iteration stators survived the 200 hour goal. However, the oxidation problem was not fully resolved and experience indicated that stator failures would occur after a weight gain of approximately 2%. The oxidation life of 2.7 g/cm³ density one-piece stators is summarized in Figure 4.4.4-8. Sufficient data exists to predict the life of a stator, with reasonable accuracy, after 16 hours of testing at 1930°F. In most cases, 2% weight gain due to oxidation occurs in less than 200 hours At present it is not exactly understood why 2% weight gain is critical.
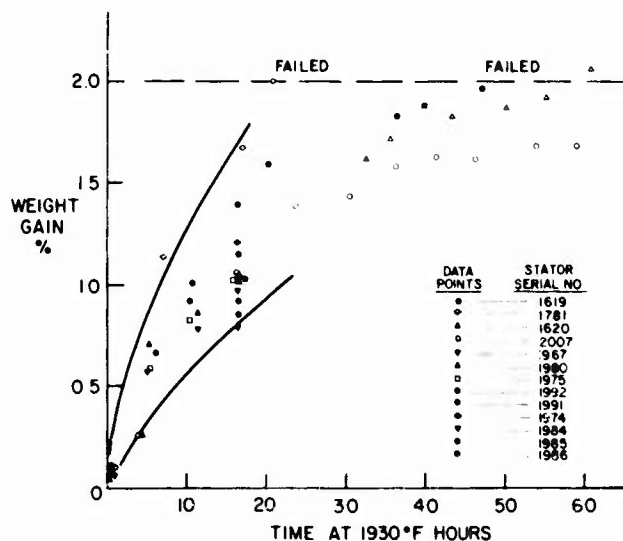
Figure 4.4.4-8 — Weight Gain Vs. Engine Test Time at 1930°F for 2.7 g/cc Density RBSN Stators

196

The second stage stator development closely paralleled that of the first stage stator. Its four major iterations are detailed in Figure 4.4.4-9.

CERAMIC SECOND STAGE STATOR DEVELOPMENT

CONFIGURATION/MODIFICATION	DEVELOPMENTAL RESULTS
• ORIGINAL OESIGN	• TEST RESULTS:
— (33) SEGMENTS OF 2.2 g/cc INJECTION MOLOEO RBSN (1)	— OUTER SHROUO SEGMENT BONO JOINT FAILURES (1)
— INTEGRAL SECOND STAGE SHROUO	• FABRICATION RESULTS:
— AEROOYNAMIC CLEARANCE AT STATOR ID (TO 2ND STAGE ROTOR PLATFORM)	— SEGMENT BONOING MATERIAL LOW OENSITY ANO LOW STRENGTH (1)
• FIRST ITERATION	• TEST RESULTS
— 2NO TIP SHROUO SEPARATE PART (1)	— OUTER SHROUO SEGMENT BOND JOINT FAILURES (2, 3)
— HIGHER OENSITY, HIGHER STRENGTH SLIP CAST MATERIAL USEO AS SEGMENTEO ASSEMBLY BACK-UP RINGS (3)	• OESIGN ANALYSIS
	— NOTCH EFFECT OF SEGMENTED ASSEMBLY INCREASES OUTER SHROUO OUTER SURFACE TENSILE STRESSES OURING START-UP TRANSIENT (4).
• SECONO ITERATION	• TEST RESULTS:
— OUTER SHROUO REDESIGN (INVERTED CHANNEL CONFIGURATION ELIMINATES OUTER SHROUO OUTER SURFACE NOTCHES (4)	— OUTER SHROUO CRACKING (SHORT TIME FAILURES) (3, 4, 5, 6)
	• FABRICATION RESULTS:
— ONE PIECE SLIP CAST SHROUO (4)	— ONE PIECE TOOLING EVALUATEO (NOT POSSIBLE WITH EXISTING BLADE OVERLAP) (7)
	• OESIGN ANALYSIS
	— FLOWPATH REOESIGNED TO ALLOW USE OF COMMON 1ST ANO 2NO STAGE STATORS (7, 6)
• THIRD ITERATION	• TEST RESULTS:
— ONE PIECE INJECTION MOLDED PART (6)	— OUTER SHROUO CRACKING POSSIBLY A FUNCTION OF RATE OF OXIOATICN
— 2.55 g/cc OENSITY RBSN (7)	• FABRICATION RESULTS:
	— EARLY 2.7 g/cc OENSITY MATERIAL OATA INOICATES LOWER OXIOATION RATE (10)
• FOURTH ITERATION	• TEST RESULTS:
— 2.7 g/cc DENSITY RBSN (9)	— EVALUATION NOT COMPLETE
— EXPANOEO PRE-ENGINE TEST QUALIFICATION	• FABRICATION RESULTS:
	— MOLDING PARAMETERS NOT OPTIMIZED FOR 2.7 g/cc OENSITY MATERIAL

Figure 4.4.4-9 — Ceramic Second Stage Stator Development

The incorporation of material developments was identical with that of the first stage stator. The original stators were fabricated in a segmented configuration from 2.2 g/cm^3 density RBSN. The original second stage stator vane, having a less massive base and a shorter chord vane than the first stage design, did not experience extensive vane root or midspan cracking. However, stator shroud cracking was prevalent as in the segmented first stage stator. One-piece tooling in the original second stage blading design was not possible because of blade overlap. A major ceramic flowpath design modification incorporated common first and second stage stators, thus providing monolithic fabrication capability. This reduced the number of components to be developed and took advantage of the successful first stage stator iterative developments.

197

4.4.4.5 Ceramic Tip Shroud Testing

The ceramic turbine rotor tip shrouds were an integral part of the stator assemblies in the original design. With the redesign of the stators to reduce their outer shroud mass, the rotor tip shrouds became separate components. The first iteration design was a simple slotted ring fabricated from cold pressed blanks. Material quality varied widely in the final processed silicon nitride parts and testing at temperature resulted in numerous failures. Figure 4.4.4-10 illustrates the progress in tip shroud development.

CERAMIC ROTOR TIP SHROUD DEVELOPMENT

CONFIGURATION/MODIFICATION	DEVELOPMENTAL RESULTS
• ORIGINAL DESIGN	
— INTEGRAL PART OF STATOR ASSEMBLIES	
• FIRST ITERATION	• TEST RESULTS
— COLD PRESSED BLANK	— FAILURES AT TEMPERATURE (3)
— RBSN	
• SECOND ITERATION	• TEST RESULTS
— SLIP CAST BLANK	— DIMENSIONAL INSTABILITY WITH TIME AT TEMPERATURE (4)
— RBSN (2 3-2 7 g cc DENSITY)	• FABRICATION RESULTS
	— HEAT TREAT BEING INVESTIGATED AS SOLUTION TO DIMENSIONAL INSTABILITY (5, 6)
• THIRD ITERATION	• TEST RESULTS
— HEAT TREATED PRIOR TO TESTING (6)	— DIMENSIONAL STABILITY ESTABLISHED (6)
— INCREASED MASS DUE TO FLOWPATH REDESIGN (7, 8)	OCCASIONAL FAILURES AT TEMPERATURE

Figure 4.4.4-10 — Ceramic Rotor Tip Shroud Development

A material improvement was incorporated through the use of slip cast blanks. Although a majority of short time test failures at temperature were eliminated, a dimensional instability problem remained. A processing heat treatment was developed which pre-oxidized and stabilized the shroud rings. Testing of heat treated rotor tip shrouds established that this heat treatment results in adequate dimensional stability. Several of these shrouds successfully completed the 200-hour goal.

4.4.4.6 Ceramic Flowpath Testing

Testing of the ceramic stationary components combined into either a partial or complete ceramic flowpath occurred when sufficient progress had been made on improving individual components to warrant a reasonable likelihood of success. Two such tests of significant importance are described in this section.

100-Hour Durability Test — The first of these tests occurred about midway in the program,[7] and comprised a 100-hour duty cycle test in an engine using metal turbine rotors (both first- and second-stage). The turbine inlet temperature was maintained at 1930°F in order to avoid degradation of the metal rotors, while engine speed was varied over repeated one-hour cycles as shown in Figure 4.4.4-11.

The ceramic flowpath consisted of the following components:

● Inlet nose cone of 2.2 g/cc density injection molded RBSN.

● One-piece Design C first-stage stator of 2.55 g/cc density injection molded RBSN.

● First- and second-stage rotor tip shrouds of 2.7 g/cc density slip cast RBSN.

● A spacer of 2.7 g/cc density slip cast RBSN was used in place of the segmented second-stage stator, because of consistent outer shroud cracking problems encountered with this design, as noted in Figure 4.4.4-9.

Before the start of the 100-hour test, each component was qualified by Light-off Qualification Testing. The durability testing was done in 15-hour segments, repeating the basic one-hour cycle noted in Figure 4.4.4-11. During each segment, the components were also subjected to two hot shutdowns followed by two hot lights.

Upon completion of the 100-hour test, the nose cone was in good shape and was crack-free. The one-piece first-stage stator had two outer shroud cracks, although the 25 vanes were undamaged and the stator was still serviceable. A complete inspection at 94 hours had shown the stator to be crack free; therefore, these outer shroud cracks occurred between 94 and 100 hours of testing. The two shroud rings and the spacer were in good condition and free from cracking. The results of this duty cycle testing were very encouraging, and constituted a major milestone of the program.
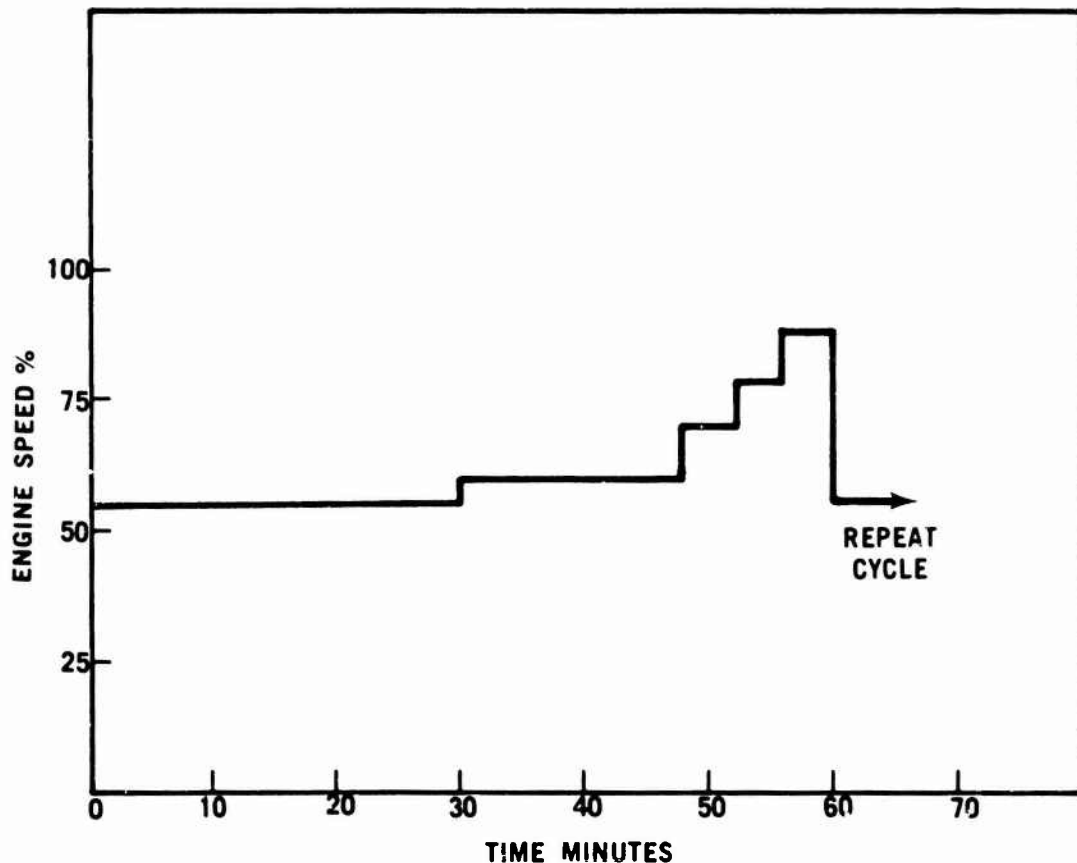
Figure 4.4.4-11 — Durability Duty Cycle For Ceramic Components Tested With Metal Turbine Rotors

200-Hour Durability Test — Later in the program,[12] a 200-hour durability test of a ceramic stationary flowpath was undertaken. The initial increment of 25 hours at 2500°F was run in the 2500°F Flowpath Qualification Test Rig, shown schematically in Figure 3.3.2-12.

The ceramic flowpath consisted of the following components:

- Inlet nose cone of 2.7 g/cc density injection molded RBSN.

- One-piece Design D first-stage stator of 2.7 g/cc density injection molded RBSN.

- First-stage shroud ring of 2.55 g/cc density slip cast RBSN.

- One-piece Design D second-stage stator of 2.7 g/cc density injection molded RBSN.

- A centering ring around the first-stage stator of 2.7 g/cc density slip cast RBSN.

- Second-stage shroud ring of 2.7 g/cc density slip cast RBSN.

Before the start of testing, each component was qualified by the Light-off Qualification Test. The stators were further qualified by the Stator Vane Bend Test and the Stator Outer Shroud Pressure Test.

The 2500°F testing was initially conducted in approximately one-hour increments at one pound per second air flow. Parts were inspected after each increment; these increments were eventually lengthened to two, five, and six hours of testing, with inspection after each increment.

The second-stage rotor tip shroud had a partial crack before testing; after five hours at 2500°F, this crack had propagated through the shroud in a radial direction, creating in effect a slotted shroud. No further change was noted throughout the testing. The first-stage stator developed one crack through the outer shroud after three hours of testing. No further change was noted in this part throughout the testing. The remaining parts were in good condition and free from cracks after 25 hours at 2500°F, and shown in Figure 4.4.4-12.

The remaining testing for 175 hours at 1930°F was conducted on these same compenents in the Ceramic Structures Test Rig, shown schematically in Figure 3.3.2-11. This test was conducted at a constant airflow of 0.75 pounds per second at time increments varying from 4 to 12 hours, with inspection after each increment.

Upon completion of the 175 hours of testing, the nose cone remained in good shape and crack-free. No further cracking was observed in the first stage stator outer shroud, and all 25 vanes were in good shape and free from cracks. The second-stage stator plus the centering ring and the first-stage rotor tip shroud were also in good shape and crack-free. The second-stage shroud ring had no further cracking. All of these hot flowpath components were still serviceable.

The successful completion of 200 hours of durability testing of the entire stationary ceramic hot flowpath at 1930°F and 2500°F constituted attainment of another program milestone, providing further confidence in the feasibility of ceramics for demanding high temperature applications.
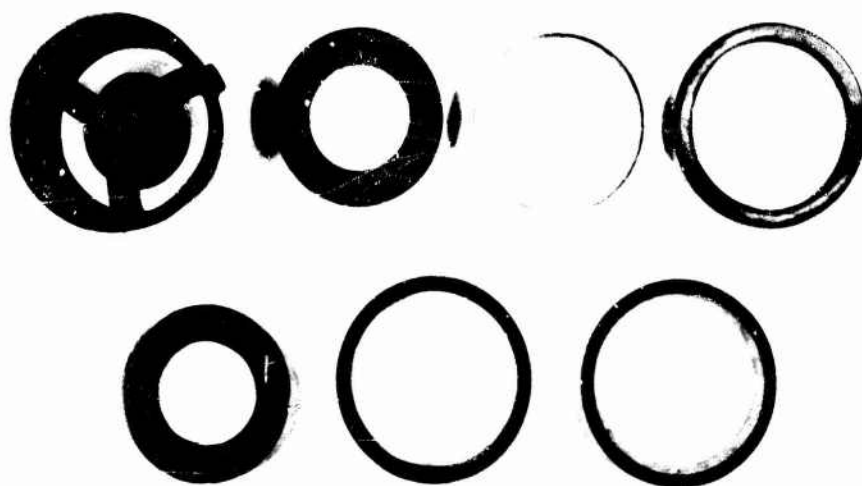
Figure 4.4.4-12 — Ceramic Flowpath Components After 25 Hours of Testing at 2500°F

4.4.4.7 Testing Conclusions

All of the ceramic flowpath components have completed the 200 hour goal, though clearly much remains to be done if these types of components are to achieve widespread application. The 200 hour demonstration is encouraging and suggests that expanded efforts in ceramic technology R&D would be worthwhile. Basic material and process development needs to be pursued as evidenced by the stator oxidation problem. Design and analysis techniques need to be refined along with quality control and NDE to explore and further develop ceramic component reliability.

5. CONCLUSIONS

The program objectives have been largely met. It has been demonstrated that ceramic gas turbine engine components will work, and that they possess adequate durability to prove feasibility. In the demonstration of these objectives, this report points out the progress made in ceramic design, ceramic material and process development, and testing and evaluation which has truly established the basic brittle materials technology goal. In so doing, the materials community has indeed been stimulated, resulting in a wide variety of new programs to further develop and exploit this basic brittle materials technology.

For a more specific exposition of the conclusions and recommendations of the Ford/DARPA program, the reader is directed to the Executive Summary at the beginning of this report.

6. REFERENCES

1. McLean, A. F. et al, "*Brittle Materials Design, High Temperature Gas Turbine,*" AMMRC-CTR-72-3, Interim Report No. 1, March, 1972.

2. ibid, CTR 72-19, No. 2, September, 1972.

3. ibid, CTR 73-9, No. 3, March, 1973.

4. ibid, CTR 73-32, No. 4, September, 1973.

5. ibid, CTR 74-26, No. 5, April, 1974.

6. ibid, CTR 74-59, No. 6, September, 1974.

7. ibid, CTR 75-8, No. 7, April, 1975.

8. ibid, CTR 75-28, No. 8, October, 1975.

9. ibid, CTR 76-12, No. 9, April, 1976.

10. ibid, CTR 76-31, No. 10, October, 1976.

11. ibid, CTR 77-20, No. 11, August, 1977.

12. ibid, TR 78-14, No. 12, Volume 1, March, 1978.

13. ibid, TR 78-14, No. 12, Volume 2, March, 1978.

14. Dukes, W. H., "*Handbook of Brittle Materials Design,*" AGARD AD719-712, Feb., 1971.

15. Weibull, W., "*Statistical Theory of Strength of Materials,*" Ing. Vetenskaps Akademien Number 151, 1939, pages 1-45.

16. Vardar, O. and Finnie, I., "*An Analysis of the Brazilian Disk Fracture Test Using the Weibull Probabilistic Treatment of Brittle Strength,*" International Journal of Fracture, June, 1975.

17. Manson, S. S., Thermal Stress and Low-cycle Fatigue. New York: McGraw Hill, 1966, p. 293.

18. Jeryan, R. A., "*Use of Statistics in Ceramic Design and Evaluation,*" Ceramics for High Performance Applications-II, edited by J. J. Burke et al, Brook Hill Publishing Company, 1978.

19. Evans, A. G. and Wiederhorn, S. M., "*Crack Propagation and Failure Prediction in Silicon Nitride at Elevated Temperature,*" Journal of Material Sciences, 9, 1974, pages 270-278.

20. Paluszny, A. and Nicholls, P. F., "*Predicting Time-Dependent Reliability of Ceramic Rotors,*" Ceramics for High Performance Applications II, edited by J. J. Burke et al, Brook Hill Publishing Company, 1978, pages 94-112.

21. Paluszny, A. and Wu, W., "*Probabilistic Aspects of Designing With Ceramics,*" Transactions of the ASME — Journal of Engineering for Power, Volume 99, Number 4, October, 1977.

22. Evans, A. G., and Wiederhorn, S. M., "*Proof Testing of Ceramic Materials — an Analytical Basis for Failure Prediction,*" International Journal of Fracture, September 1974, pp. 379-392.

23. Mooney, M., "*The Viscosity of a Concentrated Suspension of Spherical Particles,*" J. Colloid Science, Vol. 6, (1951) page 162.

24. Farris, R. T., "*Prediction of the Viscosity of Multimoded Suspensions from Unimoded Viscosity Data,*" Trans Soc Rheology, 12, 2, (1968), page 281.

25. Mangels, J. A., "*Improved Flow Molding Composition,*" U.S. Patent No. 3,926,656, Dec., 1975.

26. Atkinson, A. and Evans, A. D., "*Temperature Gradients in Nitriding Silicon Powder Compacts,*" Journal of the British Ceramics Society, Volume 72, (1974), page 43.

27. Parr, N. L. et al, "*Structural Aspects of Silicon Nitride,*" Powder Metallurgy, Number 8, 1961, page 152.

28. Popper, P. and Ruddlesden, S. N., Transactions of the British Ceramics Society, 1960, 61, 603.

29. Mangels, J. A., "*Creep Resistant Reaction Sintered Silicon Nitride,*" Ceramics for High Performance Applications, edited by J. J. Burke et al, Metal and Ceramics Information Center, Columbus, Ohio, 1974, page 195.

30. Evans, A. G. and Davidge. R. W., "*The Strength and Oxidation of Reaction Sintered Silicon Nitride,*" Journal of Material Sciences. 5, 1970, page 134.

31. Messier, D. R. and Wong, P., "*Kinetics of Nitridation of Silicon Powder Compacts,*" Journal of the American Ceramics Society, Volume 56, Number 9, 1973, page 480.

32. Mangels, J. A., "*Strength-Density-Nitriding Cycle Relationships for Reaction Sintered Silicon Nitride,*" Nitrogen Ceramics, edited by F. L. Riley. Noordhoff International Publishing, Leyden, The Netherlands, 1977, page 569.

33. Mangels, J. A., "*Development of Injection Molded Reaction Bonded Silicon Nitride,*" Ceramics for High Performance Applications II, edited by J. J. Burke et al, Brook Hill Publishing Company, 1978, page 113.

34. Messier, D. R. and Wong, P., "*Kinetics of Formulation and Mechanical Properties of Reaction Sintered Silicon Nitride,*" Ceramics for High Performance Applications, edited by Burke, J. J. et al, Metal and Ceramics Information Center, Columbus, Ohio, 1974.

35. Danforth, S. C., "*Effective Control of the Microstructure of Reaction Bonded Si₃N₄ As Related to Improved Mechanical Properties,*" Ph.D. Thesis, Brown University, 1978.

36. Lindley, M. W. and Jones, B. F., "*Reaction Sintered Silicon Nitride,*" Journal of Material Sciences, 11, 1976, page 1288.

37. Jennings, H. M. and Richman, M. H., "*Structure, Formation Mechanisms and Kinetics of Reaction Bonded Silicon Nitride,*" Journal of Material Sciences, 11, 1976, page 2087.

38. Lumby, R. J., "*Method of Manufacturing Silicon Nitride,*" U.S. Patent Number 3,591,337, July 6, 1971.

39. Mangels, J. A., "*Effect of H₂-N₂ Nitriding Atmospheres on the Properties of Reaction Sintered Silicon Nitride,*" Journal of the American Ceramics Society. Volume 58, Numbers 7 and 8, 1975.

40. Lindley, M. W. and Jones, B. F., "*The Influence of Hydrogen in the Nitriding Gas on the Strength of Reaction Sintered Silicon Nitride,*" Journal of Material Sciences, 11, 1976, page 1969.

41. Lin, S., "*Mass Spectrometric Studies of the Nitridation of Silicon,*" Journal of the American Ceramics Society, Volume 58, Number 7, 1975, page 271.

42. Wild, S. et al, "*Role of Silicon Monoxide in the Production and Stability of Silicon Nitrides and Oxynitrides,*" at 74th Annual Meeting of the American Ceramic Society, Washington, D.C., May, 1972.

43. Elias, D. P., Jones, B. F. and Lindley, M. W., "*The Formation of α and β Phases in Reaction Sintered Si₃N₄ and Their Influence on Strength*," Powder Metallurgy International, Volume 8, Number 4, November, 1976, page 162.

44. Marks, L. S., Mechanical Engineering Handbook, McGraw-Hill Book Company, 1958, pages 4-95.

45. Kirk, R. E. and Othmer, D. F., Encyclopedia of Chemical Technology, The Interscience Encyclopedia, Inc., New York, 1947, Volume I, pages 782-790.

46. Wong, P. and Messier, D. R., "*Procedure for Fabrication of Si₃N₄ by Rate Controlled Reaction Sintering*," American Ceramic Society Bulletin, Volume 57, Number 5, 1978, page 525.

47. Waugh, J. S. and Joremchuk, M. M., "*Reaction Sintered Silicon Nitride Material Optimization for Random Applications*," Air Force Materials Laboratory Interim Report S1878, Contract Number F33615-74-C-5160, September, 1975.

48. Suzuki, H., "*The Synthesis and Properties of Silicon Nitride*," Bulletin of the Tokyo Institute of Technology, Number 54, 1963, page 163.

49. Leake, J. A. and Jayaticaka, A. deS., "*The Rôle of Impurities in the Formation of Reaction Bonded Silicon Nitride*," Nitrogen Ceramics, edited by F. L. Riley, NOORDHOFF, 1977, page 289.

50. Boyer, S. M., Sang, D. and Moulson, A. J., "*The Effect of Iron on the Nitridation of Silicon Powder*," Nitrogen Ceramics, editor F. L. Riley, NOORDHOFF, 1977, page 297.

51. Mangels, J. A. and Watt, D. F., "*Creep Behavior of Reaction Sintered Silicon Nitride*," Bulletin of the American Ceramics Society, Volume 53, Number 4, 1974, page 395.

52. Mangels, J. A., "*High Temperature, Time Dependent Physical Property Characterization of Reaction Bonded Silicon Nitride*," Nitrogen Ceramics, edited by F. L. Riley, Noordhoff International Publishing, Leyden, The Netherlands, 1977, page 589.

53. Larsen, D. C., Walther, G. C., "*Property Screening and Evaluation of Ceramic Turbine Engine Materials*," Air Force Contract F33615-75-C-5196, Interim Technical Report No. 5, Jan., 1978.

54. Quinn, G. D., "*Characterization of Turbine Ceramics at the Long-Term Environmental Exposure*," AMMRC TR80-15, Final Report, April, 1980.

55. Mangels, J. A., "*Method of Increasing the Oxidation Resistance of Silicon Nitride*," U.S. Patent No. 3,983,198, Sept., 1976.

56. Hausner, H. H. and Poster, A. R., "*Slip Casting of Metal Powders and Metal-Ceramic Combinations*," Powder Metallurgy, edited by W. Leszynski, New York: Interscience Publishers, 1961, pages 461-506.

57. Overbeek, J. T. G., Colloid Science, Volume I, New York, Elsevier Publishing Company, 1952.

58. Saint Pierre, P. D. S., "*Slip Casting Metals*," General Electric Research Report 59-RL-2281M, October, 1959.

59. Kingery, W. D., Ceramic Fabrication Processes, Cambridge, Massachusetts: The M.I.T. Press, 1958.

60. Dobrovol'skii, A. G. and Dem'yanchuk, V. G., "*Production of Molybdenum Parts by Slip Casting*," Poroshkovaya Metallurgiya, Number 8(56) (August, 1967), 1-6.

61. Dobrovol'skii, A. G. and Nazarchuk, N. V., "*Slip Casting of Molybdenum Disilicide*," Poroshkovaya Metallurgiya, Number 5 (May, 1966), 1-8.

62. Ezis, A., "The Fabrication and Properties of Slip-Cast Silicon Nitride," Proceedings of the Second Army Materials Technology Conference, Brook Hill Publishing Company, Chestnut Hill, Massachusetts, 1974, pages 207-222.

63. Goodyear, M. U. and Ezis, A., "Joining of Turbine Engine Ceramics," Proceedings of the Fourth Army Materials Technology Conference, Brook Hill Publishing Company, Chestnut Hill, Massachusetts, 1976, pages 133-153.

64. Willermet, P. A. et al, "Development and Processing of Injection Molded, Reaction Sintered Silicon Carbide Compositions," Ceramic Bulletin, 57, 8, August, 1978, pages 744-747.

65. Whalen, T. J. and Anderson, A. T., "The Wetting of Silicon Carbide, Silicon Nitride and Carbon by Silicon and Binary Silicon Alloys," Journal of the American Ceramic Society, 54, 396, 1975.

66. Whalen, T. J. et al, "Progress on Injection Molded, Reaction Bonded Silicon Carbide," Ceramics for High Performance Applications II, edited by J. J. Burke et al, Brook Hill Publishing Company, 1978.

67. Whalen, R. J. and Terner, L. L., "Surface Condition and Strength of Silicon Carbide — Silicon Materials," to be published in Proceedings of the Symposium on Ceramic Machining and Surface Finishing held at the National Bureau of Standards, Gaithersburg, Maryland, November 12-15, 1978.

68. Thompson, D. O., "Proceedings of the ARPA/AFML Review of Progress in Quantitative NDE," AFML-TR-78-205, Fourth Annual Report, July 1, 1977 — June 30, 1978, January, 1979.

69. Kupperman, D. S. et al, "Nondestructive Evaluation Techniques for Silicon Carbide Heat-Exchanger Tubes," ANL-79-103, Second Annual Report, October, 1978 — September, 1979, November, 1979.

70. McLean, A. F. and Baker, R. R., "Brittle Materials Design, High Temperature Gas Turbine," AMMRC TR 79-11, Interim Report No. 13, February, 1979.

71. Ainley, D. G. and Mathieson, G. C. R., "A Method of Performance Estimation for Axial-Flow Turbines," ARC Reports and Memoranda Number 2974, December, 1951, Her Majesty's Stationery Office.

72. Dunham, J. and Came, P. M., "Improvements to the Ainley-Mathieson Method of Turbine Performance Prediction," ASME Paper 70-GT-2, 1970.

73. Katsanis, T., "FORTRAN Program for Calculating Transonic Velocities on a Blade-to-Blade Stream Surface of a Turbomachine," NASA-TN-D-5427, 1969.

74. Grant, J. W. and Davis, D. A., "Aerodynamic Design Considerations for Ceramic Axial Turbines," Proceedings of the Fifth Army Materials Technology Conference, Newport, Rhode Island March, 1977.

ARMY MATERIALS AND MECHANICS RESEARCH CENTER
WATERTOWN, MASSACHUSETTS 02172

TECHNICAL REPORT DISTRIBUTION

No. of Copies	To
	Office of the Under Secretary of Defense for Research and Engineering, The Pentagon, Washington, D. C. 20301
1	ATTN: Mr. J. Persh
1	Dr. G. Gamota
12	Commander, Defense Technical Information Center, Cameron Station, Building 5, 5010 Duke Street, Alexandria, Virginia 22314
1	National Technical Information Service, 5285 Port Royal Road, Springfield, Virginia 22161
	Director, Defense Advanced Research Projects Agency, 1400 Wilson Boulevard, Arlington, Virginia 22209
2	ATTN: Dr. Van Reuth
1	Major L. Jacobson
	Battelle Columbus Laboratories, Metals and Ceramics Information Center, 505 King Avenue, Columbus, Ohio 43201
1	ATTN: Mr. Winston Duckworth
1	Dr. D. Niesz
1	Dr. R. Wills
	Deputy Chief of Staff, Research, Development, and Acquisition, Headquarters, Department of the Army, Washington, D.C. 20310
1	ATTN: DAMA-ARZ
1	DAMA-CSS, Dr. J. Bryant
	Commander, Army Research Office, P.O. Box 12211, Research Triangle Park, North Carolina 27709
1	ATTN: Information Processing Office
1	Dr. G. Mayer
1	Dr. J. Hurt
	Commander, U. S. Army Material Development and Readiness Command, 5001 Eisenhower Avenue, Alexandria, Virginia 22333
1	ATTN: DRCDMD-ST
1	DRCLDC
	Commander, Harry Diamond Laboratories, 2800 Powder Mill, Road, Adelphi, Maryland 20783
1	ATTN: Col. W. Benoit
1	Technical Information Office
	Commander, U.S. Army Missile Command, Redstone Arsenal, Alabama 35809
1	ATTN. Mr. P. Ormsby

ARMY MATERIALS AND MECHANICS RESEARCH CENTER
WATERTOWN, MASSACHUSETTS 02172

TECHNICAL REPORT DISTRIBUTION

No. of Copies	To
	Commander, U.S. Army Aviation Research and Development Command, P.O. Box 209, St. Louis, Missouri 63166
1	ATTN: DRDAV-EXT
1	DRDAV-QE
1	Technical Library
	Commander, U.S. Army Natick Research and Development Command, Natick, Massachusetts 07160
1	ATTN: Technical Library
1	Dr. J. Hanson
	Commander, U.S. Army Tank-Automotive Research and Development Command, Warren, Michigan 48090
1	ATTN: Dr. W. Bryzik
1	Mr. E. Hamperian
1	D. Rose
1	DRDTA-RKA, Dr. J. Chevalier
1	DRDTA-UL, Technical Library
1	DRDTA-R
	Commander, U.S. Army Armament Research and Development Command, Dover, New Jersey 07801
1	ATTN: Mr. J. Lannon
1	Technical Library
	Commander, U.S. Army Armament Material Readiness Command, Rock Island, Illinois 61299
1	ATTN: Technical Library
	Commander, U.S. Army Mobility Equipment Research and Development Command, Fort Belvoir, Virginia 22060
2	ATTN: DRDME-EM, Mr. W. McGovern
1	DRDME-V, Mr. E. York
	Commander, U.S. Army Foreign Science and Technology Center, 220 7th Street, N.E., Charlottesville, Virginia 22901
1	ATTN: Military Tech., Mr. W. Marley
	Commander, Watervliet Arsenal, Watervliet, New York 12189
1	ATTN: Dr. T. Davidson
	Director, Eustis Directorate, U.S. Army Mobility Research and Development Laboratory, Fort Eustis, Virginia 23604
1	ATTN: Mr. J. Lane
1	Mr. G. Eliot

ARMY MATERIALS AND MECHANICS RESEARCH CENTER
WATERTOWN, MASSACHUSETTS 02172

TECHNICAL REPORT DISTRIBUTION

No. of Copies	To
	Technical Director, Human Engineering Laboratories, Aberdeen Proving Ground, Maryland 21005
1	ATTN: Technical Reports Office
	Chief of Naval Research, Arlington, Virginia 22217
1	ATTN: Code 471
1	Dr. A. Diness
1	Dr. R. Pohanka
	Naval Research Laboratory, Washington, D.C. 20375
2	ATTN: Mr. R. Rice
	Headquarters, Naval Air Systems Command, Washington, D.C. 20360
1	ATTN: Code 5203
1	Code MAT-042M
	Commander, Naval Weapons Center, China Lake, California 93555
1	ATTN: Mr. F. Markarian
	Commander, U.S. Air Force of Scientific Research, Building 410, Bolling Air Force Base, Washington, D.C. 20332
1	ATTN: Capt. Wax
	Commander, U.S. Air Force Materials Laboratory, Wright-Patterson Air Force Base, Ohio 45433
1	ATTN: Dr. N. Tallan
1	Dr. H. Graham
1	Dr. R. Ruh
1	Mr. K. S. Mazdiyasni
1	Aero Propulsion Labs, Mr. R. Marsh
	National Aeronautics and Space Administration, Washington, D.C. 20546
1	ATTN: Mr. G. C. Deutsch — Code RW
1	Mr. C. Bersch
1	AFSS-AD, Office of Scientific and Technical Information
	National Aeronautics and Space Administration, Lewis Research Center, 21000 Brookpark Road, Cleveland, Ohio 44135
1	ATTN: J. Accurio, USAMRDL
1	Dr. H. B. Probst, MS 49-1
1	Dr. S. Dutta
1	S. Grissaffe
	National Aeronautics and Space Administration, Langley Research Center, Hampton, Virginia 23665
1	ATTN: Mr. J. Buckley, Mail Stop 387

TECHNICAL REPORT DISTRIBUTION

No. of Copies	To
	Department of Energy, Division of Transportation, 20 Massachusetts Avenue, N. W., Washington, D.C. 20545
2	ATTN: Mr. Robert Schulz (TEC)
1	Mr. Paul Lombardi
	Department of Transportation, 400 Seventh Street, S.W., Washington D.C. 20590
1	ATTN: Mr. M. Lauriente
1	Mechanical Properties Data Center, Belfour Stulen Inc., 13917 W. Bay Shore Drive, Traverse City, Michigan 49684
	National Bureau of Standards, Washington, D.C. 20234
1	ATTN: Dr. S. Wiederhorn
1	Dr. J. B. Wachtman
1	Dr. N. Tighe
	National Research Council, National Materials Advisory Board, 2101 Constitution Avenue, Washington, D.C. 20418
1	ATTN: D. Groves
1	R. M. Spriggs
	National Science Foundation, Washington, D.C. 20550
1	ATTN: B. Koepke
	Admiralty Materials Technology Establishment, Polle, Dorset BH16 6JU, United Kingdom
1	ATTN: Dr. D. Godfrey
	The Aerospace Corporation
1	Dr. Louis Rubin, P.O. Box 92957, Los Angeles, California 90009
	AiResearch Manufacturing Company, AiResearch Casting Company, 2525 West 190th Street, Torrance, California 90505
1	ATTN: Mr. K. Styhr
1	Dr. D. Kotchick
	AiResearch Manufacturing Company, Materials Engineering Dept., 111 South 34th Street, P.O. Box 5217, Phoenix, Arizona 85010
1	ATTN: Mr. D. W. Richerson, MS 93-393/503-44
1	Dr. W. Carruthers
1	M. K. Johanson
1	Mr. D. R. Kreiner
1	Mr. R. A. Rackley
1	Mr. E. E. Strain
	AVCO Corporation, Applied Technology Division, Lowell Industrial Park, Lowell, Massachusetts 01887
1	ATTN: Dr. T. Vasilos

ARMY MATERIALS AND MECHANICS RESEARCH CENTER
WATERTOWN, MASSACHUSETTS 02172

TECHNICAL REPORT DISTRIBUTION

No. of Copies	To
	Babcock and Wilcox
1	Dr. A. W. Illyn, Technical Director, Refractories Division, Old Savannah Road, Augusta, Georgia 30903
	Bell Aerospace Company
1	Dr. Wilfred H. Dukes, Assistant Director Engineering for Development, P.O. Box 29307, New Orleans, Louisiana 70189
	Brown University
1	Professor Marc Richman, Engineering Division, Providence, Rhode Island 02912
	Cabot Corporation Stellite Division
1	Dr. H. J. Klien, Director of Technology, 1020 West Park Avenue, Kokomo, Indiana 46901
	Carborundum Company, Research and Development Division, P.O. Box 1054, Niagara Falls, New York 14302
1	ATTN: Dr. J. A. Coppola
1	Dr. M. Srinivasan
1	Dr. R. Phoenix
1	Mr. W. Long
	Caterpillar Tractor Company
1	Mr. A. R. Canady, Technical Center, Building F, Peoria, Illinois 61602
	Ceramic Finishing Company
1	Dr. H. P. Kirchner, P.O. Box 498, State College, Pennsylvania 16801
	Ceramic Systems Incorporated
1	Mr. Eldor R. Herrmann, 11402 Schaefer Highway, Detroit, Michigan 48227
	Chrysler Corporation
1	Mr. Philip J. Willson, Chemical Research, Box 1118, CIMS: 418-19-18, Detroit, Michigan 48231
	Coors Porcelain Company
1	Research Department, 17750 West 32nd Avenue, Golden, Colorado 80401
	Corning Glass Works, Research Department, Corning, New York 14832
1	ATTN: Mr. J. Lanning
	Cummins Engine Company, Columbus, Indiana 47201
1	ATTN: Mr. R. Kamo
1	Mr. M. Woods

ARMY MATERIALS AND MECHANICS RESEARCH CENTER
WATERTOWN, MASSACHUSETTS 02172

TECHNICAL REPORT DISTRIBUTION

No. of Copies	To
	Defence Research Establishment Pacific, FMO, Victoria, B.C., VOS IBO, Canada
1	ATTN: R. D. Barer
	Deposits and Composites, Inc., 1821 Michael Faraday Drive, Reston, Virginia 22090
1	ATTN: Mr. R. E. Engdahl
	Eaton Corporation
1	Dr. L. Eltinge, Research Center
	26201 Northwestern Highway, Southfield, Michigan 48076
	Electric Power Research Institute, P.O. Box 10412, 3412 Hillview Avenue, Palo Alto, California 94304
1	ATTN: Dr. A. Cohn
	European Research Office, 223 Old Maryleborne Road, London, NW1 — 5th, England
1	ATTN: Dr. F. Rothwarf
1	Lt. Col. J. Kennedy
	Gas Turbine World
1	Mr. Victor de Biasi, Editor, P.O. Box 494,
	Southport, Connecticut 06490
	General Electric Company, Research and Development Center, Box 8, Schenectady, New York 12345
1	ATTN: Dr. R. J. Charles
1	Dr. C. D. Greskovich
1	Dr. S. Prochazka
	General Electric Company, Mail Stop H-99, Cincinnatti, Ohio 45215
1	ATTN: Mr. W. Nelson
	General Electric Company, Vally Forge Space Center, Box 8555, Philadelphia, Pa. 19101
1	ATTN: Mr. L. R. McCreight
	General Motors Corporation, AC Spark Plug Division, Flint, Michigan 43556
1	ATTN: Dr. M. Berg
	General Motors Corporation, Research Laboratories, Warren, Michigan 48090
1	ATTN: Mr. Paul Vickers, Fluid Dynamics Department
	General Motors Corporation, Detroit Diesel Allison Division, P.O. Box 894, Indianapolis, Indiana 46206
1	ATTN: Dr. P. Heitman
1	D. M. Herman
	Georgia Institute of Technology, EES, Atlanta, Georgia 30332
1	ATTN: Mr. J. D. Walton

ARMY MATERIALS AND MECHANICS RESEARCH CENTER
WATERTOWN, MASSACHUSETTS 02172

TECHNICAL REPORT DISTRIBUTION

No. of Copies	To
	GTE Laboratories, Waltham Research Center, 40 Sylvan Road, Waltham, Massachusetts 02154
1	ATTN: Dr. C. Quackenbush
1	Dr. W. H. Rhodes
1	Dr. D. T. Smith
	IIT Research Institute, 10 West 35th Street, Chicago, Illinois 60616
1	ATTN: Mr. S. Bortz, Director, Ceramics Research
1	Dr. D. Larsen
	Institute for Werkstoff-Forshung, DFVLR, 505 Porz-Wahn, Linder Hohe, Germany
1	ATTN: Dr. W. Bunk
	International Harvester, Solar Division, 2200 Pacific Highway, P.O. Box 80966, San Diego, California 92138
1	ATTN: Dr. A. Metcalfe
1	Ms. M. E. Gulden
	Jet Propulsion Laboratory — C.I.T., 4800 Oak Grove Drive, Pasadena, California 91103
1	ATTN: Dr. R. Smoak
	Kawecki Berylco Industries, Inc., P.O. Box 1462, Reading, Pennsylvania 19603
1	ATTN: Mr. R. J. Longenecker
	Martin Marietta Laboratories, 1450 South Rolling Road, Baltimore, Maryland 21227
1	ATTN: Dr. J. Venables
	Massachusetts Institute of Technology, Department of Metallurgy and Materials Science, Cambridge, Massachusetts 02139
1	ATTN: Prof. R. L. Coble
1	Prof. H. K. Bowen
1	Prof. W. D. Kingery
1	Prof. R. Cannon
1	Prof. F. S. McClintock
	Materials Research Laboratories, P.O. Box 50, Ascot Vale, VIC 3032, Australia
1	ATTN: Dr C. W. Weaver
	Mechanical Technology, Incorporated
1	Mr. D. W. McLaughlin, Research and Development Division, 968 Albany-Shaker Road, Latham, New York 12110
	Midwest Research Institute, 425 Volker Boulevard, Kansas City, Missouri 64110
1	ATTN: Mr. G. W. Gross, Head, Physics Station

ARMY MATERIALS AND MECHANICS RESEARCH CENTER
WATERTOWN, MASSACHUSETTS 02172

TECHNICAL REPORT DISTRIBUTION

No. of Copies	To
	Norton Company, Worcester, Massachusetts 01606
1	ATTN: Dr. N. Ault
1	Dr. M. L. Torti
	Owens Illinois
1	Mr. Y. K. Pei, 1020 North Westwood Avenue, Toledo, Ohio 43607
	PPG Industries, Incorporated
1	Mr. F. G. Stroke, Asst. Manager Market Development, 1 Gateway Center, Pittsburgh, Pennsylvania 06108
	Pennsylvania State University, Materials Research Laboratory, Materials Science Department, University Park, Pennsylvania 16802
1	ATTN: Prof. R. Roy
1	Prof. R. E. Tressler
1	Prof. R. Bradt
1	Prof. V. S. Stubican
	Pratt and Whitney Aircraft, P.O. Box 2691, W. Palm Beach, Florida 33402
1	ATTN: Mr. M. Mendelson Mail Stop B-08
	Program Development Consultants
1	Dr. Robert Harmon, 25 Schalren Drive, Latham, New York 12110
	The Rand Corporation
1	Dr. Eugene C. Grittor., Physical Sciences Department, 1700 Main Street, Santa Monica, California 90406
	Raytheon Company
1	Ms. Madaleine Bennett, Librarian, Research Division Library, Foundry Avenue, Waltham, Massachusetts 02154
	PSC, Box 1044, APO San Francisco 96328
1	ATTN: Major A. A. Borges
	Rockwell International Science Center, 1049 Camino Dos Rios, Thousand Oaks, California 91360
1	ATTN: Dr. F. Lange
	Royal Aircraft Establishment, Materials Department, R 178 Building, Farnborough, Hants, England
1	ATTN: Dr. N. Corney
	Shane Associates, Inc., 7821 Carrleigh Parkway, Springfield, Virginia 22152
1	ATTN: Dr. R. S. Shane, Consultant

ARMY MATERIALS AND MECHANICS RESEARCH CENTER
WATERTOWN, MASSACHUSETTS 02172

TECHNICAL REPORT DISTRIBUTION

No. of Copies	To
	Solar Turbine International, 2200 Pacific Coast Highway, San Diego, California 92138
1	ATTN: Mr. A. Russel
	Stanford Research International, 333 Ravenswood Avenue, Menlo Park, California 94025
1	ATTN: Dr. P. Jorgensen
1	Dr. D. Rowcliffe
	State University of New York at Stony Brook, Department of Materials Science, Long Island, New York 11790
1	ATTN: Prof. F. F. Y. Wang
	Union Carbide Corporation
1	Dr. O. Conrad Trulson, Carbide Products Division, 270 Park Avenue, New York, New York 10017
	United Technologies Research Center, East Hartford, Connecticut 06108
1	ATTN: Dr. J. Brennan
1	Dr. F. Galasso
	University of Illinois, Engineering College, Urbana, Illinois 61801
1	ATTN: Dr. C. Bergeron
1	Dean Daniel C. Drucker
	University of California, Lawrence Livermore Laboraty, P.O. Box 808, Livermore, California 94550
1	ATTN: Mr. R. Landingham
1	Dr. C. F. Cline
	University of California, Department of Materials Science and Engineering, Hearst Building, Berkeley, California 94720
1	ATTN: Dr. D. Clarke
1	Prof. A. E. Evans
	University of Florida, Department of Materials Science and Engineering, Gainesville, Florida 32601
1	ATTN: Dr. L. Hench
	University of Massachusetts, Department of Mechanical Engineering, Amherst, Massachusetts 01003
1	ATTN: Prof. K. Jakus
1	Prof. J. Ritter
	University of Michigan
1	Professor Edward E. Hucke, Materials and Metallurgical Engineering, Ann Arbor, Michigan 48104
1	Dr. Maurice J. Sinnot, Department of Chemical and Metallurgical Engineering, Ann Arbor, Michigan 48104

ARMY MATERIALS AND MECHANICS RESEARCH CENTER
WATERTOWN, MASSACHUSETTS 02172

TECHNICAL REPORT DISTRIBUTION

No. of Copies	To
	University of Newcastle Upon Tyne, Department of Metallurgy and Engineering Materials, Newcastle Upon Tyne, NEI 7 RU, England
1	ATTN: Prof. K. H. Jack
	University of Washington, Ceramic Engineering Division, FB-10, Seattle, Washington 98195
2	ATTN: Prof. J. I. Mueller
1	Prof. R. Taggert
1	Prof. A. D. Miller
1	Prof. R. J. H. Bollard
1	Prof. W. D. Scott
1	Prof. A. S. Kobayashi
1	Prof. B. J. Hartz
1	Prof. J. L. Bjorkstam
	V.P.I., Department of Materials Engineering, Blacksburg, Virginia 24061
1	ATTN: Prof. D. P. H. Hasselman
	Westinghouse Electric Corporation, Research Laboratories, Pittsburgh, Pennsylvania 15235
1	ATTN: Dr. R. J. Bratton
1	Dr. R. Kossowsky
1	Mr. D. Miller
	Williams Research Corporation
1	Mr. W. Chapman, Walled Lake, Michigan 48088
	Mr. P. Annese, Bomas Machine Specialities, 114 North Beacon Street,
1	Brighton, Massachusetts 02135
	Mr. R. Keyes, 200 Boring Place, Martinsville, Indiana 46151
2	
	C. H. Sump, Combustion Engineering Inc., 911 West Main Street,
1	Chattanooga, Tennessee 37402

ARMY MATERIALS AND MECHANICS RESEARCH CENTER
WATERTOWN, MASSACHUSETTS 02172

TECHNICAL REPORT DISTRIBUTION

No. of Copies	To
	Director, Army Materials and Mechanics Research Center, Watertown, Massachusetts 02172
2	ATTN: DRXMR-PL
1	DRXMR-WD
1	Dr. R. Katz
1	Dr. E. Lenoe
1	Dr. E. Wright
1	Mr. M. Cahill
1	Mr. G. Quinn
1	Dr. R. Shea
1	Dr. G. Gazza
1	Dr. D. Messier
1	Dr. R. Chait
1	Dr. R. French
	FMC Corporation
1	Dr. Alvin Gorum, Ordinance Engineering Division, 1105 Coleman, Box 1201, San Jose, California
	General Electric Company
1	Mr. Al Bellin, 1000 Western Avenue, Lynn, Massachusetts 01910

AD ———

Army Materials and Mechanics Research Center
Watertown, Massachusetts 02172

BRITTLE MATERIALS DESIGN
HIGH TEMPERATURE GAS TURBINE

Arthur F. McLean, Eugene A. Fisher,
Ford Motor Company, Dearborn, Michigan 48121

Technical Report AMMRC TR 81-14, March 1981
206 pages, 211 illus. 34 tables, 74 references
Contract DAAG 46-71-C-0162, ARPA Order Number
1849 Final Report, July 1, 1971 to August 31, 1979

Key Words

Gas Turbine Engine
Brittle Design
Ceramics
High Temperature Materials
Silicon Nitride
Silicon Carbide
Non-Destructive Tests
Mechanical Properties

Starting in July 1971, the Defense Advanced Research Projects Agency (DARPA) sponsored a joint program with the Ford Motor Company to demonstrate and encourage the use of brittle materials in engineering design. The program, which was to be a total systems iterative approach to high temperature structural design with ceramics in highly stressed applications, focused on the development of ceramic components for gas turbine application. A goal of 200 hours of engine or engine rig demonstration for representative duty cycle temperatures in a regenerated vehicular gas turbine was chosen, with uncooled ceramic components to operate at least 25 hours at 2500°F, considerably beyond the temperatures possible with uncooled metal components. The total systems approach included major efforts in ceramic design, materials development, fabrication process development, and test and evaluation methodology. Considerable progress was made in each of these areas during the course of the program. For example, the strength of reaction bonded silicon nitride (RBSN) used in the stator and rotor blades was more than tripled between July 1971 and July 1977.

By the end of the program, 200 hours of duty cycle durability on turbine test rigs (between 1930°F — 2500°F) was attained on RBSN stationary components including stators, nose cones and turbine rotor tip shrouds. Similarly, 200 hours of duty cycling on test rigs was attained with reaction sintered SiC combustors and stators. A 200 hour test of a duo-density silicon nitride rotor with 1800°F rim temperatures, with maximum blade temperatures of approximately 2200°F, was run at speeds to 50,000 rpm. Engine tests of up to 100 hours duration were run with an entire uncooled ceramic stationary flow path (only the rotors being metallic) at up to 87% of engine design speed at 1930°F. A 37 hour engine rig test was run with an uncooled ceramic rotor at temperatures up to 2500°F and speeds up to 50,000 RPM (100% Design E speed).

The program demonstrated that design with brittle materials in highly stressed applications is possible and, in particular, that ceramics as major structural components in gas turbine engines are feasible.